



UCL

UNIVERSITY COLLEGE LONDON

Faculty of Mathematics and Physical Sciences

Department of Physics & Astronomy

GALACTIC-SCALE OUTFLOWS IN GALAXIES OF THE LOCAL UNIVERSE

Thesis submitted for the Degree of Doctor of
Philosophy of the University of London

by

Guido Roberts-Borsani

Supervisors:

Dr. Amélie Saintonge

Prof. Richard Ellis

Examiners:

Dr. Thomas Greve

Dr. Marc Sarzi

September 25, 2019

I, Guido Roberts-Borsani, confirm that the work presented in this Thesis is my own. Where information has been derived from other sources, I confirm that this has been indicated in the Thesis. In particular, I note these contributions:

- The work presented in Chapter 2 and Chapter 3 (and Appendix A) has been published in [Roberts-Borsani & Saintonge \(2019\)](#).
- The work presented in Chapter 4 and Chapter 5 (and Appendices B and C) will shortly be submitted for publication in Roberts-Borsani & Saintonge (in prep.).
- The work presented in Chapter 6 and Appendix D has been published in [Roberts-Borsani et al. \(2017\)](#) and was a collaborative effort conducted primarily between myself, Dr. Katherine Alatalo, Dr. Maria-Jesus Jiménez-Donaire, Dr. Mario Dapr a and the Atacama Cosmology Telescope collaboration after obtaining data during the IRAM 30m 2015 summer school. Observations with the ACT, LMT, SALT and CARMA were all conducted by the ACT collaboration or co-authors of the paper, whilst all observations with the IRAM 30m telescope were conducted by myself and the primary co-authors of the paper. The data reduction of the IRAM 30m data was conducted by Mario Dapr a and myself. The extraction of multiwavelength photometry using SExtractor was done by Dr. Nicolas Laporte, and the SED modelling of the photometry was done by both myself and Dr. Nicolas Laporte using methodologies and instructions that I outlined. The RADEX modelling was performed by Dr. Maria Jesus Jim enez-Donaire and the morphological analysis of ACT J2029 was performed by Dr. Jack Hughes.
- I also acknowledge and thank (in order of Thesis Chapters) the following people, who have contributed to aspects of the research in this Thesis either via useful discussions with myself, or via the private communication of data or codes: Yan-Mei Chen, Filippo Fraternali, Isabella Lamperti, Gicchino Accurso, Tim Heckman, Kate Rubin, Sylvain Veilleux, Claudia Maraston, Karen Masters, David Stark, Am elie

Saintonge, Thomas Greve, Richard Tunnard, Barbara Catinella and the anonymous referees of the resulting publications.

- I would also like to acknowledge and thank the Royal Society, who provided the grants to fund my Ph.D.

Abstract

Galactic-scale gas outflows form a crucial ingredient in today's galaxy evolution models and are thought to regulate the gas contents - and therefore evolution - of galaxies. However, outflows are poorly understood, and thus far have been studied primarily in extreme objects rather than the normal star-forming populations. As such, several outstanding questions remain and determining the prevalence and properties of outflows in normal, star-forming galaxies, as well as their quenching potential is a prerequisite towards obtaining a complete picture of galaxy evolution. Specifically, major questions include: What is the prevalence of outflows in normal galaxies and what are their main drivers and properties? Are the properties of outflows enhanced by the presence of an AGN? What are the kpc-scale properties of outflows? Are outflows seen in all gas phases and what are their relative fractions?

This Thesis aims to answer these questions by making use of the largest integrated and IFU spectroscopic data sets currently available such as the SDSS, MaNGA, xCOLD GASS, xGASS and ALFALFA surveys. Using the NaD ISM doublet and a variety of stacking techniques, we investigate the large-scale prevalence and properties of outflows in normal galaxies at $z \sim 0$ with SDSS spectra, the kpc-scale outflow properties and their relation to galaxy properties with MaNGA IFU spectra, and finally investigate the multi-phase (i.e., molecular, neutral and ionised) nature of outflows with a stacking analysis of CO(1-0), HI 21cm, NaD and H α tracers using the xCOLD GASS, xGASS, ALFALFA and MaNGA surveys. The Thesis finishes off with the investigation of the possible presence of a molecular gas outflow in a high redshift, lensed galaxy for which multitransitional CO and CI spectra were obtained with the IRAM 30m telescope.

Impact Statement

In this Thesis I have used some of the largest, state-of-the-art galaxy surveys to constrain the role of outflows in local galaxy evolution. Whilst the prevalence and properties of outflows on large scales has been known for some time, such constraints have been largely exclusive to exotic and extreme galaxies and relatively small samples. As such, many important questions relating to outflows and their role in galaxy evolution have so far not been adequately addressed. My Thesis aimed to improve this by using high quality data sets over statistical samples of normal galaxy populations, and the benefits are primarily geared towards the scientific community of this field.

The size and high quality of the data sets used have allowed me to refine and improve previously used detection and characterisation techniques of outflows with Bayesian methods. The first Chapters focussed on the development of new codes and applying these with stacking techniques to over 300,000 local galaxy spectra from the SDSS survey. Using well known tracers of ISM gas, the methodology and Bayesian codes I developed have helped to determine some of the strongest outflow constraints for galaxies of the local Universe, relating to their overall prevalence and potential to halt star-formation.

The third science Chapter of this Thesis made use of stacking techniques over 270,000 state-of-the-art integral field spectra taken over the last year as part of the MaNGA survey, and provided some of the first spatially-resolved analyses of outflows over statistical samples. Using the codes and knowledge developed in the first Chapters, these analyses lead to improved knowledge of resolved outflow quenching potentials, structures and relations to galaxy properties, something that had previously been addressed for only small numbers of normal and exotic galaxies.

The fourth science Chapter of this Thesis aimed to address one of the most significant deficiencies in our knowledge of outflows. The Chapter used the combined power of the large xCOLD GASS, xGASS, ALFALFA and MaNGA surveys in conjunction with stacking techniques to provide some of the strongest and most complete constraints to date for the multiphase nature of outflows in normal galaxies, determining mass outflow rates for

molecular, neutral and ionised gas phases. Previously, such attempts were exclusive to small samples of starburst and extreme AGN objects, or reduced to a comparison of one or two tracers. Here, I expanded on this by using stacking techniques over a combined sample of $>1,500$ normal galaxies and all of the most important gas tracers, resulting in important implications for local galaxy evolution.

Of the studies mentioned above, one of these has been published in the Monthly Notices of the Royal Astronomical Society, whilst the remaining two will be submitted for publication. The last Chapter of this Thesis has also been published in the Astrophysical Journal. All of the work presented here has been presented at numerous outreach events as well as over ten conferences and invited seminars. Whilst the work done in this Thesis does not present a complete picture of outflows, the constraints derived and presented to the scientific community are extremely valuable and enhance our knowledge of how local galaxy evolution works.

Acknowledgements

There are many people who have been by my side on this journey and to whom sincere thanks are due. First and foremost, I would like to give profound thanks and show my sincere gratitude to my supervisor, Dr. Amélie Saintonge, for giving me the opportunity of a lifetime to pursue my dream of a Ph.D in astrophysics. I cannot thank you enough for your unwavering support and patience, and for the wonderful opportunities you have given me to travel the world to meet interesting people, attend wonderful conferences, and visit breathtaking telescopes. I'm incredible grateful and appreciative for the kindness you have shown me, the help and advice you gave me, and your guidance over the last four years. You have been an incredible mentor to me and I could not have asked for a better supervisor.

Secondly, I would like to thank Prof. Richard Ellis, for his constant support, enthusiasm and kindness towards me and for including me in incredible projects and experiences related to high-z work that I could have only dreamed of prior to starting my Ph.D. Visits to Keck and the VLT are among my most fond memories of the past four years and I will be eternally grateful for the experiences. Thank you for the opportunities and confidence you gave me, and for being a great teacher.

Special thanks also go to Dr. Nicolas Laporte and Isabella Lamperti for the laughs, for the morning coffees, for always listening to me and helping me out when I needed it, and for being such good friends at UCL. I am sure we will have plenty more coffees, piscos and reunions in the years to come! I would also like to thank Dr. Gio Accurso, Dr. Will Hartley, Dr. Richard Tunnard and Dr. Lorne Whiteway for always being open to chatting and helping me out with whatever astrophysical questions I had over the years (there were many!). A special mention also goes out to Gio and Isabella, for being really

great academic siblings! Thanks also to Tom Wilson and Dr. Bruno Moraes for providing some great hip-hop tunes during my time writing up. I'd also like to give big thanks to Dr. Katey Alatalo, for her fantastic guidance and support.

I also want to give huge thanks to my close friends over the years, who have been by my side, motivated me, challenged me, and ultimately helped shape me into the person I am today: Justin, Kevin, Gayatri, Dylan, Nathan, Oli, Alec, the rest of the Brotherhood Group, and the SD Reunion Group, thank you for your friendships across the world and for making each encounter just as special as the last! Special thanks also go to Kyle and Samara: thanks for being awesome and for initiating Operation California, I can't wait to hang out on the beach in California all together soon! I'd also like to thank my 107 housemates, Berkay, Louise, and Martyna, for being incredible housemates, friends and sources of support during a challenging last year! I'm so glad your "interviews" worked out and that I made lifelong friends; I look forward to our paths crossing again really soon! Lastly, I'd like to thank all of the Leiden crew who helped set me on this path right at the beginning. In particular, thanks to Marissa for being a huge source of inspiration and motivation, and I hope we both get to space one day! Thanks to Mason for providing what ended up being an incredible base during my time in Leiden. We formed a close bond over those four months and I remember my time there fondly. Thanks also to Allison Hill, for being an incredible source of help when an inexperienced graduate student needed it most. I look forward to all the great reunions with everyone in the years to come, you are all welcome to visit me at any time, wherever I may be!

I also want to give a very special mention and sincere thanks to the Joseph family: Danny, Cigey and Jon. Danny, my buddy, our science sessions have been a great source of fun and inspiration for me over the past four years. Your enthusiasm and passion for science is infectious and I have no doubt you will have a great science career! Cigey and Jon, thank you so much for your incredible generosity, kindness and for the wonderful memories you have created! Words cannot express how grateful I am to you, and these past four years would not have been the same without you!

Last but not least, I would like to thank my incredible family. Your unconditional love, support and presence has been the single biggest factor in all of my successes so far and you have always been my pillar of support and motivation. Mamma, Dad, thank you for encouraging me, allowing and giving me the opportunities to reach for my dreams and teaching me that anything is possible as long as you are willing to try and work hard

enough for it. You have shaped me into the man I am today and I am so, so grateful for everything you have done for me and our family. Lorenzo, thank you for being the best younger brother in the world and for constantly pushing me to become a better person. I look up to and learn from you more than you know and you motivate me to always be the best version of myself. Marc, merci pour tout ton soutien, pour tous les mots de encouragement et pour être un des piliers de notre famille. You all are, and will continue to be, my greatest source of inspiration and gratitude. This Thesis is dedicated to you.

To my loving family, the brightest star in my Universe.

Contents

Table of Contents	10
List of Figures	14
List of Tables	29
1 Introduction	31
1.1 Galaxy Formation with Λ CDM	31
1.2 Galaxy Evolution from an Observational Perspective	34
1.2.1 A Bimodal Population	34
1.2.2 The Main Sequence of Star-Forming Galaxies	36
1.3 Gas Cycling and Outflows as Quenching Mechanisms	38
1.3.1 The Equilibrium Model	39
1.3.2 Observational Support for the Model and Challenges	42
1.4 Importance of Outflows & Current State of the Field	43
1.4.1 The Prevalence of Outflows and Their Properties	44
1.4.2 Star Formation vs AGN Feedback	46
1.4.3 Can Outflows Quench a Galaxy?	47
1.5 Tracers of Outflows	48
1.5.1 Neutral Sodium (NaD)	48
1.5.2 Ionised Gas	49
1.5.3 Atomic and Molecular Gas	51
2 Data Sets & Analysis Codes	52
2.1 Observational Data Sets	52

2.1.1	The Sloan Digital Sky Survey (SDSS)	53
2.1.2	The Mapping Nearby Galaxies at APO Survey (MaNGA)	54
2.1.3	The Arecibo Legacy Fast ALFA Survey (ALFALFA)	55
2.1.4	The Extended GALEX Arecibo SDSS Survey (xGASS)	56
2.1.5	The Extended CO Legacy Database for GASS (xCOLD GASS)	56
2.2	Modelling of Neutral Gas Outflows	57
2.2.1	Simple Stellar Population Models & the Penalised Pixel-Fitting Code	57
2.2.2	Bayesian Inference and NaD Profile Fitting	59
2.2.3	Model Completeness and Reliability	64
3	The Prevalence and Properties of Cold Gas Inflows and Outflows Around Galaxies in the Local Universe	69
3.1	Introduction	69
3.2	Sample Definition & Measurements	71
3.3	Analysis	73
3.3.1	Binning, Stacking and Continuum-Fitting of Optical Spectra	73
3.3.2	Interpretation and Fitting of NaD Doppler Shifts	75
3.4	Stacking Results	79
3.4.1	NaD Profiles Across the SFR- M_* Plane	79
3.4.2	Flow Detection Rates and Inclination Dependence	80
3.4.3	Covering Fractions	84
3.4.4	Equivalent-Widths	84
3.4.5	Flow Velocities	85
3.4.6	Mass Outflow Rates and Loading Factors	87
3.4.7	Comparison to Other Gas Phases	90
3.4.8	Upper Limits on Mass Inflow Rates	91
3.5	Discussion	92
3.5.1	The Prevalence of Outflows and Inflows	92
3.5.2	Comparison to Simulations	92
3.5.3	Star Formation vs AGN	94
3.5.4	The Fate of Outflows	96
3.6	Summary and Conclusions	98

4	Spatially Resolved Outflow Properties in the Local Galaxy Populations with MaNGA DR15 IFU	100
4.1	Introduction	100
4.2	Data and Sample	103
4.3	Stacking Procedures and Analysis	104
4.3.1	Maps of Galaxy Properties	104
4.3.2	Stacking Procedure and Outflow Modelling	105
4.4	The Galactocentric Profile of Outflows	107
4.4.1	Average Central Profiles	110
4.4.2	The Radial Extent of Outflows and Their Properties	113
4.5	The Resolved $\Sigma_{\text{SFR}}-\Sigma_{M_*}$ Plane	118
4.6	Outflow Correlations with Galaxy Properties	121
4.7	The Impact of Outflows on HI Gas Reservoirs	127
4.7.1	HI Observations	127
4.7.2	Removing the Effects of Confusion and Baseline Issues	128
4.7.3	Control Sample and Stacking Procedure	129
4.8	Discussion	131
4.8.1	Strong Correlations With Σ_{SFR}	131
4.8.2	Star Formation Histories of Outflow Hosts	133
4.9	Summary and Conclusions	137
5	The Multiphase Nature of Outflows Using the MaNGA, xCOLD GASS, xGASS and ALFALFA Surveys	140
5.1	Introduction	140
5.2	Data Sets & Sample Definition	143
5.3	Stacking Process & Results	145
5.4	Reliability of Stacking Methods and Validity of Broad CO and HI Emission	147
5.5	Results	150
5.5.1	Neutral and Ionised Outflows	150
5.5.2	Molecular and Atomic Outflows	153
5.6	Discussion	156
5.6.1	Towards a Total, Multiphase Mass Outflow Rate	156
5.6.2	Why Don't We See Atomic or Molecular Outflows?	160

5.6.3	Can Outflows Quench Normal Galaxies?	161
5.7	Conclusions	162
6	Multiwavelength Characterisation of an ACT-Selected, Lensed Dusty Star-forming Galaxy at $z = 2.64$	165
6.1	Introduction	165
6.2	Observations	167
6.2.1	Initial Spectroscopy	167
6.2.2	Imaging	168
6.2.3	IRAM 30m	168
6.3	Results	169
6.3.1	The Redshift of ACT J2029	169
6.3.2	Line Properties	171
6.4	Discussion	174
6.4.1	CO SLED Indicative of an AGN	174
6.4.2	Lensing Status and SED Fitting	178
6.4.3	The Enhanced C I Flux and Velocity	180
6.5	Conclusions	181
7	Conclusions and Future Work	184
7.1	Summary	185
7.1.1	The Prevalence and Properties of Outflows in Normal Galaxies at $z \sim 0$	185
7.1.2	Spatially Resolved Outflow Properties in Star-forming Galaxies	186
7.1.3	The Multiphase Nature of Outflows	187
7.1.4	A Possible Molecular Outflow in a High- z Galaxy	188
7.2	Future work	188
A	Appendix A	190
A.1	SDSS NaD Fitting Properties	190
A.2	SDSS NaD Profiles	204
B	Appendix B	222
B.1	MaNGA Galaxy Properties	222

<i>Contents</i>	14
<hr/>	
C Appendix C	228
C.1 Spectra from xCOLD GASS, xGASS and ALFALFA	228
D Appendix D	230
D.1 NIR Sérsic Fit and Potential Lens Morphology	230
Bibliography	232

List of Figures

1.1	A schematic of a dark matter halo merger tree with assembly history (time increasing from top to bottom) from Giocoli et al. (2010) . The blue halos on the left represent the main halo progenitor, which over time accretes “satellite” halos (A, B, C, D) which form subhalos to the main progenitor. Satellite D itself accretes smaller satellites a and b, which further form a population of subhalos.	32
1.2	The galaxy luminosity function as described by Λ CDM (red line) and the baryonic luminosity function (blue line). Large tension exists between the two curves, particular at low and high luminosity, although agreement is found at a turnover luminosity, $L_* \sim 10^{10} L_\odot$. At both low and high luminosity, SF is less efficient and the depression in efficiency is attributed to the energetics of massive stars and supernovae (at low luminosity) and injection of energy from a supermassive black hole (at high luminosity). The luminosity of a galaxy can be converted to a stellar mass by assuming a mass-to-light ratio. Figure taken from Silk & Mamon (2012)	33
1.3	The dust-corrected galaxy colour-mass diagram and bimodality shown by Schawinski et al. 2014 . The galaxies are binned by 0.1×0.1 dex and colour-coded by the mean specific SFR, with blue galaxies on average displaying higher levels of SF than their red counterparts. On the right, the dichotomy in galaxy type (i.e., early-type and late-type) is also evident, with early-type galaxies dominating the red colours and highest end of the stellar masses and late-type galaxies residing primarily in regions of blue colours whilst dominating the lowest end of the stellar masses.	35

-
- 1.4 Left: The SFR- M_* plane as shown at $z \sim 0$ by the SDSS, highlighting the Main Sequence of “blue and star-forming” galaxies and passive cloud of “red and dead” galaxies. The two dashed lines represent fits to the MS by Peng et al. (2010b) (solid line) and Saintonge et al. (2016) (dashed line). Right: The redshift evolution of the MS from $z=0.5-2.5$ with data from Karim et al. (2011). Each point represents a binned average and varying colours mark different redshifts. Both figures are courtesy of Dr. Amélie Saintonge. 37
- 1.5 The simple gas-regulated equilibrium model described by Lilly et al. (2013). Left: gas flows into the galaxy halo, some of which (f_{gal}) flows into the galaxy system at a rate Φ . The gas then makes its way into the galaxy gas reservoir, or forms into long-lived stars, and ultimately gets ejected from the reservoir via an outflow. Right: the division of Φ into three main fractions (f_{res} , f_{stars} , f_{out}), regulated by ε , η and sSFR. 39
- 1.6 A multiwavelength image of the starburst galaxy M82 and its outflow. The image is a composite between observations from the Hubble Space Telescope (yellow/green colours, tracing the UV disk, and red tracing a massive outflow seen in $H\alpha$ emission) and Chandra (blue colours, tracing X-ray emission from the outflowing gas). The gas can be traced back to the central regions of the galaxy, which hosts regions of extreme starbursts that drive the outflow. Image credit: <http://chandra.harvard.edu/photo/2006/m82/>. 44
- 1.7 A schematic of the different types of Doppler shifts one can observe in the NaD transition. Foreground gas is dominated by absorption of the background continuum, with profiles either blueshifted (outflows) or redshifted (inflows). Background gas is seen in emission of re-emitted photons. Gray lines represent continuum photons from the galaxy disk, blue lines represent blueshifted signatures, and red lines represent redshifted signatures. Small blue or red circles represent absorption, from which re-emission of the photon occurs. Included in the schematic is the role of the viewing angle in detecting outflowing or potentially inflowing gas. 49

-
- 2.1 The main telescope facilities whose data were used in this Thesis. From left to right: The Apache Point Observatory in New Mexico (USA), the IRAM 30m telescope on Pico Veleta in the Sierra Nevada (Spain), and the Arecibo telescope in Puerto Rico (USA). The three observatories were used as part of the SDSS/MaNGA, xCOLD GASS and ALFALFA surveys. 57
- 2.2 The theoretical curve of growth for the Sun. The x-axis represents the logarithm of the column density whilst the y-axis represents the EW of the line. The curve has three distinct regions, marked by numbered circles: the regions correspond to evolving relations between the EW of an absorption line and the column density, or optical depth of the line. The three regions are primarily dictated by the different conditions of the absorbing gas caused by an increase in density over orders of magnitude. This figure was adapted from [Aller & Goldberg \(1971\)](#). 60
- 2.3 The line profile of an absorption feature at low (left) and high (right) optical depths, dominated by Doppler broadening as described by a Gaussian profile. For optically thin lines, if one doubles the optical depth, τ , the EW of the line doubles as well. For optically thick lines, this relationship no longer holds as the line becomes saturated. 60
- 2.4 The line profile of an absorption feature at low (left) and high (right) optical depths, dominated by pressure and collisional broadening as described by a Lorentz profile. 61
- 2.5 A schematic describing the procedure to generate and fit synthetic spectra, for tests of completeness and reliability. First (left), a noiseless, synthetic spectrum is generated by combining a systemic absorption component and an offset component (an outflow, in the above illustration) of a given velocity. Second (middle), the profile is convolved to the resolution of the SDSS spectra and random Gaussian noise is added to match a required continuum S/N. Third, (right) the 1σ error is estimated as the standard deviation either side of the NaD line profile and the full spectrum is put through our in/outflow detection procedure. In each plot, the vertical dashed lines represent the NaD doublet. 65

-
- 2.6 Plots of completeness versus input velocity for our NaD outflow detection procedure (bottom row). The procedure is calculated for continuum S/N ratios of 6 (left), 10 (middle) and 50 (right), for both negative offset velocities (blue circles) characteristic of outflows and positive offset velocities (magenta circles) characteristic of inflows. Each inset plot shows the linear evolution of $|\Delta v|_{\text{output}}$ vs $|\Delta v|_{\text{input}}$ in each completeness plot. The top row shows representative synthetic spectra from the corresponding completeness panels directly below, each with an outflow component of 100 km s^{-1} 68
- 3.1 The locations of our main inactive (blue) and AGN (crimson) samples on the BPT diagram, with the [Kauffmann et al. \(2003b\)](#) demarcation (orange dashed line). For the selection of each sample, a $S/N > 3$ is required for each of the BPT lines ($H\alpha$, $H\beta$, $[O \text{ III}] \lambda 5007$ and $[N \text{ II}] \lambda 6584$), whilst any galaxy with insufficient S/N in any one of the lines (gray points) is added to the inactive sample. 71
- 3.2 The distributions of redshift, stellar mass, SFR, and Σ_{SFR} of our main samples. The blue histograms represent our inactive galaxies sample and the orange histograms represent our AGN sample. 72
- 3.3 Examples of stacked spectra (black) from the inactive main sample, with their best-fit pPXF continuum (orange). For each row, the full spectrum is shown on the left, whilst the plot on the right is a zoomed-in portion of the gray-shaded region, highlighting the fit to the He I line and the NaD absorption. The dashed red line in the right panels represent fits to the continuum with masked emission lines, in order to determine whether this would impact the NaD residual. The dashed black lines represent the central blueshifted and redshifted wavelengths of the NaD doublet at 5889 \AA and 5895 \AA , respectively. The spectra are taken from the stacked SFR- M_* results presented in Figure 3.5, and each number on the top left of each spectrum indicates the bin from which it is taken in Figure 3.5. 76
- 3.4 The distribution of NaD ISM profiles across the SFR- M_* plane derived by dividing high signal-to-noise stacked SDSS spectra in each bin by their best fit continuum obtained using the code and SSP models stated on the bottom right of each plot. 77

- 3.5 Left: The NaD residual profiles for inactive galaxies from our stacked spectra over the main sample SFR- M_* plane, as a result of the division of the best fit continuum given by pPXF. Absorption and emission profiles dominate the high- and low-mass galaxies, respectively, with a separation at $\log M_*/M_\odot \sim 10-10.5$ characterised by low line S/N ratios and P-Cygni profiles. The solid and dashed lines mark the Main Sequence relation defined by [Saintonge et al. \(2016\)](#), with a +0.35 dex offset in log SFR to account for the different median redshifts of our and their sample. Middle: The same plots as the left but with the mean dust A_V values for each stack, calculated via the Balmer decrement assuming the median MPA-JHU line fluxes going into each stack. Right: The same as the middle panel, but for the E(B-V) value associated with the stellar continuum fit performed with pPXF. The middle and right plots highlight an apparent correlation between the dust content and the NaD residual profile. The white numbers in certain bins correspond to the spectra displayed in Figure 3.3. 80
- 3.6 The inclination and Σ_{SFR} dependence of inflows and outflows for our DISK sample. The left and right panels shows the results for the inactive and AGN objects, respectively. Gray lines mark the limits of the defined bins over our samples (gray contours), black crosses represent non-detections, magenta points represent inflow detections and blue points represent outflow detections. Additionally, detections seen with NaD absorption use diamond symbols, whilst detections in emission use triangles. Bins without any symbol have insufficient continuum S/N for analysis. 82
- 3.7 The detections of inflows and outflows across the SFR- M_* plane for disk galaxies (left and middle columns) separated by inclination, and bulge galaxies for which inclinations cannot be accurately established (right column). The top row shows shows our sample of inactive galaxies whilst the bottom row is for AGN hosts. The symbol and color convention follow those of Figure 3.6. 83

- 3.8 (a): The distribution of total EWs for inactive galaxies and AGN. The gray bars represent the full distribution, whilst the blue bars represent outflow detections and inflows are marked by the magenta bars. Black bars are non-detections. (b): A comparison of the EWs measured blueward and redward of the 5889 Å and 5895 Å NaI lines, where outflows (blue) and inflows (magenta) are expected to be seen, respectively. The dotted black line is a straight line fit to the systemic components (black x's) whilst the dashed blue and magenta lines are best fit linear functions to outflow and inflow detections. (c) histogram distributions of the $EW_{\text{blue}}/EW_{\text{red}}$ ratio for inflows, outflows and non-detections. The orange vertical lines represent our suggested cuts to isolate each distribution. 86
- 3.9 Left: The central inflow and outflow velocities (uncorrected for inclination) as a function of SFR. Right: The same as the left panel but as a function of stellar mass. Results from [Rupke et al. \(2005a,b\)](#), [Martin et al. \(2012\)](#), [Rubin et al. \(2012\)](#) and [Rubin et al. \(2014\)](#) are overplotted for comparison, where available. The symbol and color convention follow those of Figure 3.6. 88
- 3.10 The mass outflow rates for the i -log SFR stacks of inactive and AGN galaxies defined in Section 3.4.5. A first-order polynomial fit to our data is shown in orange. Overplotted are the results from [Rupke et al. \(2005b\)](#) (gray pentagons), [Cazzoli et al. \(2016\)](#) (gray squares) and [Fluetsch et al. \(2018\)](#) (gray stars). 90
- 3.11 A comparison of the energy output from the AGN (L_{AGN}) and from star formation (ie., supernovae, L_{SF}) for our AGN stacked sample (orange) and objects from [Cicone et al. \(2014\)](#) (red). Additionally, we extract and stack the Seyfert objects in our AGN sample and plot the data points for comparison. The dashed lines denote constant lines of $L_{\text{bol,AGN}}/L_{\text{SF}}=1000, 100, 10$ and 1. 95

-
- 3.12 *Left:* The outflow velocity as a function of the galaxy’s circular velocity, compared to the results of [Heckman et al. \(2015\)](#). Blue stars are the inactive galaxies and the red stars are the AGN of the i -log M_* stacks. *Right:* A comparison of the momentum flux (or force) provided by the galaxy starburst versus the critical momentum flux necessary for the net force acting on a cloud to be outwards. The dashed diagonal lines denote constant lines of $\dot{p}_*/\dot{p}_{crit}=10, 1$ and 0.1 as well as three outflow regimes: “no outflow”, “weak outflow”, and “strong outflow”. 98
- 4.1 The SFR- M_* plane and density contours of the full MaNGA DR15 sample and selected sample for this study. Gray dots represent the 405 galaxies found using our selection criteria (blue dashed lines), whilst the blue points mark galaxies found to have outflows in their central regions and magenta points galaxies found to have inflows. The orange solid and dashed lines mark the star-forming main sequence defined by [Saintonge et al. \(2016\)](#) and its lower and upper limit. Histograms of the selected galaxies’ SFRs and stellar masses are shown to the top and right sides of the main plot. 104
- 4.2 An example of IFU MaNGA galaxy property maps. From left to right, top to bottom: The SDSS image of an example galaxy with the MaNGA footprint, the velocity of $H\alpha$ relative to the systemic, the flux of $H\alpha$, the flux of $H\beta$, the Balmer decrement, the D(4000) index. 106
- 4.3 The typical depth-to-noise ratios of NaD in the central ($<0.25 R_e$) regions of the sample of MaNGA galaxies used in this study. The gray histogram represents non-detections, whilst the blue histogram and the magenta histogram represent outflow and inflow detections, respectively. Positive values reflect profiles in absorption, whilst negative values represent profiles in emission. The dashed black line marks our minimum D/N threshold of >3 to determine detections of inflows and outflows. 109

- 4.4 The average central $0.25 R_e$ spectra of galaxies harbouring outflows (blue) and inflows (magenta), and the average spectra of an associated control sample of non-detection galaxies (light gray for inflows, dark gray for outflows). *Left:* the normalised optical spectra over virtually the full optical range. *Middle:* the continuum-normalised ISM residual of the NaD line for the four spectra in the left panel. *Right:* the continuum-normalised $H\alpha + [N II]$ emission for the four spectra in the left panel. The quantities and units quoted in the left panel are the stellar mass surface density ($M_\odot \text{kpc}^{-2}$), SFR surface density ($M_\odot \text{yr}^{-1} \text{kpc}^{-2}$), dust (magnitudes) and 4000 \AA -break. The colours correspond to the different stacks (NB: given that the average spectra - and quantities - for the two non-detection control samples are essentially identical, we display only the values of the control sample associated with the outflow detections). 112
- 4.5 The evolution of the total NaD EW (left panel), mass outflow rate (middle panel) and mass loading factor (right panel) as a function of galactocentric radius. The NaD EW is separated out into stacks of spaxels from the outflow detection sample only (circles) and non-detection+outflow spaxels (diamonds). Filled symbols indicate the detection of outflowing neutral gas, whilst empty symbols indicate non-detections. For comparison, a $1.5''$ stack is also added to each of the plots, in order to gauge what would be measured by single-fiber SDSS surveys. In the middle and right plots, we add a best fit first order polynomial (dashed line) and its 1σ error (shaded region). . . 114
- 4.6 A simplified schematic of the collimation of a galactic-scale outflow from “wind bubbles”, generated close to the galaxy disk plane. Clusters of stars in the disk generate energy and momentum from stellar winds, supernovae and high energy photons, which likely superimpose and entrain ISM gas. The energy and momentum bubbles, as well as gas, eventually collimate at larger distances from the disk to form a large-scale outflow which exits perpendicularly to the disk. 118

-
- 4.7 The normalised evolution of the geometry-independent mass outflow rate compared to several key galaxy properties (i.e., Σ_{SFR} , Σ_{M_*} , A_V , $D(4000)$). Each quantity is normalised by the maximum value across galaxy radius. The radial evolution of the normalised mass outflow rate is most closely aligned with the normalised evolution of Σ_{SFR} and Σ_{M_*} 119
- 4.8 The resolved $\Sigma_{\text{SFR}}-\Sigma_*$ plane of star-forming MaNGA galaxies with stacked bin limits (gray lines) and outflow detections (diamonds) overplotted. Non-detections are marked by a cross and detections are colour-coded according to the mean outflow EW (left panel), neutral gas mass outflow rate (middle left panel), and local mass loading factor (middle right panel). Outflows are prevalent in regions of high star formation activity and stellar mass surface density, with an EW and mass outflow rate that follows a similar pattern. The right panel is the same as the other panels except colour-coded by the total NaD EW, as measured from the stacked spectrum. The dashed navy line indicates the resolved MS relation for H II regions of star-forming galaxies from [Hsieh et al. \(2017\)](#). 120
- 4.9 The correlations between outflow properties (C_f , $N(\text{H})$, Δv , \dot{M}_{out} and η) as a function of galaxy properties as shown by stacks of individual spaxels within a given property range. The main trends occur with star-forming quantities, although the strongest correlation is seen with Σ_{SFR} 123
- 4.10 The evolution of the NaD ISM EW (top row) and blueshifted absorption EW (bottom row) as a function of Σ_{SFR} , $s\text{SFR}$, Σ_* , $D(4000)$ and A_V . The colour scheme follows that of Figure 4.9. 126
- 4.11 The mean velocity normalised, gas fraction spectra of galaxies with signatures of optical outflows (blue) and those without (gray) and their reported gas fractions and median FWHM. The stacks are created via a Monte Carlo approach of 14 outflow galaxies and a control sample of non-detection galaxies. The presence of NaD-selected outflows does not appear to significantly influence the H I gas reservoirs of their host galaxies compared to their non-detection counterparts. The inset plot shows a histogram of the average gas fraction of a given iteration going into the final stack. 130

-
- 4.12 The star formation histories as traced by the 3''-diameter stacked $H\delta_A$ and $D_n(4000)$ indices of our MaNGA DR15 sample of galaxies shown to host NaD outflows (blue points) and those that do not (gray points). The error bars represent the standard deviation of values going into the stack for each galaxy. These points are compared to the mean (dashed orange line) and median (dashed red line) of SDSS values from the MPA-JHU catalogs. The inset plots show the distributions of $\Delta H\delta_A$ ($H\delta_{A,\text{MaNGA}} - H\delta_{A,\text{SDSS}}$; top) and $H\delta_A$ (bottom) for outflows (blue lines) and non-detections (gray lines), as well as their cumulative distribution functions and associated two-sample Kolmogorov-Smirnov statistic. 135
- 5.1 The distribution of galaxies from the full MaNGA DR15 (left), xCOLD GASS (middle) and combined xGASS+ALFALFA $\alpha.100$ (right) data releases (gray points) and our selected star-forming sample of high mass galaxies with low inclinations (blue points) across the SFR- M_* plane. The blue regions and dashed lines mark our selection limits across the plane for star-forming galaxies likely to host outflows, with the SFR limit set by the definition of the MS by [Saintonge et al. \(2016\)](#). A navy diamond in each plot marks the mean SFR- M_* position of each selected star-forming sample. The orange region and dark red lines in the right panel represent the selection limits for our sample of H I passive across all inclinations and galaxy types, where outflows are not expected to be seen. 145
- 5.2 The normalised stellar mass (left), SFR (middle) and redshift (right) distributions of our three final samples derived from the MaNGA DR15 (green), xCOLD GASS (blue) and xGASS+ALFALFA $\alpha.100$ (red) surveys. The dashed line represent the mean value for each distribution. 146

-
- 5.3 H I stacks of high mass, passive galaxies (including AGN) over the full range of inclinations, where outflows are not expected to be seen. Stacks are created via a Monte Carlo sampling of 80% of the sample, repeated 300 times. The top panel shows the stacked spectrum using our measured linewidths and velocities, whilst the bottom panel repeats the same process using the catalogued W50 values. A clear difference is seen between the two, with the former stack displaying no signatures of broad emission, suggesting all of the systemic emission is encapsulated within our measurement, whilst the latter displays significant broadening at high normalised velocities, indicative of leaking systemic emission at higher normalised velocities. Such a comparison is imperative in a search for outflows, since the broad emission could be interpreted as outflowing signal in star-forming samples. 149
- 5.4 A comparison of the catalogued H I FWHMs (W50) versus our measured full linewidths (left) and the same for H I velocities (right). Our linewidths are systematically larger than the catalogued values, with a median difference of $\sim 46 \text{ km s}^{-1}$. The difference between H I velocities is much smaller, with a median difference of only $\sim 5 \text{ km s}^{-1}$. In both plots, the dashed purple line denotes a 1:1 relation. The difference in H I linewidths is crucial in our search for broad emission outflows, since an underestimation of the linewidth can result in leaked systemic emission which can mimic the signature of outflows. 150
- 5.5 The final stacked spectra of our NaD (left column), H α + [N II] (middle left column), CO(1-0) (middle right column) and H I 21cm (right column) tracers from the MaNGA DR15, xCOLD GASS and xGASS+ALFAFA $\alpha.100$ surveys. The top row shows the stacked spectra only, whilst the bottom row shows the stacked spectra with their best fit models. Stacked flux is outlined by the navy line and light blue fill, whilst orange lines mark fits of a systemic component, blue lines mark outflowing components, and purple mark the total fit. 151

- 5.6 The reliability of our code’s outflow detections at various amplitude ratios for simulated spectra of the same S/N of our stacked CO (left) and HI (right) spectra, given an assumed outflow velocity of 200 km s^{-1} . The lowest outflow amplitude ratio (compared to the peak flux of the total spectrum) we can measure whilst maintaining 90% reliability is $A_{\text{broad}}/A_{\text{stack,peak}}=0.075$ (CO) and $A_{\text{broad}}/A_{\text{stack,peak}}=0.031$ (HI). 155
- 5.7 The mean H_2 (left), HI (middle) and ionised (right) mass outflow rates compared to the mean SFRs of normal galaxies at $z \sim 0$, as traced by CO(1-0), HI 21cm and NaD, and $\text{H}\alpha$, respectively. Upper limits of the H_2 and HI 21cm mass outflow rates are marked by blue arrow upper limits, whilst the rates derived with NaD and $\text{H}\alpha$ are marked by blue circles with errors. The errors quoted here included the 1σ errors from our fitted parameters, whilst the error associated with the mean SFR is simply the standard deviation over all the galaxies in the stack (and galaxy spaxels, in the case of MaNGA data). The results from this study (light blue points and arrows) are compared to the mass outflow rates derived for H II (navy points) and (U)LIRG/AGN (purple points) galaxies from the literature, using multi-transition CO for molecular gas, NaD or C^+ for neutral gas, and $\text{H}\alpha$ or $\text{H}\beta$ for ionised gas. The classification of galaxy type is taken from each relevant study. We further mark the region of SFRs that roughly probe the lower and upper limits of the high mass ($M_* \geq 10^{10} M_\odot$) galaxy MS (gray shaded region) and draw dashed lines to represent constant mass loading factors of $\eta=0.1, 1, \text{ and } 10$ 157
- 5.8 The outflow depletion time of molecular gas, defined as $\tau_{\text{depl}}=M_{\text{gal}}(\text{H}_2)/\dot{M}_{\text{out}}(\text{H}_2)$, as a function of host SFR. The colour scheme is the same as in Figure 5.7 and we additionally plot the values found for starburst and AGN galaxies in [Fluetsch et al. \(2018\)](#). 162

- 6.1 Observed ^{12}CO and C I transitions for ACT J2029, taken with the IRAM 30m. The 4 CO transitions observed with WILMA are $J = 3-2$ (panel 1), $5-4$ (panel 2), $7-6$ (panel 3), and $8-7$ (panel 4). Panels 1 and 5 display the upper limits on the other dense gas tracers and the tentative $\text{HCO}^+(4-3)$ detection (taken with the FTS). Panel 3 also shows the C I detection, with a linear baseline fit. The red line indicates the best fit Gaussian function from CLASS and the gray shaded regions mark the limits of our data. The orange line in panel 3 represents a Gaussian fit to the C I line fixed to width of $\text{CO}(7-6)$ 170
- 6.2 The distribution of ^{12}CO line fluxes, normalized to that of the $^{12}\text{CO}(5-4)$ line, for the HerCULES sample of Class I (star-forming objects, left panel), Class II (starbursts and Seyferts, middle panel), and Class III (ULIRGs and QSOs, right panel) objects (Rosenberg et al. 2015). The filled circles represent the mean CO SLED, the colored shaded regions show their $\pm 1\sigma$ deviations off the mean, and the error bars represent the uncertainty of the mean. The ACT J2029 fluxes are represented by the (yellow) stars. The dashed red line in each panel represents the best RADEX fit to the observed CO fluxes, which corresponds to $T_{\text{kin}} = 117 \text{ K}$, $n_{\text{H}} = 2 \times 10^5 \text{ cm}^{-3}$ and $N_{\text{CO}}/\Delta v = 10^{16} \text{ cm}^{-2}(\text{km s}^{-1})^{-1}$. A T vs. n_{H_2} probability plot is shown as an inset to the right panel, highlighting a range of other possible fits allowed by temperature-density degeneracies. The best RADEX fit is represented by the red crosshairs. 177
- 6.3 A Pan-STARRS i -band image of ACT J2029 and 2MASX J20295548 with the CARMA contours overplotted (white). The ellipse at lower right represents the CARMA beamsize. An riz color image and the positions of ACT J2029 and 2MASX J20295548 is shown at upper right. The CARMA integrated emission line is shown in the middle right. The two sources in the i -band image have positions less than $0.5''$ apart and are spatially blended. However, what appears to be a lensed arc is clearly visible in the riz image. 179

- 6.4 The best-fit SEDs for ACT J2029 (black and blue) and 2MASX J20295548 (yellow), fixed to redshifts of $z = 2.64$ and $z = 0.32$, respectively. The gray shaded region represents wavelengths where the photometry is likely contaminated by both the high- z object and the foreground object. The black line illustrates the best fit ACT J2029 SED making use of all available photometry, while the blue line uses the same data but with upper limits to all photometry blueward of the *WISE* W3 band (ie., the shaded region). The yellow line shows the best-fit SED to 2MASX J20295548, applying upper limits to all the photometry in the shaded region. A Calzetti et al. (2000) extinction law was preferred for all fits. 180
- 6.5 The $L'_{\text{CI}(2-1)}/L'_{\text{CO}(3-2)}$ ratio of ACT J2029 (yellow and red, uncorrected and corrected for lensing, respectively) is overplotted with other lensed and unlensed high-redshift QSOs (navy blue) and SMGs (teal) from Walter et al. (2011). All Walter et al. (2011) L' values are uncorrected for lensing. The average $L'_{\text{CI}(2-1)}/L'_{\text{CO}(3-2)}$ line is overplotted, with the 1σ standard deviation limits shaded in gray. Even taking magnification into account, ACT J2029 has a $L'_{\text{CI}(2-1)}/L'_{\text{CO}(3-2)}$ ratio substantially higher than other high-redshift galaxies. Classifications of SMGs and QSOs were taken from the DÍGAME catalogs (<http://www.digame-db.online>). 182
- A.1 The normalised NaD ISM profiles from inflow and outflow detections in the DISK, LOW- i , HIGH- i and BULGE samples for inactive galaxies. The black line line is the NaD profile and the gray shade is the flux error. The best-fit two-component models are overplotted: purple denotes the total fit, red is the systemic component, and blue represents the blueshifted or redshifted flow component. 205
- A.2 The same as Figure A.1 but for the AGN sample. 213
- C.1 The 1.25'x1.25' SDSS image (left), IRAM 30m CO(1-0) spectrum (middle) and Arecibo HI 21 cm spectra for 10 random galaxies from the selected sample defined in Section 5.2. Each spectrum has been checked for confusion (within a normalised velocity of ± 5) and baseline issues and the quoted widths and velocities are those measured in the study. 229

-
- D.1 The GALFIT analysis of the foreground galaxy in the Pan-STARRS *i*-band image. The left panel shows the *i*-band image, centered on ACT J2029, the middle panel shows the GALFIT Sérsic profile fit of the foreground galaxy, and the right panel shows the difference between the left and middle panels (ie., the data minus the the model). NIR excess can be seen towards the northeast and southwest of the center. 231

List of Tables

2.1	The priors applied to our model when used for detection and characterization purposes. Note that for emission profiles the covering factor prior changes to $-1 \leq C_f \leq 0$. The free parameters are: $ C_f $, absolute covering fraction; b_D , Doppler linewidth in km s^{-1} ; $\log N(\text{Na I})$, column density in cm^{-2} ; $ \Delta v_{\text{offset}} $, absolute velocity offset in km s^{-1}	64
3.1	The number of galaxies in each sub-samples defined for this study.	73
3.2	The detection rate of inflows and outflows in the SFR- M_* plane across all bins with continuum S/N>100, and median properties of their galaxy hosts.	84
5.1	The mean properties and parameters of our stacked spectra used to derive multiphase mass outflow rates in this work.	156
6.1	All IRAM 30m line detections.	173
A.1	The properties of the flow parameters measured over the DISK, HIGH- i , LOW- i , BULGE, i -log SFR and i -log M_* samples for inactive galaxies. For profiles with blueshifted absorption and redshifted emission, b superscript indicates the blueshifted component, whilst the r superscript refers to the redshifted component of the profile.	191
A.2	The same as Table A.1 but for AGN.	197
B.1	The global properties of galaxies identified to host outflows in their central regions.	223

Chapter 1

Introduction

1.1 Galaxy Formation with Λ CDM

One of the most significant discoveries in modern cosmology is that, at the current epoch, baryonic matter comprises only $\sim 5\%$ of the total mass-energy budget of the Universe, whilst cold dark matter (CDM) and dark energy (Λ) form the rest (and majority) of it with $\sim 25\%$ and $\sim 75\%$, respectively (Planck Collaboration et al. 2016; Guo et al. 2016). Consequently, the Λ and CDM framework (Λ CDM; Blumenthal et al. 1984) is the current preferred model in astrophysics for predicting and describing the evolution of the Universe from a state of virtual uniformity at infancy, as measured by the cosmic microwave background (Planck Collaboration et al. 2016), to its highly structured web-like nature measured today from observations of matter at large scales (~ 1 -100 Mpc). The framework is based on two fundamental assumptions: on large scales (i) the Universe is isotropic and homogeneous and (ii) gravity is the dominant force that shapes the Universe and is described by the theory of General Relativity.

In such a picture, the seeds of cosmic structure are sowed by primordial quantum fluctuations, giving rise to the first under- and over-densities which are amplified through gravity. Over time, the DM halos become increasingly massive by growing in a hierarchical fashion, where satellite halos form around a central progenitor and merge to form larger and larger halos. This is illustrated in Figure 1.1. The formation of galaxies occurs within the gravitational potential of DM halos, where cosmological gas cools and star formation

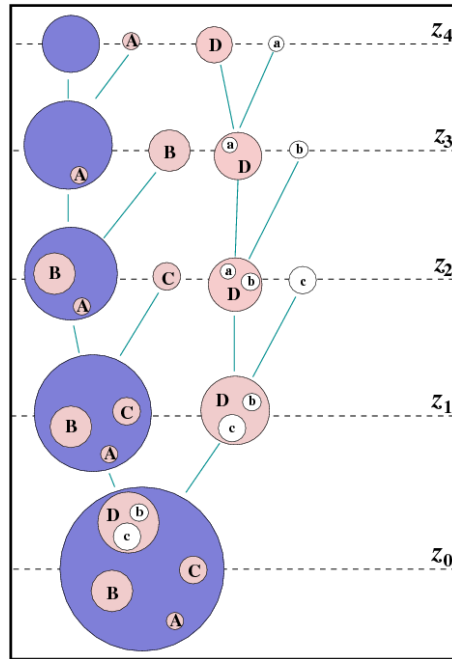


Figure 1.1. A schematic of a dark matter halo merger tree with assembly history (time increasing from top to bottom) from [Giocoli et al. \(2010\)](#). The blue halos on the left represent the main halo progenitor, which over time accretes “satellite” halos (A, B, C, D) which form subhalos to the main progenitor. Satellite D itself accretes smaller satellites a and b, which further form a population of subhalos.

(SF) begins ([White & Rees 1978](#)), and the evolution of galaxies is then dictated largely by local processes. Such a picture is now considered the standard paradigm for galaxy formation and evolution.

Although a physical understanding of DM and Λ are proving elusive, the Λ CDM framework has, through remarkable advances in simulations, been extremely successful in predicting and reproducing observations of large scale structure and the detailed properties of galaxies, such as their number counts, clustering properties, colours, morphologies, and overall evolution throughout cosmic time ([Vogelsberger et al. 2014](#); [Schaye et al. 2015](#)).

Despite its remarkable success, however, the Λ CDM model does, on its own, display some fatal contradictions compared to observations. Arguably the most glaring of these is that the assumption that the mean growth of DM halos dictates the cosmological accretion rate of cool gas onto galaxies causes an overprediction of SF activity in low-mass halos at early times, and in high-mass halos at later times ([Bell et al. 2003](#); [Li & White 2009](#)). In essence, gas cools too quickly and forms too many stars, despite being extremely inefficient ([Schmidt 1959](#); [Kennicutt 1998](#); [Bigiel et al. 2008](#)). The introduction of feedback mechanisms (defined as an ensemble of processes that provide enough energy to disrupt

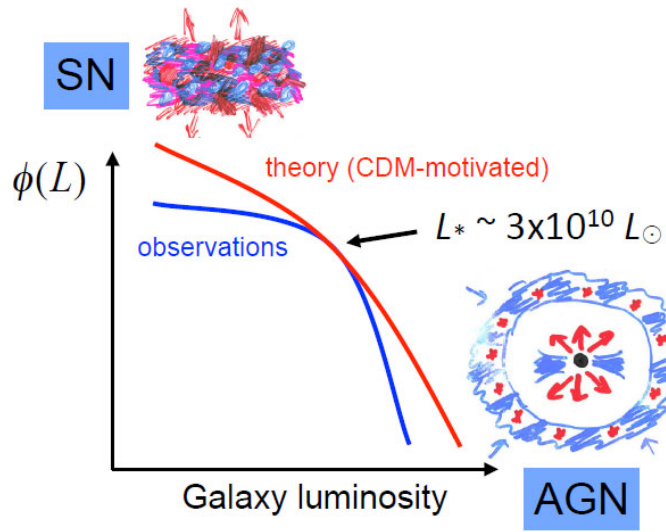


Figure 1.2. The galaxy luminosity function as described by Λ CDM (red line) and the baryonic luminosity function (blue line). Large tension exists between the two curves, particular at low and high luminosity, although agreement is found at a turnover luminosity, $L_* \sim 10^{10} L_\odot$. At both low and high luminosity, SF is less efficient and the depression in efficiency is attributed to the energetics of massive stars and supernovae (at low luminosity) and injection of energy from a supermassive black hole (at high luminosity). The luminosity of a galaxy can be converted to a stellar mass by assuming a mass-to-light ratio. Figure taken from Silk & Mamon (2012).

SF), such as outflows, goes a long way towards reconciling these important discrepancies (Somerville et al. 2008; Bouché et al. 2010) by expelling gas or preventing accretion, and are now regularly invoked in hydrodynamical simulations (e.g., Oppenheimer et al. 2010; van de Voort et al. 2011). Chief among these are quenching via supernova feedback in low-mass galaxies at early times and from an active galactic nucleus (AGN) at later times, as illustrated in Figure 1.2.

The need to accommodate the cycling of gas in and out of galaxies (known as the “baryon cycle”) has brought out new observational frameworks - known as “bathtub” or “equilibrium” models (Bouché et al. 2010; Davé et al. 2012; Lilly et al. 2013) - which place emphasis on the accretion of cold gas, the efficiency of SF, and the role of metal-enriched outflows ejected into the circumgalactic (CGM) and intergalactic medium (IGM). These models have now taken center stage in galaxy evolution (Saintonge et al. 2013) and provide the framework for this Thesis. We describe these in more detail in Section 1.3.1.

1.2 Galaxy Evolution from an Observational Perspective

From an observational standpoint, the advent of large photometric and spectroscopic surveys such as the Sloan Digital Sky Survey (SDSS; York et al. 2000), Two Micron All-Sky Survey (2MASS; Skrutskie et al. 2006) and the 2dF Galaxy Redshift Survey (2dFGRS; Colless et al. 2001), among others, have revolutionised the field of astronomy and enabled great strides in the characterisation of galaxy properties, their environments, and the Universe as a whole. Observations over ultra-violet (UV), optical, and infrared (IR) wavelengths have allowed astronomers to measure crucial galaxy properties such as photometric colour, the rate of SF (SFR) and stellar masses (M_*) (among others), with which to constrain the statistical properties of galaxies over time (e.g., Brinchmann et al. 2004; Kauffmann et al. 2003a; Tremonti et al. 2004; Salim et al. 2007).

1.2.1 A Bimodal Population

One of the main tools to study galaxies are their colours as measured through different photometric filters. The optical colour of a galaxy can yield important information about its SF history, chemical evolution, and/or dust attenuation, given that dust and stellar populations of different masses, ages and metallicities all emit the majority of their light at different wavelengths. When comparing the colours and stellar masses (or luminosities) of large samples of galaxies, two distinct populations become apparent: galaxies with blue colours (the “blue cloud”) and galaxies with red colours (the “red sequence”) (Strateva et al. 2001; Blanton et al. 2003; Baldry et al. 2004; Balogh et al. 2004; Baldry et al. 2006; Ball et al. 2008; Schawinski et al. 2014). Between the two populations lies a far smaller third population of galaxies with intermediate colours, known as the “green valley”. This colour bimodality is in place at least out to $z \sim 1$ (Faber et al. 2007). In such observations, two important trends become apparent, namely that (i) the most luminous galaxies (i.e., most massive galaxies) are described by a narrow distribution of red colours and the faintest galaxies (i.e., the least massive galaxies) are described by a broader distribution of blue colours, and (ii) that galaxies with higher masses appear redder in colour. This is illustrated in Figure 1.3 from the study of Schawinski et al. (2014) with the Galaxy Zoo project.

This colour bimodality is also matched in galaxy morphology, SFR, sizes, and ages. By quantifying the galaxies’ radial surface brightness and classifying their morphologies,

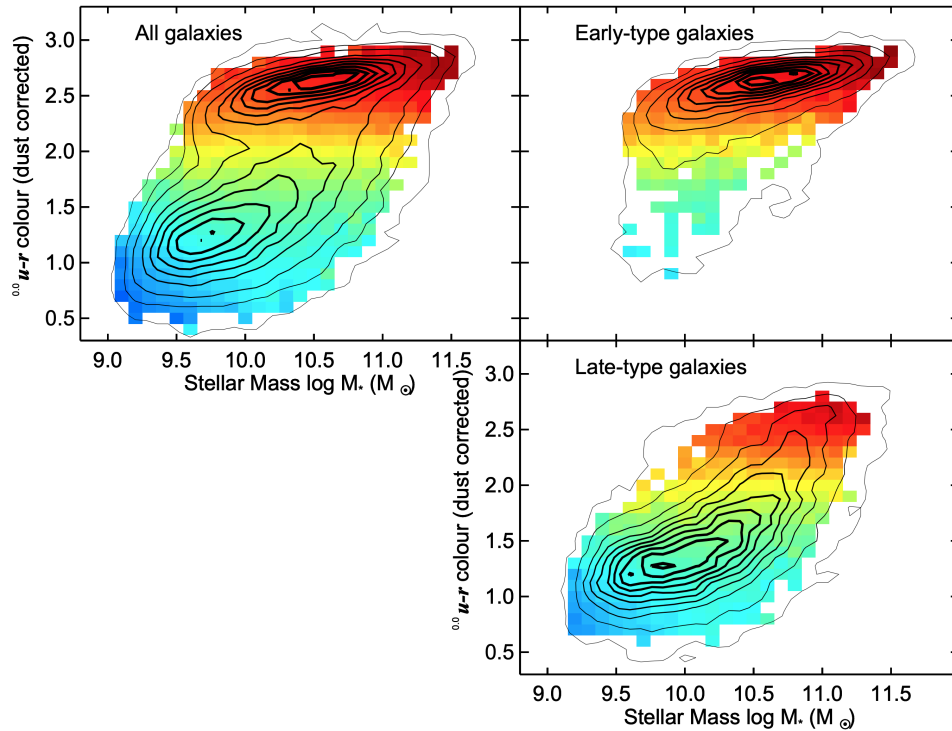


Figure 1.3. The dust-corrected galaxy colour-mass diagram and bimodality shown by Schawinski et al. 2014. The galaxies are binned by 0.1×0.1 dex and colour-coded by the mean specific SFR, with blue galaxies on average displaying higher levels of SF than their red counterparts. On the right, the dichotomy in galaxy type (i.e., early-type and late-type) is also evident, with early-type galaxies dominating the red colours and highest end of the stellar masses and late-type galaxies residing primarily in regions of blue colours whilst dominating the lowest end of the stellar masses.

galaxies in the blue cloud are found to be more disk-like, with well defined spiral arms (so-called “late-type” galaxies), whilst red galaxies are generally found to be more spheroidal and elliptical in nature (“early-type” galaxies), with a central bulge dominating their light profile (Schawinski et al. 2014). At fixed stellar mass, the late-type galaxies are also found to be on average younger (Kauffmann et al. 2003a), larger than their early-type counterparts (Shen et al. 2003) and display elevated SFRs compared to the suppressed rates seen in the latter (Schawinski et al. 2014). This has led to labels of “blue and star-forming” and “red and dead” to describe the two populations.

The colour bimodality, combined with the distinct differences in galaxy SFRs and morphologies, is expected to reflect the underlying stellar population and an evolutionary pathway for galaxies. Young, massive stars emit the majority of their light at UV and

bluer wavelengths and, once SF stops, the young stars die off and the optical spectrum becomes dominated by the red light emitted by more mature stars. As such, young galaxies likely start off in a blue cloud of star-forming, disk-like galaxies, transition through the green-valley where SF is suppressed, and finally end up on the red sequence of quenched, passive galaxies (Bell et al. 2004; Faber et al. 2007; Martin et al. 2007; Gonçalves et al. 2012).

As mentioned at the beginning of this Section, however, galaxy colours are also subject to a variety of internal processes which can mimic intrinsic stellar properties. The main culprit of this is dust, which can significantly enhance a galaxy’s colour to redder magnitudes (Wise & Silva 1996; Masters et al. 2010). Despite this caveat, when properly analysed galaxy colours offer a powerful tool to explore and quantify evolutionary trends.

1.2.2 The Main Sequence of Star-Forming Galaxies

The galaxy evolutionary pathway is perhaps more compelling when comparing the SFRs, stellar masses and gas reservoirs of galaxies over time. A comparison of the first two quantities over statistical samples in the SFR- M_* plane at $z \sim 0$ reveals a tight sequence of star-forming galaxies, with elevated SFRs, known as the galaxy “Main Sequence” (MS) (Brinchmann et al. 2004; Daddi et al. 2007; Elbaz et al. 2007; Noeske et al. 2007; Magdis et al. 2010; Peng et al. 2010b; Whitaker et al. 2014). For galaxies on this Sequence, as the stellar mass of the galaxy increases, so does its SFR. The dependence of the MS is mostly redshift independent and well characterised out to $z \sim 2-3$ (Magdis et al. 2010; Karim et al. 2011; Whitaker et al. 2014), but the normalisation of the relation increases to higher SFRs with redshift. Power-law fits to the data have revealed the relation

$$\text{SFR} \sim M_*^a (1+z)^b, \quad (1.1)$$

where $a \sim 0.8-1$ and $b \sim 2.5-3$, although the exact shape of the Sequence is debated between a power law and curve-like shape with a flatter slope at high-mass compared to the low mass regime (Rodighiero et al. 2010, 2014; Whitaker et al. 2014; Schreiber et al. 2015; Whitaker et al. 2015; Tomczak et al. 2016). The MS at $z \sim 0$ and its redshift evolution are illustrated on the left and right plots of Figure 1.4, respectively. With high duty cycles (i.e., the fraction of a galaxy’s life spent forming stars) of 40-70% (e.g., Noeske et al. 2007), galaxies lying on the MS provide $\sim 90\%$ of the total SF in the Universe (Rodighiero et al. 2011) and are the most representative star-forming galaxy populations

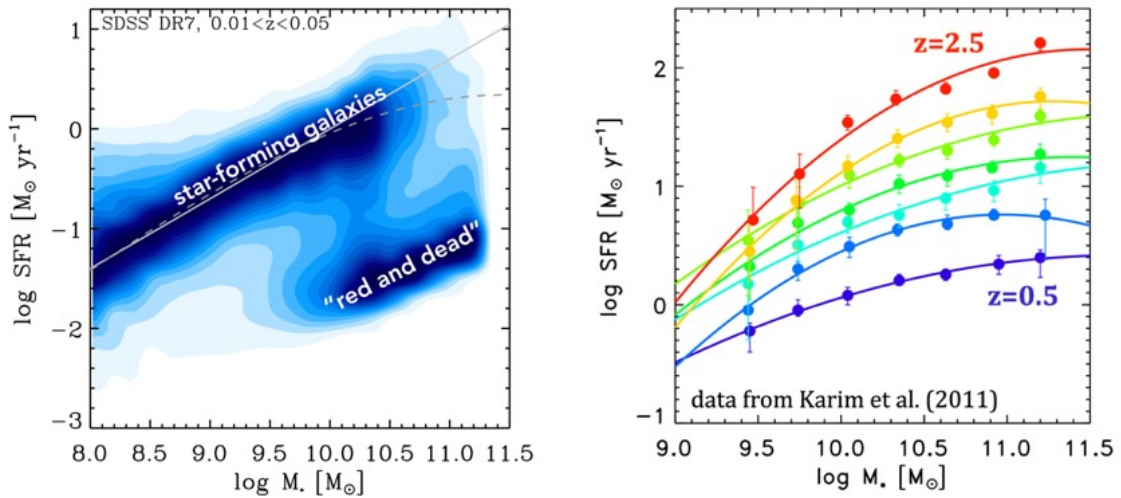


Figure 1.4. Left: The SFR- M_* plane as shown at $z \sim 0$ by the SDSS, highlighting the Main Sequence of “blue and star-forming” galaxies and passive cloud of “red and dead” galaxies. The two dashed lines represent fits to the MS by Peng et al. (2010b) (solid line) and Saintonge et al. (2016) (dashed line). Right: The redshift evolution of the MS from $z=0.5$ -2.5 with data from Karim et al. (2011). Each point represents a binned average and varying colours mark different redshifts. Both figures are courtesy of Dr. Amélie Saintonge.

at any given epoch. Galaxies residing above the MS generally display extreme rates of SF and are considered “starbursts”. The existence of the MS, combined with its surprising tightness and simplicity, suggests that the SF histories the galaxies on it are generally regular and governed by simple underlying processes rather than stochastic events, thereby downplaying the role of mergers and starbursts in the global SF budget of the Universe (Rodighiero et al. 2011; Sargent et al. 2012; Kaviraj et al. 2013).

Below the MS lies a cloud of high mass, passive galaxies with little to no SF (i.e., the red sequence) which forms the second main locus on the SFR- M_* plane. Due to their extremely low specific SFRs (sSFR, defined as SFR/M_*), these galaxies are considered quenched and the endpoint of an evolutionary pathway. We illustrate the main two of these populations in the left plot of Figure 1.4.

Similar to trends seen in the colour-mass plane, star-forming and passive galaxies provide different number contributions at different stellar masses. It is generally agreed that the low-mass end of the stellar mass function is dominated by the blue, star-forming populations, whilst at the high-mass end, quenched, red sequence galaxies are the dominant population (Baldry et al. 2004; Pozzetti et al. 2007; Ilbert et al. 2010, 2013; Muzzin et al. 2013). Such a trend continues out to $z \sim 4$ (Ilbert et al. 2013; Muzzin et al. 2013). An

additional similarity to the colour-mass diagram is the presence of a reduced population of so-called green valley galaxies immediately below the MS, displaying reduced rates of SF. Due to the scarce numbers of this intermediate population, they are touted as galaxies representing a phase transition between the MS and the passive population, whose reduced SFRs are the result of (rapid) ongoing quenching processes (i.e., single or multiple physical mechanisms that halt or prevent SF). As mentioned in Section 1.1, outflows are thought to represent one such mechanism, although they remain poorly understood.

Understanding the transition between star-forming and “red and dead” galaxies is one of the major goals of galaxy evolution and modern astronomy and thus a thorough understanding of the physical processes that govern the MS (e.g., SF histories, gas contents, environments) and the quenching mechanisms (e.g., outflows, gas strangulation, mergers) of their SF, which give rise to the galaxy bimodality and red sequence, are prerequisites to understanding galaxy evolution as a whole. Significant progress has been made towards understanding the former through simple galaxy evolution frameworks (see Section 1.3.1) and observations of molecular gas, however still lacking is a robust understanding of the latter. One of the main goals of this Thesis is, therefore, to constrain the role of outflows as a potential quenching mechanism in normal galaxies.

1.3 Gas Cycling and Outflows as Quenching Mechanisms

The current framework for galaxy evolution is able to explain the positions of the star-forming MS and the red sequence through the amount of cold gas available to galaxies to form stars. Pioneered by intuition from hydrodynamical simulations, the framework – known as the “equilibrium” or “bathtub” model (Bouché et al. 2010; Davé et al. 2012; Dekel et al. 2013; Lilly et al. 2013) – downplays the role of major mergers as the main mechanism for galaxy growth (Rodighiero et al. 2011; Sargent et al. 2012) and instead places the regulation of gas at centre stage. In such a scenario, gas is fed into the galaxy system, converted into stars within the disk, and ultimately ejected from the system in the form of metal-enriched outflows (Oppenheimer & Davé 2008; Bouché et al. 2010). Thus, the triggering of SF, the chemical enrichment, and the overall growth of galaxies is regulated by the gas reservoirs of galaxies. In the following Section we present the main components of such a model, based on the framework described by Lilly et al. (2013).

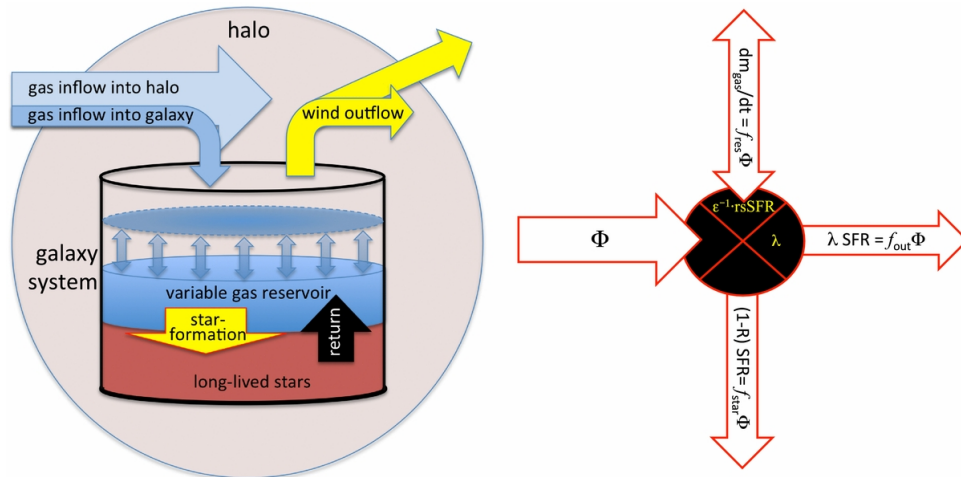


Figure 1.5. The simple gas-regulated equilibrium model described by Lilly et al. (2013). Left: gas flows into the galaxy halo, some of which (f_{gal}) flows into the galaxy system at a rate Φ . The gas then makes its way into the galaxy gas reservoir, or forms into long-lived stars, and ultimately gets ejected from the reservoir via an outflow. Right: the division of Φ into three main fractions (f_{res} , f_{stars} , f_{out}), regulated by ε , η and sSFR.

1.3.1 The Equilibrium Model

The basic idea behind the equilibrium model is the following: baryonic gas mixed with dark matter makes its way into a galaxy halo through smooth cosmological accretion (Kereš et al. 2005; Dekel et al. 2009) from the surrounding medium and some fraction of the baryons, f_{gal} , enters the central galaxy system (or disk) at a rate Φ in the form of cool ($T \lesssim 10^4$ K) gas, where it forms part of the galaxy gas reservoir. In this reservoir, the gas is converted into stars and the instantaneous SFR is said to be regulated by the instantaneous gas mass available (M_{gas}) and an efficiency of SF. Although stars form from molecular gas, the gas referred to here describes both the atomic *and* molecular gas. Some of this gas is immediately returned to the reservoir (or interstellar medium; ISM) via stellar winds and supernovae (which also pollute the ISM with metals), whilst a fraction of it gets locked up into long-lived stars (f_{star}) which steadily increase the net stellar mass of the galaxy system (M_*).

As such, Φ can be divided into three main components: (i) f_{res} , the fraction of baryons entering the galaxy reservoir, (ii) f_{stars} , the fraction of baryons converted into long-lived stars and (iii) f_{out} , the fraction of baryons ejected out of the system via an outflow, where

$$f_{stars} + f_{res} + f_{out} = 1 . \quad (1.2)$$

At any given time the system is said to be in a state of near equilibrium and the instan-

taneous SFR taking place in the reservoir is proportional to the instantaneous gas mass (M_{gas}) available, with a SF efficiency (ε) dictating the amount of gas getting converted into stars:

$$\text{SFR} = \varepsilon \cdot M_{\text{gas}} , \quad (1.3)$$

The gas consumption timescale (i.e., the gas depletion time, τ_{gas}) is the inverse of ε . In an ideal case where ε is constant across epoch and galaxy mass, the SFR of the reservoir depends only on the gas mass. In reality, however, ε could plausibly vary with galaxy mass and as a function of time (although assumed to vary on timescales longer than the gas depletion time). By defining the ratio of gas-to-stellar mass as $\mu = M_{gas}/M_*$, Equation 1.3 can also be expressed in terms of the galaxy’s specific SFR (sSFR=SFR/ M_*):

$$\mu = \varepsilon^{-1} \cdot \text{sSFR} . \quad (1.4)$$

As mentioned above, not all of the gas gets returned to the ISM of the galaxy, since a fraction $(1 - R)$ of it gets locked up in the form of long-lived stars which steadily build up the total stellar mass of the system. It follows, then, that the net increase in stellar mass of the system is described by

$$\dot{M}_* = (1 - R) \text{SFR} . \quad (1.5)$$

The energy and momentum generated by the SF is able to produce an outflow which ejects gas out of the galaxy reservoir with a mass loss rate (\dot{M}_{out}) scaled by a so-called “mass loading factor”, defined as

$$\eta = \dot{M}_{out}/\dot{M}_* . \quad (1.6)$$

If η is constant, the mass loss rate of the system is regulated solely by the galaxy’s SFR. As such, we can see that these basic equations serve to *regulate* the SFR of the system from variations in the gas accretion rate of the system and/or ε and η . From mass conservation, a star-forming system is therefore said to be in a state of near equilibrium

$$\Phi = \dot{M}_* + \dot{M}_{out} + \dot{M}_{gas} . \quad (1.7)$$

where \dot{M}_{gas} is an allowed change in the reservoir gas mass. In [Davé et al. \(2012\)](#), this term is set to zero with the assumption that the reservoir has a non-varying gas mass based on the idea that star-forming galaxies generally lie close to a state of equilibrium. However, [Lilly et al. \(2013\)](#) argue that a nonzero treatment is crucial given that the gas reservoir regulates the galaxy’s SFR. In the case where $\dot{M}_{gas}=0$ and R is constant, through

replacement of terms and rearranging we see that the SFR history of a given galaxy is dictated solely by its accretion history and evolution of the mass loading factor:

$$\text{SFR} = \frac{\Phi}{(1 - R + \eta)} . \quad (1.8)$$

If the reservoir gas mass is allowed to vary, however, we can express the last term in Equation 1.7 in terms of the change in gas-to-stellar mass ratio, $\frac{d\mu}{dt}$. By substituting in Equation 1.3 and $M_* = \mu^{-1} M_{gas}$, the relation becomes:

$$\dot{M}_{gas} = \left[\mu(1 - R) + \varepsilon^{-1} \frac{d \ln \mu}{dt} \right] \cdot \text{SFR} . \quad (1.9)$$

The regulator is assumed to be in a quasi-steady state if the last term in the brackets is small. Finally, replacing Equation 1.7 with the above equations, the expression for the rate of gas infall into the galaxy system - and ultimately the equilibrium equation - is given by:

$$\Phi = \left[(1 - R)(1 + \mu) + \eta + \varepsilon^{-1} \frac{d \ln \mu}{dt} \right] \cdot \text{SFR} . \quad (1.10)$$

By inserting Equation 1.10 into the fractional splitting equations of Φ described by Equation 1.2, we can format the splitting as follows:

$$\begin{aligned} f_{star} &= \frac{(1 - R) \cdot \text{SFR}}{\Phi} = \frac{1}{1 + (1 - R)^{-1} \eta + \varepsilon^{-1} (s\text{SFR} + (1 - R)^{-1} \frac{d \ln \mu}{dt})} \\ f_{out} &= \frac{\eta \cdot \text{SFR}}{\Phi} = \frac{(1 - R)^{-1} \eta}{1 + (1 - R)^{-1} \eta + \varepsilon^{-1} (s\text{SFR} + (1 - R)^{-1} \frac{d \ln \mu}{dt})} \\ f_{res} &= \frac{(\mu(1 - R) + \varepsilon^{-1} \frac{d \ln \mu}{dt}) \cdot \text{SFR}}{\Phi} = \frac{\varepsilon^{-1} s\text{SFR} + (1 - R)^{-1} \varepsilon^{-1} \frac{d \ln \mu}{dt}}{1 + (1 - R)^{-1} \eta + \varepsilon^{-1} (s\text{SFR} + (1 - R)^{-1} \frac{d \ln \mu}{dt})} . \end{aligned} \quad (1.11)$$

The above three equations demonstrate that fundamentally the equilibrium model is regulated by three key parameters, i.e., ε , η and the sSFR, which serve to ensure the galaxy system remains as close as possible to a state of equilibrium. In the case of an ideal regulator, the rate of change of μ is large compared to the gas consumption timescale and $\frac{d \ln \mu}{dt}$ can be set to zero, simplifying the equations even further.

Whilst the equilibrium model relies on three primary quantities, which are all derivable from galaxy observations, they fundamentally rely on an assumed Initial Mass Function (IMF). The IMF is an empirical function that describes the fractional distribution in mass

of a newly-formed population of stars. Whilst the exact shape of the IMF is still heavily debated, the general form describes an initial population of stars with large fractions of mass taken up by low mass stars and low fractions taken up by high mass stars. Thus, the general form is assumed to be a power law from high to low mass, which likely flattens out (and possibly decreases) at low stellar mass. The IMF is one of the most important and fundamental functions in stellar and galaxy evolution studies and, whilst progress has been made through e.g., observations of the Milky Way, constraining and confirming its shape and universality remains one of the holy grails of astrophysics.

1.3.2 Observational Support for the Model and Challenges

The simplicity of the equilibrium model combined with its success in reproducing fundamental galaxy laws with a small number of free parameters, leads credibility to its use as a framework for observational studies of galaxy evolution. To date, the strongest observational support for the model has come in the form of molecular gas observations. With strong evidence to support a limited contribution from mergers and starburst galaxies to the global SFRs (Rodighiero et al. 2011; Sargent et al. 2012), such molecular gas observations - typically using the CO molecular gas tracer - have targeted the *normal* galaxy populations across a variety of redshifts with the aim of determining their cold gas contents, SF efficiencies, and outflow strengths. Simple tests using these parameters at low redshift have revealed an observational picture where a galaxy's position relative to the MS generally depends on the neutral and molecular gas fraction (Bothwell et al. 2013b; Saintonge et al. 2016, 2017), with star-forming galaxies on average having significantly larger gas fractions than passive galaxies at a fixed stellar mass. This was shown with CO(1-0) and HI observations of ~ 500 SDSS-selected normal galaxies at $z \sim 0$ by Saintonge et al. (2017) and a secondary dependence found with the efficiency of SF (Saintonge et al. 2012, 2016). Molecular and far-infrared observations of high redshift galaxies further support these claims out to $z \sim 2.5$ (Magdis et al. 2012; Tacconi et al. 2013; Bothwell et al. 2013b; Saintonge et al. 2013). Further tests of the model through the redshift evolution of the sSFR with 17 MS lensed galaxies at $z \sim 1.4-3.1$ and a compilation of sources from the literature was presented by Saintonge et al. (2013), who found excellent agreement between observations of the molecular gas fraction and the $\text{sSFR}(M_*, z)$ relation presented by Lilly et al. (2013) and argued that a rapidly increasing sSFR with redshift was a consequence of increased gas fractions and slowly varying SF efficiencies, as predicted by Equation 1.4 of

the equilibrium model. The mean depletion timescale of the high redshift ($z > 2$) galaxies was found to be only ~ 450 Myr, a factor of ~ 1.5 (~ 5) shorter than measurements of galaxies at $z \sim 1$ ($z \sim 0$), consistent with a scaling of $(1+z)^{-1}$. Such an evolution for MS galaxies can be explained by the equilibrium model if the gas reservoirs act as the main driver of the evolution.

Further support for the model has also come in the form of detections of outflowing gas in galaxies; an important component in the equilibrium model. Such detections have come over a variety of wavelengths, objects, and redshifts (e.g., [Weiner et al. 2009](#); [Chen et al. 2010](#); [Sturm et al. 2011](#); [Martin et al. 2012](#); [Cicone et al. 2014](#)) and have revealed a complex picture relating to the natures of outflows. Outflows have been found to be prevalent (e.g., [Rupke et al. 2005a,b](#)) and in some cases strong enough to remove significant amounts of gas from the galaxy reservoir (e.g., [Cicone et al. 2014](#)). We present a more in depth assessment of the history and current state of the field of outflows in Section 1.4.

Despite the success of observations in constraining the simple framework of the equilibrium model, several outstanding issues remain. One of these is a lack of constraints on the prevalence and power of outflows over the *normal* star-forming galaxies at each epoch and their multiphase nature: due to the difficulty in obtaining high signal-to-noise spectra of outflows, observations have typically relied on extreme objects which are not representative of the bulk of the star-forming populations. As such, questions of outflows over the normal populations remain: How prevalent are they? How much cold gas gets ejected? What are their structures? Furthermore, in determining the power and mass loss rates of outflows, studies are required to make largely unconstrained assumptions about outflow geometry and the state of the gas being ejected out from single-phase gas tracers, leading to order-of-magnitude differences between studies and objects and rendering a direct comparison difficult. These questions provide the main focus of this Thesis and are described further in the following Section.

1.4 Importance of Outflows & Current State of the Field

As described in Section 1.3.1, outflows clearly play a crucial role in regulating the gas content of galaxies across cosmic time. They can arise due to large amounts of energy and momentum given off by stellar winds, supernovae, or an active galactic nucleus (AGN) and have been observed and found to be ubiquitous at all epochs (see review by [Veilleux et al.](#)



Figure 1.6. A multiwavelength image of the starburst galaxy M82 and its outflow. The image is a composite between observations from the Hubble Space Telescope (yellow/green colours, tracing the UV disk, and red tracing a massive outflow seen in $H\alpha$ emission) and Chandra (blue colours, tracing X-ray emission from the outflowing gas). The gas can be traced back to the central regions of the galaxy, which hosts regions of extreme starbursts that drive the outflow. Image credit: <http://chandra.harvard.edu/photo/2006/m82/>.

2005). Most observations, however, have typically focused on a variety of more extreme objects such as mergers, (U)LIRGs and QSO hosts (e.g., [Cicone et al. 2014](#); [Rupke et al. 2005a,b, 2017](#)) and much less is known on the more normal objects at each epoch. An example of a massive outflow seen in the M82 starburst galaxy is shown in Figure 1.6.

1.4.1 The Prevalence of Outflows and Their Properties

Over the past decade, several pioneering studies have helped to observationally constrain the prevalence of low- z ($z \lesssim 1$) outflows in samples of less extreme star-forming galaxies (e.g., [Weiner et al. 2009](#); [Chen et al. 2010](#); [Martin et al. 2012](#); [Rubin et al. 2014](#)). In one of the first major systematic searches, [Weiner et al. \(2009\)](#) used a sample of 1,406 DEEP2 galaxy spectra at $z \sim 1.4$ to search for cool, low-ionisation outflowing gas and found detections in more than half of their sample. They found evidence that their detection rate had a weak positive dependence on stellar mass and SFR. [Martin et al. \(2012\)](#) followed

up on this with an investigation of 200 deep Keck/LRIS spectra of highly star-forming galaxies with $\log M_*/M_\odot > 9.4$ at $0.4 < z < 1.4$. They also found a high detection rate of $\sim 50\%$, however unlike [Weiner et al. \(2009\)](#), they did not find any dependence of outflow properties with stellar mass or SFR. Despite the success of the aforementioned studies in demonstrating the ubiquity of outflows at $z \sim 1$, the selected samples were primarily of a starburst nature. [Rubin et al. \(2014\)](#) improved on this with their sample of 105 galaxies derived from the GOODS fields and Extended Groth Strip, at a median redshift $z \sim 0.5$. These objects spanned a larger range of stellar mass ($\log M_*/M_\odot \gtrsim 9.6$) and SFRs (SFR $\gtrsim 2 M_\odot \text{ yr}^{-1}$) than the previous studies. The detection rate for their sample remained high ($\sim 66\%$), despite sampling lower SFRs. Arguably the most representative study for normal star-forming galaxies of the local Universe, however, was that of [Chen et al. \(2010\)](#). The authors selected a large sample of massive ($\log M_*/M_\odot > 10.4$) star-forming galaxies from SDSS at redshifts $0.05 \leq z \leq 0.18$, and by means of stacking found strong and clear dependencies of neutral gas outflow properties with galaxy viewing angle, stellar mass, and SF surface density (Σ_{SFR}). Chapters 2 and 3 of this Thesis are similar to the pioneering work of [Chen et al. \(2010\)](#) in that stacking approaches of near-identical samples of SDSS DR7 star-forming galaxies are used, as well as the same analytical model for characterisation of NaD. However, these Chapters differ and expand significantly on that work by (i) adopting a much more complex, thorough and reliable method to detect and characterise outflows, (ii) by adopting stacking techniques over a larger variety of parameter spaces and galaxy types (e.g., AGN, disk-like galaxies and bulge-dominated galaxies), and finally (iii) by providing in depth analyses of the quenching potential of outflows towards their host galaxies and exploration of the fate of such outflowing gas.

Each of the aforementioned studies has found winds to be prevalent in the low- z Universe and, due to them arising in galaxies with high SFRs, have suggested they are generally a consequence of high levels of SF or Σ_{SFR} . In fact, a critical Σ_{SFR} threshold of $0.1 M_\odot \text{ yr}^{-1} \text{ kpc}^2$ is regularly suggested in order to launch a galactic wind ([Heckman 2002](#)). However, the detection rates of winds have also been found to vary strongly as a function of galaxy disk inclination: working under the assumption that outflows have a biconical structure which exits perpendicular to the disk, one would expect to have fewer detections in absorption at high inclinations (where one views the disk edge-on) and more at low inclination (viewing the disk face-on). Indeed this appears to be the case, with the majority of detections in absorption arising from low inclinations ([Martin et al. 2012](#); [Rubin](#)

et al. 2014; Chen et al. 2010). For starburst galaxies with inclinations less than $i \sim 60^\circ$, Heckman et al. (2000) found a $\sim 70\%$ probability of detecting outflows in absorption.

Deep observations of local galaxies also revealed the presence of a diffuse, secondary layer of extraplanar gas (known as a “lagging halo”) which extends kiloparsecs (kpcs) out of the disk. The extraplanar gas has been observed in the atomic (e.g., Fraternali et al. 2002; Matthews & Wood 2003; Oosterloo et al. 2007; Zschaechner et al. 2015) and ionised (e.g., Rossa & Dettmar 2003a,b; Heald et al. 2007; Kamphuis 2008) gas phases, in both external galaxies and the Milky Way (Marasco & Fraternali 2011). Accompanying the extraplanar gas are often signatures of accretion (e.g., Fraternali et al. 2002; Fraternali & Binney 2008; Zschaechner et al. 2015), and dynamical modeling of the gas suggests outflows or accretion alone cannot account for the observed kinematics and gas masses (Fraternali & Binney 2006). As such, the emerging picture appears to be a cyclic scenario, where gas gets blown out from the disk by stellar winds and supernovae (this “blowout” phase has been observed by e.g., Boomsma et al. (2008), who report holes of H I gas in the disk of NGC 6946 with high rates of SF) and eventually condenses and mixes into colder gas which gets re-accreted and fuels SF. This scenario is known as the “galactic fountain” (Shapiro & Field 1976) and plays a crucial role in regulating the gas contents and SFRs of local galaxies.

1.4.2 Star Formation vs AGN Feedback

Although SF certainly appears to play an important role in launching winds, the dominant energy source for outflows in the present day Universe is not always obvious. Several recent studies have aimed to address this by comparing the detection rates of outflows in local galaxies displaying signatures of SF and AGN. For instance, Sarzi et al. (2016) used a sample of 456 objects for which both optical and radio data were available and found that none of the 23 objects displaying signatures of neutral gas outflows showed radio emission or optical line ratios indicative of an AGN. Concas et al. (2017) conducted a similar study with SDSS-selected galaxies and found outflows traced by the same neutral gas to be present in both star-forming galaxies and AGN hosts. These results appear to suggest that weak, optically-selected AGN do not have a major influence on the detection rates of neutral gas outflows. Studies of more extreme AGN/QSOs and starbursts, however, generally portray a more distinct picture: many such objects exhibit very powerful outflows (e.g., Walter et al. 2002; Cannon et al. 2005; Feruglio et al. 2010; Combes

et al. 2013; Cicone et al. 2014; García-Burillo et al. 2015; Fiore et al. 2017) which appear significantly enhanced by the presence of an AGN. For example, using a sample of 19 strong Seyferts, LINERs and “pure” starburst galaxies, Cicone et al. (2014) found strong molecular outflows in all galaxy types, but with significantly boosted outflow velocities and mass loss rates in the AGN hosts. The latter quantity was also found to increase with the AGN luminosity.

1.4.3 Can Outflows Quench a Galaxy?

These results inevitably lead to the crucial question of whether outflows ultimately halt the SF processes in galaxies (coined “negative feedback”) or not. This can happen via the removal of gas necessary to fuel SF, prevention of accretion, or a combination of both. Spectroscopic studies have found cases of AGN-driven outflows expelling mass at a rate many times that of the host galaxy’s SFR, thereby clearly able to remove significant fractions of gas and eventually quench the host (e.g., Cicone et al. 2014; Sturm et al. 2011). Additionally, some Integral Field Unit (IFU) studies have also shown a spatial coincidence with outflowing material and an absence of SF (e.g., Cresci et al. 2015; Carniani et al. 2016), although it is often unclear whether there is causality in this. Further complicating this picture are instances where SF has seen itself reignited due to the turbulence created by the presence of an outflow (coined “positive feedback”, e.g., Maiolino et al. 2017; Gallagher et al. 2018). Simulations of the Milky Way even suggest weak outflows form a necessary ingredient to stimulate and *sustain* accretion - and therefore SF - by transferring gas from a surrounding hot corona to the disk (e.g., Marinacci et al. 2010; Marasco et al. 2012).

A quantity often used to describe how efficiently outflows can remove mass is the *mass loading factor*, η , defined as the mass outflow rate divided by the SFR of the host. This value is used in simulations to dictate the strength of outflows (e.g., Oppenheimer et al. 2010; Muratov et al. 2015; Vogelsberger et al. 2013), yet important discrepancies exist with results found in observations, with the latter often finding order-of-magnitude lower values (e.g., Weiner et al. 2009; Martin et al. 2012; Rubin et al. 2014; Chisholm et al. 2017) for normal galaxies. This demonstrates the need to understand whether observations are missing large fractions of ejected mass traced by different gas phases, or simulations are invoking outflows that are stronger than those seen in the present day Universe.

1.5 Tracers of Outflows

Outflows are typically observed via Doppler shifts of low-ionisation ISM gas, characterized by blueshifted signatures in absorption or broad components in emission spectra. The former method is known as the “down the barrel” technique, where gas in front of a galaxy absorbs the background continuum. Since the gas is moving toward the observer along the line of sight (or “barrel”), it appears blueshifted with respect to the systemic (galaxy) component. Equally, redshifted absorption is suggestive of gas moving towards the galaxy, in the shape of inflowing gas. Although such signatures may arise from anywhere along the sight line to the galaxy, such that the technique offers no information as to whether the gas reaches (in the case of an inflow) or fully escapes (in the case of an outflow) the galaxy, red/blueshifted absorption has typically been interpreted as an unambiguous signature of in/outflowing gas relative to the galaxy. A schematic of this method is shown in Figure 1.7.

1.5.1 Neutral Sodium (NaD)

One of the most commonly used tracers for neutral gas in outflow studies - and the one used throughout this Thesis - is the resonant NaI absorption doublet at 5889.95 Å and 5895.92 Å (also referred to as NaD, with $\sim 300 \text{ km s}^{-1}$ between the two lines), which traces cool ($T \lesssim 10^4 \text{ K}$), metal-enriched gas (Rupke et al. 2005a; Chen et al. 2010; Cazzoli et al. 2016). With an ionising potential of 5.1 eV, NaD is easily ionised by near-UV radiation ($\lesssim 2430 \text{ Å}$) and requires a significant amount of shielding by dust. As such, it is generally a good tracer of dusty, dense regions of cool neutral gas.

The ground state of Sodium is given by the $1s^2 2s^2 2p^6 3s^1$ configuration. If Sodium absorbs a photon with energy less than 5.1 eV, the outermost $3s^1$ electron can be excited up to the $3p$ level with either a $j=3/2$ or $j=1/2$ total angular momentum configuration (due to spin-orbit effects) at wavelengths of 5890 Å and 5896 Å, respectively. The excited electron can spontaneously de-excite back down to the ground state, emitting a photon in the process; as such, NaD is seen both in absorption and in emission (Prochaska et al. 2011). Given that Sodium is a resonant transition (defined as a transition where a ground state electron is excited and can only spontaneously de-excite back down to the same ground state), the electron can only fall back down to the $3s^1$ level.

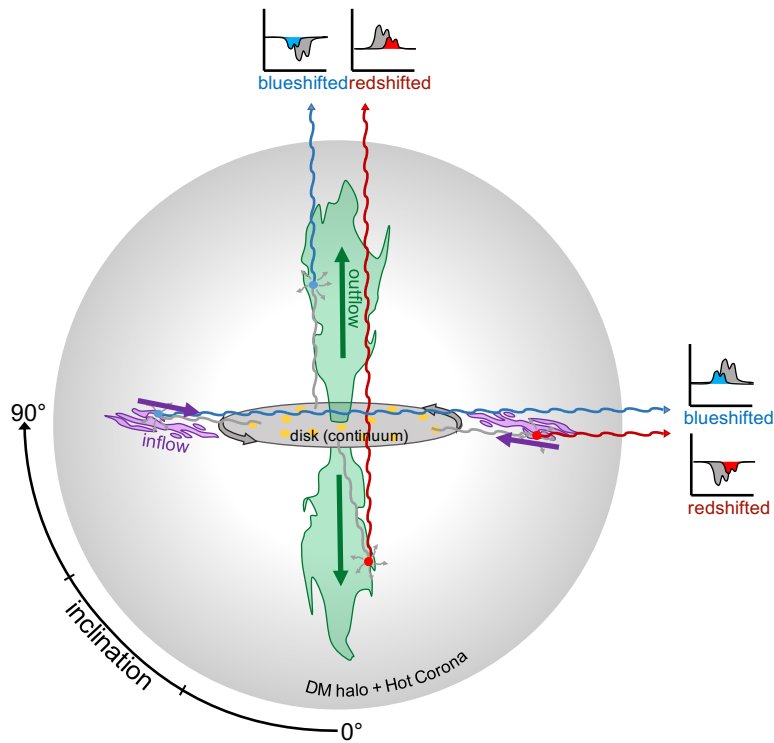


Figure 1.7. A schematic of the different types of Doppler shifts one can observe in the NaD transition. Foreground gas is dominated by absorption of the background continuum, with profiles either blueshifted (outflows) or redshifted (inflows). Background gas is seen in emission of re-emitted photons. Gray lines represent continuum photons from the galaxy disk, blue lines represent blueshifted signatures, and red lines represent redshifted signatures. Small blue or red circles represent absorption, from which re-emission of the photon occurs. Included in the schematic is the role of the viewing angle in detecting outflowing or potentially inflowing gas.

1.5.2 Ionised Gas

In principle, a variety of ionised emission lines can be used to characterize outflowing warm ($T \gtrsim 10^4$ K), ionised gas, and the choice depends on a variety of factors such as brightness, excitation conditions and observational feasibility. The most commonly used optical emission lines are $H\alpha$ λ 6563, $H\beta$ λ 4861, $[O\text{ III}]$ $\lambda\lambda$ 4959, 5007, $[N\text{ II}]$ $\lambda\lambda$ 6549, 6583 and $[S\text{ II}]$ $\lambda\lambda$ 6717, 6731. Unlike for NaD, outflow detections in emission are not observed “down the barrel” but rather as an additional broad component to the systemic narrow component of the galaxy emission. The reason for this is the larger velocities of an outflow moving toward or away from the observer relative to the galaxy’s systemic velocity, thereby creating a broader distribution of velocities compared to the galaxy disk rotation. The assumption that the distribution of velocities relative to the mean is well described by a

Gaussian profile holds for a narrow galaxy component and to first order also for a broad component (Förster Schreiber et al. 2018; Gallagher et al. 2018). However, to higher order, such a distribution for a broad component may not be true given potential red/blue asymmetries caused by a variety of factors such as geometry, viewing angle, dust, etc.

Since the emission lines occur predominantly in the proximity of hot, young stars, shocks, or a supermassive black hole, the lines and their ratios in principle serve as useful diagnostics to determine the conditions of the ionising gas (e.g., density and temperature), its ionising source, and for calculating a variety of quantities such as the SFR or amount of dust present, which can aid in more accurately constraining outflow properties directly. We provide here a brief summary of how these are calculated:

1. SFRs:

The H α line is a so-called “recombination” line because it’s predominantly found in the proximity of ionising young stars, and typically forms from recombined electrons and protons. As such, there is a correlation between the luminosity of H α and the rate of SF that produces the line. Throughout this Thesis we assume a Kennicutt (1998) calibration with a Chabrier IMF, after accounting for dust obscuration. However, H α can also be excited by other mechanisms (e.g., AGN) and as such SFR derivations must be handled with care.

2. The Balmer decrement:

Dust plays an important role in regulating the shape of galaxy spectra and the intensity of emission lines, with emission at bluer wavelengths suppressed by scattering from dust and re-emitted at IR wavelengths. The H α and H β are part of the Balmer series of hydrogen ($n \geq 3 \rightarrow n=2$) lines and have an intrinsic intensity ratio of $I(\text{H}\alpha)/I(\text{H}\beta)=2.86$ (the so-called Balmer decrement) and given that H β lies $\sim 1700 \text{ \AA}$ away from H α , any difference in this ratio is attributed to dust obscuration of the H β flux, which can be calculated assuming a wavelength-dependent extinction law (e.g., Calzetti et al. 2000; Battisti et al. 2016). Throughout this Thesis we use the Balmer decrement and assume a Battisti et al. (2016) extinction law to derive dust quantities for local galaxies. Whilst a Calzetti et al. (2000) extinction law is most often assumed for studies of star-forming galaxies, the decision to use a Battisti et al. (2016) extinction law is motivated by the fact that the former law is calibrated to starburst galaxies, which are not representative of the normal, star-forming popula-

tions (and therefore data sets used in this Thesis), whilst the latter law is calibrated using large samples ($>10,000$) of normal, star-forming galaxies from the SDSS.

3. Electron temperature and density:

Forbidden emission lines (so-called because of the low probability of spontaneous de-excitation of electrons in metastable energy levels) provide useful tools to measure the ambient temperatures and densities of electrons in H II regions. At low atomic and electron densities (n_e), the excitation of an electron is followed by spontaneous decay back to the ground level and emission of photons. For a pair of lines originating from closely spaced metastable energy levels, the intensity ratio of the two is virtually independent of temperature and the departure from their intrinsic value is due to a varying density. An example of such lines are the [O II] and [S II] doublets at $\lambda\lambda$ 3729, 3726 and $\lambda\lambda$ 6716, 6731.

1.5.3 Atomic and Molecular Gas

Arguably the most valuable tracers are those of the atomic and molecular gas phase, which directly trace the fuel for SF in galaxies. The most typical lines used for these phases are the hydrogen 21cm line and multi-transitional CO emission, respectively. Given that cold H₂ does not have a permanent electric dipole and is therefore unobservable, CO suitably serves as an alternate tracer and can be converted to an H₂ gas mass via a conversion factor, α_{CO} . As for ionised gas, outflows in H I and CO are seen as an additional broad emission component (e.g., [Feruglio et al. 2010](#); [Cicone et al. 2014](#); [Fluetsch et al. 2018](#)). However, unlike ionised gas, H I and CO both trace diffuse gas throughout the galaxy and as such often display a systemic double-horn profile, characteristic of a rotating system. As such, these require more complex and precise modelling to disentangle the systemic and broad components.

Data Sets & Analysis Codes

The work described throughout this Chapter forms the first half of [Roberts-Borsani & Saintonge \(2019\)](#) “The Prevalence and Properties of Cold Gas Inflows and Outflows Around Galaxies in the Local Universe”.

2.1 Observational Data Sets

Given the aim of characterising outflows in normal, low redshift galaxies, the choice of data sets is important so that our samples provide us with large numbers of representative galaxies with which to perform detailed stacking analyses. The data sets described below serve as the primary observational data sets for this Thesis and are selected primarily due to their large sample sizes of low redshift galaxies, the representative nature of those observed galaxies, and finally the availability of commonly-used outflow tracers. These considerations apply to spectroscopic surveys conducted with single fibers, integral field units, or integrated observations. Thus, for studies describing the prevalence and integrated properties of neutral gas outflows, the Sloan Digital Sky Survey is chosen due to its large sample size and visibility of the NaD absorption tracer. For resolved studies of the kpc-scale properties of outflows, the Mapping Nearby Galaxies at APO Survey is chosen since it is the largest survey of normal galaxies at low redshift with access to the NaD transition and ionised gas tracers. Finally, for studies of the multiphase nature of outflows, the Extended CO Legacy Database for GASS, Extended GALEX Arcibo SDSS and the

Arecibo Legacy Fast ALFA surveys are chosen since these provide the largest samples of representative galaxies at low redshift with observations of CO and HI emission. Each of these surveys are described in detail below.

2.1.1 The Sloan Digital Sky Survey (SDSS)

The Sloan Digital Sky Survey (York et al. 2000) is one of the largest and most ambitious imaging and spectroscopic survey conducted in modern astronomy, with the goal of mapping out the formation and evolution of stars, galaxies, and the large scale structure of the Universe. Using the 2.5m optical telescope at the Apache Point Observatory (APO) in New Mexico, United States, the survey has provided the scientific community with images and spectra for >1,000,000 objects, charting over a third of the night sky. The SDSS is separated out into four phases of operations (SDSS-I, SDSS-II, SDSS-III and, currently, SDSS-IV), each comprising a number of individual surveys dedicated to a different science goal. The 7th Data Release (DR7; Abazajian et al. 2009), the final one of SDSS-II, consists of three subprojects - The Legacy Survey, SEGUE and the Supernova Survey - which span a total of >10,000 square degrees in five photometric bands and image nearly 400 million unique objects with just over 1.5 million spectra. For each spectroscopic observation, 3'' fibers are used and plugged into a fixed position on an SDSS plate and whose position is dictated by the science goal (e.g., object observation or sky subtraction). Out of the ~1.5 million DR7 spectra, 929,555 are observations of galaxies and serve as the data set for the SDSS studies in this Thesis.

For the majority of observed galaxies in DR7, the MPA-JHU catalog¹ provides derived quantities for objects at $z < 0.7$. The catalog is a joint initiative by researchers at the Max Planck Institute for Astrophysics (MPA) and Johns Hopkins University (JHU) to derive global galaxy properties from SDSS DR7 spectra and imaging with methods developed by a number of important studies (e.g., Kauffmann et al. 2003b; Brinchmann et al. 2004; Tremonti et al. 2004; Salim et al. 2007). From this catalog, the primary quantities used by this Thesis are the SFRs, stellar masses, inclinations and line fluxes. In brief, these quantities are derived with the following methods:

- SFRs: the SFRs are derived based on the method described by Brinchmann et al. (2004), who estimate these from emission line luminosities (i.e., H α) for star forming

¹<https://www.mpa.mpa-garching.mpg.de/SDSS/DR7/>

galaxies. For those galaxies where an emission line cannot be used due to low S/N or non-thermal contributions (i.e., AGN and composite galaxies), a sSFR ($=\text{SFR}/M_*$) is derived from the D(4000) Å break and converted to a SFR. Since these are derived for fiber observations, which more often than not sample only the nuclear regions of the galaxy, aperture corrections are used to extrapolate the SFRs to the total SFR of the galaxy.

- M_* : the stellar masses are computed via Simple Stellar Population (SSP) fitting of the photometric fluxes both inside and outside the fiber and assuming a stellar mass-to-light ratio and Kroupa (2001) Initial Mass Function (IMF).
- b/a, axis ratio: the axis ratio of a galaxy - i.e., the ratio of the semi-minor to semi-major axis - is estimated via isophotoal r -band photometry and using this, a galaxy inclination can be derived for a galaxy disk with intrinsic thickness, q .
- $H\alpha$, $H\beta$, $[\text{O III}]\lambda 5007$, and $[\text{N II}]\lambda 6583$ line fluxes: the fluxes from each of the lines are derived from Gaussian fits to the continuum-subtracted fiber spectra and corrected for foreground Galactic extinction (https://wwwmpa.mpa-garching.mpg.de/SDSS/DR7/raw_data.html). Amongst other purposes, the selection of these four lines allows us to characterise whether they are excited by an AGN or by SF, using the so-called BPT diagram (Baldwin et al. 1981) and a chosen prescription, which compares the intensity ratios of the lines and can reveal the principal excitation mechanism, since higher ratios of a set of lines (i.e., $[\text{O III}]\lambda 5007/H\beta$ and $[\text{N II}]\lambda 6583/H\alpha$) require harder radiation fields.

2.1.2 The Mapping Nearby Galaxies at APO Survey (MaNGA)

Galaxies are complex systems whose properties evolve over small and large scales. As such, the need to understand and connect the pc- and kpc-scale properties of galaxies to their integrated properties is a current major focus in galaxy evolution. This is helped by the advent of IFUs, which act to divide the field of view (FoV) into multiple pixels and provide spectra for each of these. As such, for extragalactic objects, IFU observations provide spatially resolved spectra over multiple regions of the target. The Mapping Nearby Galaxies at APO (MaNGA; Bundy et al. 2015) survey is part of the SDSS-IV phase and is an IFU survey of the local Universe with the aim of obtaining spatially-resolved spectra for an unbiased sample of $\sim 10,000$ galaxies with $\log M_*/M_\odot \gtrsim 9$ at $0.01 \leq z \leq 0.15$ from the

NASA-Sloan Atlas (NSA) catalog, by 2020. Using the SDSS 2.5m telescope at the Apache Point Observatory, the MaNGA survey offers 29 differently-sized IFUs, each of which consists of a set of optical fibers grouped to form a hexagon and fed into the two BOSS spectrographs on the telescope. 17 IFUs can be used to observe chosen targets at a given time, with the remaining 12 used for flux calibration and additional single fibers for sky subtraction. The bundles cover up to $1.5 R_e$ and $2.5 R_e$ for the targeted galaxy sample and the resulting spectra have a wavelength coverage of 3600-10400 Å with spectral resolution $R \sim 2000$. As such, each observation of a galaxy offers a 3D “cube” of observations, where each pixel (or “spaxel”) offers an optical spectrum.

The 15th Data Release (DR15) provides MaNGA observations for $\sim 4,800$ galaxies and releases detailed maps of derived properties (e.g., line fluxes, stellar velocity dispersions, emission line ratios, continuum fits) for each object, provided by the Data Analysis Pipeline (DAP; [Westfall et al. 2019](#)) after each 3D cube has been placed through the MaNGA Data Reduction Pipeline (DRP). Further data products for $\sim 4,600$ galaxies are also provided by value-added catalogs such as the Pipe3D catalog, which makes use of the Pipe3D cube reduction pipeline ([Sánchez et al. 2016a,b](#)). For studies in this Thesis which make use of MaNGA DR15 data, sample selections are done using the Pipe3D DR15 catalog, whilst all other properties are taken from the DAP and DRP data products.

2.1.3 The Arecibo Legacy Fast ALFA Survey (ALFALFA)

As the most abundant element in galaxies, the importance of constraining the atomic H I fraction of gas cannot be overstated. The Arecibo Legacy Fast ALFA (ALFALFA) survey is a large blind observational program dedicated to mapping out the H I content of galaxies in the local Universe. Using the Arecibo telescope in Puerto Rico, the survey completed observations for $>30,000$ extragalactic H I sources out to $z \sim 0.06$, spanning ~ 7000 square degrees of the sky and overlapping significantly with large multiwavelength surveys such as SDSS, 2MASS, WISE and GALEX. As such, it is the largest H I galaxy survey to date. For this Thesis, we use the final release of the ALFALFA catalogs, $\alpha.100$ ([Haynes et al. 2018](#)), which provides H I–derived quantities for all detected galaxies out to $z \sim 0.01$.

2.1.4 The Extended GALEX Arecibo SDSS Survey (xGASS)

The extended GALEX Arecibo SDSS Survey (xGASS) survey provides a gas fraction-limited census of the H I content of galaxies at $0.01 < z < 0.05$ with the Arecibo telescope. The xGASS sample was constructed via a random sampling of a parent sample of SDSS galaxies with UV observations from GALEX All-sky (or Medium) Imaging Survey, which also overlapped with the ALFALFA footprint. The final sample of 1,179 xGASS galaxies with stellar masses $9 < \log M_*/M_\odot < 11.5$ was chosen to balance the distribution across stellar mass above and below $10^{10} M_\odot$. Of the final sample, 285 were previously observed through the ALFALFA $\alpha.40$ survey (Haynes et al. 2011), whilst another 20 were available through the Cornell H I digital archive (Springob et al. 2005) and were not reobserved. As such, the xGASS survey provides spectra of an additional 874 galaxies, observed until either detected or until a H I gas mass fraction of a few percent. Throughout this Thesis, we make use of spectra and data from the xGASS “representative sample” catalogs.

2.1.5 The Extended CO Legacy Database for GASS (xCOLD GASS)

For studies aiming to characterise the molecular gas in galaxies, the most widely used tracer is the CO molecule. However, until the CO Legacy Database for GASS (COLD GASS) survey, such observations were exclusive to small samples of relatively abnormal objects and a large dedicated survey for normal galaxies in the local Universe was missing. The extended COLD GASS survey (xCOLD GASS; Saintonge et al. 2017) is an IRAM 30m reference survey with the objective of characterising the molecular gas content in local galaxies and its impact on the gas cycle and SFRs within those galaxies. The survey builds on observations from SDSS, GALEX, WISE and the xGASS survey, and mass-selects objects from SDSS above $\log M_*/M_\odot > 9$ at a redshift interval $0.01 < z < 0.05$, thereby providing an unbiased sample of >500 galaxies. The survey consists of two large programmes spanning 6 years of observations on the IRAM 30m telescope and provides CO(1-0) and CO(2-1) spectra for a total of 532 galaxies, further complemented by UV and optical observations as well as atomic H I gas measurements and global galaxy properties such as SFR, stellar mass, AGN presence and inclination. In this Thesis, we make use of the full data release of the survey.



Figure 2.1. The main telescope facilities whose data were used in this Thesis. From left to right: The Apache Point Observatory in New Mexico (USA), the IRAM 30m telescope on Pico Veleta in the Sierra Nevada (Spain), and the Arecibo telescope in Puerto Rico (USA). The three observatories were used as part of the SDSS/MaNGA, xCOLD GASS and ALFALFA surveys.

2.2 Modelling of Neutral Gas Outflows

As discussed in the Introduction of this Thesis, the primary tracer of outflows used in these works is the Sodium absorption doublet, which is primarily a stellar absorption feature. To constrain the properties of blue/redshifted absorption or broad emission components, accurate modelling of a stellar continuum and the absorption or emission line’s features are crucial.

2.2.1 Simple Stellar Population Models & the Penalised Pixel-Fitting Code

A crucial aspect in determining properties of galaxies is to correctly fit and analyse the stellar continuum. Nearby stars in our Milky Way galaxy are generally resolved and obtaining a spectrum of them is fairly straightforward. However, galaxies are complex systems containing hundreds of millions of unresolved stars with a variety of metallicities, ages, and histories, making any analysis far more complicated. Astronomers have aimed to overcome this challenge by using Simple Stellar Population (SSP) models. Since stars are generally not born in isolation but rather in clusters of stars from the same giant molecular cloud (GMC), we can model an observed spectrum of a population of stars with the same age and metallicity and create a Simple Stellar Population. These are generally based on theoretical spectra or observed spectra from stars in our own Milky Way. Given that a galaxy should contain a mix of stellar populations, the approach is to fit a galaxy spectrum with a non-negative linear combination of SSP models (ranging in age and metallicity) and assuming an IMF, which describes the initial distribution of masses for a given stellar

population.

The Penalised Pixel-Fitting (pPXF; Cappellari 2017) routine is a publically-available IDL and Python code developed by Cappellari & Emsellem (2004), which allows the user to perform stellar continuum fitting of an optical spectrum. The code is able to fit both the stellar continuum and nebular emission lines simultaneously, or separately. This is done by describing the line-of-sight velocity distribution (LOSVD) of stellar absorption features through Gauss-Hermite parametrizations, using a linear combination of SSP models for the stellar continuum and a set of Gaussian profiles for the nebular emission lines. The choice of SSP models is a crucial step in determining an accurate fit of the continuum, and as such, in this Thesis we aim to give the code maximum flexibility by providing it with the full MILES (Sánchez-Blázquez et al. 2006; Vazdekis et al. 2010) empirical stellar library (and assume a Chabrier IMF) with BaSTI isochrones and $[\alpha/\text{Fe}]$ -enhanced models where available. The library contains $\sim 1,000$ stellar spectra obtained with the 2.5m Isaac Newton Telescope (INT) in Spain and has a wavelength coverage of 3525-7500 Å with spectral resolution of 2.51 Å (FWHM).

The Sodium doublet is a predominantly photospheric transition and is particularly strong in the spectra of cool stars, with peak strengths for stars of types K3-M0 (Jacoby et al. 1984). The prevalence of bulge K-giants in nuclear regions of galaxies means they are likely to make an important contribution to the spectra used in this Thesis. As such, the careful removal of any stellar contribution is imperative in order to model the residual. Thus, prior to any line modelling, we fit the stellar continuum with pPXF and adopt a Battisti et al. (2016) extinction law to account for dust effects. As mentioned in Section 1.5, the choice of the Battisti et al. (2016) extinction law is to account for the fact that our stacks are largely representative of normal, star-forming galaxies rather than the starburst galaxies which are used to calibrate the Calzetti et al. (2000) extinction law. We carefully mask the Ca II (K and H) and NaD transitions, since these are all in our spectral fitting range and we assume they are the result of a stellar+ISM contribution, which the models cannot account for. We also mask the red half of the He I emission line at 5875.67 Å, which is close enough to the NaD line that it could affect the residual profile. Furthermore, we allow for non-Gaussian line-of-sight velocity distributions (LOSVD), since there is a very small possibility this could influence our results if unaccounted for, although this is most likely a very minor effect (if present).

2.2.2 Bayesian Inference and Nad Profile Fitting

When modelling the absorption feature of a given spectrum, the parametrisation of its features and derivations of the physical state of the absorbing gas (e.g., covering fraction, column density, velocity, turbulence) are possible due to the curve of growth assumption. The assumption is a theoretical relation between the equivalent width (EW) of the line and the optical depth (or column density, N), where the optical depth is defined as the probability of a continuum photon being absorbed by the gas.

We can assume that the optical depth (τ) is related to the flux in the following way:

$$\frac{F_\lambda}{F_c} = e^{-\tau}, \quad (2.1)$$

where F_λ is the observed flux and F_c the flux from the continuum at a given wavelength. The EW of the absorption feature can be defined as:

$$\begin{aligned} \text{EW} &= \int \frac{F_c - F_\lambda}{F_c} d\lambda \\ &= \int \left(1 - \frac{F_\lambda}{F_c}\right) d\lambda \end{aligned} \quad (2.2)$$

As such, the absorption profile relative to the continuum level depends on the density of the absorbing gas and the intensity of the continuum. The curve of growth can be separated into three distinct regions, shown in Figure 2.2.

1. For ordinary stars like our own, weak absorption lines are dominated by thermal Doppler broadening and as such the width of the profile is due to the random motions of the light-absorbing gas present in the atmosphere of the star. As such, if one doubles the density of the absorbing gas, the EW of the line is also doubled: at this point the two quantities are tied by a linear relationship and $\text{EW} \propto \tau \propto N$. This is highlighted in region (1) in Figure 2.2 and illustrated in Figure 2.3.
2. However, as the line becomes optically thick ($\tau > 1$), the EW no longer grows linearly with the optical depth (or number of absorbing gas atoms) and the absorption line begins to saturate ($\tau \gtrsim 5$). At this point, the Doppler wings change very little as the number of atoms grow: the EW can only increase by increasing the wings of the profile, which are characterised by high-velocity clouds. However, at moderate values of τ , such clouds are scarce and so an increase in gas density does little to increase the EW. At this point, $\text{EW} \propto \sqrt{\ln N}$ and this is shown by region (2) in Figure 2.2.

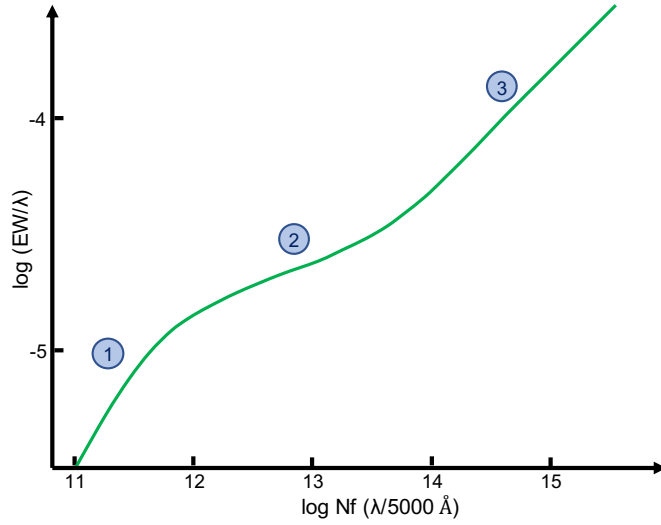


Figure 2.2. The theoretical curve of growth for the Sun. The x-axis represents the logarithm of the column density whilst the y-axis represents the EW of the line. The curve has three distinct regions, marked by numbered circles: the regions correspond to evolving relations between the EW of an absorption line and the column density, or optical depth of the line. The three regions are primarily dictated by the different conditions of the absorbing gas caused by an increase in density over orders of magnitude. This figure was adapted from [Aller & Goldberg \(1971\)](#).

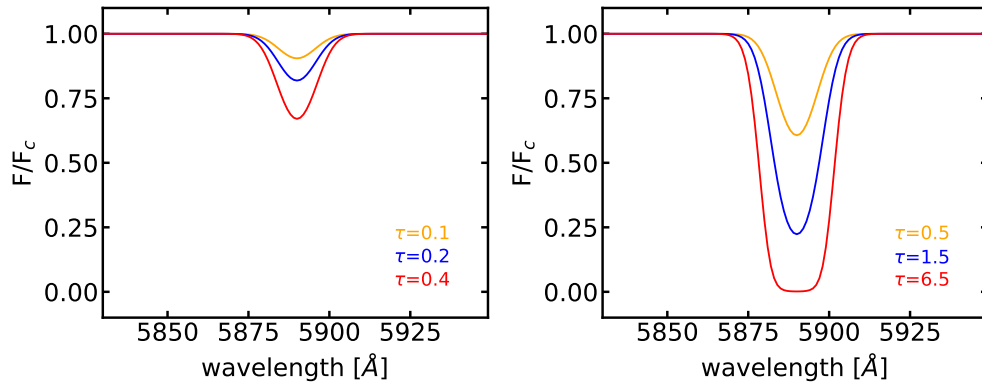


Figure 2.3. The line profile of an absorption feature at low (left) and high (right) optical depths, dominated by Doppler broadening as described by a Gaussian profile. For optically thin lines, if one doubles the optical depth, τ , the EW of the line doubles as well. For optically thick lines, this relationship no longer holds as the line becomes saturated.

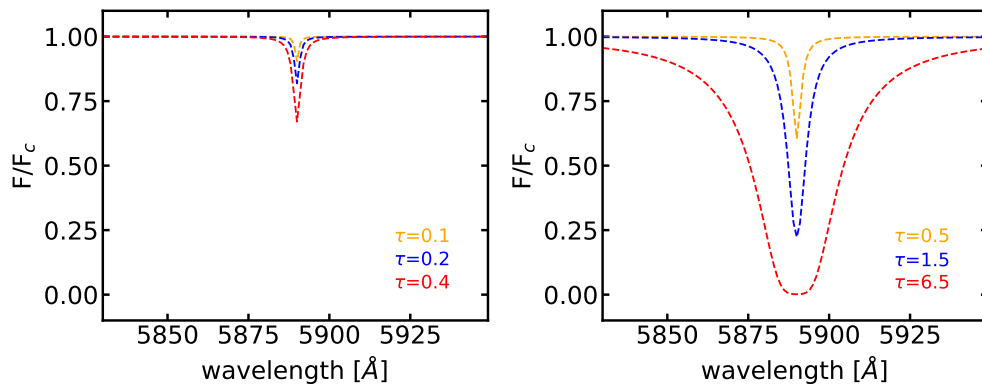


Figure 2.4. The line profile of an absorption feature at low (left) and high (right) optical depths, dominated by pressure and collisional broadening as described by a Lorentz profile.

3. Since the profile is saturated, the only way the EW can increase is through the wings, which at very high optical depths are dominated by pressure and collisional broadening (plus the natural Doppler broadening). This is well described by a Lorentzian line profile, where the distribution of high velocities falls off much more slowly than thermal broadening. As a result, the lines have much wider wings and, at very high optical depths, an increase in τ leads to an increase in EW. This is illustrated in Figure 2.4 and region (3) of Figure 2.2. In reality, however, a line profile is dictated by the interplay of both line profiles and is therefore a combination of both.

Using the curve of growth assumption, we are able to fit the ISM residual of NaD with an analytical expression to search for outflows. Because multiple components may contribute to the NaD signal, many degeneracies exist in the profile fitting. For this reason, we employ a Bayesian inference approach using PyMultinest (Buchner et al. 2014), a Python wrapper for the popular nested sampling code, Multinest (Feroz et al. 2009). We make the assumption that our priors follow a Gaussian distribution and that our data points are uncorrelated. For our NaD modelling, we use the analytical function described by Rupke et al. (2005a). The model follows the form

$$I(\lambda) = 1 - C_f + C_f \times e^{-\tau_B(\lambda) - \tau_R(\lambda)}, \quad (2.3)$$

where C_f is the velocity-independent covering factor, and $\tau_B(\lambda)$ and $\tau_R(\lambda)$ are the optical depths of the Na I λ 5891 and Na I λ 5897 lines, respectively. The optical depth of the line,

$\tau(\lambda)$, can be expressed as

$$\tau(\lambda) = \tau_0 \times e^{-(\lambda - \lambda_0 + \Delta\lambda_{\text{offset}})^2 / ((\lambda_0 + \Delta\lambda_{\text{offset}}) b_D / c)^2}, \quad (2.4)$$

where τ_0 and λ_0 are the central optical depth and central wavelength of each line component, b_D is the Doppler line width, and c is the speed of light. The wavelength offset is converted from a velocity offset, given $\Delta\lambda_{\text{offset}} = \Delta v \cdot \lambda_0 / c$. For NaD $\tau_{0,B} / \tau_{0,R} = 2$ (Morton 1991), meaning the Na I λ 5891 line has twice the depth of the Na I λ 5897 line. The optical depth parameter can be derived from the column density of Sodium, which is described as

$$N(\text{Na I}) = \frac{\tau_0 b}{1.497 \times 10^{-15} \lambda_0 f}, \quad [\text{cm}^{-2}], \quad (2.5)$$

where λ_0 and f are the rest frame wavelength (vacuum) and oscillator strength. Throughout this Thesis we assume $\lambda_0 = 5897.55 \text{ \AA}$ and $f = 0.318$ (Morton 1991).

To determine whether the NaD profiles used in this Thesis display signatures of an outflow, our approach is the following. We first fit a first-order polynomial to the continuum-normalised flux immediately blueward and redward of the profile and divide the residual by this, to account for any systematic continuum-fitting errors that could give rise to artificial residuals. We subsequently fit the NaD line with single parametrizations of the model given in Equation 2.3 (i.e., only one component), once assuming no offset (i.e., with no $\Delta\lambda_{\text{offset}}$), a second time allowing the single component to shift towards bluer wavelengths only (i.e., $\Delta\lambda_{\text{offset}} > 0$) and a third time allowing only shifts towards redder wavelengths (i.e., $\Delta\lambda_{\text{offset}} < 0$). The motivation for this is to determine whether out/inflowing signal is prominent enough to significantly shift a simple single component model from fitting only systemic absorption, thereby demonstrating a necessity for additional components.

The two shifted fits are then subsequently compared to the systemic fit with a Bayesian Information Criterion (BIC) in order to determine whether an out/inflowing component is necessary (i.e., if the blueshifted fit is preferred then an outflowing component is necessary, if the redshifted fit is preferred then an inflowing component is necessary, and if neither shifted fit is preferred then only a single, systemic component is necessary). The BIC makes use of the likelihood for each model but penalises for additional free parameters and is defined as

$$\text{BIC} = -2\mathcal{L} + k \cdot \log(N), \quad (2.6)$$

where \mathcal{L} is the log-likelihood, k is the number of free parameters and N is the number of data points that get fit. Thus, the BIC guards against overfitting with additional free parameters and small values are preferred. However, the current procedure allows for very small velocities in the blue/redshifted single fits, which can be susceptible to noise. As such, a degree of guarding is necessary by requiring a minimum velocity offset, Δv , and a minimum required BIC ratio, defined as $K = \text{BIC}_{\text{fixed}} / \text{BIC}_{\text{offset}}$, to confirm an out/inflow detection that is highly unlikely to be the result of noise. We discuss the minimum required BIC ratio, K , and minimum Δv values necessary to confirm flow detections in Section 2.2.3.

Once a flow is detected, we characterize the absorption line profile with two components (a systemic component and a blue or redshifted component). In the case of an outflow detection, the profile is also fit with an additional redshifted emission component with $20 < \Delta v_{\text{offset}} < 200 \text{ km s}^{-1}$, in order to be consistent with the findings of [Prochaska et al. \(2011\)](#), who highlight the importance of redshifted re-emission from resonant transitions. All three profiles are allowed a maximum linewidth of 250 km s^{-1} . These priors are chosen so as to restrict the redshifted emission to near-systemic velocities (e.g., [Prochaska et al. 2011](#)) and prevent unrealistically large absorption and emission profiles which overfit the data and try to cancel each other out (e.g., [Veilleux et al. 2013](#)). A K -ratio then determines the preferred model out of the two, and the final fit is selected accordingly.

The allowed ranges for the parameters in Equation 2.3 are separated in two categories, “detection” and “characterization”, with the former being slightly more restrictive in linewidth and velocity offset compared to the latter. These are presented in Table 2.1. The “detection” ranges apply to single-component fits used for detecting flow signatures, as described above, and the “characterization” ranges to multiple-component fits once a detection has been established. The reasons for this are a) we wish to limit the amount of degenerate and unrealistic fits that are allowed in the determination of flow detections: e.g., a flow detection could be determined by unrealistically large linewidths ([Veilleux et al. 2013](#)) and/or velocity offsets that attempt to fit noise or baseline residuals, and b) once a robust detection is found we wish to sample a large enough parameter range to ensure both the systemic and flow components are well described. The above procedure works well for profiles of NaD excess in absorption and emission.

Table 2.1. The priors applied to our model when used for detection and characterization purposes. Note that for emission profiles the covering factor prior changes to $-1 \leq C_f \leq 0$. The free parameters are: $|C_f|$, absolute covering fraction; b_D , Doppler linewidth in km s^{-1} ; $\log N(\text{Na I})$, column density in cm^{-2} ; $|\Delta v_{\text{offset}}|$, absolute velocity offset in km s^{-1} .

Parameter	Priors (detection)	Priors (characterization)	
		Systemic	Flow
$ C_f $	0-1	0-1	0-1
b_D [km s^{-1}]	20-300	50-450	50-450
$\log N(\text{Na I})$ [cm^{-2}]	9-15.3	9-15.3	9-15.3
$ \Delta v_{\text{offset}} $ [km s^{-1}]	0-200	–	0-500

2.2.3 Model Completeness and Reliability

It is fundamental that the limitations of our fitting models and procedures be understood, and their completeness and reliability quantified. For completeness, we wish to determine the sensitivity of our code to flow components, and do this by generating synthetic spectra consisting of systemic and offset components and subsequently fitting them with our one-component detection procedure described in the previous Section. Thus, using Equation 2.3, we generate synthetic NaD absorption profiles consisting of a systemic absorption component and a single flow component. For both components, we fix the linewidth to 150 km s^{-1} , the column density to 10^{11} cm^{-2} , and the covering fraction to 1 and 0.5 (for the systemic and offset component, respectively). The reason for fixing the parameters and relative amplitudes is due to considerable degeneracies between the covering fraction and the optical depth (or column density). We acknowledge this is a limitation of our code and that smaller in/outflow signals may be overlooked when comparable to the surrounding noise. The flow component is subsequently given an offset velocity ranging from -100 to 100 km s^{-1} in 5 km s^{-1} intervals and the combined profile is then convolved to the FWHM resolution of SDSS with a Gaussian function, before adding random Gaussian noise. This procedure is repeated for three different continuum S/N ratios of 6, 10 and 50 at each velocity offset. A schematic describing the procedure is illustrated in Figure 2.5.

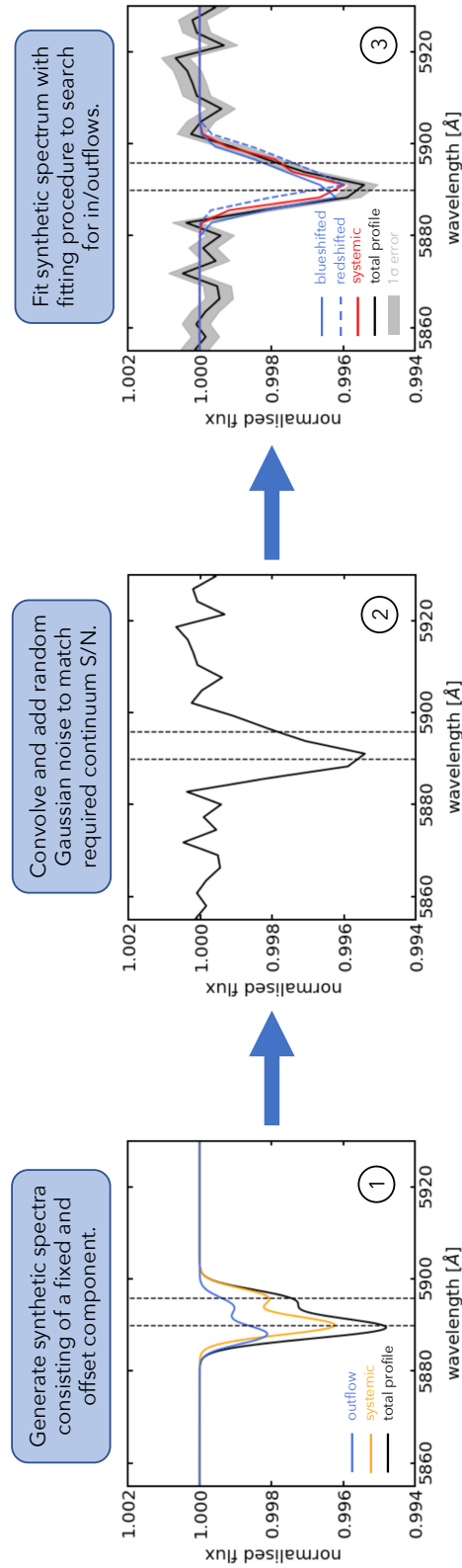


Figure 2.5. A schematic describing the procedure to generate and fit synthetic spectra, for tests of completeness and reliability. First (left), a noiseless, synthetic spectrum is generated by combining a systemic absorption component and an offset component (an outflow, in the above illustration) of a given velocity. Second (middle), the profile is convolved to the resolution of the SDSS spectra and random Gaussian noise is added to match a required continuum S/N. Third, (right) the 1σ error is estimated as the standard deviation either side of the NaD line profile and the full spectrum is put through our in/outflow detection procedure. In each plot, the vertical dashed lines represent the NaD doublet.

The spectrum is then fitted according to our detection technique described in Section 2.2.2 and the measured blue/redshifted velocity recorded. To ensure the result is not dependent on the random noise added to the spectrum, we repeat this sequence 50 times for each continuum S/N ratio, each with different random Gaussian noise. The completeness is defined as the fraction of recovered non-zero velocity offsets as a function of input Δv , for each S/N ratio. This is shown in Figure 2.6. In the inset plots of Figure 2.6 we show the *measured* Δv as a function of input Δv for each completeness plot. Based on these results, we adopt a $|\Delta v|_{\text{input}}$ threshold of 40 km s^{-1} for S/N ratios greater than 10 and 50 km s^{-1} for S/N ratios less or equal to 10, which corresponds to $>90\%$ and $\sim 85\%$ completeness, respectively. This translates to $|\Delta v|_{\text{output}}=15 \text{ km s}^{-1}$ and $|\Delta v|_{\text{output}}=20 \text{ km s}^{-1}$, respectively, using the linear $|\Delta v|$ evolution shown in the inset plots of Figure 2.6.

Arguably the most important test, however, is the reliability of our detections, since there are a number of factors that could mimic a Doppler shift: the main culprit of this would likely be ISM residuals or artifacts created from bad continuum-fitting. Since outflows are generally understood to emanate perpendicularly from galaxy disks, we can perform this test on galaxies with high inclinations, where we don't expect to see outflows and any detection would be considered a false-positive. For this, we construct a sample of high inclination ($i > 60^\circ$) galaxies across the SFR- M_* plane (containing both inactive galaxies and AGN hosts), which we assume will not display signatures of outflows due to unfavorable inclinations. We define bins of SFR- M_* and create 50 stacked bootstrap samples for each bin, in the same fashion as described in Section 3.3.1. Each stacked spectrum is then fitted with pPXF and the NaD residual put through our detection procedure and all *measured* (output) Δv s are recorded. The reliability of each bin is defined as the difference between a perfect case of no false-positives (100% reliability) and the percentual number of false-positives detected out of the 50 stacks, allowed by a set of selection criteria.

Our selection criteria should rely on a combination of thresholds given by the K ratio (defined in Section 2.2.2), a minimum measured Δv , and a quantity to guard against residuals left from bad continuum fitting. For this latter consideration, we look at the Mg *b* absorption residuals, since they are stellar in origin. For the minimum measured velocity we use $|\Delta v|_{\text{output}} > 15 \text{ km s}^{-1}$ and $|\Delta v|_{\text{output}} > 20 \text{ km s}^{-1}$, as derived from our completeness tests and $K > 1$. The reliability for our samples based on these criteria remains above 85% over the whole plane. Although our criteria do a good job of guarding against false-positive outflow detections, we note that these tests cannot be performed in the same manner for

inflowing gas since we have no *a priori* information on their angle of incidence. However, the selected thresholds should also limit the number of false-positive inflow detections, since the main culprit for these would be bad continuum fitting, which we account for.

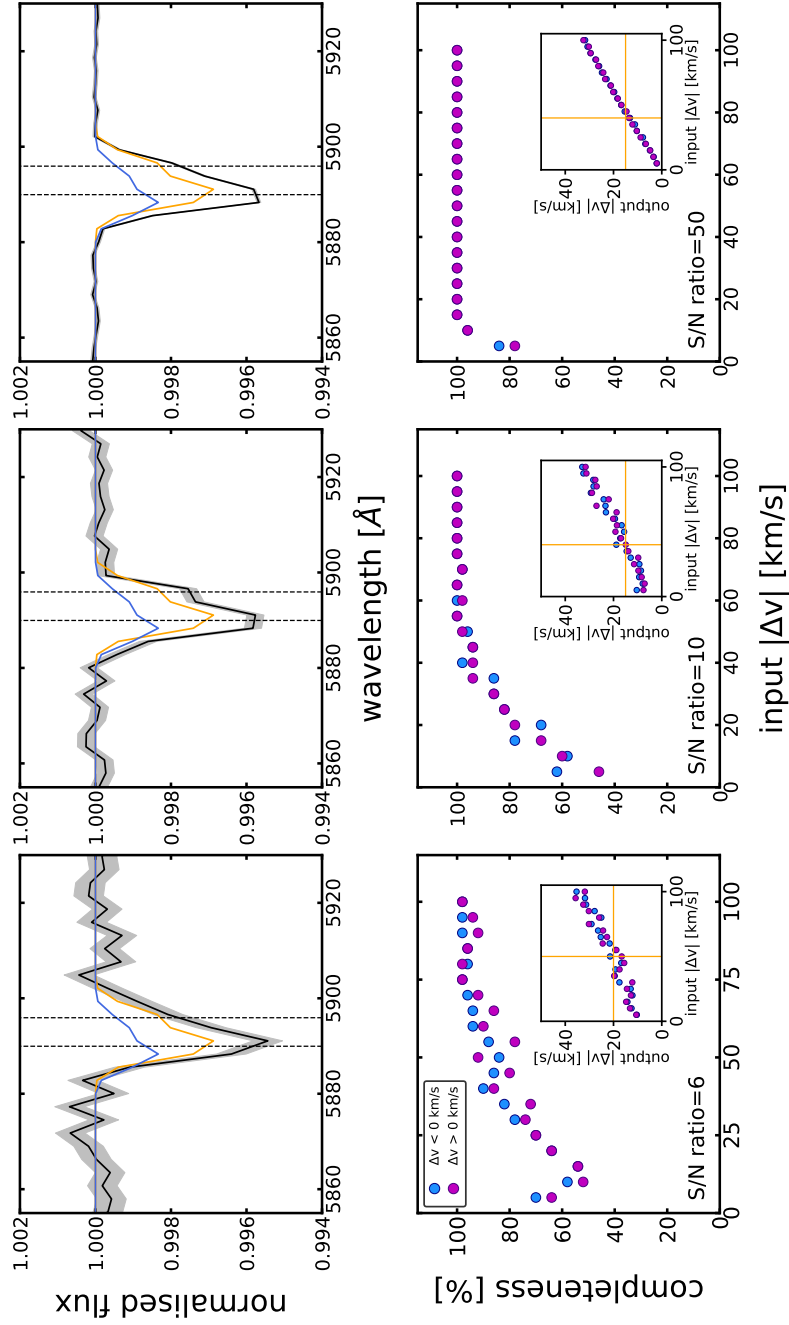


Figure 2.6. Plots of completeness versus input velocity for our NaD outflow detection procedure (bottom row). The procedure is calculated for continuum S/N ratios of 6 (left), 10 (middle) and 50 (right), for both negative offset velocities (blue circles) characteristic of outflows and positive offset velocities (magenta circles) characteristic of inflows. Each inset plot shows the linear evolution of $|\Delta v|_{\text{output}}$ vs $|\Delta v|_{\text{input}}$ in each completeness plot. The top row shows representative synthetic spectra from the corresponding completeness panels directly below, each with an outflow component of 100 km s^{-1} .

The Prevalence and Properties of Cold Gas Inflows and Outflows Around Galaxies in the Local Universe

The work described throughout this Chapter forms the second half of [Roberts-Borsani & Saintonge \(2019\)](#) “The Prevalence and Properties of Cold Gas Inflows and Outflows Around Galaxies in the Local Universe”.

3.1 Introduction

In recent years, much progress has been made in characterising the properties of outflows in galaxies out to $z \sim 2$ ([Heckman et al. 2000](#); [Martin 2005](#); [Rupke et al. 2005a](#); [Chen et al. 2010](#); [Feruglio et al. 2010](#); [Martin et al. 2012](#); [Newman et al. 2012](#); [Cicone et al. 2014](#); [Rubin et al. 2014](#)). Their presence has been found to be ubiquitous across all epochs and in galaxies where the global star formation rate surface density exceeds $\sim 0.1 \text{ M}_{\odot} \text{ yr}^{-1} \text{ kpc}^{-2}$ ([Heckman 2002](#)). Studies have added valuable constraints on the prevalence of outflows in star-forming galaxies ([Martin et al. 2012](#); [Rubin et al. 2014](#)), their properties and relations relative to host galaxy properties ([Rupke et al. 2005a](#); [Chen et al. 2010](#); [Chisholm et al.](#)

2016; Cicone et al. 2016), and their quenching potential (Feruglio et al. 2010; Cicone et al. 2014). However, a clear picture of outflows and their place in the baryon cycle remains elusive.

The use of different tracers in rest-frame UV or optical wavelengths (e.g., FeII $\lambda\lambda$ 2586,2600, MgII $\lambda\lambda$ 2796,2803, NaI,D $\lambda\lambda$ 5890,5896, [O III] λ 5007, SiII) and (in many cases) the use of a biased sample (e.g., containing objects selected *a priori* to have high SFRs, Σ_{SFRs} or stellar masses), have limited the extent to which general conclusions can be made. An alternative is to use a single tracer and stacking approach over a large and representative sample to create much higher signal-to-noise (S/N) composite spectra, allowing for flow detections over the *general* galaxy population. This is especially useful to probe regions of parameter space that single spectra cannot (e.g., very low M_* or low SFR galaxies) and derive accurate measurements of flow properties. Recently, such a stacking approach has been adopted with data from the SDSS to constrain the links between neutral and ionised outflows in the general population of galaxies in the low- z Universe (e.g., Chen et al. 2010; Cicone et al. 2016; Concas et al. 2017; Sugahara et al. 2017). These studies have allowed for strong constraints on the evolution of outflow properties as a function of key global galaxy parameters (e.g., SFR, M_* , Σ_{SFR} , z , inclination, excitation mechanism). However, still lacking are firm thresholds on the detection rates of outflows over the general population (both star-forming and AGN), the impact of a normal AGN towards enhancing an outflow, and crucial estimates of a neutral mass loading factor in order to determine whether normal outflows are able to quench a typical $z \sim 0$ star-forming galaxy.

In this study we aim to expand on this work by using the SDSS DR7 data set and stacking techniques in order to sample large ranges of global galaxy properties with which to infer detection rates, properties (e.g., outflow velocities, covering fractions, equivalent widths, and AGN contributions), and mass flow rates of inflows and outflows. We focus on the resonant NaI absorption doublet at 5889.95 Å and 5895.92 Å (also referred to as NaD), which traces cool ($T \lesssim 10^4$ K), metal-enriched gas. We present our observational data set and selection criteria in Section 3.2, stacking and fitting procedures in Section 3.3, and present our results in Section 3.4, including details on covering fractions, equivalent widths, mass inflow/outflow rates, central velocities and the mass loading factor. Section 3.5 discusses the implications of our detections and results by offering a comparison to recent simulation results, the role of SF vs AGN feedback, a dissection of the sources of inflow, and a brief discussion on the fate of the outflows. Finally, we summarize our main

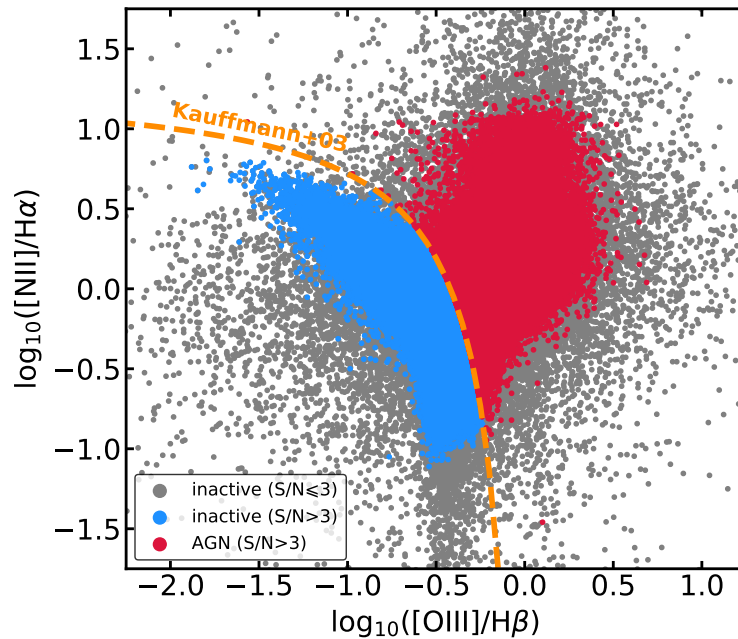


Figure 3.1. The locations of our main inactive (blue) and AGN (crimson) samples on the BPT diagram, with the [Kauffmann et al. \(2003b\)](#) demarcation (orange dashed line). For the selection of each sample, a $S/N > 3$ is required for each of the BPT lines ($H\alpha$, $H\beta$, $[O\text{ III}] \lambda 5007$ and $[N\text{ II}] \lambda 6584$), whilst any galaxy with insufficient S/N in any one of the lines (gray points) is added to the inactive sample.

conclusions in Section 3.6.

3.2 Sample Definition & Measurements

In this Chapter, we wish to define representative samples of galaxies with and without a central AGN, whilst maintaining a high level of SFR and M_* completeness that avoids biasing towards particular types of galaxies and allow us to make claims over the general populations of galaxies. Thus, using the full SDSS DR7 catalogs, we begin by requiring all objects to satisfy an SDSS type of “GALAXY”, and select all objects with a redshift of $0.025 \leq z \leq 0.1$. This redshift range allows for a robust derivation of the galaxy morphology whilst the SDSS $3''$ diameter spectroscopic fiber samples the central ~ 1.6 - 6.7 kpc of the galaxy.

To separate the AGN hosts from those without an AGN, we look at the so-called “BPT” diagram ([Baldwin et al. 1981](#); [Kauffmann et al. 2003b](#); [Kewley et al. 2006](#)), which separates star-forming galaxies from AGN by means of their $[N\text{ II}]/H\alpha$ and $[O\text{ III}]/H\beta$ ratios; the idea

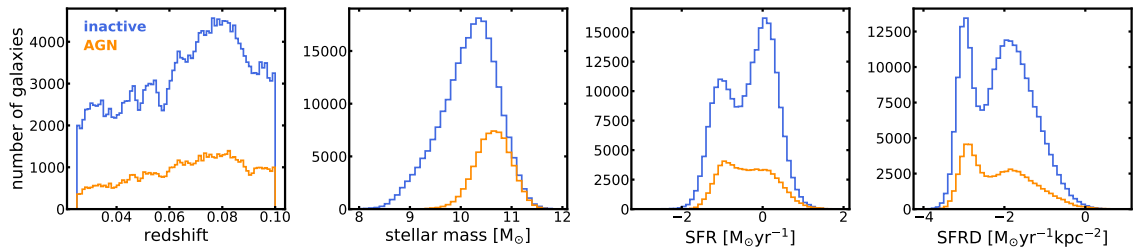


Figure 3.2. The distributions of redshift, stellar mass, SFR, and Σ_{SFR} of our main samples. The blue histograms represent our inactive galaxies sample and the orange histograms represent our AGN sample.

being that elevated ratios require ionisation from harder radiation or shock fields, from e.g., AGN. For AGN selection, we require that each of the aforementioned lines ($\text{H}\alpha$, $\text{H}\beta$, $[\text{O III}] \lambda 5007$ and $[\text{N II}] \lambda 6584$) have a S/N ratio >3 and satisfy the [Kauffmann et al. \(2003b\)](#) BPT prescription - i.e., all galaxies in the BPT diagram with sufficient line S/N that reside above the [Kauffmann et al. \(2003b\)](#) demarcation are considered AGN hosts. Galaxies residing below the [Kauffmann et al. \(2003b\)](#) demarcation are considered inactive galaxies (we stress that the term “inactive” makes no reference to the SF of the galaxy - since we apply no cuts in SFR or stellar mass - and relates to the AGN contribution to the galaxy only). Additionally, any galaxy with insufficient S/N in any one of the BPT lines is also classified as inactive. This selection yields a parent sample of 240,567 inactive galaxies and 67,753 AGN hosts unbiased in stellar mass or SFR, and we refer to this sample as the main sample. We do note, however, that due to the line S/N requirements in this selection criteria, contamination of the inactive sample by a number of e.g., (i) passive galaxies or (ii) very weak AGN may still be possible. The two samples’ distributions in redshift, stellar mass, SFR and Σ_{SFR} are shown in Figure 3.2 whilst their positions on the BPT diagram are shown in Figure 3.1.

For starburst galaxies with inclinations less than $i \sim 60^\circ$, [Heckman et al. \(2000\)](#) found that a high probability ($\sim 70\%$) existed of detecting outflows in absorption. This motivates an additional cut to separate galaxies based on their inclination. We therefore define a subsample from our main sample, called DISK, which includes all galaxies with a measurable inclination. In Section 3.4.2 we show that $i \sim 50^\circ$ is a more suitable inclination cut and therefore further divide the DISK sample into two sub-samples, HIGH- i and LOW- i , with inclinations $>50^\circ$ and $<50^\circ$, respectively. For this, one can use the “fracDeV” parameter, which determines the fraction of a galaxy’s light that emanates primarily from a bulge

Table 3.1. The number of galaxies in each sub-samples defined for this study.

Sample	Inactive	AGN
main	240,567	67,753
DISK	165,571	32,728
LOW- i	75,739	13,282
HIGH- i	86,558	19,446
BULGE	43,724	19,558

component or the rest of the disk (1 representing a galaxy dominated by bulge light and 0 representing galaxies dominated by light from the disk). It is based on the so-called De Vaucouleurs law, which is a parametrisation of the radial light profile of elliptical galaxies. Thus, we require an r -band fracDeV parameter of < 0.8 to ensure we select disk galaxies, from which an inclination angle can be calculated from the r -band axis ratio, b/a , as

$$i = \cos^{-1} \left[\left(\frac{(b/a)^2 - q^2}{1 - q^2} \right) - \frac{1}{2} \right], \quad (3.1)$$

where $q=0.13$ (Giovanelli et al. 1994) is the assumed intrinsic axial ratio. Finally, we define a BULGE sample with a fracDeV parameter equal to 1, to select objects completely dominated by a bulge. We do not include objects with fracDeV parameters between 0.8 and 1, since these might have some disk structure from which we cannot accurately determine an inclination and therefore do not complement the DISK or BULGE samples. The size of each sub-sample is listed in Table 3.1.

We use the global galaxy properties from the MPA-JHU catalog and derive Σ_{SFR} ($\Sigma_{\text{SFR}} = \text{SFR} \cdot \cos(i) / \pi r^2$), where r is the physical radius of the galaxy probed by the fiber, in kpc. As described in

3.3 Analysis

3.3.1 Binning, Stacking and Continuum-Fitting of Optical Spectra

In order to achieve high S/N, we opt for a spectral stacking analysis over planes of global galaxy properties (e.g., SFR- M_* or i - Σ_{SFR}). Bins are constructed via an adaptive approach, where the edges are defined such that the resulting bin is larger than the mean uncertainty of the relevant property, and the stacked spectrum has a continuum S/N ≥ 100 . For bins of stellar mass and SFR we require bins larger than 0.2 dex and 0.5 dex, respectively. The spectra in each bin are first sorted by parameter of interest before being cor-

rected for galactic extinction using the [Schlegel et al. \(1998\)](#) dust maps and a [O'Donnell \(1994\)](#) Milky Way extinction curve.

To create the stack, each galaxy spectrum is converted to air wavelengths and shifted to the rest-frame, before being interpolated over a common wavelength array. The spectrum is then normalized to the median flux between 5440 Å and 5550 Å, where it is uncontaminated by emission or absorption lines - this normalization ensures no preferential weighting is given to the lowest redshift galaxies in our sample. The normalized spectrum is then weighted by a mask array (with values of 0 for bad pixels identified in the SDSS spectrum array, and 1 for everything else) and added to the stack. The final stack is then simply the mean over N galaxies with a normalized spectrum, over each wavelength element. The flux uncertainties associated with the composite spectrum are derived by adding in quadrature the mean flux uncertainties calculated from the SDSS error arrays and the sampling error, which we estimate via a bootstrapping method with replacement.

Each stack is subsequently fit with a stellar continuum and emission lines from pPXF, as described in Section 2.2.1, and divided by the best fit. An example stacked spectrum and its best fit continuum model are shown in Figure 3.3. In evaluating the quality of our pPXF fits, we begin by noticing that the residuals of the continuum fit are very small (the mean residual over all spectra in Figure 3.3 is 0.04 with a standard deviation of 0.17) and thus can be considered generally very good. However, we do notice that in some cases, the code struggles to completely match the luminosities of some nebular emission lines, which could impact the estimated dust content (stellar and nebular contributions) of the galaxy if [O III] and H β lines are not well fit and potentially the NaD residual. Thus, to gauge whether this has an impact on the NaD residual, we refit the representative spectra in Figure 3.3 whilst masking the nebular emission lines and plot the resulting fit in the right panels of the Figure as dashed red lines. The fits over the NaD region - our region of interest - are virtually identical to the fits that include the nebular emission lines and suggests the NaD residual is not significantly impacted by the aforementioned emission line mismatch.

To ensure a level of robustness in our continuum fits, we look at the Mg I $\lambda\lambda\lambda$ 5167, 5173, 5184 (Mg b) triplet. Since Mg b has a similar ionizing potential as NaD and is produced in similar nuclear processes of hot stars, several studies of NaD outflows in ULIRGs (e.g., [Martin 2005](#); [Rupke et al. 2005a,b](#)) estimated the stellar contribution of NaD from Mg b . We instead look at the EW of the Mg b residuals left over from our

continuum fitting: assuming the stellar continuum is well modeled, the residual should be very small and can be used as a proxy for goodness-of-fit. Over our stacked samples, we find that the distribution of residual EWs is roughly bimodal, with one mode containing the majority of (small) residuals and the other mode a smaller population of larger residuals, and can be well described by two Gaussian functions. We interpret the larger EWs as a result of poor continuum fitting and define a range of acceptable residuals with a lower limit $EW_{\text{Mgb,low}}=0 \text{ \AA}$ and an upper limit $EW_{\text{Mgb,upp}}=0.112 \text{ \AA}$ given by the 1σ width of the main Gaussian containing the small residuals. We further assess the validity of using Mg *b* as a goodness-of-fit measure by comparing the standard deviation of the residuals around the absorption with the mean residuals across the rest of the spectrum. We find that the mean residuals of the rest of the spectrum fall within the 1σ distribution of “good” Mg *b* residuals, ensuring the our goodness-of-fit criteria described above would not bias against well-fit stacks and reinforcing the notion that Mg *b* can serve as an indicator for stellar contributions over the optical continuum.

Finally, to ensure the resulting NaD residual is not a consequence of the choice of continuum-fitting code or choice of SSP models, we perform a comparison of the residual across bins over the SFR- M_* plane, using pPXF and a custom continuum-fitting code with widely used SSP models from Bruzual & Charlot (2003) and Maraston & Strömbäck (2011). We make use of both the MILES (Vazdekis et al. 2010) and STELIB (Le Borgne et al. 2003) libraries for the custom code and compare these to results derived with pPXF. The profile type (absorption, P-Cygni, emission, or unknown) of the NaD ISM residual is recorded and presented in Figure 3.4. The distribution of the ISM profiles remains constant throughout all four cases, demonstrating that our results are independent of the choice of SSP models or codes.

3.3.2 Interpretation and Fitting of NaD Doppler Shifts

Prior to modeling the NaD residual, it is important to consider which types of Doppler shifts we consider to be signatures of outflows and inflows. In the Introduction we described how blueshifted or redshifted absorption can be interpreted as foreground gas moving along the line of sight, and therefore as unambiguous signatures of outflows and inflows. Being a resonant transition, NaD also re-emits all absorbed photons isotropically and as such, blueshifted or redshifted resonant *emission* becomes an important consideration. Due to the isotropic nature of the re-emission, on average one cannot have more

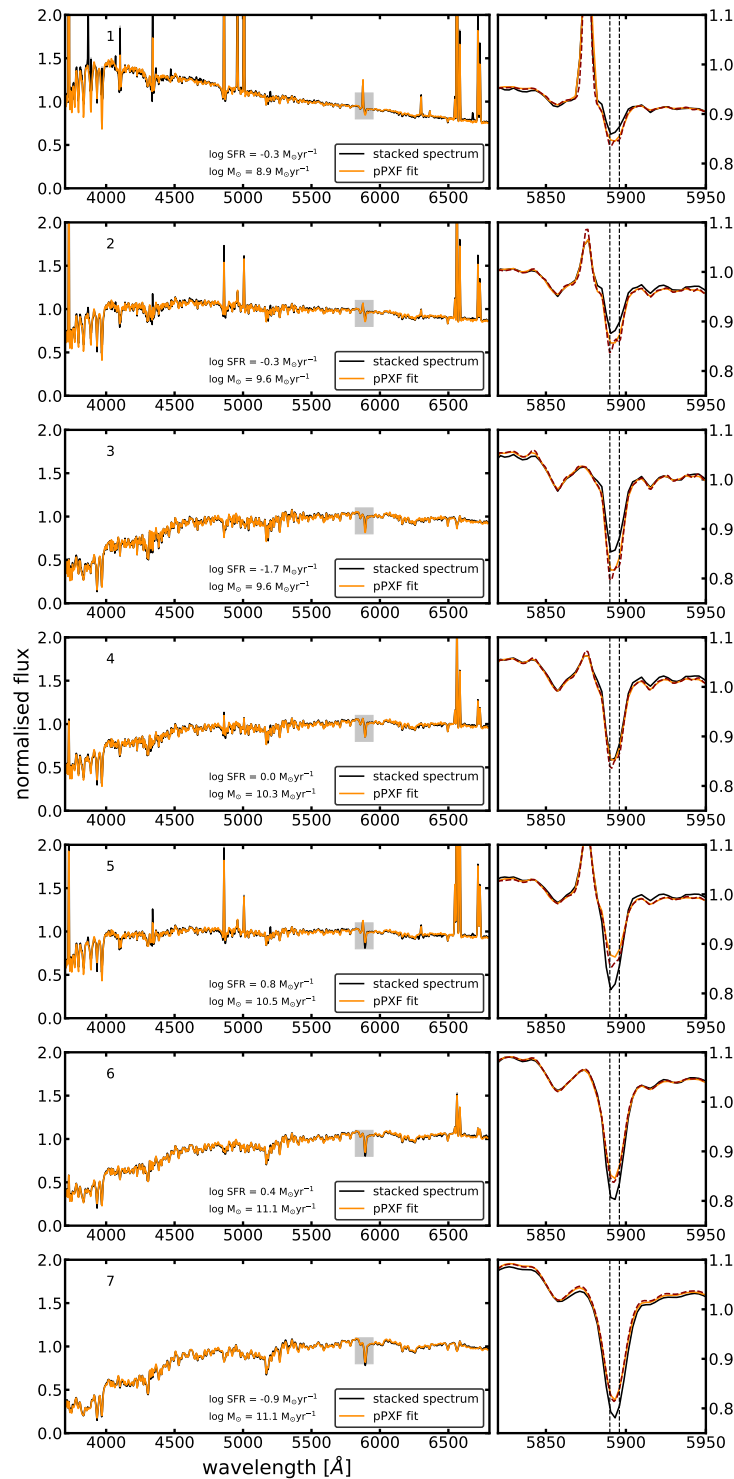


Figure 3.3. Examples of stacked spectra (black) from the inactive main sample, with their best-fit pPXF continuum (orange). For each row, the full spectrum is shown on the left, whilst the plot on the right is a zoomed-in portion of the gray-shaded region, highlighting the fit to the HeI line and the NaD absorption. The dashed red line in the right panels represent fits to the continuum with masked emission lines, in order to determine whether this would impact the NaD residual. The dashed black lines represent the central blueshifted and redshifted wavelengths of the NaD doublet at 5889 Å and 5895 Å, respectively. The spectra are taken from the stacked SFR- M_* results presented in Figure 3.5, and each number on the top left of each spectrum indicates the bin from which it is taken in Figure 3.5.

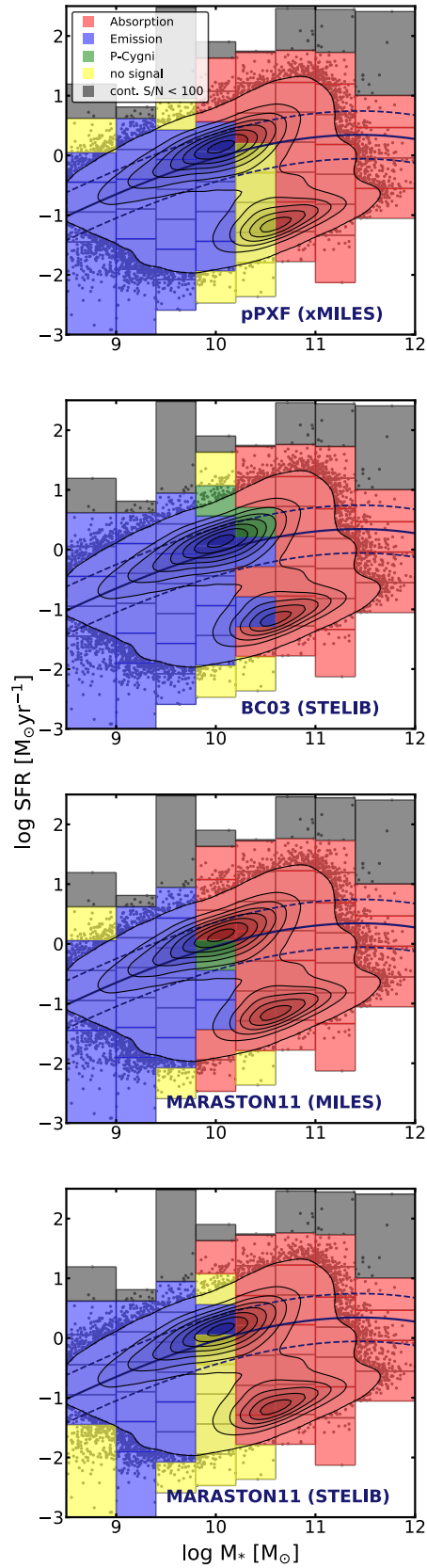


Figure 3.4. The distribution of NaD ISM profiles across the SFR- M_* plane derived by dividing high signal-to-noise stacked SDSS spectra in each bin by their best fit continuum obtained using the code and SSP models stated on the bottom right of each plot.

emission than absorption from forefront gas (the observer sees each absorption signature from the continuum but many re-emitted photons may follow a different sightline), and it is therefore reasonable to assume that absorption dominates the signatures of foreground gas. Following this logic, for a clump of gas on the backside of the galaxy, absorption signatures of the continuum are not visible but photons that are absorbed and then re-emitted by the clump can fall back along the line of sight towards the observer. If the gas is moving away from the observer, the re-emitted photons are redshifted and therefore signatures of outflowing gas, whilst if they are moving towards the observer then they are blueshifted and signatures of inflowing gas. Several studies (e.g., [Chen et al. 2010](#); [Rupke & Veilleux 2015](#)) have demonstrated a correlation between the visibility of redshifted emission and the dust content of the galaxy, suggesting the redshifted emission comes from a backside receding outflow seen through a dust-poor, face on disk. In some cases redshifted emission is also accompanied by blueshifted absorption ([Phillips 1993](#)) in the form of a P-Cygni profile. Additionally, [Prochaska et al. \(2011\)](#) showed via radiative transfer models of cold gas winds that redshifted emission was in fact a prominent and important feature to consider in outflow studies. Our interpretation of Doppler shifted NaD is consistent with this picture. However, in this Chapter we consider only profiles of net absorption to characterise the physical state of the gas.

To summarise, the sources of inflows and outflows from Doppler shifts (based on geometry) are: blueshifted absorption (outflow), redshifted absorption (inflow), blueshifted emission (inflow) and redshifted emission (outflow). All of these are highlighted in Figure 1.7. However, we note that the line (amplitude) S/N ratio of absorption and emission are significantly different; absorption signatures generally have S/N ratios larger than 10, whilst emission signatures have ratios less than 10. This is important because it means emission signatures are more sensitive to noise and errors in continuum fitting, as well as residuals from fits to the He I line immediately blueward of NaD. For these reasons, we consider only blueshifted absorption, redshifted absorption, and redshifted emission as signatures of flows, since blueshifted emission is highly sensitive to a larger number of residuals and noise, and therefore much less reliable. Thus, after dividing each stack with a best-fitting continuum model, we model the NaD profile as described in Section 2.2.2.

3.4 Stacking Results

3.4.1 NaD Profiles Across the SFR- M_* Plane

The profiles (absorption, emission, P-Cygni or unknown) of the NaD residual in each stack are identified via visual examination, and reveal a stark bimodality in type occurring between low mass ($\log M_*/M_\odot < 10$) and high mass ($\log M_*/M_\odot > 10$) galaxies, with the former showing average profiles in emission and the latter in absorption. A few profiles at $\log M_*/M_\odot \sim 10-10.5$ have near zero line amplitude or show a P-Cygni profile. This distribution is shown in Figure 3.5 and is similar to the distribution of Sodium excess found by [Concas et al. \(2017\)](#). The change in NaD profile type with stellar mass is most likely attributed to the nebular or diffuse (stellar) dust attenuation in each stack. This is shown in the middle and right panels of Figure 3.5, where we plot the median dust values calculated from the Balmer decrement (using the median MPA-JHU line fluxes going into each stack) and the stellar continuum. It is well known that NaD has a low ionizing potential (5.14 eV) and therefore requires dust shielding and high gas filling factors in the ISM for its survival. At high mass, galaxies have sufficient amounts of dust to allow NaD to survive and therefore absorb incident photons. Inclination can also play an important effect, since highly inclined galaxies are viewed along the plane of the disk, with an increased quantity of intervening dust. The exception to these rules are red sequence galaxies below the Main Sequence, which have low dust contents and filling factors yet still show profiles in absorption. We find that in such cases the EW of the NaD residual correlates with the Mg *b* residual, and is therefore attributed to template mismatch; we do not consider flow detections in these galaxies.

At low masses ($\log M_*/M_\odot \lesssim 10-10.5$) the NaD profile is seen in emission. The reasons for this are not fully understood. As discussed in [Chen et al. \(2010\)](#), this could be due to a template mismatch in the continuum fitting. Whilst we cannot completely rule out this possibility, we greatly reduce such a risk by constructing very high S/N stacked spectra and by checking the quality of our continuum fits through the Mg *b* residual. Another possibility is that the emission excess is caused by our choice of SSP models and continuum fitting code. In Section 3.3.1, however, we demonstrate that the strong $\log M_*/M_\odot$ dependence on the ISM profile is reproduced using several different codes and SSP models. Finally, due to the fact it is possible to observe NaD in emission, we must also consider the notion that these profiles may be real.

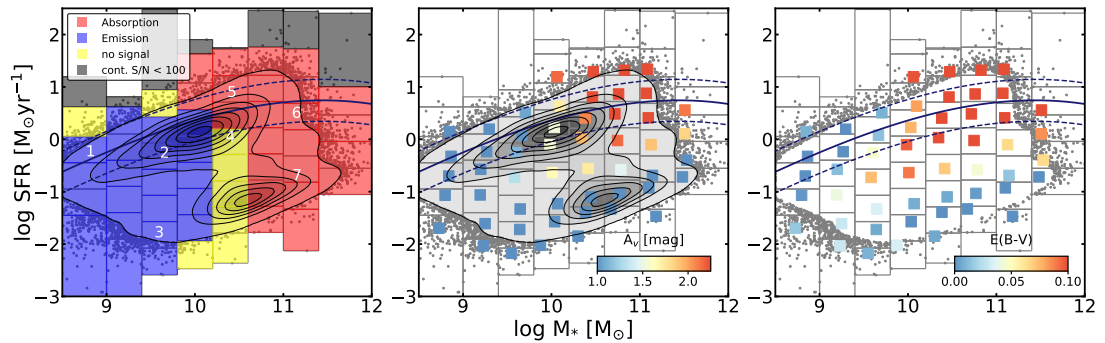


Figure 3.5. Left: The NaD residual profiles for inactive galaxies from our stacked spectra over the main sample SFR- M_* plane, as a result of the division of the best fit continuum given by pPXF. Absorption and emission profiles dominate the high- and low-mass galaxies, respectively, with a separation at $\log M_*/M_\odot \sim 10$ -10.5 characterised by low line S/N ratios and P-Cygni profiles. The solid and dashed lines mark the Main Sequence relation defined by [Saintonge et al. \(2016\)](#), with a +0.35 dex offset in log SFR to account for the different median redshifts of our and their sample. Middle: The same plots as the left but with the mean dust A_V values for each stack, calculated via the Balmer decrement assuming the median MPA-JHU line fluxes going into each stack. Right: The same as the middle panel, but for the $E(B-V)$ value associated with the stellar continuum fit performed with pPXF. The middle and right plots highlight an apparent correlation between the dust content and the NaD residual profile. The white numbers in certain bins correspond to the spectra displayed in Figure 3.3.

It is important to note, however, that while dust may play an important role in regulating the NaD profile, a lower specific dust content does not preclude the absence of NaD in absorption: as shown by [Sarzi et al. 2016](#), for a given continuum S/N the EW of the line depends solely on the amplitude-to-noise ratio of the line and its width. Thus, the net emission seen at lower stellar masses is most likely due to "filling in" ([Martin et al. 2012](#)) of the profile at systemic wavelengths, rather than an *absence* of absorption.

Over all SFR- M_* stacks for inactive and AGN galaxies we find absorption profiles in $\sim 50\%$ of all high continuum S/N bins, emission profiles in $\sim 35\%$, P-Cygni profiles in $\sim 0.3\%$, and $\sim 14\%$ of profiles are classified as 'unknown'.

3.4.2 Flow Detection Rates and Inclination Dependence

Many studies have found strong dependencies of outflow detection rates on Σ_{SFR} ([Heckman et al. 2000](#)) and inclination (e.g., [Chen et al. 2010](#); [Concas et al. 2017](#)). To test the prevalence of inflows and outflows in our sample, we therefore begin by analyzing the NaD ISM component in bins of i - Σ_{SFR} for the DISK sample. The results of the stacks are shown

in Figure 3.6 for inactive galaxies and AGN hosts. We also observe a clear dependence of outflow detections on Σ_{SFR} and inclination: outflows are found most prominently in face-on systems that are characterised by low inclinations ($i < 50^\circ$) and high Σ_{SFR} s. Heckman et al. (2000) found outflows to be ubiquitous above a threshold of $\Sigma_{\text{SFR}} > 0.1 \text{ M}_\odot \text{ yr}^{-1} \text{ kpc}^{-2}$ and with low ($i < 60^\circ$) inclinations. Our results decrease the former threshold by an order of magnitude (to $0.01 \text{ M}_\odot \text{ yr}^{-1} \text{ kpc}^{-2}$) and reduce the latter to $i < 50^\circ$ (in agreement with results found by Concas et al. 2017). We note that Heckman et al. (2000) do not assume an intrinsic thickness in their inclination calculations (i.e., they are based purely on the observed axis ratio), however we find that this is unable to explain the 10° difference between our results and theirs and thus suggests such a difference is physical. We measure the detection rate of outflows as the number of bins with detections divided by the total number of bins in a sample or set of thresholds. The detection rate over these thresholds is 74% (inactive and AGN). All detections with $\Sigma_{\text{SFR}} > 0.1 \text{ M}_\odot \text{ yr}^{-1} \text{ kpc}^{-2}$ are characterised by profiles in absorption, whilst those with $0.01 < \Sigma_{\text{SFR}} < 0.1 \text{ M}_\odot \text{ yr}^{-1} \text{ kpc}^{-2}$ are found in emission or via P-Cygni profiles, highlighting the necessity to consider all sources of Doppler shifted gas.

We also find a large number of inflow detections in regions of high inclinations ($i > 50^\circ$) and a large range of Σ_{SFR} s, with a detection rate that mildly increases with higher Σ_{SFR} s. Such a clear inclination dependence for inflowing gas has not been seen before, with several studies claiming contrasting results: e.g., Rubin et al. (2012) found that out of a sample of six disk-like galaxies, five displayed inflow signatures at high inclinations ($i > 55^\circ$), yet Martin et al. (2012) reported that out of four galaxies reporting inflows, only one had a similarly high inclination ($i \sim 61^\circ$) and the remaining three had low inclinations ($i < 55^\circ$; Kornei et al. 2012). The properties of the i - Σ_{SFR} detections are discussed throughout the rest of Section 3.4, although due to the slightly uncertain nature of the detections in emission, we focus only on detections in absorption, where the nature of the residual is better understood.

From the above results, we can now repeat our analysis over the SFR- M_* plane for our samples of disk galaxies with inclinations less or greater than $i = 50^\circ$, and bulge-dominated objects. The results for these are shown in Figure 3.7. Similarly to our findings over the i - Σ_{SFR} plane, we find a high number of outflow detections in star-forming regions ($\log \text{SFR} \gtrsim 0 \text{ M}_\odot \text{ yr}^{-1}$) of high mass ($\log M_*/M_\odot \gtrsim 10$) galaxies with low inclinations. Detections are found in absorption, emission and in P-Cygni profiles. No outflow detections are found

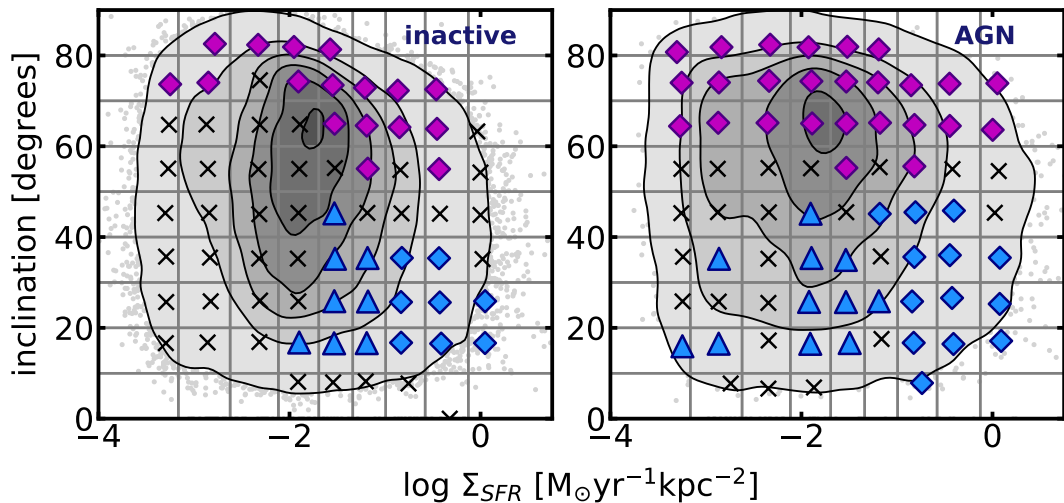


Figure 3.6. The inclination and Σ_{SFR} dependence of inflows and outflows for our DISK sample. The left and right panels show the results for the inactive and AGN objects, respectively. Gray lines mark the limits of the defined bins over our samples (gray contours), black crosses represent non-detections, magenta points represent inflow detections and blue points represent outflow detections. Additionally, detections seen with NaD absorption use diamond symbols, whilst detections in emission use triangles. Bins without any symbol have insufficient continuum S/N for analysis.

in low mass ($\log M_*/M_\odot \lesssim 10$) galaxies or galaxies with high inclinations and this applies to both inactive galaxies and AGN hosts. The detection rates and median galaxy-host properties of our detections are shown in Table 3.2, whilst the properties of the gas flows are presented in Table A.1 and Table A.2. For bins with $\log \text{SFR} > -0.5 M_\odot \text{yr}^{-1}$ - which roughly coincides with the lower limit of the star-forming Main Sequence at low mass - over our LOW- i and BULGE samples, we find an outflow detection rate of 53.5%.

We find detections of inflows in star-forming galaxies with high inclinations. No inflow detections are found in low inclination galaxies or bulge-dominated galaxies. If we apply the same SFR lower limit as above to the HIGH- i sample, we find an inflow detection rate of 43.7% for inactive galaxies and AGN.

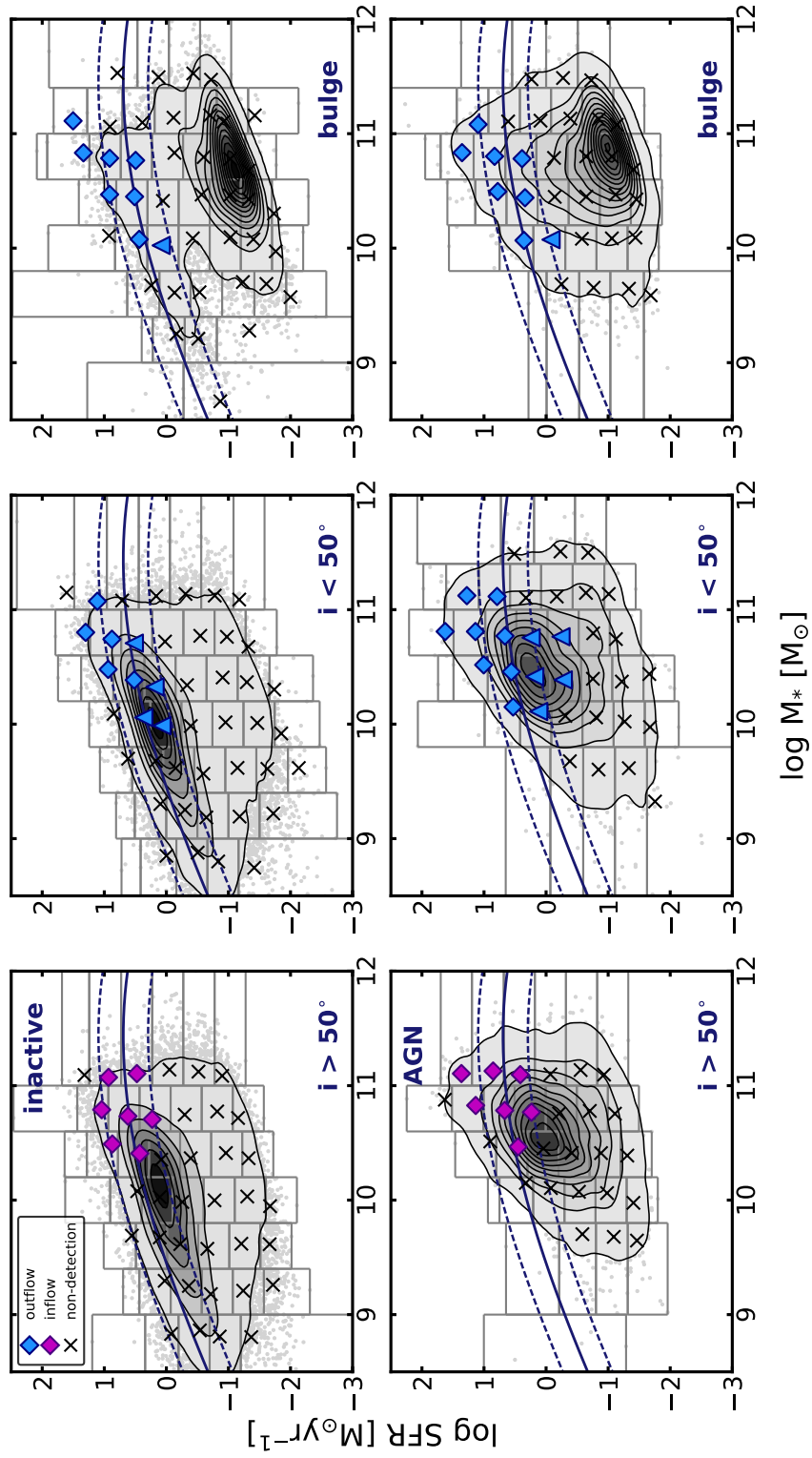


Figure 3.7. The detections of inflows and outflows across the SFR- M_* plane for disk galaxies (left and middle columns) separated by inclination, and bulge galaxies for which inclinations cannot be accurately established (right column). The top row shows our sample of inactive galaxies whilst the bottom row is for AGN hosts. The symbol and color convention follow those of Figure 3.6.

Table 3.2. The detection rate of inflows and outflows in the SFR- M_* plane across all bins with continuum S/N>100, and median properties of their galaxy hosts.

Sample	Inactive		AGN	
	Inflows	Outflows	Inflows	Outflows
HIGH- i	18%	0%	26%	0%
LOW- i	0%	20%	0%	39%
BULGE	0%	19%	0%	26%
Median Properties of host Galaxy				
SFR ($M_\odot\text{yr}^{-1}$)	4.15	3.29	4.64	3.63
Σ_{SFR} ($M_\odot\text{yr}^{-1}\text{kpc}^{-2}$)	0.09	0.21	0.12	0.11
M_* ($\log M_\odot$)	10.73	10.47	10.82	10.75
nebular A_V (mag)	2.94	2.20	3.22	2.35
D_n4000	1.42	1.30	1.45	1.35
Concentration Index	2.45	2.53	2.54	2.43

3.4.3 Covering Fractions

The covering fraction of the flow, C_f , is a measure of the local clumpiness of the gas along the line of sight. In Table A.1 and Table A.2 we report the covering fractions determined by our analysis for inactive galaxies and AGN hosts, respectively. For each of our samples, the covering fractions span the full range of allowed values and there appears to be no difference between the covering fractions of outflows and inflows. We note, however, that in many cases we also find flows characterized by very low covering fractions, $|C_f| \lesssim 0.25$. Unlike for point sources at high redshift where the gas completely covers the background source, for low redshift sources where the background source subtends a large angle on the sky, a covering fraction less than unity is not unexpected. However, such low covering fractions are likely not a result of geometry alone. Very low fractions have also been observed by [Chen et al. \(2010\)](#) who stack over similar samples of galaxies. One explanation to describe such low values is that we are observing small amounts of neutral NaD gas with low dust shielding in very dense clouds within the outflow, where ionizing radiation and shocks no longer dominate.

3.4.4 Equivalent-Widths

The EW of a line is a measure of its strength, and therefore can provide information about the strength of an outflow or inflow. Figure 3.8 plots the distributions of EWs measured from fits to our NaD absorption profiles over the i - Σ_{SFR} and SFR- M_* planes. The measurements are also presented in Table A.1 and Table A.2. Figure 3.8a plots the distri-

bution of the *total* line EW. We report a narrow range of outflow EWs ($0 < \text{EW}_{\text{NaD}} < 1.2$) for the combined inactive and AGN samples, with a median 0.24 \AA and a standard deviation 0.26 \AA . These values are similar to those found by [Chen et al. \(2010\)](#) but have a median which is an order of magnitude smaller than that found by [Rupke et al. \(2005b\)](#), who report a median of 3.3 \AA and a maximum of value 9.1 \AA for NaD in (U)LIRGs. The higher values found by [Rupke et al. \(2005b\)](#) are most likely attributed to the increased column densities found in their samples, whilst [Chen et al. \(2010\)](#) study galaxies more closely matched to this sample. We note that our AGN sample have a slightly higher median value of 0.29 \AA compared to 0.25 \AA for inactive galaxies, and a higher maximum value of 1.2 \AA (AGN) compared to 0.93 \AA (inactive). A Kolmogorov-Smirnov (K-S) test between the two distributions, however, reveals a low coefficient of 0.16 suggesting the two distributions are still very similar.

The difference in reported values between [Rupke et al. \(2005b\)](#) and the distributions in Figure 3.8a clearly illustrate the difference in outflow strength between normal galaxies and more extreme objects. By preselecting systems with large NaD residuals, it is likely that a large number of weaker outflow signatures would be overlooked. In Figure 3.8b we show an alternative measurement of EW, where we plot the EW of the flux blueward of the Na I 5889 \AA line vs the EW of the flux redward of the Na I 5895 \AA line. A clear separation of outflow detections, inflow detections, and non-detections becomes evident, which is not apparent from measurements of the *total* EW of the NaD doublet. A histogram of the $\text{EW}_{\text{blue}}/\text{EW}_{\text{red}}$ ratio is shown in Figure 3.8c and three distinct distributions appear. By applying a cut of $\text{EW}_{\text{blue}}/\text{EW}_{\text{red}} > 1.35$ for outflows and a cut of $\text{EW}_{\text{blue}}/\text{EW}_{\text{red}} < 0.75$ for inflows, one selects 100% of outflow detections and 86% of inflow detections, with only $\sim 10\%$ contamination from the non-detections (subject to uncertainties in the EW measurements). Using “edge-EWs” instead of the total EW of NaD provides a more complete and unbiased way to select potential outflow candidates.

3.4.5 Flow Velocities

The central velocity of a flow is a measure of the velocity at which the bulk of the material is traveling. In Figure 3.9 we plot the central velocity measurements of inflow and outflow detections in absorption as a function of global galaxy properties, and compare them to results in the literature which study samples of outflows in galaxies at $z < 1$. The stacks shown in these plots are created from a sample of high mass ($\log M_*/M_\odot > 10$) and high

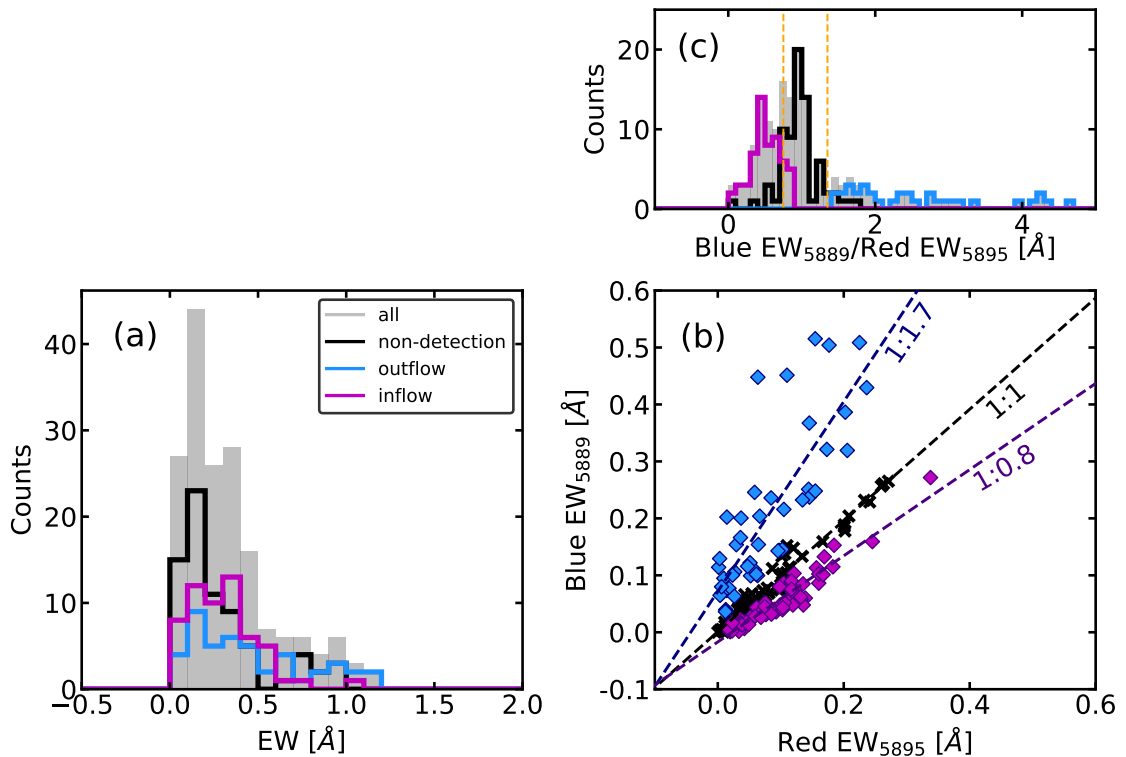


Figure 3.8. (a): The distribution of total EWs for inactive galaxies and AGN. The gray bars represent the full distribution, whilst the blue bars represent outflow detections and inflows are marked by the magenta bars. Black bars are non-detections. (b): A comparison of the EWs measured blueward and redward of the 5889 Å and 5895 Å Na I lines, where outflows (blue) and inflows (magenta) are expected to be seen, respectively. The dotted black line is a straight line fit to the systemic components (black x's) whilst the dashed blue and magenta lines are best fit linear functions to outflow and inflow detections. (c) histogram distributions of the $EW_{\text{blue}}/EW_{\text{red}}$ ratio for inflows, outflows and non-detections. The orange vertical lines represent our suggested cuts to isolate each distribution.

Σ_{SFR} ($\Sigma_{\text{SFRS}} > 0.1 \text{ M}_{\odot}\text{yr}^{-1}\text{kpc}^{-2}$) DISK galaxies, since in Section 3.4.2 we have shown these thresholds to be important in finding outflows. The left panel of Figure 3.9 shows stacks binned by $i\text{-log SFR}$, whilst the points in the right panel are binned by $i\text{-log } M_{*}$.

We report absolute outflow velocities in the range $69\text{-}370 \text{ km s}^{-1}$ with a median of 160 km s^{-1} , consistent with results for samples of normal star-forming galaxies (e.g., [Chen et al. 2010](#); [Martin et al. 2012](#); [Rubin et al. 2012, 2014](#)). Our reported values are not characteristic of particularly high outflow velocities compared to some cases of extreme starburst or AGN hosts, which are able to launch $\sim 1000\text{-}2000 \text{ km s}^{-1}$ outflows with different gas phases (e.g., [Tremonti et al. 2007](#); [Chung et al. 2011](#); [Cicone et al. 2014](#); [Carniani et al. 2015](#)). We find no significant difference between outflow velocities from the inactive

sample compared to the AGN hosts: we report medians of 155 km s^{-1} (inactive) and 167 km s^{-1} (AGN), with maximum central velocities of 234 km s^{-1} (inactive) and 370 km s^{-1} (AGN). This suggests that whilst the presence of an optically-selected AGN might slightly enhance an outflow’s velocity, it does not do so by a significant amount.

In the left panel, we see there appears to be little to no correlation of outflow velocity with total SFR (unlike in eg., [Heckman et al. 2015](#)) within our sample, although the scatter appears to increase with SFR. We also note that a correlation may not appear present due to the small range of SFRs probed by our stacks, which also appears to be the case in [Chen et al. \(2010\)](#) for a near identical sample and SFR range. In the right panel we also find little to no correlation between outflow velocity and increasing stellar mass. Inflow velocities are also consistent with the results from the studies mentioned above, spanning a range $139\text{-}193 \text{ km s}^{-1}$ with a median central velocity of 151 km s^{-1} . Only a $\sim 6 \text{ km s}^{-1}$ difference exists between the median inactive and AGN inflow velocities. Furthermore, we find no correlations of velocity with SFR or stellar mass.

It is important to note that none of these velocities have been corrected for inclination, and as such they may be (and are likely to be) underestimated (we observe a difference of $\sim 20\text{-}30 \text{ km s}^{-1}$ between the inclination-corrected and uncorrected median outflow velocities in Figure 3.9). Since the velocity offset is used in several calculations (e.g., the mass outflow rates in Section 3.4.6), this underestimation is propagated throughout the analysis and therefore such outflow quantities serve as lower limits. We present the inclination-corrected velocities in Tables A.1 and A.2, however do not use these in our plots for the sole purpose of facilitating comparison with other results in the literature, who also use uncorrected velocities.

3.4.6 Mass Outflow Rates and Loading Factors

Two of the most important quantities one can derive in studies of galactic-scale flows are the mass outflow rate (\dot{M}_{out}) and mass-loading factor (η), which describes the rate of mass ejected from the galaxy per unit of SFR. These measurements help quantify the rate at which galaxies are expelling mass and the extent to which they are able to quench the star formation. Before deriving these rates, however, there are several important assumptions to consider. For a spherically symmetric, mass conserving wind that travels at velocity v , the average mass flow rate across a radius r can be expressed as the following:

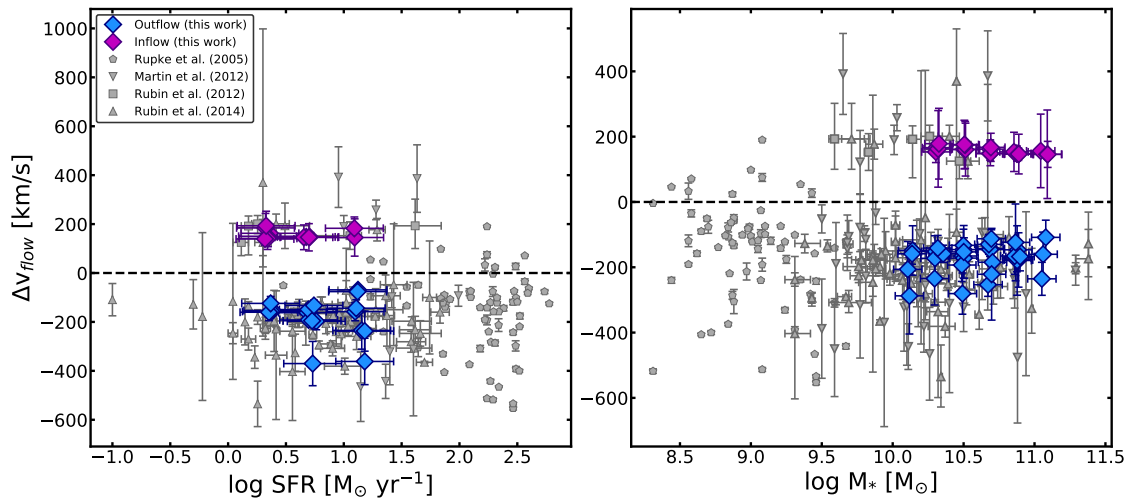


Figure 3.9. Left: The central inflow and outflow velocities (uncorrected for inclination) as a function of SFR. Right: The same as the left panel but as a function of stellar mass. Results from [Rupke et al. \(2005a,b\)](#), [Martin et al. \(2012\)](#), [Rubin et al. \(2012\)](#) and [Rubin et al. \(2014\)](#) are overplotted for comparison, where available. The symbol and color convention follow those of Figure 3.6.

$$\dot{M}_{\text{out}} = \Omega \mu m_{\text{H}} N(\text{H}) v r, \quad (3.2)$$

where Ω is the solid angle subtended by the wind at its origin (i.e., the global covering factor of the wind), m_{H} is the mean atomic weight (with a $\mu=1.4$ correction for relative He abundance), $N(\text{H})$ is the column density of hydrogen along the line of sight, v is the central velocity of the wind, and r is the distance from the galaxy. The equation computes the outflowing gas of a given column density and velocity over the outflow area subtended by a given solid angle. The full derivation of the equation is described in detail in [Rupke et al. \(2005b\)](#) and as such we refer the reader to that paper for details. Additionally, we also make the same assumptions as the aforementioned paper: in short, we assume a solid angle less than 4π , a radius of 5 kpc, and that the column density of hydrogen can be expressed as

$$N(\text{H}) = \frac{N(\text{Na I})}{\chi(\text{Na I}) d(\text{Na I}) Z(\text{Na I})}, \quad (3.3)$$

where $N(\text{Na I})$ is the Sodium column density, $\chi(\text{Na I})=N(\text{Na I})/N(\text{Na})$ is the assumed ionization fraction, $d(\text{Na I})$ is the depletion onto dust, and $Z(\text{Na I})$ is the Na abundance. We assume a 90% ionization fraction ($\chi(\text{Na I})=0.1$), a Galactic value ([Savage & Sembach](#)

1996) for the depletion onto dust ($\log d(\text{Na I}) = -0.95$), and solar metallicity ($Z(\text{Na I}) = \log[N(\text{Na})/N(\text{H})]_{\odot} = -5.69$). We report a wide distribution of total outflow column densities for our i - Σ_{SFR} and SFR- M_* stacks of $17.85 < \log N(\text{H})/\text{cm}^{-2} < 21.98$, with a median of 19.77 cm^{-2} . We observe little difference between the medians of the inactive objects (19.46 cm^{-2}) and AGN hosts (19.89 cm^{-2}). These values are similar (albeit slightly lower) to those observed for (U)LIRGs at low- z (Rupke et al. 2005b; Cazzoli et al. 2016). The distribution of column densities for the inflows is somewhat narrower and shifted towards lower values, with a range $18.94 < \log N(\text{H})/\text{cm}^{-2} < 20.28$ and median 19.60 cm^{-2} .

From the above assumptions, Equation 3.2 can be expressed as

$$\dot{M}_{\text{out}} = 115 \sum \left(\frac{C_{\Omega}}{0.4} C_f \right) \left(\frac{r}{10 \text{ kpc}} \right) \times \left(\frac{N(\text{H})}{10^{21} \text{ cm}^{-2}} \right) \left(\frac{|\Delta v|}{200 \text{ km s}^{-1}} \right) M_{\odot} \text{ yr}^{-1}, \quad (3.4)$$

where the global covering fraction, Ω is split into two components: the global covering fraction of the outflow on the continuum dictated by the opening angle of the outflow (C_{Ω}) which we assume is given by the detection rates of outflows (see Rupke et al. 2005b), and the local covering fraction (C_f) which describes the clumpiness of the gas - more diffuse gas ensures more of the continuum is covered, whilst more clumpy gas covers less of the continuum and thus allows for more continuum photons to pass through it.

Figure 3.10 shows the derived mass outflow rates versus SFR for the i -log SFR stacks defined in Section 3.4.5, and we compare these to the (U)LIRGs of Rupke et al. (2005b) and Cazzoli et al. (2016), as well as the H II galaxies of Fluetsch et al. (2018), who all use the same tracer and similar assumptions. All uncertainties associated with our calculated values incorporate those from the fit free parameters. We note that the main drivers of the mass outflow uncertainties are the covering factor and the assumed radius of the wind. We report mass outflows rates of $0.17 \lesssim \log \dot{M}_{\text{out}}/M_{\odot} \text{ yr}^{-1} \lesssim 1.24$ for a SFR range of $-0.16 \lesssim \log \text{SFR}/M_{\odot} \text{ yr}^{-1} \lesssim 1.23$. We find that mass loss rates close to the associated global SFR and that a positive (linear) correlation between the two quantities exists with a near constant mass-loading factor $\eta \approx 1$, suggesting the mass outflow rate of a galaxy is closely traced by its SFR. The relation has a measured Pearson coefficient of $r_p = 0.83$ using our data only and an increased coefficient of $r_p = 1$ when also using the results from Rupke et al.

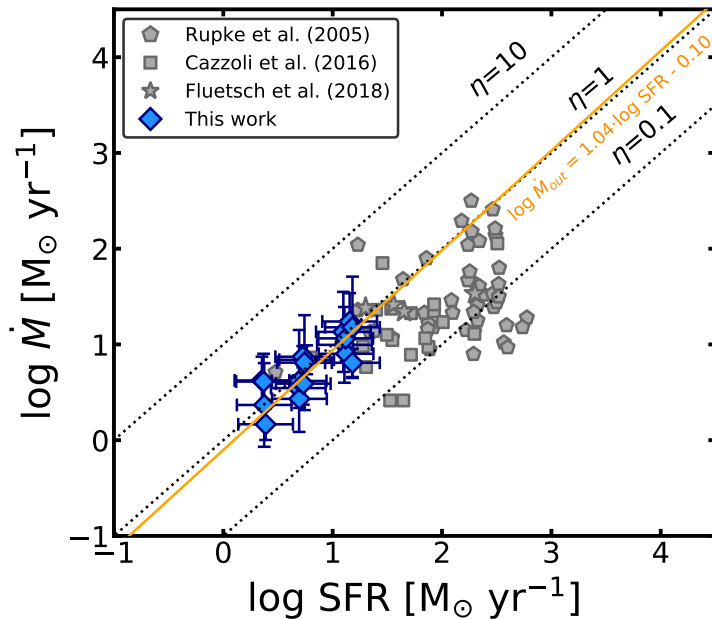


Figure 3.10. The mass outflow rates for the i -log SFR stacks of inactive and AGN galaxies defined in Section 3.4.5. A first-order polynomial fit to our data is shown in orange. Overplotted are the results from [Rupke et al. \(2005b\)](#) (gray pentagons), [Cazzoli et al. \(2016\)](#) (gray squares) and [Fluetsch et al. \(2018\)](#) (gray stars).

(2005b), [Cazzoli et al. \(2016\)](#) and [Fluetsch et al. \(2018\)](#). A first-order polynomial fit to our data returns

$$\log \dot{M}_{\text{out}} = (1.04 \pm 0.18) \cdot \log \text{SFR} - (0.10 \pm 0.15). \quad (3.5)$$

The near constancy of η is perhaps surprising, however such a value is consistent with other observed loading factors observed in studies of similar objects (e.g., [Veilleux et al. 2005](#); [Martin et al. 2012](#); [Rubin et al. 2014](#); [Sugahara et al. 2017](#)), suggestive of low- z starbursts and Milky Way-type galaxies being unable to drive particularly strong winds (defined by high mass-loading factors of $\eta \gg 1$). We also note a mean difference of $0.07 \text{ M} \cdot \text{yr}^{-1}$ between inclination-corrected outflow rates and the uncorrected rates presented above.

3.4.7 Comparison to Other Gas Phases

In the previous section we derived mass outflow rates using the NaD tracer of neutral gas. However, this is only one gas phase and does not account for the molecular and ionized gas phases, which likely contribute non-negligible amounts of ejected gas. A direct and

comprehensive comparison is challenging due to the lack of uniform datasets, however some studies have made notable attempts. Recently, [Fluetsch et al. \(2018\)](#) looked at molecular outflows with ALMA CO data and cross-matched their sample with optical data (where available). They found that for star-forming galaxies the ratio of molecular mass outflow rates (\dot{M}_{H_2}) to ionized (\dot{M}_{ion}) mass outflow rates was close to unity, whilst AGN hosts displayed much stronger molecular mass outflow rates (correlating with AGN luminosity). Of particular interest to this study is the comparison of \dot{M}_{H_2} to the atomic mass outflow rates (\dot{M}_{HI}): for their sample of AGN hosts, they find \dot{M}_{H_2} is generally ~ 1 order of magnitude higher than \dot{M}_{HI} using NaD. However, for their star-forming sample large scatter dominates and prevents a clear conclusion. To work around this, an alternative tracer (C^+) is used and the ratio $\dot{M}_{H_2}/\dot{M}_{HI}$ is found to be roughly equal for AGN. They tentatively conclude that for starburst-driven galaxies, the ionized, atomic and molecular phases contribute in roughly equal quantities to the total mass outflow rate. As such, it is likely our mass outflow rates are only lower limits to the total outflow rate, and a multiwavelength estimation of such rates would lead to more complete and slightly higher values, given the added mass from the other gas phases.

3.4.8 Upper Limits on Mass Inflow Rates

In Figure 3.6 and Figure 3.7 we find detections of inflowing gas among disk galaxies. The infalling gas could come from cosmological filaments, from galactic fountains, minor mergers, or from gas cooling from the CGM. Due to the uncertain source of the inflows, the assumptions made for Equation 3.4 may not hold. In particular, assumptions about the metal content, ionization fraction and depletion onto dust become highly uncertain when converting to a column density of hydrogen. Nonetheless, we can assume these as upper limits to convert to mass inflow rates, since it is likely metallicity and abundances would decrease outside of the galaxy disk. With this in mind, we report upper limit inflow rates of $0.8\text{-}3.8 M_{\odot}\text{yr}^{-1}$. No significant trend is found with the SFRs or stellar mass of the galaxies.

In Figure 3.7 we see that inflows have a strong inclination dependence, and are only seen at high ($i > 50^\circ$) inclinations. This suggests that we are seeing the gas accreting along the plane of the disk. [Ho et al. \(2017\)](#) used Mg II absorption and quasar sightlines to probe the CGM of a sample of 15 highly-inclined, local star-forming galaxies with known rotation curves. They showed that much of the Doppler shifted Mg II gas was consistent

with the rotational motion of the host galaxies and the implication for this was radial infall of gas into the disk plane. It is possible that our results suggest a similar scenario, where inflowing gas (from a variety of sources) falls radially before becoming dominated by the circular motions of the galaxy disk.

3.5 Discussion

3.5.1 The Prevalence of Outflows and Inflows

Several studies have claimed a ubiquity of outflows over the star-forming Main Sequence (e.g., [Weiner et al. 2009](#); [Rubin et al. 2014](#)). Our results are partially consistent with this picture in that outflows appear prevalent in star-forming systems with $\text{SFR} > 1 \text{ M}_{\odot} \text{ yr}^{-1}$ or $\Sigma_{\text{SFR}} \geq 0.01 \text{ M}_{\odot} \text{ yr}^{-1} \text{ kpc}^{-2}$ and stellar masses $\log M_{*}/M_{\odot} > 10$. We don't, however, find outflows in low mass galaxies. Reasons for this could be due to lower Σ_{SFR} s, or limitations of NaD as a tracer (e.g., in the absence of dust). We therefore cannot claim ubiquity over the whole of the Main Sequence. Additionally, we find that outflows are also found in bulge-dominated objects with sufficiently high SFRs, and therefore are not dependent on morphology. We find this to be true for both AGN and inactive galaxies.

3.5.2 Comparison to Simulations

In this section, we compare the flow properties derived in this study to results from simulations, namely those of [Muratov et al. \(2015\)](#) and [Anglés-Alcázar et al. \(2017\)](#) using the Feedback in Realistic Environments (FIRE) simulations at $z < 0.5$, as well as those from [Oppenheimer et al. \(2010\)](#).

1. *The prevalence of inflows and outflows in star-forming galaxies.*

The prevalence of outflows in our samples of star-forming galaxies appears only partially consistent with results from simulations. Both [Muratov et al. \(2015\)](#) and [Oppenheimer et al. \(2010\)](#) find that high-mass galaxies have stable discs and a more continuous, quiescent mode of star formation at $z < 1$ that can no longer drive very *strong* outflows into the halo. Dwarf galaxies instead maintain a bursty state of star formation which allows them to produce outflows ([Muratov et al. 2015](#)). Our results both agree and contrast with these simulations in that we find low-velocity outflows to be common among star-forming galaxies with high stellar mass but no

detections in low-mass ($\log M_*/M_\odot < 10$) galaxies, whose $\Sigma_{\text{SF}}^{\text{FRS}}$ are significantly lower. If outflows are indeed present at low-mass, it is possible that we are unable to detect them due to a) the outflows being too weak for our code to detect, or b) a resolution issue where the velocities are blended by the SDSS spectral resolution, or c) the unreliability of NaD as a tracer in low A_V environments.

The above simulations also predict non-negligible amounts of accreting gas onto star-forming galaxies. Our study agrees with this, as we find inflow detections in star-forming, high mass disk galaxies. The source of the inflowing gas is impossible to ascertain from our data, however it is likely a combination of material coming from pristine cold gas, gas from nearby companions, minor mergers, and/or recycled gas (“galactic fountains”).

2. Outflow central velocities and mass loading factors.

By using the stellar-halo mass (M_*-M_h) relation described in Behroozi et al. (2013) and Equation 1 in Mo & White (2002), we are able to derive halo circular velocities, v_c , and compare the central velocities of our outflow detections to those reported in simulations. We find our central velocities are within the broad range of median velocities ($20 \lesssim \Delta v \lesssim 4000 \text{ km s}^{-1}$) reported by Muratov et al. (2015) and lie right on the power law relation calibrated for their medium- z ($0.5 < z < 2.0$) and high- z ($2.0 < z < 4.0$) samples. However, our velocities appear more than an order of magnitude larger than the upper limits of their L_* progenitors at $z < 0.5$, which have velocities less than 100 km s^{-1} .

We also compare our mass loading factors to those found in simulations and find them to be ~ 1 order of magnitude larger than the upper limits for the low- z L_* progenitors of Muratov et al. (2015). Muratov et al. (2015) make an approximate comparison between their mass loading factors and those derived in the Illustris project (Vogelsberger et al. 2013), and find the Illustris results to be systematically higher than theirs ($\eta \approx 7$ for a Milky Way-mass galaxy at $z=0$, compared to $\eta \ll 1$). Although we caution a direct comparison due to the differences by which the mass loading factors are measured in each study, such high mass loading factors are in contrast with our results and suggest some prescriptions may be adopting abnormally strong outflows than what are typically seen in the local Universe.

3.5.3 Star Formation vs AGN

Several recent studies have discussed the implications of AGN on the baryon cycle and their influence in the launching of outflows. In these studies, the NaD tracer was used to detect outflows in samples of AGN and star-forming galaxies and determine which energy source was the primary driver of the outflows. For example, Sarzi et al. (2016) used SDSS spectra of 456 local star-forming galaxies from the mJIVE-20 survey to determine whether these hosted both an optical outflow and showed radio emission as part of the Very Large Array’s (VLA) FIRST survey. Not a single object showed an outflow detection together with radio emission and therefore the authors concluded outflows were regulated by star formation, not AGN feedback. Nedelchev et al. (2017) also compared the effects of AGN feedback in a sample of $\sim 9,900$ SDSS Seyfert 2 galaxies and a control sample of $\sim 44,000$ inactive galaxies. Only 0.5% of their Seyfert 2 sample displayed potential outflows compared to 0.8% for the control sample, suggesting AGN activity did not enhance outflow activity. Figure 3.7 from our study extends these results to the regime of normal star-forming galaxies and modest AGN. As reported in Section 3.4.5 and Section 3.4.6, there is a mild increase in outflow velocity and mass outflow rates with the presence of an AGN, although the differences between the median inactive and AGN values are only $\sim 12 \text{ km s}^{-1}$ and $\sim 2.3 \text{ M}_{\odot} \text{ yr}^{-1}$. Such small values suggest these AGN do not *significantly* enhance outflow activity or strength. We can therefore conclude that the presence of an optically-selected AGN does not significantly enhance outflows in *normal* galaxies of the local Universe, and that such winds are unlikely to be able to quench a galaxy via “ejective” feedback, where gas is removed from the galaxy via the outflow.

This may appear somewhat at odds with recent observations of strong AGN feedback in both the local and high- z Universe (e.g., Feruglio et al. 2010; Alatalo et al. 2011; Maiolino et al. 2012; Ciccone et al. 2014), however there are several plausible reasons for this. The first is that we may not be observing the same types of AGN: our BPT cut and binning procedure ensure we are selecting and mixing weak AGN which could be drowning out much of the signal produced by rarer and much stronger AGN (e.g., Seyferts). This is highlighted in Figure 3.11, where we compare the energy output from the AGN versus the energy output of supernovae.

The AGN luminosity is calculated using Equation 3 of Netzer (2009), which makes use of the [O III] and [O I] luminosities, whilst the energy output of star formation (i.e.,

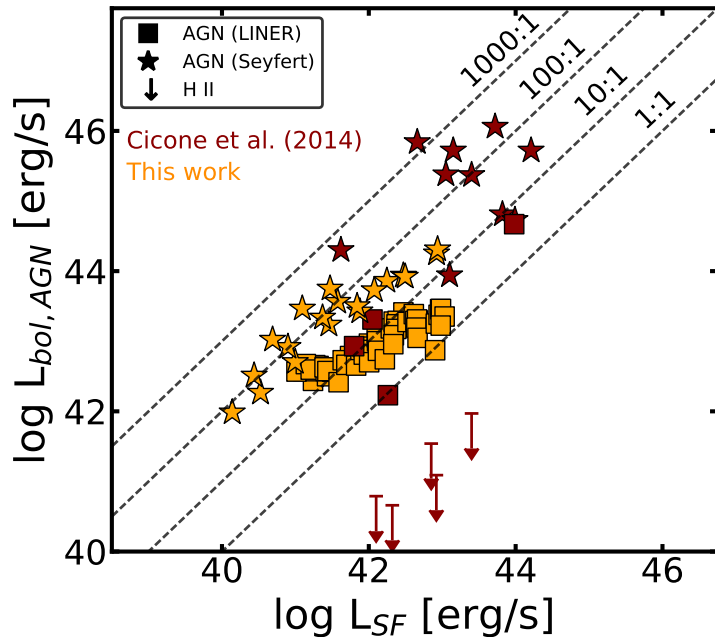


Figure 3.11. A comparison of the energy output from the AGN (L_{AGN}) and from star formation (ie., supernovae, L_{SF}) for our AGN stacked sample (orange) and objects from [Cicone et al. \(2014\)](#) (red). Additionally, we extract and stack the Seyfert objects in our AGN sample and plot the data points for comparison. The dashed lines denote constant lines of $L_{\text{bol,AGN}}/L_{\text{SF}}=1000, 100, 10$ and 1 .

supernovae) is derived using the relation presented by [Veilleux et al. \(2005\)](#):

$$L_{\text{SF}} = 7 \times 10^{41} \text{SFR}(M_{\odot} \text{yr}^{-1}) \text{ [erg s}^{-1}\text{]}. \quad (3.6)$$

For comparison, we plot the quantities (where available) for the sample of [Cicone et al. \(2014\)](#) and also stacked spectra of the Seyferts within our AGN sample (selected with an additional BPT cut of $\log [\text{O III}]/\text{H}\beta > 0.5$).

As evident from the plot, the AGN feedback found by the aforementioned studies are observed in extreme objects which host very strong AGN, not typical of the samples of galaxies that we probe. We find a median luminosity (uncorrected for dust) $\log L_{\text{AGN, bol}}=42.8$ erg/s over the DISK AGN sample. For comparison, the median $\log L_{\text{AGN}}$ of [Cicone et al. \(2014\)](#)'s extended sample is $\log L_{\text{AGN}}=44.76$ erg/s, about two orders of magnitude higher. This highlights the comparative weakness of optically-selected AGN in normal galaxies. Additionally, it is important to note that SF can significantly contribute to the $[\text{O III}]$ flux and therefore deducing an accurate L_{AGN} value from this method is challenging. These values are, in essence, upper limits of the true AGN energy contribution.

Nevertheless, a comparison of AGN in normal star-forming objects - not just in extreme objects - remains useful towards constraining the extent to which an active nucleus may impact the prevalence and properties of galactic winds.

A second, less likely, reason is to do with the dynamical timescales of AGN activity and outflows: it is possible that we are also observing a) objects with AGN that are in the process of turning off due to reduced rates of gas accretion and/or b) outflows which are relics of the strong feedback found in more extreme objects or at high- z . All of these scenarios are consistent with our observations and findings and our study does not rule out strong feedback by more extreme AGN.

3.5.4 The Fate of Outflows

Several useful quantities exist to obtain an approximation of an outflow's energy relative to the gravitational well of the host galaxy. The most obvious quantity to compare to would be the escape velocity of the host galaxy, however in order to be able to compare to both simulations and another similar outflow study by [Heckman et al. \(2015\)](#), we opt to compare the circular velocity (v_{circ}) of the galaxy instead. As such, in Figure 3.12a we plot the outflow velocity versus the circular velocity of the host galaxy for stacks over the i - $\log M_*$ plane with the samples defined in Section 3.4.5, and add the results of [Heckman et al. \(2015\)](#) for local star-forming galaxies for comparison. This provides us with an idea of whether an outflow is traveling at speeds close to the escape velocity of the galaxy or not. The circular velocity is derived from the stellar mass of the host galaxy: $v_{\text{circ}} = \sqrt{2}S$, where S is the kinematic parameter ([Weiner et al. 2006](#); [Kassin et al. 2007](#)) found to have a good fit with stellar mass for low- z star-forming galaxies, $\log S = 0.29 \log M_* - 0.93$ ([Simons et al. 2015](#); [Heckman et al. 2015](#)). We see that most of our detections (23/33) lie below the 1:1 line, suggesting the outflow velocity does not exceed the circular velocity of the host. However, we also notice there are some detections (10/33) which have outflow velocities greater than the circular velocity of the galaxy. These all occur in the lower mass systems, suggesting that outflowing gas may become unbound from the galaxy's gravitational potential.

Another useful comparison is of the force provided by the host galaxy's starburst (caused by stellar winds, supernovae and radiation pressure) to the critical force needed to have a net force acting outward on the outflow. Assuming a momentum-driven outflow consisting of a population of filamentary clouds (e.g., [Chevalier & Clegg 1985](#)) dense

enough to produce the observed absorption line profile (e.g., the outflow in M82), the momentum flux (or force) provided by the starburst is $\dot{p}_* = 4.8 \times 10^{33}$ SFR and the critical momentum flux acting on a cloud needed for the net force acting on it to be outward is $\dot{p}_{\text{crit}} = 4\pi r_* N(H) m_{\text{H}} v_{\text{circ}}^2$ (for more details, see Section 4 of Heckman et al. 2015). In Figure 3.12b we plot these two quantities for the LOW- i SFR- M_* stacks and compare them to the results of Heckman et al. (2015). We find that 10/12 detections fall under the “weak outflow” regime defined by Heckman et al. (2015), where the starburst provides $\dot{p}_* \sim 1\text{-}10 \dot{p}_{\text{crit}}$, and 2/12 detections fall under the “no-outflow” regime where $\dot{p}_* < \dot{p}_{\text{crit}}$ and the starburst cannot match or exceed the force needed to overcome gravity. None of our detections fall in the “strong outflow” regime where $\dot{p}_* > 10\dot{p}_{\text{crit}}$ and the outflow exceeds the escape velocity of the galaxy.

These basic results provide rough approximations of the force provided to the outflows and suggest the vast majority of our detections are unable to escape the host galaxy’s gravitational hold. In fact, such arguments are based on ballistic models which do not account for the presence of a surrounding gaseous corona, while in reality hydrodynamical processes should play a crucial role in slowing down the outflow, making it even more difficult to escape the galaxy system. This is likely to play an even more important role in the most massive systems, since they reside in denser environments (Oppenheimer & Davé 2008). Given the low velocities of our inflow/outflow detections, the inclination dependence and the relatively low median SFRs of our stacks, it is likely we are viewing aspects of a galactic fountain scenario, where the gas is expelled from the galaxy disk into the surrounding medium, before it mixes and cools with potential pristine gas to fall back down into the disk as an inflow. The low velocities are unlikely to be high enough to escape the host system and it is therefore not unreasonable to assume these outflows could be fueling (in part) the extra-planar gas observed in external galaxies (e.g., Fraternali et al. 2002; Oosterloo et al. 2007; Rossa & Dettmar 2003a) and the Milky Way (Marasco & Fraternali 2011). The simultaneous detections of outflows *and* inflows in virtually the same regions of parameter space - separated only by inclination effects - are most easily explained by the scenario of a galactic fountain (Fraternali & Binney 2006).

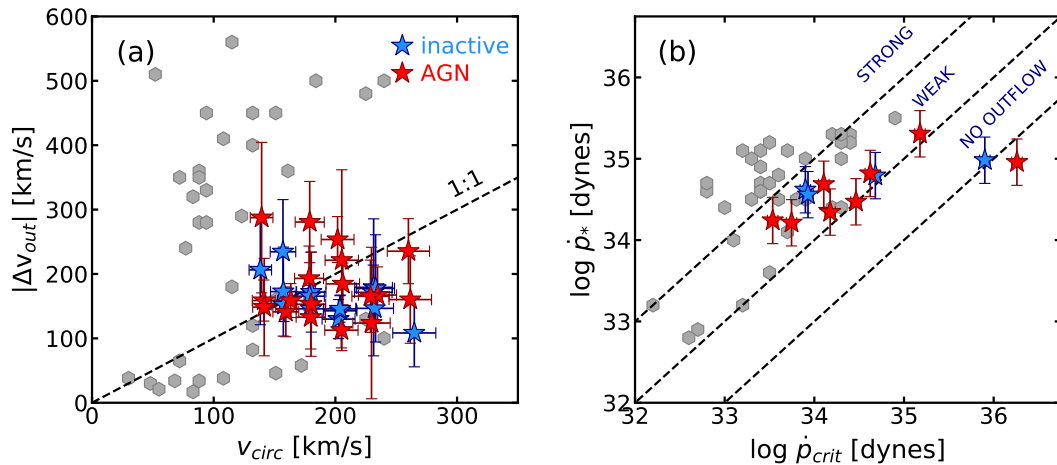


Figure 3.12. *Left:* The outflow velocity as a function of the galaxy’s circular velocity, compared to the results of Heckman et al. (2015). Blue stars are the inactive galaxies and the red stars are the AGN of the i -log M_* stacks. *Right:* A comparison of the momentum flux (or force) provided by the galaxy starburst versus the critical momentum flux necessary for the net force acting on a cloud to be outwards. The dashed diagonal lines denote constant lines of $\dot{p}_*/\dot{p}_{crit}=10$, 1 and 0.1 as well as three outflow regimes: “no outflow”, “weak outflow”, and “strong outflow”.

3.6 Summary and Conclusions

In this study we conduct a stacking analysis of 240,567 inactive galaxies and 67,753 AGN hosts from the SDSS DR7 survey. We stack spectra over bins of global galaxy properties and place constraints on the detection rates and properties of inflows and outflows in the local Universe. Our main conclusions can be summarized as the following:

- Signatures of outflowing gas are detected along the Main Sequence of star-forming galaxies for a large range of stellar masses ($10 \lesssim \log M_*/M_\odot \lesssim 11.5$). We also find detections of inflows in star-forming, disk galaxies over a similar range of stellar mass ($10 \lesssim \log M_*/M_\odot \lesssim 11$). These results hold for both inactive galaxies and AGN hosts.
- We find a strong inclination dependence for the detection rates of both outflows and inflows in disk galaxies, with outflows prevalent at low inclinations ($i \lesssim 50^\circ$) and inflows at high inclinations ($i \gtrsim 60^\circ$). This is suggestive of outflowing gas perpendicular to the galaxy disk and accretion along the plane of the disk. Galaxy morphology does not appear to play a major role in the detection rates of outflows.

- We report low ($\sim 1.5\text{-}17.4 M_{\odot}\text{yr}^{-1}$) mass outflow rates and compare these to other results in the literature. These comparisons reveal a strong linear relationship between the mass outflow rate and the SFR of the host galaxy, and a prescription is provided. The mass loading factor, given by the ratio of these two quantities, is calculated to be near-constant ($\eta \approx 1$) for local, normal star-forming objects.
- We find only minor differences in outflow detection rates and properties of inactive and AGN galaxies, suggesting that the presence of a weak AGN does not significantly enhance either. Neither galaxy type appears able to launch winds strong enough to quench a galaxy.

Galaxy-scale outflows are an integral element of galaxy evolution models and play a key role in shaping the environments and mass build up of galaxies across cosmic time. Here we have studied outflows in stacks of large samples of local galaxies over a range of stellar mass and SFRs and found them to be common among star-forming galaxies. However, none of the outflows are powerful enough to quench their hosts via ejective feedback, but may nonetheless be able to significantly influence the surrounding environments of the galaxies. To verify this, more work is required to link the properties of outflows to the gas content and distribution in the CGM. To obtain a better understanding and a more comprehensive picture of outflows, large dedicated surveys (UV, optical and submillimetre) and IFU observations of neutral, ionized and molecular gas in normal star-forming objects are required in order to constrain and link the multiphase nature of outflows. Such observations would also allow more concrete constraints on the geometries of outflows, which have until now relied on crude and unconstrained assumptions. Finally, still required are detailed analyses of inflows and their interplay with outflows and the host galaxies. In combination with simulations that track the accretion of pristine, merged, and recycled gas, such observations would greatly complement and enhance our knowledge of the conditions necessary to fuel star formation across cosmic time.

Spatially Resolved Outflow Properties in the Local Galaxy Populations with MaNGA DR15

IFU

4.1 Introduction

Observations from long slit or single-fiber spectroscopy have made progress in constraining the prevalence and bulk properties of outflows, finding them to be common at all epochs among star-forming systems and AGN (Veilleux et al. 2005; Rupke et al. 2005a; Feruglio et al. 2010; Chen et al. 2010; Coil et al. 2011; Cicone et al. 2016; Cazzoli et al. 2016; Roberts-Borsani & Saintonge 2019). In particular, for normal galaxies of the local Universe, we showed in the previous Chapter of this Thesis that outflows traced by absorption are particularly common in high mass galaxies ($\log M_*/M_\odot > 10$) along the galaxy MS.

However, recent attention has also turned to understanding the origins of galaxy evolution on kpc-scales, where the intrinsic correlations that govern small scale star formation activity ultimately give rise to the large scale properties observed over whole galaxy systems. Obtaining the necessary observations and determining such relations was previously

challenging and exclusive to small samples of galaxies with generally extreme properties, however the vast improvement in interferometric capabilities and arrival of IFU surveys has now opened a new window into studying galaxies at pc and kpc resolution. One example of this is understanding the theory of star formation via the exploration of the Schmidt-Kennicutt relation (Schmidt 1959; Kennicutt 1998) from pc to integrated scales (e.g., Usero et al. 2015; Bigiel et al. 2016; Gallagher et al. 2018) and the variations of star formation efficiency with galaxy properties (Usero et al. 2015; Bigiel et al. 2016; Gallagher et al. 2018).

Similar studies have also extended to outflows, although early efforts focussed primarily on small samples of extreme objects. For example, using Gemini IFU observations and a combination of ionised emission and absorption tracers, Liu et al. (2015) and Rupke et al. (2017) explored the properties of outflows in a combined sample of 12 AGN and QSOs, determining and placing constraints on outflow mass loading factors, radii and geometries. Specifically, Liu et al. (2015) and Rupke et al. (2017) were able to infer both spherical and bipolar geometries of the outflows from the determination of their orientations and radii extending out to $\lesssim 10$ kpc from the galaxy disks. Measurements of mass outflow rates revealed a large range of values, from 1 to $>1000 M_{\odot}\text{yr}^{-1}$, and in conjunction with their other results demonstrated a diverse suite of outflow types in extreme AGN and QSOs.

The advent of large IFU surveys such as CALIFA (Sánchez et al. 2012), SAMI (Croom et al. 2012) and MaNGA (Bundy et al. 2015), however, has heralded in a new era for statistical studies of representative galaxies and their outflows at kpc resolution. To date, most such studies have focused on the kinematics and ionisation diagnostics of outflowing ionised gas, using nebular emission lines such as H α and [OIII] λ 5007 (e.g., Rich et al. 2011; Ho et al. 2014; Liu et al. 2015; Rich et al. 2015; Ho et al. 2016; Rupke et al. 2017; López-Cobá et al. 2019; Rodríguez del Pino et al. 2019). For instance, using combinations of data from MUSE, VLT/X-Shooter and MaNGA DR2, Maiolino et al. (2017) and Gallagher et al. (2018) used optical ionised emission lines to determine the presence of outflows and the main ionising mechanisms in the central regions of 38 individual galaxies and revealed, for the first time, potential *in situ* star formation traced by H α within 15 of the galactic-scale outflows themselves. The result showed that the combination of outflow turbulence with entrained dense gas can lead to significant levels of star formation (i.e., so called “positive feedback”) and raises important implications for the morphological evolution of galaxies and chemical enrichment of the CGM.

In another large IFU study of galaxy outflows, [Ho et al. \(2016\)](#) used 40 edge-on normal objects from the SAMI galaxy survey and ionised emission lines to identify objects with outflows and determine the star formation histories of their hosts. Using the $H\alpha+[NII]$ tracers as well as the $D_n(4000)$ and $H\delta_A$ indices, they revealed ionised outflows in galaxies with elevated Σ_{SFR} values that had shown evidence for recent bursts of star formation. Both [López-Cobá et al. \(2019\)](#) and [Rodríguez del Pino et al. \(2019\)](#) extended these analyses toward determining the prevalence and properties of ionised outflows in a variety of normal galaxies using data from the CALIFA and MaNGA surveys, respectively. With a sample of 17 high-inclination MS galaxies from CALIFA, [López-Cobá et al. \(2019\)](#) found evidence for extraplanar gas in $<10\%$ of their objects, with the outflows located in the central regions of high mass ($\log M_*/M_\odot > 9.5$) galaxies with high values of Σ_{SFR} . [Rodríguez del Pino et al. \(2019\)](#) used a sample of $\sim 1,000$ galaxies from the MaNGA DR2 to determine the presence of $H\alpha$ -traced outflows and the difference in outflow properties between regions dominated by star formation, composite, AGN and LI(N)ER activity. Consistent with the results from [López-Cobá et al. \(2019\)](#), they too found outflows in $<10\%$ of their sample and also illustrated differences in outflow kinematics between regions traced by star formation, AGN and LI(N)ER activity, with the latter demonstrating significantly enhanced velocities compared to the former two, by a factor of 2.5 and 2, respectively. However, as with integrated studies, they found little difference between outflow velocities in regions of normal star formation and AGN activity, with differences of only ~ 100 km/s, consistent with values found from similar comparisons with SDSS ([Sarzi et al. 2016](#); [Roberts-Borsani & Saintonge 2019](#)).

The breadth and diversity of the aforementioned outflow studies illustrate the power and potential, as well as necessity, of IFU studies in constraining their properties and demonstrate a complexity of outflows not probed by single observations. Still lacking, however, are statistical constraints on the radial extent of the outflows and their power, as well as the coveted mass loading factor with which to derive a first order evaluation of quenching on small scales. Thus, determining the intricate kpc-scale relations of outflows and their hosts is imperative towards gaining a thorough and complete understanding of galaxy evolution. Here, we aim to make progress in this respect by providing constraints on the average kpc prevalence, radial extent and properties of star formation-driven outflows found in normal galaxies with the MaNGA DR15 IFU survey, as well as determining their power and quenching potential via a local mass loading factor. We present our

observational data set in Section 4.2, stacking and analysis procedures in Section 4.3 and results in Sections 4.4, 4.5, 4.6, 4.7. We provide a discussion in Section 4.8 and present the conclusions to our findings in Section 4.9.

4.2 Data and Sample

Motivated by the results from Chapter 3, we begin our selection by performing cuts on galaxy stellar mass ($\log M_*/M_\odot > 10$), SFR ($\log \text{SFR}/M_\odot \text{ yr}^{-1} > -2.332 (\log \text{SFR}/M_\odot \text{ yr}^{-1}) + 0.4156 (\log \text{SFR}/M_\odot \text{ yr}^{-1})^2 - 0.01828 (\log \text{SFR}/M_\odot \text{ yr}^{-1})^3 - 0.4$, corresponding to a rough lower limit of the galaxy main-sequence defined by [Saintonge et al. 2016](#)) and inclination ($i \leq 50^\circ$, derived from the galaxy's r -band axis ratio, b/a) - three key galaxy properties known to influence the detection rates of neutral gas outflows. The stellar masses and SFRs used for this selection are taken from the Pipe3D catalog¹, which for each galaxy derives a SFR based on the integrated $H\alpha$ luminosity, and the axis ratio of the galaxy is taken from the NASA-Sloan Atlas catalog. Finally, given that broad line regions in AGN can cause overestimation of $H\alpha$ -derived SFRs and/or mimic the presence of outflows in ionised gas tracers, we choose to identify and remove objects with AGN signatures in their central regions using the [Kauffmann et al. \(2003b\)](#) BPT diagnostic. Motivation for this also comes from several recent studies (e.g., [Sarzi et al. 2016](#); [Concas et al. 2017](#); [Roberts-Borsani & Saintonge 2019](#)) which have demonstrated the limited influence of a weak AGN in the normal galaxy populations. Our resulting sample consists of 422 star-forming galaxies. To ensure our sample is not contaminated by the presence of mergers, stars, or pointing offsets, we visually inspect the MaNGA footprint image of each galaxy: 17 galaxies fail these criteria and are removed from the sample. Our final sample, therefore, consists of 405 star-forming galaxies, whose position on the SFR- M_* plane is shown in Figure 4.1 along with histograms of their SFRs $_{H\alpha}$ and stellar masses. The sample spans virtually the full MaNGA redshift range, with a median redshift of $z=0.04$ which corresponds to a pixel sampling of ~ 0.4 kpc and an effective spatial resolution of $\text{FWHM} \sim 2$ kpc.

¹https://www.sdss.org/dr15/data_access/value-added-catalogs/?vac_id=manga-pipe3d-value-added-catalog-spatially-resolved-and-integrated-properties-of-galaxies-for-dr15

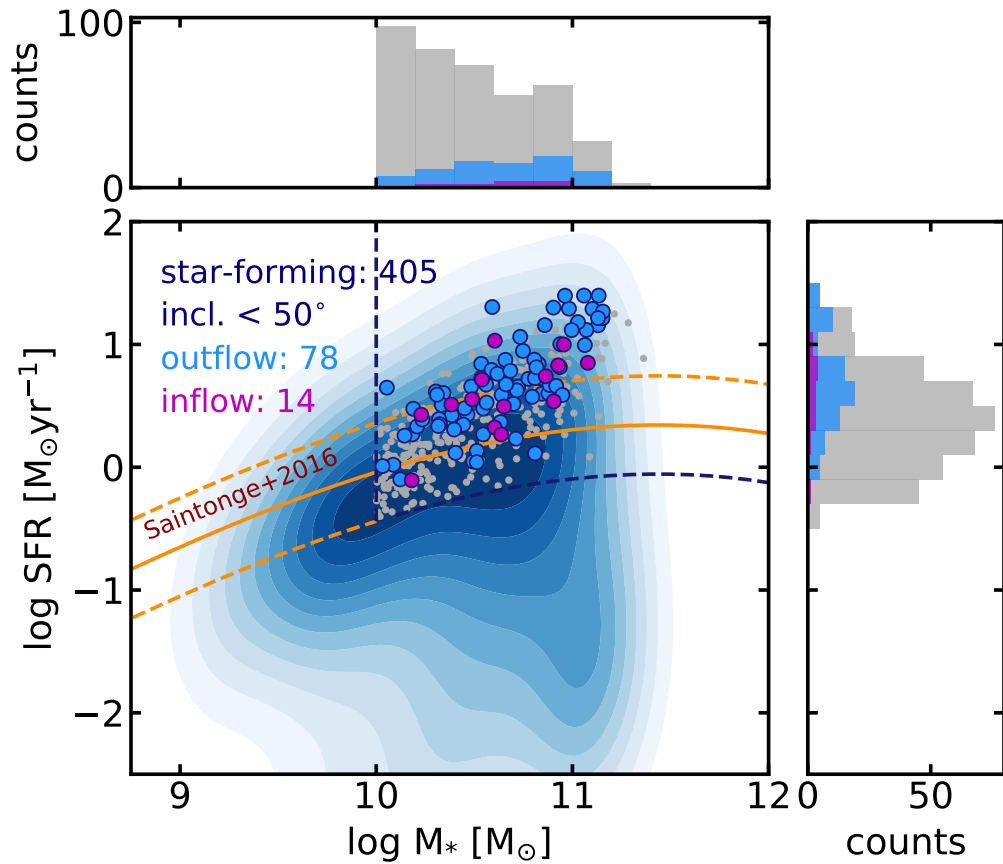


Figure 4.1. The SFR- M_* plane and density contours of the full MaNGA DR15 sample and selected sample for this study. Gray dots represent the 405 galaxies found using our selection criteria (blue dashed lines), whilst the blue points mark galaxies found to have outflows in their central regions and magenta points galaxies found to have inflows. The orange solid and dashed lines mark the star-forming main sequence defined by Saintonge et al. (2016) and its lower and upper limit. Histograms of the selected galaxies’ SFRs and stellar masses are shown to the top and right sides of the main plot.

4.3 Stacking Procedures and Analysis

4.3.1 Maps of Galaxy Properties

As a first step in our analysis, we create maps of spatially-resolved galaxy properties (i.e., SFR, Σ_{SFR} , M_* , Σ_* , A_V and $D(4000)$) using the MaNGA DR15 Pipe3D IFU maps for each galaxy in our selected sample and the new MaNGA Python tool, MARVIN, which facilitates access to spectroscopic quantities associated with each spaxel. We begin by using the spatially resolved $H\alpha$ and $H\beta$ emission in order to derive a Balmer decrement for each spaxel, which we translate into an A_V and $A_{H\alpha}$ magnitude, assuming an intrinsic

ratio of $H\alpha/H\beta=2.68$. The maps of $H\alpha$ are subsequently corrected for dust and converted to a luminosity using luminosity distances derived with an $H\alpha$ redshift and the assumed cosmology. The $H\alpha$ luminosities are subsequently converted to a Σ_{SFR} using a [Kennicutt \(1998\)](#) prescription converted to a Chabrier IMF ($\text{SFR} [M_{\odot}\text{yr}^{-1}] = L_{H\alpha}/[2.1 \times 10^{41} \text{ erg/s}]$) and the physical area probed by each $0.5''$ spaxel. Not all spaxels, however, are appropriate for analysis and we therefore ensure a quality control by applying the MaNGA bitmask flags and require the following criteria for science use:

- A line $S/N > 3$ for $H\alpha$, $H\beta$, $[\text{O III}]\lambda 5006$, $[\text{N II}]\lambda 6583$ and $[\text{O I}]\lambda 6302$.
- A BPT “star-forming” nature determined by MARVIN, which identifies the ionisation mechanism for each spaxel via the combination of the [Kauffmann et al. \(2003b\)](#) and [Kewley et al. \(2006\)](#) prescriptions, which make use of the $[\text{N II}]\lambda 6583$ and $[\text{O I}]\lambda 6302$ lines, respectively. By default, only spaxels with $S/N > 3$ in the relevant lines are considered.
- An r -band $S/N > 5$ to guard against spaxels with very little continuum signal.

The redshifts for each spaxel are derived from the [Talbot et al. \(2018\)](#) value added catalog². 15 galaxies do not have determined spaxel redshifts and we exclude these from our analysis, resulting in a sample of 390 galaxies. In total, this results in 276,619 science spaxels and an example of the MaNGA maps for a representative galaxy in our sample is shown in Figure 4.2. We find that the planes of galaxy properties as traced by the full spaxel sample are fully sampled by each of the galaxy in our sample, ensuring stacks over any particular region of parameter space include virtually the full sample of galaxies.

4.3.2 Stacking Procedure and Outflow Modelling

Throughout this study we make use of stacking approaches to construct high S/N composite spectra with which to analyse outflow properties as a function of galactocentric radius (i.e., annuli) and a variety of galaxy or spaxel properties (described in the following sections). The basic stacking procedure is virtually identical to that described in Section 3.3.1, but we provide a short summary here. For all stacks, the spaxels are first divided into a set of bins according to a given property (e.g., deprojected radius, SFR,

²https://www.sdss.org/dr15/data_access/value-added-catalogs/?vac_id=manga-spectroscopic-redshifts

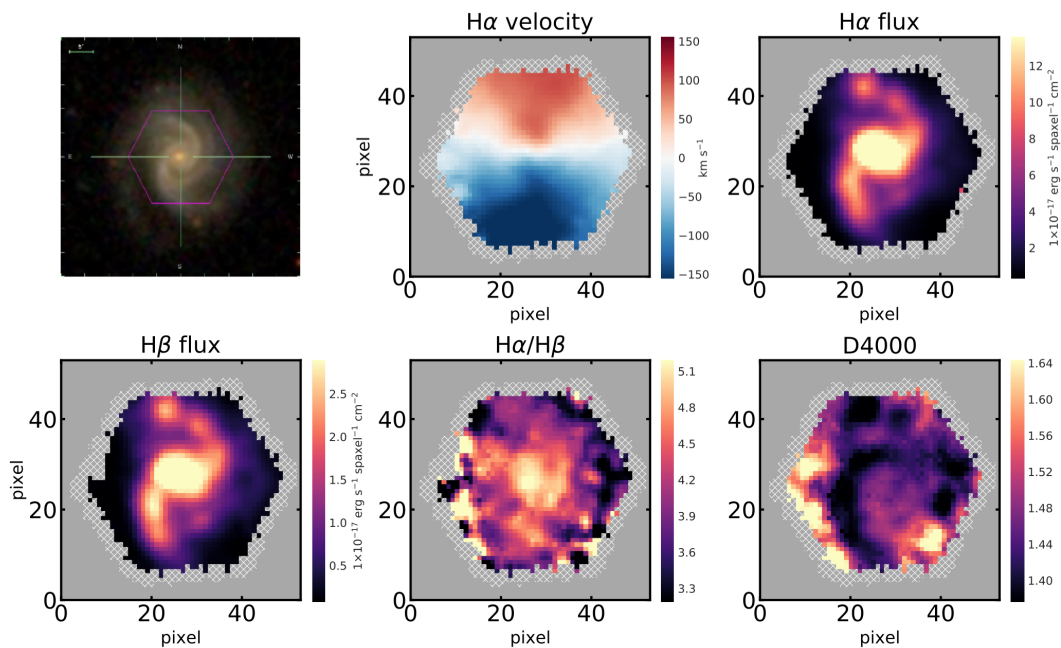


Figure 4.2. An example of IFU MaNGA galaxy property maps. From left to right, top to bottom: The SDSS image of an example galaxy with the MaNGA footprint, the velocity of H α relative to the systemic, the flux of H α , the flux of H β , the Balmer decrement, the D(4000) index.

A_V , D4000, etc) and each spectrum in an associated bin is subsequently corrected for foreground galactic extinction using the associated [Schlegel et al. \(1998\)](#) E(B-V) values and an [O’Donnell \(1994\)](#) Milky Way extinction curve, after converting the wavelength arrays of the spectra to air wavelengths. Each spectrum is then shifted to the rest-frame, before being interpolated over a common wavelength grid.

We subsequently mask all flux points in a given spectrum that are deemed unfit for science by its associated mask array and normalise the spectrum by the median flux between 5450 Å and 5550 Å (since this region is free of absorption and emission lines), thereby giving equal weight to each spectrum. Each spectrum is then added to the stack and the final spectrum is taken as the mean over all stacked spectra. The associated uncertainties of the mean stack are derived by adding in quadrature the bootstrapped sampling uncertainties and the mean flux uncertainties of each individual spectrum within the stack. In order to model outflow quantities associated with NaD, we use the same approach as described in Section 2.2 to model the line and use the blueshifted absorption component to derive outflow quantities. Given the low covering fractions found in Section 3.4.3, however, we limit the allowed values to $|C_f| \leq 0.5$.

To derive mass outflow rates we assume a slightly different approach to that described in Section 3.4.6. In Chapter 3 we attempted to derive mass outflow rates based on a spherically symmetric thin shell geometry emanating from the centre of the galaxy and extending out to 5 kpc. However, because of the resolved nature of our data sets, our stacks do not necessarily follow a well defined geometry. This is particularly relevant when stacking spaxels from different regions of a galaxy. Furthermore, calculating an outflow rate based on the area probed would result in direct correlation between the mass outflow rate and the number of spaxels in each stack, thereby removing much of any correlation with galaxy property. As such, we opt only to assume a radius of the outflowing gas of 1 kpc - where the outflowing gas is unlikely to be collimated by the disk - and not to assume a geometry. The advantage of this is that our absolute values are less subject to uncertain geometrical assumptions and are almost entirely derived from our fitted parameters, whilst the disadvantage is that the true values are likely to be higher than what we present here. Thus, our expression for a mass outflow rate becomes:

$$\dot{M}_{\text{out}} = C_f \mu m_{\text{H}} N(\text{H}) v r, \quad (4.1)$$

where each term is as defined in Section 3.4.6.

4.4 The Galactocentric Profile of Outflows

We begin by stacking spaxels as a function of deprojected galactocentric radius (i.e., accounting for the galaxy's inclination and rotation on the plane of the sky) for our sample of 390 galaxies, in order to create multiple independent annuli for each of our galaxies which probe the full range of the galaxy disk. The first annulus is centred at the centre of the galaxy disk and subsequent annuli extend outward from the border of the inner annulus. Each annulus contains spaxels within a full width of $0.25 R_e$ from its centre, and the distribution of annuli probe from the centre of the galaxy out to $\sim 2 R_e$. For each galaxy, all relevant spaxels are first deprojected from the position of the central spaxel using the galaxy's position angle (PA) and inclination:

$$\text{RA}_{\text{deproj}} = (\text{RA} - \text{RA}_{\text{central}}) \cdot \cos(\text{PA}) + (\text{DEC} - \text{DEC}_{\text{central}}) \cdot \sin(\text{PA}) \quad (4.2)$$

$$\text{DEC}_{\text{deproj}} = \frac{-(\text{RA} - \text{RA}_{\text{central}}) \cdot \sin(\text{PA}) + (\text{DEC} - \text{DEC}_{\text{central}}) \cdot \cos(\text{PA})}{\cos(i)} \quad (4.3)$$

The deprojected radius between a given spaxel and the central spaxel is then taken to be $r_{\text{deproj}} = \sqrt{\text{RA}_{\text{deproj}}^2 + \text{DEC}_{\text{deproj}}^2}$, and the mean spectrum and quantities quoted here are those over the central spaxels. The motivation here is to determine and select galaxies that display signatures of outflows, in order for them to be used in subsequent analyses where we can tie global galaxy properties to outflow properties. Since the signature of blueshifted absorption can easily be “diluted” by strong systemic absorption in a stack, we wish to maximise our chances of outflow detection and characterisation by preselecting galaxies with outflows in their central regions. Thus, to determine whether a gas flow is present in the central region ($R < 0.25 R_e$), we compare NaD fits of a fixed systemic component to a single blueshifted or redshifted absorption component. We derive a BIC ratio ($K = \text{BIC}_{\text{fixed}} / \text{BIC}_{\text{flow}}$) of the two models to account for the extra free parameter (i.e., a velocity offset) in the shifted model and determine a flow detection if the ratio is greater than unity and a minimum blueshift velocity is found. Furthermore, in Chapter 3 we showed the fraction of outflow detections seen in NaD decreases rapidly as the net profile changes towards emission. Given that the nature of the NaD emission is still poorly understood, we opt to analyse only galaxies which show net absorption at their centres, and require an absorption depth-to-noise (D/N) ratio > 3 in the central region, with a minimum blue shifted of 15 km s^{-1} if $\text{D/N} > 5$ and 20 km s^{-1} if $3 < \text{D/N} < 5$. In total, 92 galaxies satisfy these criteria, with 78 objects displaying outflow detections and 14 displaying inflow detections. The remaining 298 galaxies either do not show sufficient absorption ($\sim 80\%$), with a typical (median) D/N ratio of 1.62, do not show blueshifted absorption ($\sim 18\%$), or have insufficient spatial resolution to stack within $0.25 R_e$ ($\sim 2\%$). We report the flow galaxies and their main properties in Table B.1 and illustrate the typical D/N ratios in Figure 4.3.

We note that the vast majority of the galaxies presented here show significant NaD emission within the central $0.25 R_e$. This is in contrast to $3''$ -fiber observations from the SDSS, where in Chapter 3 we find NaD in net emission only in stacks of galaxies with stellar masses below $\sim 10\text{--}10.5 M_{\odot}$. One explanation for this difference could be due to different inclinations between the high mass galaxies of the two samples: as shown by [Chen et al. \(2010\)](#), the EW of *systemic* NaD rapidly decreases with decreasing inclination,

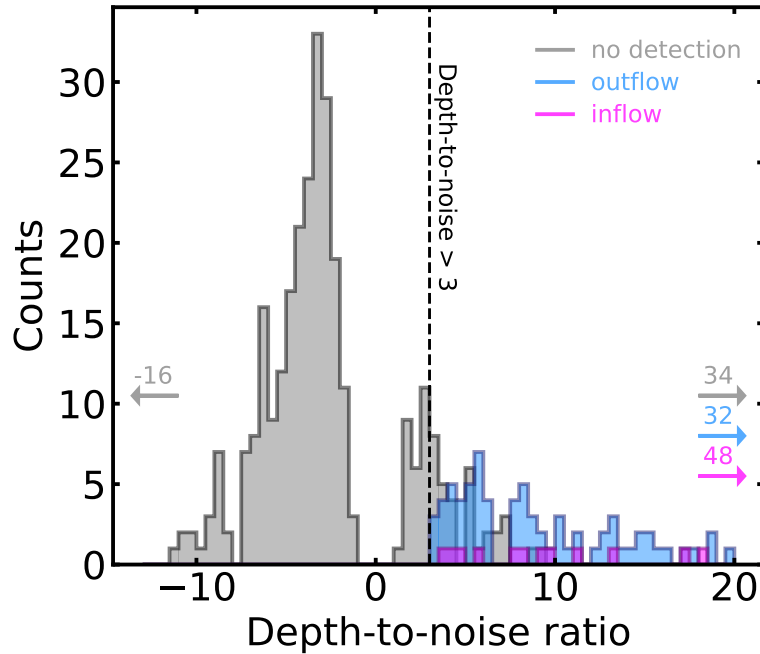


Figure 4.3. The typical depth-to-noise ratios of NaD in the central ($<0.25 R_e$) regions of the sample of MaNGA galaxies used in this study. The gray histogram represents non-detections, whilst the blue histogram and the magenta histogram represent outflow and inflow detections, respectively. Positive values reflect profiles in absorption, whilst negative values represent profiles in emission. The dashed black line marks our minimum D/N threshold of >3 to determine detections of inflows and outflows.

most likely due to the smaller column density of gas probed along the line of sight through the thickness of the disk. With inclinations lower than $i \sim 40^\circ$, [Chen et al. \(2010\)](#) observe systemic NaD transitioning from absorption into pure emission, possibly due to difficulties of the continuum-fitting code to reproduce such low column densities of systemic NaD gas. In Chapter 3, we note the median inclination of high mass SDSS galaxy stacks in [Figure 3.5](#) is $\sim 45^\circ$, high enough to push the EW to significantly positive values, whilst the median inclination of the high mass MaNGA galaxies displaying net emission here is significantly lower at $\sim 35^\circ$ and enough to push the NaD EW to net emission. Thus, the high mass MaNGA galaxies presented here are even more face-on than the SDSS stacks presented in [Figure 3.5](#) and thus probe less NaD gas along the line of sight. It is important to stress this does not necessarily impact the EW of the outflowing gas, which requires low inclinations for its Doppler blueshift to be detected, but only the gas at systemic wavelengths sitting in the disk. We also note a possible secondary consideration, in that the SDSS fiber typically probes galaxy regions slightly larger than $0.25 R_e$, meaning more

NaD absorption can possibly be seen in the fiber.

4.4.1 Average Central Profiles

We begin by examining and comparing the mean spectra of galaxies with and without flow detections in the inner $0.25 R_e$ of their effective radii. We adopt a Monte Carlo approach to constructing the mean central stacks over samples of outflow and inflow galaxies, using a control sample of non-detection galaxies for comparison: a random sample of 10 outflow (or inflow) galaxies is selected and for each galaxy we randomly select a non-detection “counterpart”, defined as such if it lies within ± 0.2 dex in stellar mass and SFR, before averaging the central spectra. This is repeated 100 times and the final spectrum is simply the mean over all iterations, with the stack flux errors derived from a combination of individual flux uncertainties and bootstrapping errors. The results of these are shown in Figure 4.4, where we show the differences in spectra between galaxies with outflows, inflows, and those without, along with some key galaxy properties. From the left panel, we note that the optical spectra over $\sim 3700 < \lambda < 8000 \text{ \AA}$ for outflow and non-detection galaxies are virtually identical, with minor differences only in the strength of the emission lines and depth of the absorption lines. The similarity is less pronounced for inflow galaxies, however, which display a considerably redder continuum slope than their non-detection counterparts.

A much starker contrast, however, appears when comparing the average NaD profiles (middle panel) profiles. For NaD we note a large difference in the total EW of the profile, with $\sim 0.5 \text{ \AA}$ for outflow detections, $\sim 0.95 \text{ \AA}$ for inflow detections, and -0.1 \AA for non-detections. A visual comparison of the profiles shows that both inflow and outflow detections are characterised by significant and unambiguous absorption. The NaI $\lambda 5889$ line has an intrinsic line depth twice the size of its NaI $\lambda 5895$ redshifted counterpart (Morton 1991), however the flow profiles display a clear asymmetry: the outflow spectrum is blueshifted with respect to the systemic wavelengths and the inflow spectrum, while not as significantly redshifted, shows nearly equal line depth for the two NaD lines which can arise due to an additional redshifted component. Both profiles are well-characterised by an additional blueshifted or redshifted component offset by $|\Delta v| \sim 120 \text{ km s}^{-1}$ and $|\Delta v| \sim 85 \text{ km s}^{-1}$, respectively. The average non-detection spectra, on the other hand, are characterised by virtually no absorption and even display net emission. In stacking the full non-detection sample, we find this emission becomes even more pronounced.

Although less pronounced, similar comparisons are found with the ionised gas traced by $\text{H}\alpha + [\text{N II}]$ (right panel): the average non-detection spectrum is characterised by a narrow profile that is less luminous than its detection counterpart, by a factor of ~ 0.7 . In contrast to the outflow observed in the mean NaD profile, a significant broadening of the ionised gas is not immediately obvious, however a BIC ratio between a one- and two-component fit strongly favours the latter fit, with an outflow velocity of $\sim 130 \text{ km s}^{-1}$, similar to that observed with the neutral gas and suggestive of the emission emanating both from the disk of the galaxy and a broader outflowing component.

To gain some indication of the driver for the different profiles, we compare the mean values of several galaxy properties likely to be important in determining both the shape of the NaD and $\text{H}\alpha + [\text{N II}]$ profiles and flow presence. NaD requires significant amount of shielding from dust to survive, and dust obscuration has been found to correlate with the EW of the line (e.g., [Chen et al. 2010](#); [Roberts-Borsani & Saintonge 2019](#)). Here we find average A_V magnitudes of ~ 1.4 - 1.9 mag (detections) and ~ 1.2 mag (non-detections), suggesting somewhat of a limited impact in regulating the shape of the two flow profiles. A similar conclusion can be said for a dependence on the D(4000) break, which varies only by ~ 0.1 between the spectra. The difference in Σ_{SFR} , on the other hand, we find to be much more significant: for non-detections, the average value ($0.048 \pm 0.001 \text{ M}_{\odot} \text{ yr}^{-1} \text{ kpc}^{-2}$) is lower compared to the average values of detections, which are both higher than $> 0.1 \text{ M}_{\odot} \text{ yr}^{-1} \text{ kpc}^{-2}$ (0.116 ± 0.001 and 0.126 ± 0.002 for outflows and inflows, respectively). Although the differences between the average values is not, at first glance, particularly large or significant, it is their absolute values which is of greater interest: the Σ_{SFR} s of the flow spectra are consistent with (and above) what is generally invoked as a minimum threshold for outflow activity seen in absorption ($0.1 \text{ M}_{\odot} \text{ yr}^{-1} \text{ kpc}^{-2}$; [Heckman 2002](#)). Finally, we also find elevated stellar mass surface densities for the detection spectra, compared to the non-detections and this is most likely the result of a positive correlation with Σ_{SFR} (i.e., the “resolved” Main Sequence; e.g., [Sánchez et al. 2013](#); [Cano-Díaz et al. 2016](#); [González Delgado et al. 2016](#); [Abdurro’uf & Akiyama 2017](#); [Hsieh et al. 2017](#); [Maragkoudakis et al. 2017](#)). We attempt to disentangle these intrinsic correlations and explore further the main regulating properties of the outflows in Section 4.6.

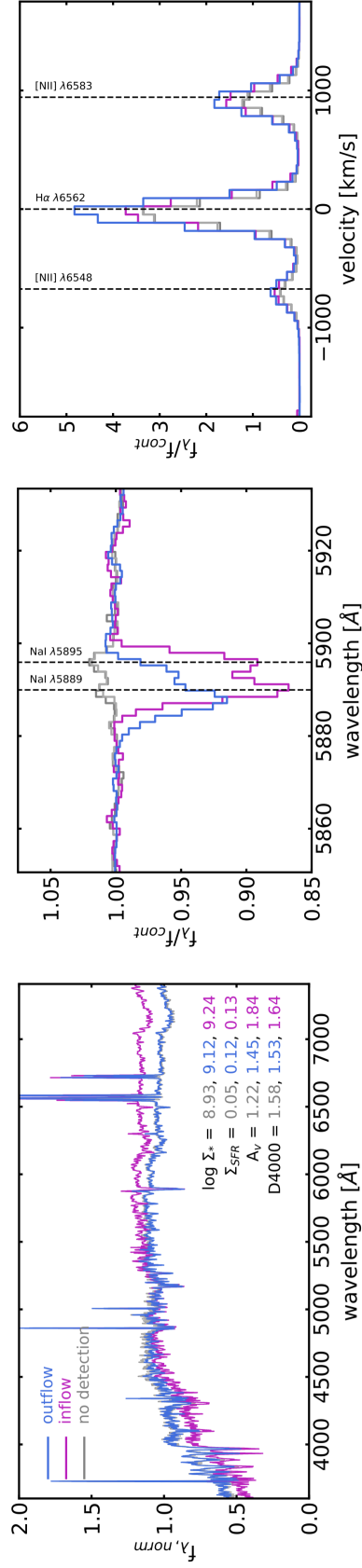


Figure 4.4. The average central $0.25 R_e$ spectra of galaxies harbouring outflows (blue) and inflows (magenta), and the average spectra of an associated control sample of non-detection galaxies (light gray for inflows, dark gray for outflows). *Left:* the normalised optical spectra over virtually the full optical range. *Middle:* the continuum-normalised $H\alpha + [N II]$ emission in the line for the four spectra in the left panel. The quantities and units quoted in the left panel are the stellar mass surface density ($M_{\odot} \text{kpc}^{-2}$), SFR surface density ($M_{\odot} \text{yr}^{-1} \text{kpc}^{-2}$), dust (magnitudes) and 4000 \AA -break. The colours correspond to the different stacks (NB: given that the average spectra - and quantities - for the two non-detection control samples are essentially identical, we display only the values of the control sample associated with the outflow detections).

4.4.2 The Radial Extent of Outflows and Their Properties

Outflows are typically described as bipolar, collimated jets that emanate from the central regions of a galaxy. Here, we test this picture by looking at the extent and properties of outflows over a range of galactocentric radii, R/R_e . This is done by stacking spaxels in the shape of annuli around the central $0.25 \cdot R_e$ regions of each galaxy. Thus, each annulus begins where the previous one ended and extends further out by $0.25 \cdot R_e$. Once this is performed for each galaxy, each annulus is stacked and average over all galaxies. This is shown in Figure 4.5, where we plot the evolution of the ISM NaD EW (left panel), mass outflow rate (middle panel), and mass loading factor (right panel) as a function of radius. For reference, we also compare these to what would be measured by an SDSS $1.5''$ -radius fiber.

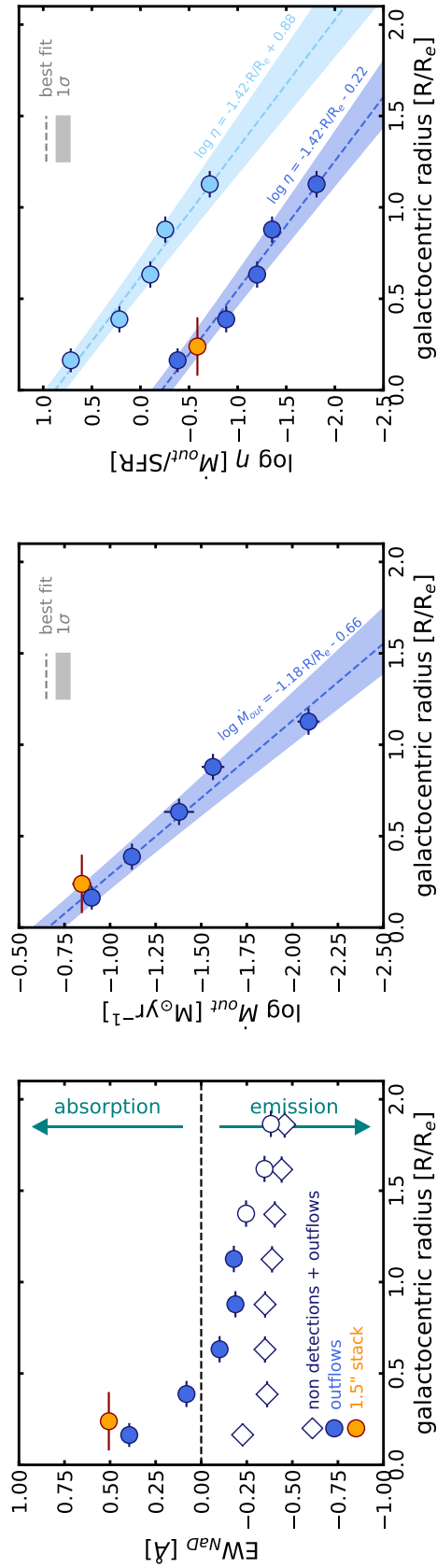


Figure 4.5. The evolution of the total NaD EW (left panel), mass outflow rate (middle panel) and mass loading factor (right panel) as a function of galactocentric radius. The NaD EW is separated out into stacks of spaxels from the outflow detection sample only (circles) and non-detection+outflow spaxels (diamonds). Filled symbols indicate the detection of outflowing neutral gas, whilst empty symbols indicate non-detections. For comparison, a 1.5" stack is also added to each of the plots, in order to gauge what would be measured by single-fiber SDSS surveys. In the middle and right plots, we add a best fit first order polynomial (dashed line) and its 1σ error (shaded region).

In the left panel of Figure 4.5 we plot the EW of the NaD residual for stacks containing only the outflow galaxies (circles) and stacks with both the non-detection and outflows galaxies (diamonds). For the former, we observe a rapid decrease in EW as a function of radius, with a roughly exponentially declining profile which begins to flatten out slightly at $>0.75 R_e$. The central regions of the galaxy ($<0.5 R_e$) are dominated by absorption, although this quickly transitions to net emission outward of $\sim 0.5 R_e$. A $1.5''$ stack of the detection galaxies shows that SDSS measurements would be consistent and similar to what we measure here. Although we cannot compare directly, we note that this is similar to the distribution of molecular gas (i.e., cold gas) in disk galaxies traced by CO (Bigiel et al. 2008; Leroy et al. 2008; Schruba et al. 2011; Bigiel & Blitz 2012), where observations of molecular gas as a function of galactocentric radius have found a roughly exponential decrease. Outflow detections are observed only out to $\sim 1 R_e$, with the majority of the blueshifted absorption occurring within $0.5 R_e$ and the outer regions detected primarily due to the imprint of redshifted emission that backscatters off of the receding side outflow (see Section 3.3.2). The result suggests star formation-driven outflows may not produce distinct, central bipolar jets similar to AGN/QSO feedback, however some collimation could be present.

A milder trend is observed in stacks containing both the non-detection galaxies and outflow galaxies (diamond symbols in the left panel of Figure 4.5), albeit with some important differences: the strength of NaD emission increases slightly with radius, but in general maintains a much flatter slope compared to when only outflow galaxies are considered. Additionally, the added presence of the non-detection galaxies ensures the EW never reaches absorption at any radius and is observed only in emission; no detections of outflows are observed in these stacks. The contrast between the two samples is particularly evident below $\sim 1 R_e$, where outflow detections are present, and becomes less great outward of this limit. Such a comparison highlights the ease with which signals of outflows in normal galaxies can be overlooked if not selected appropriately. It is unclear, however, what induces such a rapid change in the NaD profile. Although typically assumed to be an absorption transition, several studies using SDSS (Chen et al. 2010; Concas et al. 2017; Roberts-Borsani & Saintonge 2019) have also found NaD in emission in stacked spectra. One obvious hypothesis is that SSP models at such low NaD EW are unable to accurately reproduce the stellar contributions and as such overestimate them, although there is a possibility that at outer radii there is insufficient gas and dust to produce significant NaD

absorption and potential background NaD re-emission begins to dominate.

We also wish to determine the radial evolution of the mass outflow rates in our stacks. To do this, we use Equation 4.1 to derive values of \dot{M}_{out} for the detections presented in the left panel of Figure 4.5 and plot these as a function of radius in the middle panel. We immediately note an important decrease in \dot{M}_{out} as a function of galaxy radius, similar to the trend observed for the NaD EW in the left panel. The outflow appears strongest in the central regions of the galaxy, with values starting at $\sim 0.13 \text{ M}_{\odot} \text{ yr}^{-1}$ and decreasing down to $\sim 0.01 \text{ M}_{\odot} \text{ yr}^{-1}$. A comparison with the $1.5''$ stack shows SDSS observations only probe the strongest parts of the outflow, with a mass outflow rate of $0.14 \text{ M}_{\odot} \text{ yr}^{-1}$, and likely overlook important contributions from the outer regions (i.e., out to $\sim 1 R_e$). Specifically, an SDSS $3''$ fiber would miss $\sim 50\%$ of the total mass outflow rate integrated over all the MaNGA radial stacks, which we calculate to be $\dot{M}_{\text{out}} \sim 0.28 \text{ M}_{\odot} \text{ yr}^{-1}$. The trend observed by the MaNGA points is well described by a linear fit, with a slope of ~ -1 :

$$\log_{10} \dot{M}_{\text{out}} = (-1.18 \pm 0.12) \cdot R/R_e - (0.66 \pm 0.08) \quad (4.4)$$

Such a trend is perhaps not surprising: the outflows are selected to be star formation-driven and as such are likely to correlate with star formation- and gas-dependent quantities, which are known to be mostly centrally concentrated (e.g., [Bigiel et al. 2008](#); [Ellison et al. 2018](#)).

The derivation of mass outflow rates in conjunction with the mean SFRs associated with each ring stack allow us to compute a resolved mass loading factor, η , and to first order, determine the extent of the outflows' potential for quenching. The mass loading factors are shown in the right panel of Figure 4.5. We observe a very similar trend to the mass outflow rate, with a rapidly decreasing $\log \eta$ as a function of radius, characterised by a slightly steeper slope of -1.4.

$$\log_{10} \eta = (-1.42 \pm 0.15) \cdot R/R_e - (0.22 \pm 0.10) \quad (4.5)$$

The values range from mass loading factors of $\eta \sim 0.4$ in the central regions of the outflow and decrease to $\eta \sim 0.02$ in the outermost regions, suggesting the potential for ejective quenching by the outflows is strongest in the central regions and not a galaxy-wide phenomenon - i.e., only in the central regions does the outflow have any sort of potential to quench the galaxy host by removing gas faster than the rate of star formation and halting

star formation activity - although none of the values ever reach unity, suggesting quenching even in the central regions remains unlikely. Integrating over all outflow detections, we find the galaxy-wide mass loading factor is $\eta \approx 0.1$, supporting this hypothesis.

However, as mentioned in Section 4.3.2, our choice not to assume an outflow geometry for these outflow rates means we are, to a degree, likely underestimating the absolute values. As such, for comparison we calculate mass loading factors with outflow rates derived with an assumed geometry. We assume here the outflowing gas from each stack is coming from an individual “wind bubble”, which we measure as a spherically symmetric shell subtending 4π steradians, whose origin resides in the galaxy disk and extends out to 1 kpc. The base assumption here is that the large-scale outflow is formed via the superposition and collimation of such “wind bubbles” at larger radii (e.g., 5 kpc) above the disk. Such a scenario is described via a simplified schematic in Figure 4.6. Following such a picture, we therefore multiply the outflow rates derived with Equation 4.1 by 4π and show these as light blue points in Figure 4.5. The result shows mass loading factors ~ 1.1 dex greater than our fiducial measurements, with a range $0.2 \gtrsim \eta \gtrsim 5.2$, suggesting an enhanced possibility of first order ejective quenching in the central regions of the galaxy and highlighting the importance of geometrical assumptions. We note that for a spherically symmetric thin shell geometry at 1 kpc, the two ranges of outflow rates presented here reflect the lower and upper limits of the model.

It is unclear whether it is a radial dependence or the average galaxy properties which drive the main trends seen in Figure 4.5. In fact, by comparing galaxy properties associated with each radial bin to the evolution of the mass outflow rate, we find the latter quantity follows most closely the evolution of Σ_{SFR} and Σ_* . This is shown in Figure 4.7, where we plot the normalised evolution of galaxy properties and the mass outflow rate. However, from these stacks alone it is difficult to determine whether the selected properties or the radial dependence are the primary regulators of the outflows, given that intrinsic correlations exist between galaxy radius and the chosen properties. We further inspect the correlation of (or lack of) the NaD EW and outflow properties with global galaxy properties in Section 4.6.

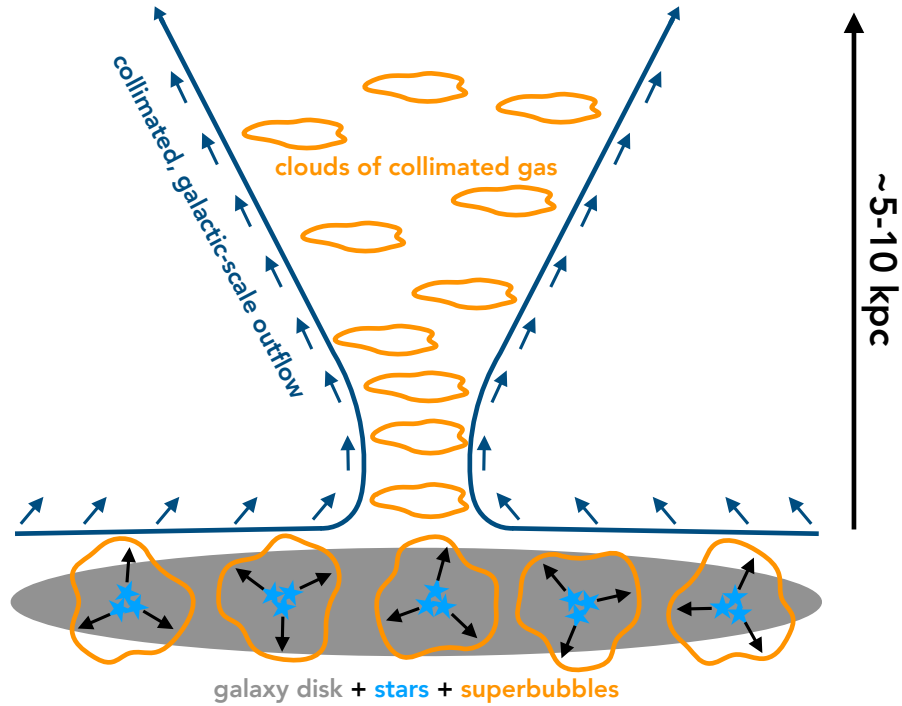


Figure 4.6. A simplified schematic of the collimation of a galactic-scale outflow from “wind bubbles”, generated close to the galaxy disk plane. Clusters of stars in the disk generate energy and momentum from stellar winds, supernovae and high energy photons, which likely superimpose and entrain ISM gas. The energy and momentum bubbles, as well as gas, eventually collimate at larger distances from the disk to form a large-scale outflow which exits perpendicularly to the disk.

4.5 The Resolved $\Sigma_{\text{SFR}}-\Sigma_{M_*}$ Plane

Since the discovery of the galaxy Main Sequence (MS) and the development of basic frameworks to describe a galaxy’s position relative to it, much work has gone into determining the prevalence and influence of outflows relative to the MS (e.g., [Chen et al. 2010](#); [Rubin et al. 2014](#); [Cicone et al. 2016](#); [Concas et al. 2017](#); [Roberts-Borsani & Saintonge 2019](#)). The arrival of large IFU surveys such as MaNGA, SAMI and CALIFA, has also revealed a resolved MS ([Sánchez et al. 2013](#); [Cano-Díaz et al. 2016](#); [González Delgado et al. 2016](#); [Abdurro’uf & Akiyama 2017](#); [Hsieh et al. 2017](#); [Maragkoudakis et al. 2017](#)), indicative of a link between small scale processes and the integrated properties of galaxies. As such, it is interesting to look at the prevalence and properties of outflows over such a resolved sequence. We therefore present a stacked analysis over the local MS in Figure 4.8, using spaxels from our sample of outflow galaxies. Here, the mean stacks and properties are

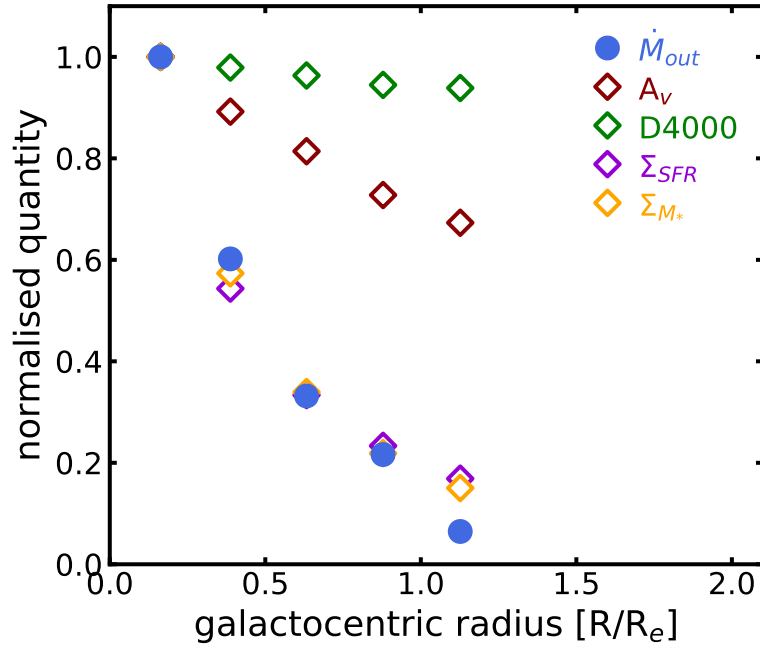


Figure 4.7. The normalised evolution of the geometry-independent mass outflow rate compared to several key galaxy properties (i.e., Σ_{SFR} , Σ_{M_*} , A_V , $D(4000)$). Each quantity is normalised by the maximum value across galaxy radius. The radial evolution of the normalised mass outflow rate is most closely aligned with the normalised evolution of Σ_{SFR} and Σ_{M_*} .

taken over all spaxels in a bin, rather than over the galaxies going into the stack. From the left panel of Figure 4.8, we find a very similar trend of outflow prevalence and strength to what is found in integrated analyses: outflows are found predominantly in regions of high Σ_{SFR} and Σ_{M_*} , with increasing strength (as traced by the outflow EW and mass outflow rates) higher up the MS. Here we find that detections span a Σ_* range of $7.5 < \log \Sigma_*/M_\odot \text{kpc}^{-2} < 9.5$ and Σ_{SFR} of $-2 < \log \Sigma_{\text{SFR}}/M_\odot \text{yr}^{-1} \text{kpc}^{-2} < 0$, in agreement with limits found in Section 3.4.2 for neutral gas outflows of similar galaxies.

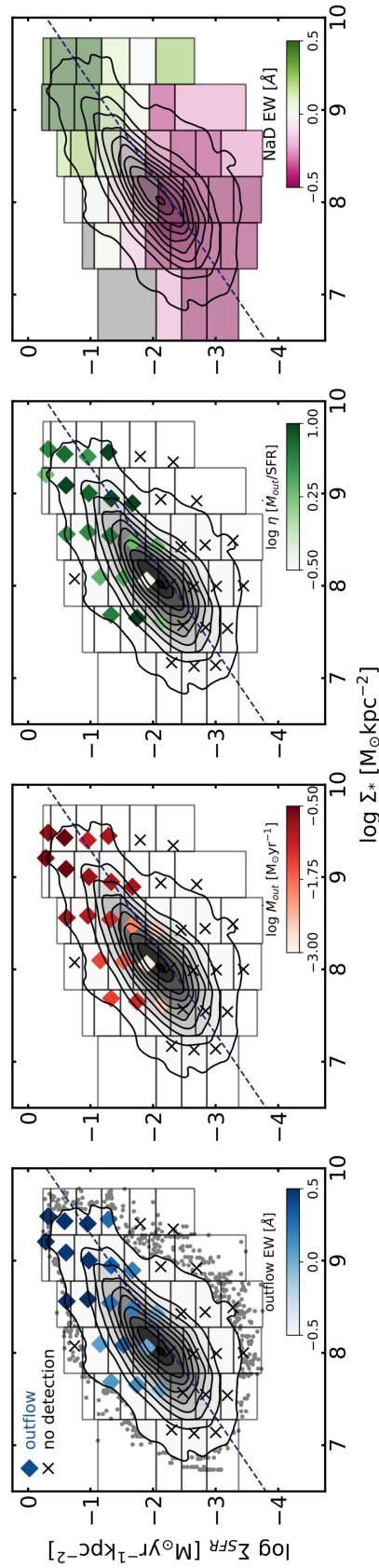


Figure 4.8. The resolved $\Sigma_{\text{SFR}}\text{-}\Sigma_{M^*}$ plane of star-forming MaNGA galaxies with stacked bin limits (gray lines) and outflow detections (diamonds) overlaid. Non-detections are marked by a cross and detections are colour-coded according to the mean outflow EW (left panel), neutral gas mass outflow rate (middle left panel), and local mass loading factor (middle right panel). Outflows are prevalent in regions of high star formation activity and stellar mass surface density, with an EW and mass outflow rate that follows a similar pattern. The right panel is the same as the other panels except colour-coded by the total NaD EW, as measured from the stacked spectrum. The dashed navy line indicates the resolved MS relation for H II regions of star-forming galaxies from [Hsieh et al. \(2017\)](#).

Additionally, we also investigate the evolution of the outflow EW, mass loss rate and mass loading factor (shown by the colour-coding of detections in the first three panels of Figure 4.8). We find the first two quantities correlate positively with the outflow’s position along the resolved MS: spaxels higher up the MS produce stronger outflows with significantly larger EWs and mass loss rates, consistent with the notion that more intense star formation activity drives stronger outflows. The mass outflow rates range from $-3 \lesssim \log \dot{M}_{\text{out}}/M_{\odot}\text{yr}^{-1} \lesssim 0$ with HI column densities $18.6 < \log N(\text{H})/\text{cm}^{-2} < 22.0$ and median values of $\log \dot{M}_{\text{out}} \sim -1.0 M_{\odot}\text{yr}^{-1}$ and $\log N(\text{H}) \sim 20.32 \text{ cm}^{-2}$, respectively. However, the picture is not as clear cut for the mass loading factor, which does not appear to display significant evolution as a function of MS position (although there is tentative indication of higher factors further up the MS). The values here range from $-0.4 \lesssim \log \eta \lesssim 1.5$, with a median mass loading factor of $\log \eta \sim 0.6$.

From the right panel of Figure 4.8, we find that outflows detections are found predominantly in absorption and the lower limit of their detections corresponds to regions of reduced ISM absorption (or P-Cygni profiles), where the NaD profile transitions into emission. Profiles of pure emission generally do not display any outflow signatures. The total NaD profile also shows a similar transition across the plane as observed in the SFR- M_{*} plane with $3''$ fibers (Concas et al. 2017; Roberts-Borsani & Saintonge 2019): absorption at high stellar mass and SFRs transits to emission at low values of the same quantities. However, the dichotomy of the two profile types with $\log \Sigma_{\text{SFR}}$ is more evident than with $\log \Sigma_{*}$, $\log \text{SFR}$, or $\log M_{*}$, and as such likely assigns Σ_{SFR} as the main regulator of the ISM profile.

It is important to note that the evolution in outflow prevalence and properties seen over the local $\Sigma_{\text{SFR}}-\Sigma_{*}$ plane also corresponds to the same radial evolutions seen in Figure 4.7, given that the evolution of these particular galaxy properties also evolve with galaxy radius (i.e., both Σ_{SFR} and Σ_{*} decrease with increasing radius). Thus, the strongest outflow detections are found predominantly in the central regions of galaxies.

4.6 Outflow Correlations with Galaxy Properties

As hinted at by Figure 4.7, the evolution of outflow properties is likely tied to one or several underlying galaxy properties. This has often been investigated for integrated galaxy quantities (such as total SFR, stellar mass and Σ_{SFR} ; Chen et al. 2010), however such

investigations generally rely on single or stacked spectra of the central regions of a galaxy, making the isolation of the regions of interest challenging.

However, due to the power of IFU spectroscopy, we are in the fortunate position of being able to identify and separate individual spaxels (and therefore kpc-scale regions) in individual galaxies corresponding to a specific range of a given global galaxy property, thereby removing many of the intrinsic correlations that exist between a given property and e.g., galaxy radius. We therefore perform this analysis for key galaxy quantities such as Σ_{SFR} , Σ_* , specific SFR (sSFR), A_V , and D(4000), which for each galaxy we divide into galactocentric radial bins in order to eliminate underlying correlations between properties, and stack over all outflow galaxies. We present this analysis in Figure 4.9. Our choice of galaxy properties is motivated in part due to the availability of the tracers from optical spectra, but more importantly due to their inferred influence on outflows from integrated studies: star formation-related quantities are invoked as the main drivers for outflows in the absence of an AGN (e.g., Heckman et al. 2000; Veilleux et al. 2005; Chen et al. 2010), whilst both stellar mass and dust are influential in regulating the escaping potential of outflows and the survivability of NaD respectively. The D(4000) break traces the age of the underlying stellar populations, and as such can provide a first order indication as to which stellar populations may be driving the outflowing gas.

We begin by noting that outflow detections are detected over a large range in each galaxy property. The ranges span $-2.25 \lesssim \log \Sigma_{\text{SFR}} / \text{M}_{\odot} \text{yr}^{-1} \text{kpc}^{-2} \lesssim -0.25$, $-11 \lesssim \log \text{sSFR} / \text{yr} \lesssim -9$, $7.5 \lesssim \log \Sigma_* / \text{M}_{\odot} \text{kpc}^{-2} \lesssim 9.5$, $1.2 \lesssim \text{D}(4000) \lesssim 2.0$, and $0 \lesssim A_V / \text{mag} \lesssim 3$, consistent with ranges presented in all of our stacked analyses so far. Most of the detections are found in the inner radii, with the detection rate falling rapidly as a function of radius.

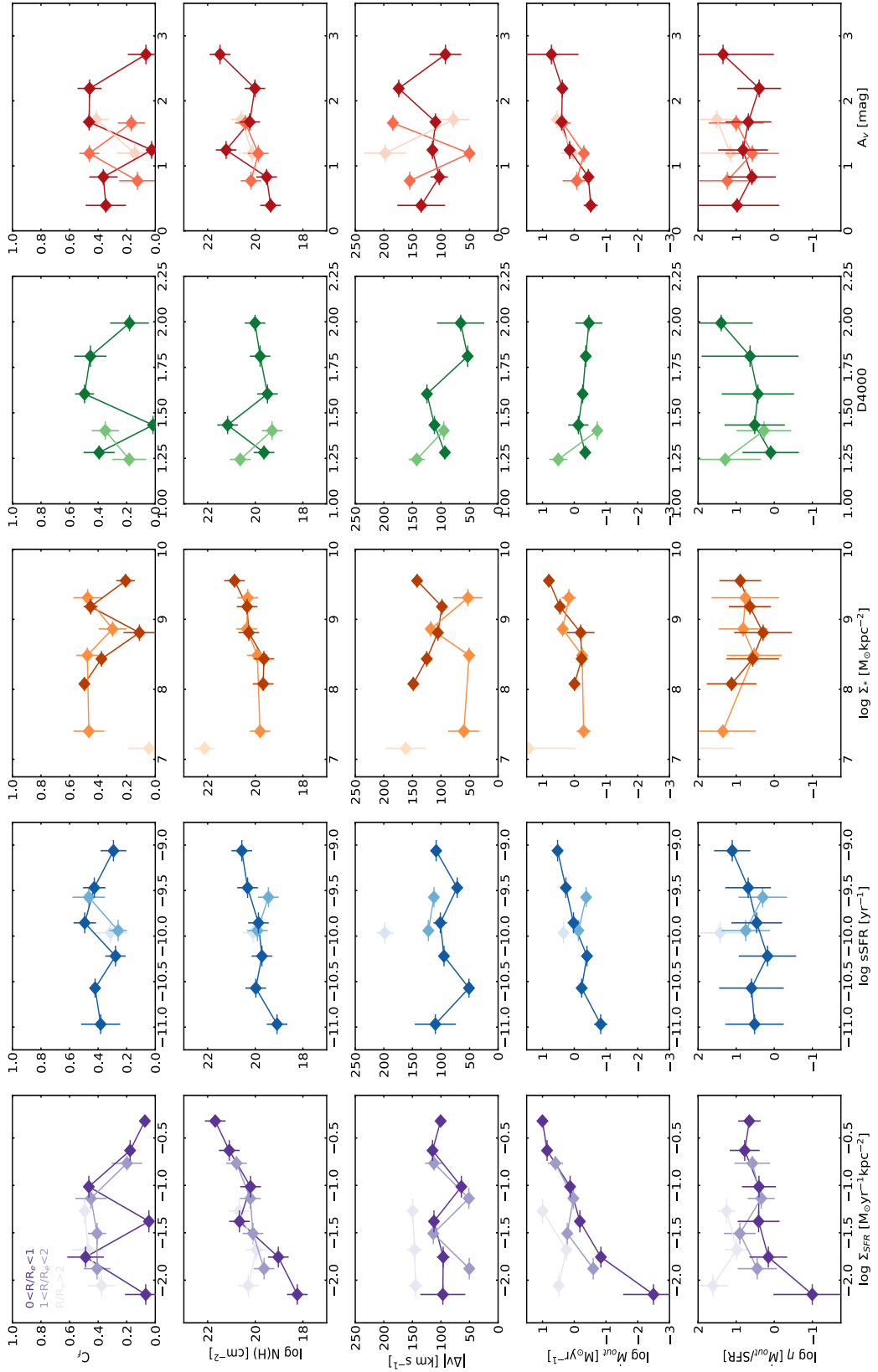


Figure 4.9. The correlations between outflow properties (C_f , $N(\text{H})$, Δv , \dot{M}_{out} and η) as a function of galaxy properties as shown by stacks of individual spaxels within a given property range. The main trends occur with star-forming quantities, although the strongest correlation is seen with Σ_{SFR} .

Next, we inspect the local covering fraction of the gas, C_f , which is an estimate of its clumpiness; low values indicate that the gas is clumpy and therefore not covering much of the background continuum source, whilst values closer to unity indicate a more diffuse component. For SDSS-selected galaxies, small values ($C_f < 0.5$) for NaD gas have been found, and this is attributed to the low ionisation potential (5.1 eV) of the atom, which requires significant self- and dust-shielding to survive. As such, a more compact and clumpy nature ensures it can survive harsher environments (e.g., from shocks and hard stellar radiation fields). We find significant scatter in the covering fraction of the gas spanning the full range of allowed values, with no clear evolution as a function of galaxy property or galaxy radius. Given that these stacks are constructed over a variety of radii and the estimates of C_f are velocity-independent measurements, the scatter is perhaps not surprising.

We also look at the column density of the outflowing hydrogen gas, since it is interesting to determine where the densest regions of the outflows reside. We find clear, positive correlations of the column density with $\log \Sigma_{\text{SFR}}$, $\log \text{sSFR}$ and dust, with a minor correlation found with $\log \Sigma_*$ and no correlation with the D(4000) break. The first three quantities all strongly correlate with the amount of cold gas present and the star formation activity of galaxy regions, therefore such trends are perhaps not surprising: higher concentrations of gas induce more star formation which produce stronger outflows which expel more gas. This is particularly evident from the strongest correlation with $\log \Sigma_{\text{SFR}}$ which spans 4 dex in column density and suggests the densest parts of the outflowing gas correlate directly with the densest regions of star formation and cold gas.

In measuring the blueshift of absorbed gas, we report absolute outflow velocities of $\sim 50\text{-}200 \text{ km s}^{-1}$, similar to those reported for normal galaxies at $z \approx 0$ (Chen et al. 2010; Sugahara et al. 2017; Roberts-Borsani & Saintonge 2019; Rodríguez del Pino et al. 2019), however we observe essentially no correlations of the outflow velocity with any of the chosen galaxy properties. The evolution of the outflow velocity with galaxy properties and redshift has long been debated, with some studies claiming a velocity evolution over SFR (Sugahara et al. 2017) and others showing little to no evolution (Martin 2005; Chen et al. 2010; Roberts-Borsani & Saintonge 2019; Rodríguez del Pino et al. 2019). Such debate is also subject to the manner of measuring outflow velocities: for instance, in stacked spectra at $z \sim 0$, Sugahara et al. (2017) find convincing evidence for a velocity evolution across SFR when measured at the maximal blueshifted velocity of the absorption, however

this evolution disappears when using the central velocity of the outflow, as shown here. Evolution in outflow velocity is also found to be more prominent at higher redshifts, with larger values of SFR and Σ_{SFR} found to correlate with enhanced outflow velocities traced by neutral and ionised gas at $z \sim 2$ (Sugahara et al. 2017; Davies et al. 2019a). As such, our results are in agreement with outflow velocities found in normal galaxies at $z \sim 0$, but in contrast with what is found by studies at $z \sim 2$.

Perhaps the most important quantities to look at, however, are the evolution of the (geometry-independent) mass outflow rate and mass loading factor as a function of galaxy property. Here, we are able to directly link the kpc-scale galaxy properties to the outflow by selecting spaxels with relevant galaxy properties. Using Equation 4.1, we find $\log \dot{M}_{\text{out}}$ correlates most strongly (based on the slope and range of the observed correlations) with quantities most closely related to star formation activity, however the strongest correlation is associated with $\log \Sigma_{\text{SFR}}$: the mass outflow rate increases rapidly from $\log \dot{M}_{\text{out}} \sim -3$ at $\log \Sigma_{\text{SFR}} < -2.25$ to $\log \dot{M}_{\text{out}} \sim 1$ at $\log \Sigma_{\text{SFR}} \sim 0.25$. Milder correlations are seen with $\log \text{sSFR}$, $\log \Sigma_*$, and A_V , likely due to their own correlations with $\log \Sigma_{\text{SFR}}$, although these all have both shallower slopes and probe smaller ranges.

Finally, we also show that the mass loading factor of the outflows again correlates most strongly with star formation activity, with values ranging $-1 \lesssim \log \eta \lesssim 1$ in the central regions, and generally following the evolution of the mass outflow rate. These values and trends are similar to those found for outflowing ionised gas in star formation-driven outflows by (Rodríguez del Pino et al. 2019) with MaNGA DR2, who also report loading factors of $\eta \lesssim 1$. We are also in partial agreement with reports from Davies et al. (2019a), who determine strong evolution between η and Σ_{SFR} from ionised gas at $z \sim 2$: we observe a virtually identical slope and report similar values of the loading factor, although the overlap in data is small.

Thus, from this analysis we can infer that (i) the mass outflow rate is driven primarily by the evolution of $\log \Sigma_{\text{SFR}}$ and (ii) the loading factor is most closely tied to the evolution of the mass outflow rate (and hence also $\log \Sigma_{\text{SFR}}$), and (iii) that in the absence of extreme AGN, outflows are predominantly driven by the star formation activity in galaxies, traced most strongly by its surface density.

We also look at the evolution of both the NaD ISM EW and the blueshift absorption EW as a function of galaxy properties, shown in Figure 4.10.

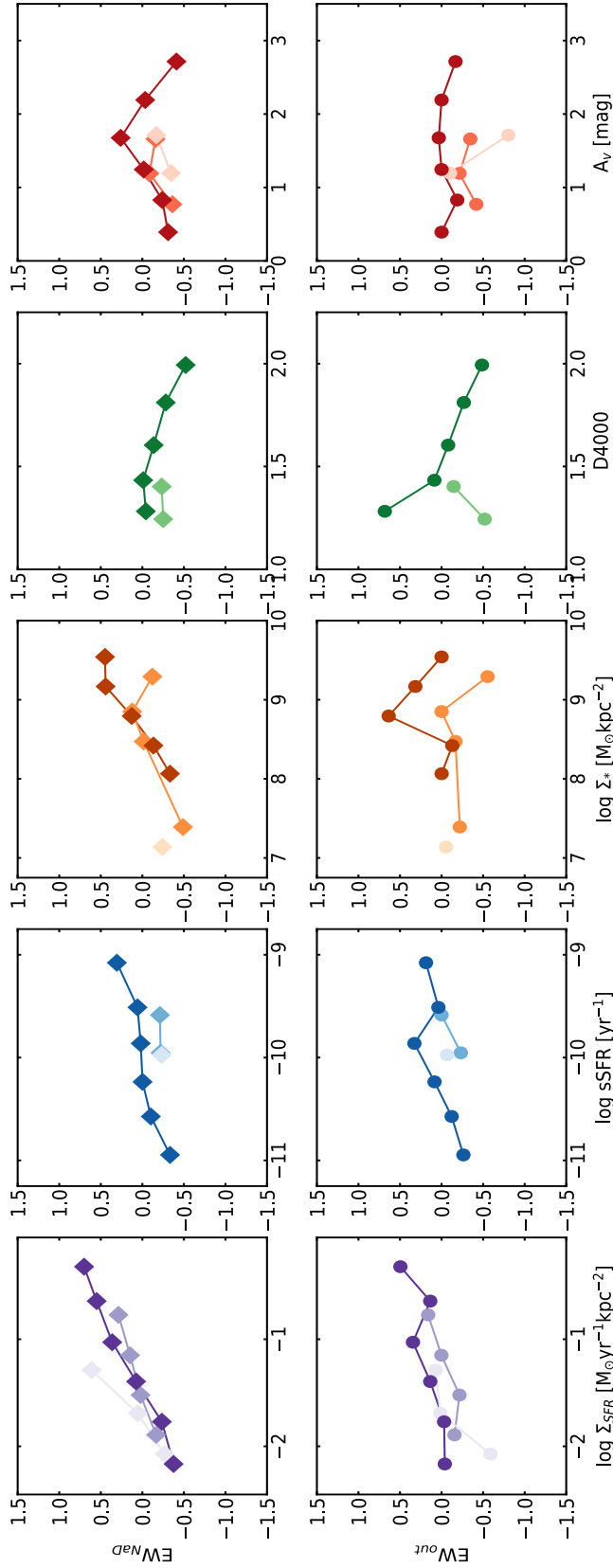


Figure 4.10. The evolution of the Nad ISM EW (top row) and blueshifted absorption EW (bottom row) as a function of Σ_{SFR} , $sSFR$, Σ_{*} , $D(4000)$ and A_V . The colour scheme follows that of Figure 4.9.

For the NaD ISM EW, strong positive trends become immediately clear, with the strongest trends again occurring with quantities related to star formation (Σ_{SFR} , sSFR , Σ_*). Curiously, no significant trends are found with $D(4000)$ or dust, given that the latter property is thought to regulate (in part) the survivability of NaD in harsh environments. Once again, the strongest of the trends is found with Σ_{SFR} and we interpret the increase EW and NaD absorption as being due to the increased presence of cold gas with higher levels of Σ_{SFR} . We also note that the majority of NaD is found in absorption, particularly at higher values of Σ_{SFR} , sSFR , Σ_* and A_V , but transforms into net emission at lower values. Interestingly, the transition of NaD from absorption to emission in stacks of Σ_{SFR} occurs right around our lower detection limit at $\sim 0.01 \text{ M}_{\odot} \text{ yr}^{-1} \text{ kpc}^{-2}$ and consistent with what we find in the right panel of Figure 4.8. The evolution of the outflow EW as traced by blueshifted absorption is similar but less clear than what we observe for the entire ISM line: positive trends are found with Σ_{SFR} and sSFR , with higher values corresponding to stronger outflowing gas, whilst Σ_* , $D(4000)$ and A_V show no notable trends. Such findings are consistent with the conclusions derived above and support the notion that quantities related to star formation are the main regulators of both the NaD EW and outflow EW.

4.7 The Impact of Outflows on HI Gas Reservoirs

4.7.1 HI Observations

One of the most important questions in outflow studies is whether they have some impact on the cold atomic and molecular gas reservoirs of their host galaxies (i.e., can they quench the galaxy?). So far, we have inferred this from derivations of a neutral gas mass loading factor. However, an alternate approach is to examine the effect of outflows on the integrated HI contents of their hosts. To do this, we make use of HI 21 cm single-dish observations of galaxies in our outflow+non-detection samples with the Green Bank (GBT) and Arecibo Telescopes. The GBT observations form part of the HI-MaNGA (Masters et al. 2019) program aimed at carrying out follow up HI observations for MaNGA galaxies and the DR1 contains 331 galaxy observations to date. Of these, 33 are matched to our selected sample, however we also add an extra 53 galaxies which were observed after the data release (Karen Masters and Dave Stark, private communication), bringing the MaNGA GBT observations used here up to 86 galaxies. Additionally, some of our sample

also overlaps with observations from the blind ALFALFA survey (Haynes et al. 2018) conducted with the Arecibo telescope. 55 galaxies from our sample are matched to ALFALFA and as such we are able to compile HI observations for a total of 141 galaxies in our combined outflow and non-detection samples, of which 34 fall under the outflow category and 107 in the non-detection category. We refer to this as our MaNGA-HI sample.

4.7.2 Removing the Effects of Confusion and Baseline Issues

Spectroscopic confusion in radio observations from single-dish facilities is an important concern, and in particular for stacking and outflow studies, since real signal from nearby galaxies at similar velocities can mimic the signatures of outflowing gas.

Although the rate of spectroscopic confusion is generally small (less than $\sim 15\%$ for the ALFALFA $\alpha.40$ data release; Jones et al. 2015), given the large beam sizes of the facilities used to obtain the HI data in this study (FWHM $\approx 9'$ and FWHM $\approx 3.5'$ at 21cm for the GBT and Arecibo, respectively) and the potential for false-positive outflow detections, this remains a particularly important consideration.

Therefore, to ensure none of our spectra suffer from confusion, we use the MPA-JHU catalog to identify objects within $3\times$ FWHM of the beam used to observe each of our 141 HI galaxies (but further than $10''$ away from the target galaxy). Combining this with a velocity cut of ± 500 km s $^{-1}$ from the target source (relative to the HI velocity of the target if detected, or optical redshift in the case of non-detections), we flag 78/141 of our objects as containing one or more additional optical galaxies over the search area and potentially subject to confusion. The criteria used here are extremely conservative, however we believe a rigorous approach to avoid false-positive outflow detections is crucial, and given that $\sim 80\%$ of the contaminating sources fall outside the FWHM of the beam (where the sensitivity drops from 50% to effectively 0%) combining the analysis with the beam sensitivity (see below) is likely to decrease this number significantly.

We next estimate the HI gas masses of the contaminants, using gas fraction scaling relations (Catinella et al. 2018), and in particular the relation between $\log M_{HI}/M_*$ and \log sSFR. However, given that the sensitivity of the beam drops dramatically past its FWHM and we probe an area a factor of 3 larger (effectively spanning the full sensitivity of the beam) we multiply the derived HI masses by the beam sensitivity at their separation in order to obtain an effective M_{HI} and compare this to the target's HI gas mass. If a given contaminant contributes less than 10% to the target's HI mass (in the case of a non-

detection we assume upper limits as calculated in [Masters et al. 2019](#)), it is considered to have a negligible effect on the spectrum ([Jones et al. 2015](#)). We flag a galaxy as confused if it has one or more surrounding contaminants (within the velocity cut defined above) that contribute $\geq 10\%$ of the target’s measured HI gas mass. 32/141 of our MaNGA-HI sample are flagged as confused and discarded from the analysis.

A second important consideration in our stacking analysis is the possible effects resulting from badly removed baselines, which can result in artificially low or high fluxes over various regions of the spectrum. To ensure our spectra are free from such effects, we visually inspect each of the remaining 109 galaxies that are free from confusion and determine whether a baseline correction is required. 6 galaxies are found to have major baseline issues, with an additional 7 found with minor issues. For these galaxies, we fit the baseline-unsubtracted spectrum with a polynomial (generally of 3rd or 4th order) to the baseline and subtract this from the spectrum. During this procedure we consider only the regions within $\pm 1000 \text{ km s}^{-1}$ of the target galaxy velocity, since fitting an accurate baseline across the entire spectrum can be challenging and our region of interest is largely confined to those velocity limits. Only 2 galaxies have major baseline issues which we are unable to correct for and an additional target contains obvious spectral artefacts, and are therefore discarded from the analysis, leaving a total of 106 galaxies free from confusion and baseline issues, which we refer to as our MaNGA-HI_{corr} sample.

4.7.3 Control Sample and Stacking Procedure

In this analysis, we wish to determine whether there is significant difference between the HI gas reservoirs of galaxies with NaD outflows and those without. Thus, for each of the outflow galaxies in our MaNGA-HI_{corr} sample, we select a control galaxy without NaD outflows which is matched in its position on the SFR- M_* plane and in inclination. We allow a difference of ± 0.2 dex in log SFR and log M_* , as well as 20 degrees in inclination. Of our MaNGA-HI_{corr} sample, we can successfully identify control galaxies for 17 of our outflow galaxies.

In order to construct mean HI spectra, we stack in “gas fraction units”, that is to say we multiply each spectrum by the standard conversion factors necessary to convert to an HI gas mass, described in Equation 4.6 and divide by the stellar mass of the galaxy.

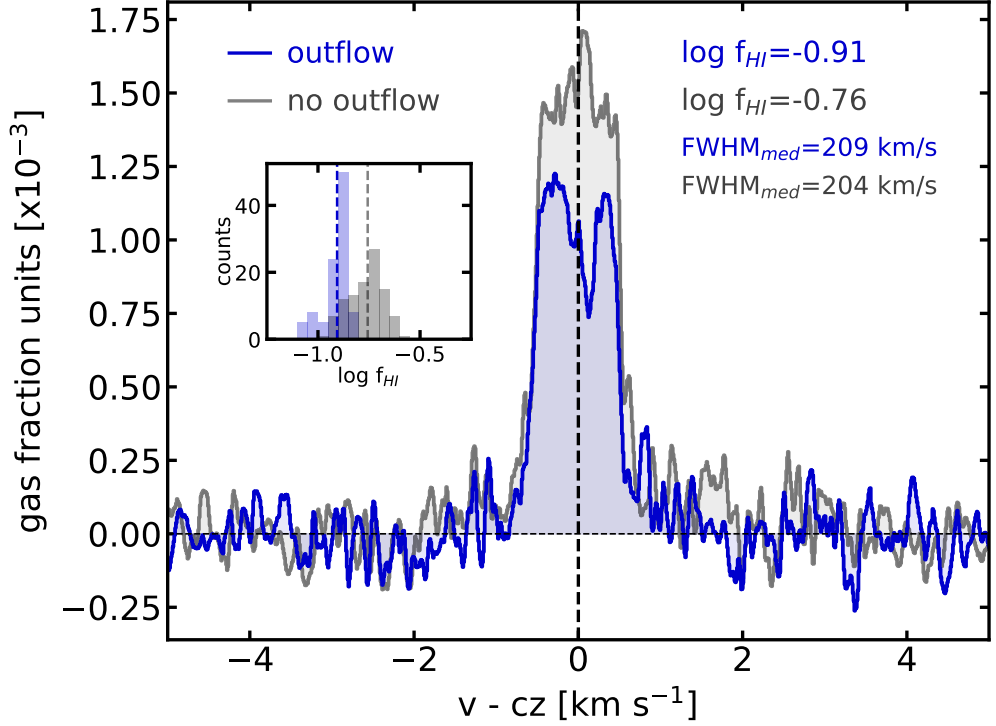


Figure 4.11. The mean velocity normalised, gas fraction spectra of galaxies with signatures of optical outflows (blue) and those without (gray) and their reported gas fractions and median FWHM. The stacks are created via a Monte Carlo approach of 14 outflow galaxies and a control sample of non-detection galaxies. The presence of NaD-selected outflows does not appear to significantly influence the HI gas reservoirs of their host galaxies compared to their non-detection counterparts. The inset plot shows a histogram of the average gas fraction of a given iteration going into the final stack.

$$M_{\text{HI}}/M_{\odot} = 2.356 \times 10^5 \left(\frac{D}{\text{Mpc}} \right)^2 \left(\frac{F_{\text{HI}}}{\text{Jy}} \right) \quad (4.6)$$

All scaled spectra are first shifted to the rest frame prior to being normalised by the FWHM of the spectrum, then interpolated over a common velocity grid, and finally added to the stack irrespective of whether they display a clear HI detection or not. The stack is then averaged to produce a mean gas fraction spectrum. We further adopt a Monte Carlo approach and repeat this process 100 times, each time with a random sample of 14 outflow galaxies ($\sim 80\%$ of our outflow HI sample) and a different control sample, to ensure our results are not biased by a particular selection of galaxies. The final spectra are then taken as the mean over the 100 iterations and shown in Figure 4.11.

The resulting velocity-normalised spectra display significant differences between them-

selves, with outflow galaxies displaying reduced fluxes compared to their non-detection counterparts, suggestive of non-negligible variation in the H I gas mass fractions. The mean FWHM is 209 km s^{-1} for the outflow galaxies and 205 km s^{-1} for the non-detection galaxies, with integrated H I gas fractions of $\log f_{\text{HI}} = -0.906 \pm 0.001$ and $\log f_{\text{HI}} = -0.757 \pm 0.001$, respectively. We also present an inset plot in Figure 4.11 displaying the distributions of gas fractions of the individual galaxies going into the stack, over all Monte Carlo iterations. The two distributions are distinctly offset, with means of $\log f_{\text{HI}} = -0.91$ and $\log f_{\text{HI}} = -0.76$ (outflow detections and non-detections, respectively) consistent with the integrated spectra, and spreads characterised by standard deviations of $\log \sigma_{f_{\text{HI}}} \approx -1.79$ (outflow detections) and $\log \sigma_{f_{\text{HI}}} \approx -1.47$ (non-detections). The two distributions reinforce the apparent lack of similarity between the two stacked spectra and the combination of the two is suggestive of a non-negligible difference between the H I gas fractions of the outflow-selected galaxies and those without outflows. Although causality is challenging to establish, we have been careful to match the outflow-detection and non-detection galaxies in several key properties that could influence the observed H I gas fraction, to ensure the primary difference is the detection of an optical outflow. With this in mind, it would appear the outflows are able to eject non-negligible amounts of neutral H I gas from the galaxy centre (hence the suppression of flux at central velocities) - either now or in the past if they are relics - although this is unlikely to be enough to quench the entire galaxy purely from ejective arguments. Furthermore, the higher H I gas fractions at virtually all velocities in the non-detection stack are suggestive of some gas replenishment and could provide indirect evidence for the interplay between outflows and inflows - i.e., a galactic fountain scenario. However, confirming such a scenario is beyond the capabilities of the current data sets.

4.8 Discussion

4.8.1 Strong Correlations With Σ_{SFR}

Throughout each of the previous Sections, we have seen that Σ_{SFR} plays a key role in regulating the output of outflows in normal galaxies at $z \sim 0$. Whilst other quantities (e.g., sSFR, Σ_* and A_V) also correlate with outflow quantities, these appear secondary to the dominant correlations found with Σ_{SFR} and likely exist due to their own correlations with Σ_{SFR} . Similar correlations have also been observed in other studies, both at low

and high redshifts (Chen et al. 2010; Newman et al. 2012; Roberts-Borsani & Saintonge 2019; Davies et al. 2019a). For galaxies at $z \sim 2$, Newman et al. (2012) suggested the possibility of a critical “blow out” Σ_{SFR} , where star formation feedback is able to generate enough pressure to perpendicularly break out of the dense gas of the disk in the form of a momentum-driven outflow. By assuming a baryon dominated galaxy disk that sits in pressure equilibrium, one can test this via simple assumptions that equate the weight of the disk gas to the pressure exerted outward by star formation feedback, and determine a minimum Σ_{SFR} threshold above which pressure from the feedback exceeds the weight of the gas.

Following Equations 1 and 7 from Ostriker & Shetty (2011), the weight of the disk can be expressed as

$$w = \frac{\pi G \Sigma_{\text{gas}}^2}{2}, \quad (4.7)$$

where Σ_{gas} is the cold gas density and G is the gravitational constant. The vertical momentum flux injected into the ISM by stellar feedback can be described as

$$P = \frac{p_*}{4m_*} \Sigma_{\text{SFR}}, \quad (4.8)$$

where (p_*/m_*) is the mean radial momentum injected into the ISM per unit mass of stars formed. As described by Equation 2 of Newman et al. (2012), one can rearrange these two equations and insert a dependence on gas fraction, f_g and stellar mass density to derive a minimum Σ_{SFR} threshold. This is particularly useful given that such quantities are well constrained for local, normal galaxies and by the data presented here. As such, our final equation is

$$\Sigma_{\text{SFR,thresh}} = \frac{\pi G f_g}{2(p_*/m_*)} \Sigma_*^2. \quad (4.9)$$

Assuming $f_g \sim 0.5$, $(p_*/m_*) \sim 1000 \text{ km s}^{-1}$ and $\Sigma_{\text{gas}} \sim 500\text{-}1000 \text{ M}_\odot \text{pc}^{-2}$ for their sample of normal SFGs at $z \sim 2$, Newman et al. (2012) found a critical threshold of $\sim 1 \text{ M}_\odot \text{yr}^{-1} \text{kpc}^{-2}$, in good agreement with their observations of ionised outflows. Assuming typical values ($f_g \sim 0.07$, $\Sigma_{\text{gas}} \sim 500$) for $z \sim 0$ normal SFGs, this threshold is lowered down to $\sim 0.1 \text{ M}_\odot \text{yr}^{-1} \text{kpc}^{-2}$, in agreement with the canonical value typically assumed as the minimum threshold to launch outflows (Heckman 2002; Veilleux et al. 2005; Ostriker &

Shetty 2011).

However, this threshold is typically observed in more turbulent, starburst systems and not in normal SFGs along the MS. Here, we expand on this by using values directly inferred from our MaNGA data set. Assuming a cold (molecular) gas fraction for high mass galaxies of $f_g \sim 0.04$ (Saintonge et al. 2017) and a mean, galaxy-wide mass surface density of $\log \Sigma_*/M_\odot \text{kpc}^{-2} \sim 8.24$ over all of our sample of 376 outflow+non-detection galaxies, we derive a critical threshold of $\Sigma_{\text{SFR}} \sim 0.01 M_\odot \text{yr}^{-1} \text{kpc}^{-2}$, in agreement with the results presented here and in Chapter 3. Additionally, we also note that the mean galaxy-wide Σ_{SFR} for our outflow selected galaxies is $\sim 0.02 M_\odot \text{yr}^{-1} \text{kpc}^{-2}$ whilst that of the non-detection galaxies is $\sim 0.01 M_\odot \text{yr}^{-1} \text{kpc}^{-2}$, sitting above and on our derived threshold, respectively.

For reference, we compare this value to the average SFR surface density of the Milky Way, which does not harbour a strong outflow. Assuming a SFR of $0.3 M_\odot \text{yr}^{-1}$ and a disk radius of 10 kpc (Olsen et al. 2015, and references therein), the area of the disk is 314kpc^2 and thus the SFR surface density is calculated to be $\Sigma_{\text{SFR}} \sim 0.001 M_\odot \text{yr}^{-1} \text{kpc}^{-2}$, an order of magnitude below our derived threshold.

4.8.2 Star Formation Histories of Outflow Hosts

Given that star formation quantities appear to be the primary drivers of our selected outflows, it is instructive to look at the star formation histories associated with the host galaxies which give rise to the outflows. As such, we use the $D_n(4000)$ and $H\delta_A$ indices provided by the MaNGA DAP, whose combination can reveal and distinguish between continuous and bursty star formation histories (Kauffmann et al. 2003a). The $D_n(4000)$ index measures the strength of the 4000\AA absorption break, which is a discontinuity in the optical spectrum of galaxies due to a variety of absorption features primarily arising from ionised metals in the atmospheres of stars. The index is linked to the age of the galaxy's stellar populations, given that young, hot stars ionise the surrounding metals, leading to a decreased opacity, whilst this is not the case for old, metal rich stars which display considerably more metal absorption. As such, a large 4000\AA break is indicative of older stellar populations, whilst a smaller one is indicative of younger stellar populations and a generally increasing break is found with time, as the stellar populations evolve. The index itself is measured as the ratio of the average continuum flux in regions blue and redward of the break, with several sources in the literature adopting differently-sized

regions (broad or narrow). The advantage of adopting a more narrow-sized region either side of the break is that the ratio is less sensitive to the effects of dust. As such, we use the narrow-band definition adopted by MaNGA (3850-3950 and 4000-4100 Å for the blue and red continuum bandpasses, respectively; [Westfall et al. 2019](#)).

H δ absorption at 4101 Å, on the other hand, arises from Balmer absorption in the atmospheres of stars and is an indication of the timing of a recent burst of star formation. Beginning with weak intrinsic absorption by hot O and B stars (characterised by short lifetimes of a few 10 Myrs) at the time of the burst, the absorption increases monotonically over time until ~ 300 Myr where it reaches its peak. The rapid increase and peak of the evolution is due to the deaths of the OB stars and domination of the optical light by late-B to early-F stars (characterised by longer lifetimes of $\lesssim 1$ Gyr). After the peak absorption at ~ 300 Myr, the H δ absorption rapidly decreases as the A and F stars die off. As such, H δ absorption is a measure of recent bursts of star formation that ended only ~ 0.1 -1 Gyr ([Kauffmann et al. 2003a](#)), and its index (H δ_A) is measured using a central bandpass marked by two pseudo-continuum bandpasses either side of the line (4083-4122, 4041-4079, 4128-4161 Å for the main, blue and red bandpasses, respectively; [Westfall et al. 2019](#)).

The two indices are largely independent of reddening effects, however metallicity can play a role in regulating them at later times. However, as shown by [Kauffmann et al. \(2003a\)](#), metallicity only becomes an important consideration for both tracers at ages of $>10^9$ years after a burst (corresponding to rough values of $D_n(4000) > 1.5$ and $H\delta_A < 3-4$).

To conduct our analysis, we use the average of the two tracers within a galactocentric radius of 1.5'' for each of our outflow and non-detection galaxies and compare these to results in the MPA-JHU catalog as measured by the SDSS DR7 3''-diameter fiber. The SDSS relations are taken by binning star-forming galaxies selected by the same MaNGA selection criteria described in Section 4.3 in steps of $\Delta D_n(4000) = 0.2$ and taking the mean and median values, before fitting a 5th order polynomial. We present these fits and data points in Figure 4.12.

We find our data points span a wide range over both indices and generally sit slightly above the mean (and median) SDSS relation, regardless of whether they are selected to have NaD outflows or not. For the outflow galaxies, $\sim 63\%$ of the data points sit above the mean SDSS relation and $\sim 37\%$ below, suggesting the majority of the data points have experience higher bursts of star formation in their recent past. However, comparing this to the non-detection data points, which reveal a slightly higher percentage

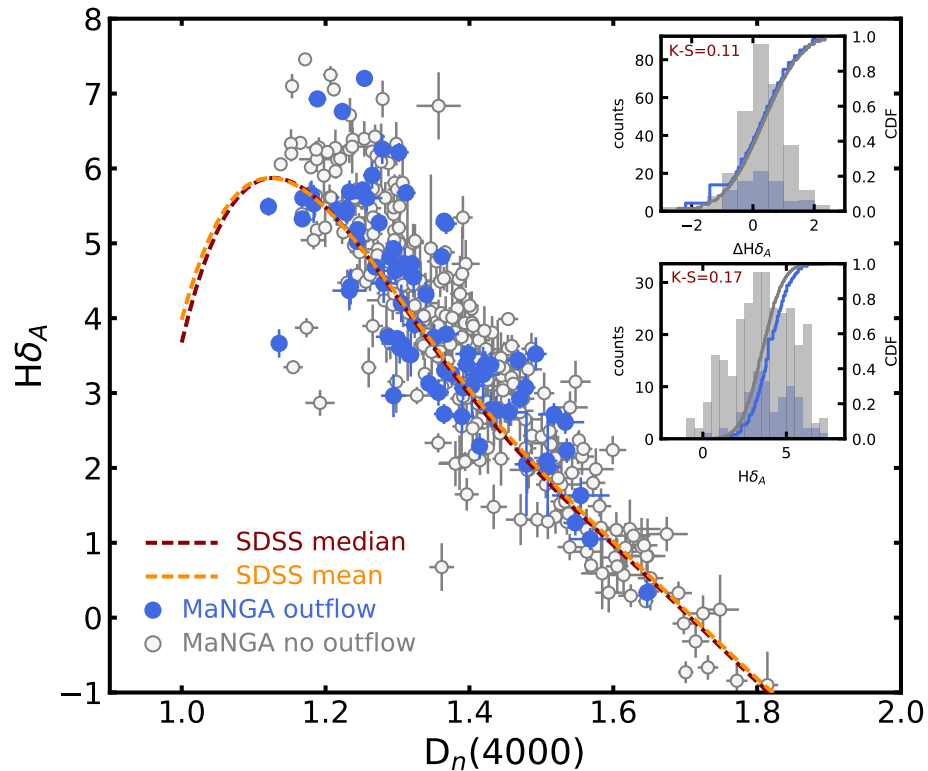


Figure 4.12. The star formation histories as traced by the $3''$ -diameter stacked $H\delta_A$ and $D_n(4000)$ indices of our MaNGA DR15 sample of galaxies shown to host NaD outflows (blue points) and those that do not (gray points). The error bars represent the standard deviation of values going into the stack for each galaxy. These points are compared to the mean (dashed orange line) and median (dashed red line) of SDSS values from the MPA-JHU catalogs. The inset plots show the distributions of $\Delta H\delta_A$ ($H\delta_{A,\text{MaNGA}} - H\delta_{A,\text{SDSS}}$; top) and $H\delta_A$ (bottom) for outflows (blue lines) and non-detections (gray lines), as well as their cumulative distribution functions and associated two-sample Kolmogorov-Smirnov statistic.

of $\sim 70\%$ sitting above the SDSS relation and $\sim 30\%$ sitting below, we find very similar values. This is in contrast to IFU observations of ionised tracers in edge-on galaxies found by [Ho et al. \(2016\)](#), who observe 80% of their outflow galaxies and 50% of their non-detection galaxies to sit above the median SDSS relation, albeit with sample sizes a factor of ~ 5 and ~ 12 smaller than those used here, respectively. We expand on this by comparing the distribution and mean values of our data points with the corresponding SDSS values ($\Delta H\delta_A = H\delta_{A, \text{MaNGA}} - H\delta_{A, \text{SDSS}}$), inferred from our fit relation. We present this in the top inset plot in Figure 4.12. The two distributions are very similar, with outflows characterised by a mean difference of 0.27 and standard deviation of 0.78, and non-detections with a mean of 0.32 and identical standard deviation. This is reinforced by near identical cumulative distribution functions (CDFs) and a low Kolmogorov-Smirnov statistic of 0.11, suggesting little difference between the two distributions and supporting the notion that both the outflow and non-detection samples have both experienced more recent star formation bursts compared to their SDSS counterparts. Such similarity extends to the two MaNGA samples, which we compare via their $H\delta_A$ distributions in the bottom inset plot in Figure 4.12. The two distributions are once again quite similar, with means of 4.02 and 3.56 and standard deviations of 1.42 and 1.82 for the outflow and non-detection samples, respectively. The two CDFs and a K-S statistic of 0.17 reinforce this similarity, albeit with a slight offset for outflow galaxies towards higher $H\delta_A$ values. We do note, however, that the distribution of the non-detection galaxies does fall down to $H\delta_A < 3-4$, where the tracer becomes uncertain due to metallicity effects, and the differences in mean values is attributed to this extension.

The similarities between the two MaNGA samples suggest both the outflow-detected and non-detected samples may be undergoing similar episodes of short bursts of more intense star formation that may be capable of launching outflows. If this is the case, both samples would display similar values of $H\delta_A$ and $D_n(4000)$, although one may also expect more of the non-detection galaxies to display signatures of optical outflows. Thus, the lack of (detected) outflow signatures in the non-detection sample is perhaps surprising. Following on from this, whilst our results are in agreement with the ionised gas results of [Ho et al. \(2016\)](#) in that the majority of our outflow data points lie above the mean SDSS relation, the considerable similarity between our larger distributions of outflow and non-detection samples is in contrast to theirs and suggests that (i) our two MaNGA samples may be undergoing similar episodes of star formation and (ii) that the timing of the last

burst of star formation may not a crucial parameter in driving (weak) NaD outflows.

4.9 Summary and Conclusions

We use the SDSS-IV/MaNGA DR15 data set and spectral stacking techniques to constrain the main kpc-scale properties that give rise to and regulate neutral outflows in star-forming galaxies. We use a sample of 405 $z \sim 0$ face on galaxies along the galaxy MS to determine the detection fraction, galactocentric radial profile and kpc-scale properties of galaxies with signatures of blueshifted NaD absorption. Our main findings can be summarised as follows:

- Out of 390 useable galaxies in our sample, the stacking of the central $0.25 R_e$ regions of the galaxies reveals 78 objects with signatures of outflowing gas, 14 objects with signatures of inflowing gas, and 298 galaxies with no significant detection of blue/redshifted gas. Galaxies with signatures of outflows and inflows show considerably higher values of Σ_* and Σ_{SFR} compared to their non-detection counterparts.
- Stacking as a function of deprojected galactocentric radius, we find detections of outflowing gas out to $1 R_e$ and compare these to detections as observed by an $3''$ -diameter fiber. Derivations of a mass outflow rate show a rapidly declining trend with galactocentric radius, with a range $-2.1 \lesssim \log \dot{M}_{\text{out}} \lesssim -0.9$ and best fit slope of -1.2 . A near identical trend is found with the mass loading factor, which also decreases as a function of galaxy radius, demonstrating that outflows are at their strongest in the central regions ($< 0.5 R_e$) of galaxies. The range of reported mass loading factors is $-1.8 \lesssim \log \eta \lesssim -0.4$, consistent with previously reported values in relatively normal galaxies at $z \sim 0$, and a slope of -1.4 . We provide prescriptions for both of these trends for use in simulations.
- Signatures of outflowing gas are found along and above the resolved star-forming MS, in parameter space above $\log \Sigma_* \gtrsim 7.5 \text{ M}_\odot \text{ kpc}^{-2}$ and $\log \Sigma_{\text{SFR}} \gtrsim -2 \text{ M}_\odot \text{ yr}^{-1} \text{ kpc}^{-2}$, similar to trends found along the galaxy MS. A comparison of the outflow EW, mass outflow rate and mass loading factor shows an increase in each of these values as one moves up the resolved MS, suggestive of stronger outflows in regions of increase

star formation activity.

- By stacking $>57,500$ individual spaxels associated with a variety of galaxy properties (Σ_{SFR} , Σ_* , specific SFR, $D(4000)$ and A_V), we find significant positive correlations between outflow properties (namely, gas column density, mass outflow rate and mass loading factor) and all of the aforementioned galaxy properties, except $D(4000)$. The strongest correlations are found with $\log \Sigma_{\text{SFR}}$ and we extend the lower limit of detections down to $\log \Sigma_{\text{SFR}} \approx -2 \text{ M}_{\odot}\text{yr}^{-1}\text{kpc}^{-2}$, about an order of magnitude lower than canonical values. We suggest that this is due to a minimum Σ_{SFR} threshold of $\Sigma_{\text{SFR}} \approx 0.01 \text{ M}_{\odot}\text{yr}^{-1}\text{kpc}^{-2}$ necessary for star formation feedback to break out of the dense gas in the disk.
- Using H I follow up observations of a sample of 106 MaNGA galaxies, we compare the cold H I gas reservoirs of galaxies selected to have NaD outflows to control samples of galaxies without NaD outflows, matched by their position in the SFR- M_* plane and inclination. Stacking the H I spectra, we find considerable differences between gas reservoirs of outflow and non-detection galaxies, suggesting the presence of optically-selected outflowing gas could potentially have some (minor) effect on the cold gas reservoirs, although combining this with our NaD mass loading factors strongly suggests that it is not enough for normal galaxies to be quenched by ejective feedback.
- Finally, we compare the star formation histories of our outflow and non-detection galaxies, using the central ($3''$) stacked $H\delta_A$ and $D_n(4000)$ indices. In comparing to average SDSS DR7 values, we find our sample of MaNGA galaxies have slightly elevated values of $H\delta_A$ compared to the SDSS galaxies for a given $D_n(4000)$, however, crucially we find virtually no difference between the values of our outflow sample and non-detection sample, suggesting that the timing since the last burst of star formation is not a crucial parameter in driving NaD outflows.

The arrival of large IFU surveys has greatly aided studies of local galaxy evolution and, in particular, studies of outflows. The kinematics and key properties of outflows and

their hosts are being studied in unprecedented detail and the small, kpc-scale processes that give rise to the large scale processes are being constrained. Here, we have used samples of star-forming galaxies and $>275,000$ galaxy resolved spectra to determine the prevalence of outflows on kpc-scales, their power and quenching potential across a variety of galaxy regions and properties and determined whether any significant impact on the HI gas reservoirs is seen. However, still missing are crucial constraints on the multiphase nature of outflows in normal, MS galaxies at $z \sim 0$ in order to infer their true quenching potential. Verifying this will require rest-frame optical, (sub)millimetre and radio spectra over statistically meaningful samples of galaxies with which to probe and compare the different outflowing gas phases, with the aim of deriving total mass loading factors over large regions of parameter space. Large surveys such as the SDSS, xCOLD GASS and ALFALFA provide unique opportunities to do this, whilst the arrival of optical and radio surveys such as MaNGA, SAMI and PHANGS will allow similar analyses to be achieved on resolved scales.

The Multiphase Nature of Outflows Using the MaNGA, xCOLD GASS, xGASS and ALFALFA Surveys

5.1 Introduction

Integrated optical and (sub)millimetre studies of neutral, ionised and molecular gas outflows have had significant success in determining the properties of outflows and their hosts in recent years (Veilleux et al. 2005; Rupke et al. 2005a; Chen et al. 2010; Feruglio et al. 2010; Martin et al. 2012; Cicone et al. 2014; Rubin et al. 2014; Fluetsch et al. 2018). The two primary purposes of such studies have been to determine the prevalence of outflows in galaxies and whether such feedback could extinguish the SF in the hosts via ejective feedback of the gas on large scales, thereby adding observational support to SF and AGN feedback as quenching mechanisms of galaxies.

In determining the prevalence of outflows, significant progress has been made via absorption- and emission-line studies of neutral and ionised gas in star-forming, (U)LIRG and AGN objects, both in the local Universe and extending out to $z \sim 2$ (Rupke et al.

2005b; Chen et al. 2010; Newman et al. 2012; Rubin et al. 2014; Cicone et al. 2016; Sarzi et al. 2016; Roberts-Borsani & Saintonge 2019; Davies et al. 2019a). Such studies, typically using NaD, MgII or FeII absorption and/or H α or [OIII] emission, have generally found outflows to reside in massive ($M_* > 10^{10} M_\odot$) galaxies either along or above the MS and correlating with the level of SF or AGN activity (Heckman et al. 2000; Chen et al. 2010; Newman et al. 2012). These results also hold on kpc-scales, with IFU observations revealing prominent outflow signatures in regions of high Σ_{SFR} and AGN luminosity (see the previous Chapter and e.g., Ho et al. 2016; López-Cobá et al. 2019; Rodríguez del Pino et al. 2019), and across redshift, with significant detection rates found out to $z \sim 2$ (Newman et al. 2012; Genzel et al. 2014; Sugahara et al. 2017; Davies et al. 2019b) most likely due to enhanced SF activity.

In addressing whether outflows can quench their host galaxies, however, the picture becomes considerably less clear. Studies of normal galaxies find outflow velocities and mass loss rates of several 100 km s^{-1} and a few $M_\odot \text{ yr}^{-1}$ (Rupke et al. 2005b; Chen et al. 2010; Martin et al. 2012; Roberts-Borsani & Saintonge 2019), respectively, and more extreme objects showing significantly more powerful outflows with velocities up to several 1000 km s^{-1} and mass loss rates $10\text{-}1000 M_\odot \text{ yr}^{-1}$ (Feruglio et al. 2010; Cicone et al. 2014; Rupke et al. 2017; Fluetsch et al. 2018). As such, the power of outflows also appears to scale with an increase in SF activity or AGN luminosity, and with redshift: normal star-forming galaxies display the weakest outflows at $z \sim 0$ (Chen et al. 2010; Cicone et al. 2016; Chisholm et al. 2017; Concas et al. 2017; Roberts-Borsani & Saintonge 2019; Fluetsch et al. 2018) but increase in strength towards early times (e.g., Newman et al. 2012; Genzel et al. 2014; Sugahara et al. 2017; Davies et al. 2019b). The mass loading factor (η) of outflows, defined as the mass outflow rate per SFR and used as a proxy for quenching, has generally been found to be near unity (Martin et al. 2012; Rubin et al. 2014; Roberts-Borsani & Saintonge 2019), with normal galaxies displaying generally low values and starburst or extreme AGN significantly enhancing those to higher values (Rupke et al. 2005b; Cazzoli et al. 2016; Cicone et al. 2014; Fluetsch et al. 2018), indicative of quenching. More direct evidence for quenching from outflows is perhaps seen in high- z AGN and QSOs, where the presence of ionised outflows is found to spatially anti-correlate with the presence of SF in the host galaxy (Cano-Díaz et al. 2012; Carniani et al. 2016, 2017).

Arguably the most important consideration, however, is what effect the outflows have on the cold atomic and molecular gas phase, which directly trace the fuel for SF. Inter-

ferometric and single dish observations of molecular gas as traced by low- J CO emission lines have aimed to determine whether outflows are capable of expelling significant fractions of the cold gas reservoirs of galaxies through the derivations of mass loss rates and η . Given such observations have been almost entirely exclusive to starburst and strong AGN/QSO due to the intrinsic faintness of outflow signatures on the molecular gas, values of $\eta > 1$ have generally been found, with increasing mass loss rates as a function of AGN luminosity (Cicone et al. 2014; Fiore et al. 2017; Fluetsch et al. 2018). As such, studies have shown AGN feedback can be an effective way to expell significant amounts of cold gas from galaxies and could provide a viable method for quenching (Feruglio et al. 2010; Cicone et al. 2012; Combes et al. 2013; Cicone et al. 2014; García-Burillo et al. 2014; Fiore et al. 2017; Fluetsch et al. 2018).

However, with the aim of gaining an unbiased and clear census of the quenching potential of outflows in galaxies, two major issues remain. The first is the tendency to observe extreme objects, which undoubtedly increase the chance of outflow detections due to enhanced kinematics, but are not representative of the general galaxy populations. The second is a comparison of mass outflow rates from single tracers across a variety of objects: given the varying assumptions that go towards converting column densities or luminosities of outflow tracers to mass outflow rates, comparisons across different tracers and objects can lead to systematic order of magnitude differences in mass outflow rates. Additionally, considering only one gas phase effectively provides only lower limits to the outflow rates, given other gas phases are not accounted for. One of the few studies attempting to address this was that by Fluetsch et al. (2018), who obtained a compilation of 45 starburst and AGN sources with observations of molecular, neutral and/or ionised gas tracers. For galaxies with overlapping observations, they derived the relative fractions of the different gas phases to the total mass outflow rate and provided scaling relations, determining that for AGN the outflowing molecular gas was at least a factor of 10 greater than the ionised gas, with this ratio increasing rapidly as a function of AGN luminosity. In contrast, the ratio of molecular-to-atomic gas remained constant at roughly unity over all AGN luminosities probed. Such a comparison allowed the authors to determine total mass loading factors and establish useful scaling relations with which to determine the plausibility of AGN quenching: whilst the contributions of molecular gas to the total outflow rates were important, they deemed that when considering all gas phases and entire galaxy gas contents, AGN may be able to quench the central regions of the galaxy but were unlikely to

clear galaxies of their entire gas reservoirs.

Despite the success of the study, conclusions for normal star-forming and starburst galaxies remain unclear. As such, in order to obtain an unbiased view of outflow quenching in galaxies, observations of the multiphase nature in representative samples of normal galaxies are crucial in order to obtain a total mass outflow rate consisting of the neutral, ionised and molecular gas phases. With this in mind, this Chapter aims to address this by determining the prevalence of cold (molecular and atomic) gas outflows in *normal* galaxies at $z \sim 0$ and determine the relative fractions of the gas phases contained in those outflows, with the aim of placing valuable constraints on the total mass loading factor.

5.2 Data Sets & Sample Definition

Here, we make use of the full xCOLD GASS (Saintonge et al. 2017), xGASS (Catinella et al. 2018) and ALFALFA $\alpha.100$ (Haynes et al. 2018) data sets, providing IRAM 30m CO(1-0) observations for 532 galaxies and Arecibo observations for a combined 32,111 galaxies, respectively. Observations of CO(1-0) at 3 mm allow us to trace directly the cold ($T \lesssim 100$ K) molecular gas used for SF in galaxies in the local Universe, whilst the H I 21cm line in emission traces more diffuse, cool ($T \lesssim 5,000$ K) hydrogen gas. We begin by defining sub-samples of galaxies which are most likely to host outflows, based on their position on the SFR- M_* plane and inclination. All xCOLD GASS and xGASS galaxies have SDSS optical counterparts and therefore catalogued stellar masses and SFRs, whilst 18,727/31,502 galaxies from ALFALFA also have SDSS counterparts within $10''$ of the target. Here we use the SFRs and stellar masses as measured by the MPA-JHU DR7 catalog. For both our CO and H I data, we select galaxies lying above the lower limit of the MS, as defined by Saintonge et al. (2016), with $M_* \geq 10^{10} M_\odot$, and inclinations less than or equal to 60° . Additionally, we select only star-forming galaxies based on a Kauffmann et al. (2003b) BPT cut (therefore rejecting AGN-dominated objects). Although results from Chapter 3 suggest a slightly lower inclination cut (i.e., $i < 50^\circ$), outflows have been observed with inclinations up to $i \sim 60^\circ$ and the modest sample size of xCOLD GASS motivates us to maximise our outflow sample where possible. The selection criteria we impose results in a sample of 69 star-forming galaxies from xCOLD GASS and 1,535 H I galaxies from ALFALFA and xGASS, and we refer to these as our parent samples. Additionally, we also make use of the 78 MaNGA DR15 IFU observations of galaxies

selected to show NaD-outflows in Section 4.4, with which we can constrain the neutral and ionised contributions to outflows from NaD absorption and ionised emission. The motivation for choosing MaNGA rather than SDSS optical observations is due to the fact that IFU observations allow us to probe higher S/N and larger regions of the galaxy, which we have shown to contain non-negligible contributions of outflowing gas that would be missed by a 3'' fiber (see Section 4.4.2).

As discussed in the previous Chapter, observations with single dish radio facilities can be prone to confusion. Whilst the IRAM 30m telescope has a modest FWHM \sim 22'' at 3 mm, the observations of H I used in this study are observed with the 3.8' Arecibo beam, significantly enhancing the potential for confusion. We therefore remove all galaxies deemed confused using the same method outlined in Section 4.7.2 (assuming a beam of FWHM=22'' for observations with the IRAM 30m and FWHM=3.8' for observations with the Arecibo telescope). However, because our stacking process (described below) requires us to normalise the spectrum by the width of the emission line, applying a fixed velocity cut could miss a significant portion of confused galaxies. As such, in addition to the requirements imposed in Section 4.7.2, we require galaxies to be within $5\times$ the width of the target's emission line for them to be contaminating. This procedure is performed over all xCOLD GASS, xGASS and ALFALFA galaxies, so that even galaxies observed in ALFALFA without optical counterparts are accounted for. In total, we flag 3/69 CO and 303/1487 H I galaxies as confused and discarded them from any remaining analysis. Finally, we visually inspect the spectra of the remaining galaxies for evidence of baseline, artefact or radio frequency interference (RFI) issues and remove 1 CO and 107 H I sources with suspect spectra. In total, this results in 78 optical galaxies, 65 CO galaxies and 1,077 H I galaxies which form the final samples for this analysis. We show the CO(1-0) and H I spectra, as well as the SDSS postage stamp image, of 10 randomly chosen galaxies in our final samples with overlapping observations in Figure C.1.

The positions of our selected samples of optical, CO and H I galaxies on the SFR- M_* plane are shown in Figure 5.1 and their stellar mass, SFR and redshift distributions are shown in Figure 5.2, where one can see that the maximum difference between the median SFRs and stellar mass of each star-forming sample is 0.4 dex and 0.36 dex, respectively.

For each detected emission line (CO or H I), we remeasure the width and velocity of the line prior to any analysis. This is because the conventionally defined W50 (or FWHM) parameter may not always encapsulate all of the flux of the line and its use could

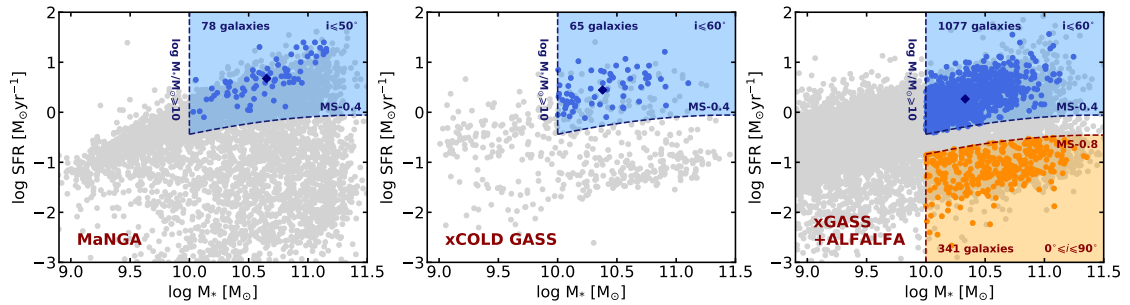


Figure 5.1. The distribution of galaxies from the full MaNGA DR15 (left), xCOLD GASS (middle) and combined xGASS+ALFALFA α .100 (right) data releases (gray points) and our selected star-forming sample of high mass galaxies with low inclinations (blue points) across the SFR- M_* plane. The blue regions and dashed lines mark our selection limits across the plane for star-forming galaxies likely to host outflows, with the SFR limit set by the definition of the MS by [Saintonge et al. \(2016\)](#). A navy diamond in each plot marks the mean SFR- M_* position of each selected star-forming sample. The orange region and dark red lines in the right panel represent the selection limits for our sample of H I passive across all inclinations and galaxy types, where outflows are not expected to be seen.

lead to false-positive outflow detections. As such, we guard against this by measuring a *full width* (FW) which encapsulates virtually all of the systemic emission. For spectra where an emission line is not detected, we use the optical SDSS redshift and the Tully-Fisher relation from [Tiley et al. \(2016\)](#) to estimate a velocity and width, respectively. We explore the suitability of this approach in Section 5.4. Finally, because H I spectra can often display particularly noisy or asymmetrical spectra where the width of the line is not well constrained, we define a “pristine” sample of 220 H I galaxies for which the emission is of significant S/N with well defined widths.

5.3 Stacking Process & Results

In order to obtain high S/N spectra with which to search for broad component emission, we opt for a stacking approach. For both the CO and H I spectra, the emission line is shifted to its rest frame, before being normalised by its width and interpolated over a common normalised-velocity array. Because we are interested in deriving mass outflow rates of potential outflowing gas, we stack each spectrum in “gas mass units”, that is to say:

- For CO(1-0): each spectrum is multiplied by all the standard factors in the [Solomon](#)

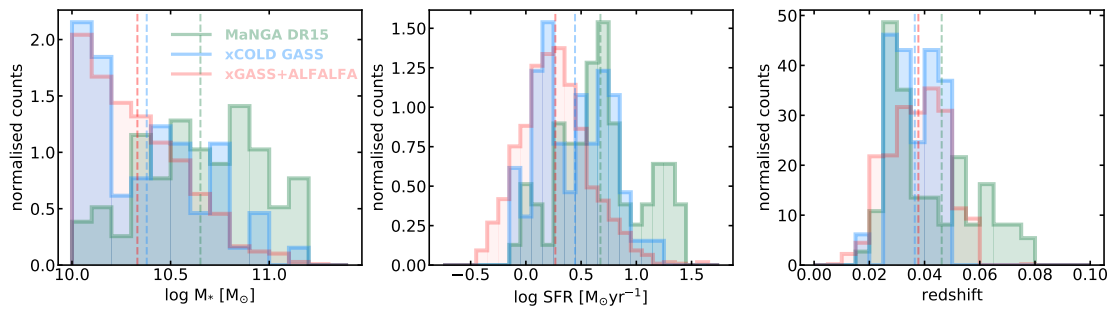


Figure 5.2. The normalised stellar mass (left), SFR (middle) and redshift (right) distributions of our three final samples derived from the MaNGA DR15 (green), xCOLD GASS (blue) and xGASS+ALFALFA $\alpha.100$ (red) surveys. The dashed line represent the mean value for each distribution.

et al. (1997) prescription and an assumed conversion factor for normal star-forming galaxies, $\alpha_{\text{CO}} = 4.35 M_{\odot} (\text{K km s}^{-1} \text{pc}^{-2})^{-1}$, which includes a correction for the abundance of Helium.

- For H I : each spectrum is converted to an H I gas mass via the relation presented in Equation 4.6.

Each spectrum is subsequently added to the stack and the final stacked spectrum is taken as the mean over all galaxies in the stack. The errors associated with the final spectrum in all of our stacks are taken as the combination of bootstrapped sampling errors (with replacement) and the average flux uncertainties of each spectrum.

For each of the 78 MaNGA galaxies, we select spaxels within a $0.5 R_e$ galactocentric radius, since this is shown to be a rough limit to display NaD in absorption (see Section 4.4.2). Each spectrum is then put through the steps outlined in Section 3.3.1, converted to a luminosity, and then summed. We then take two slightly different approaches, depending on the tracer of interest. For NaD each galaxy spectrum is normalised and added to a stack, which is then averaged and subsequently fit with a continuum model from pPXF, with which we divide the average galaxy spectrum to obtain the NaD ISM contribution. The NaD profile is then fit with the procedure described in Section 2.2.2. For the ionised gas, on the other hand, we fit and subtract a pPXF continuum model from each galaxy spectrum prior to adding it to the stack, then take the average of the stacked spectra. This is to ensure the final spectra have the correct units and the weighting of the optical spectra are the same. The final residual luminosity is then converted to “outflow gas mass units” via the relation,

$$M_{\text{H}\alpha} = \frac{1.4 m_{\text{H}} L_{\text{H}\alpha, \text{out}}}{\gamma_{\text{H}\alpha} n_e}, \quad (5.1)$$

where $\gamma_{\text{H}\alpha}$ is the H α emissivity at a temperature $T=10^4$ K ($\gamma_{\text{H}\alpha}=3.56\times 10^{-25}$ erg cm³ s⁻¹) and n_e is the local electron density *of the outflow*. Such an approach allows us to simulate a single long exposure for each MaNGA galaxy (similar to our (sub)mm and radio observations) whilst maintaining high S/N and maximising the area of the galaxy covered.

5.4 Reliability of Stacking Methods and Validity of Broad CO and HI Emission

To ensure potential outflow components are not the result of artefacts or neighbouring sources, a number of factors must be taken into consideration, which could all mimic a broad component.

A first consideration is that broad emission is not the result of nearby sources that confuse the spectra of our targets. However, we already account for this possibility by removing galaxies subject to confusion in Section 5.2.

A second consideration is to ensure any resulting broad CO or HI emission would not be an artefact of our stacking approach. To test this, we create a stack of CO and HI spectra where, for each spectrum going into the stack, we place the systemic component of the emission line - as defined by our measured FW - in a random region (within 1,000 km s⁻¹) of the spectrum and replace the previous location of the emission line with the (noise) portion of the spectrum now taken up by the emission line, thereby redefining the central velocity of the line. It follows that, since we have selected only systemic emission defined by the width of the line, a broad component would only appear as a result of our stacking process. After taking the mean of the stack, we inspect whether a broad component arises from our (systemic) emission spectra, due to our procedure. However, the final stack of each tracer (CO and HI) reveals no evidence of a broad component and therefore validates our stacking method.

A third - and most important - consideration is to ensure that the systemic flux of each galaxy is completely encapsulated by the width of the line, in order that systemic emission does not “leak” into broad emission once normalised by the width of the line. To

test this, we define a sample of HI -detected, high mass, passive galaxies of all inclinations and galaxy types from xGASS and ALFALFA, where we do not expect to observe outflows and therefore any potential broad emission would be the result of systemic emission not captured by our measured width. Specifically, this sample of galaxies is defined as having $\log M_*/M_\odot \geq 10$ and $\log \text{SFR}/M_\odot \text{yr}^{-1} \leq \text{MS}-0.8$ dex and includes AGN. Just as for the galaxies defined in Section 5.2, for each galaxy we redefine the HI line velocity and measure the FW and remove any object subject to confusion and/or contaminated by artefacts or RFI. This results in a sample of 341 passive galaxies with useable spectra. We subsequently adopt a Monte Carlo approach to randomly select and stack 80% of this sample 300 times, where the final mean spectrum is taken as the average over all Monte Carlo iterations. We present this final stack in the top panel of Figure 5.3. Additionally, to validate our choice of using the FW and remeasured velocity the CO and HI spectra used in this study, we perform the same stack using the velocities and FWHM (W50) derived from the xGASS and ALFALFA catalogs, and present this in the bottom panel of Figure 5.3. Both stacks reach depths of $\text{RMS} \sim 1.4\text{-}1.6$ mJy.

From the top panel of Figure 5.3, we immediately note a complete lack of broad emission, suggesting our measured widths encapsulate all (and serve as reliable measurements of) the systemic emission of the line. However, from the bottom panel of the same Figure, we note that significant broad wings appear in the high S/N spectrum, indicating that the catalogued W50 values are inadequate tracers of systemic emission for our purposes. Using the W50 widths for our star-forming sample could result in broad emission that could falsely be interpreted as an outflow component and highlights the precarious nature of searching for broad components in emission spectra. We illustrate the differences between our measured widths and velocities compared to the catalogued values in Figure 5.4, with median differences of 46 km s^{-1} and 5 km s^{-1} , respectively. The tests performed here validate our choice of remeasuring the line widths and velocities, for which we find the catalogued W50 values underestimate the systemic component by $\sim 46 \text{ km s}^{-1}$, and ensure potential outflowing signal is not due to artefacts of our stacking procedure or measurements.

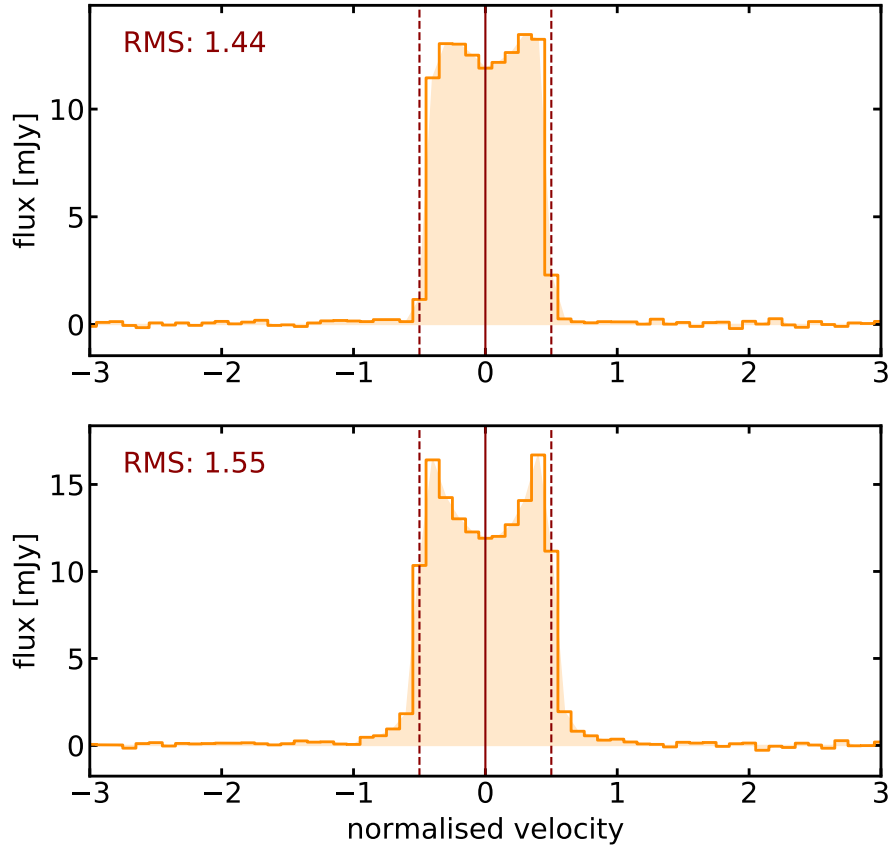


Figure 5.3. HI stacks of high mass, passive galaxies (including AGN) over the full range of inclinations, where outflows are not expected to be seen. Stacks are created via a Monte Carlo sampling of 80% of the sample, repeated 300 times. The top panel shows the stacked spectrum using our measured linewidths and velocities, whilst the bottom panel repeats the same process using the catalogued W50 values. A clear difference is seen between the two, with the former stack displaying no signatures of broad emission, suggesting all of the systemic emission is encapsulated within our measurement, whilst the latter displays significant broadening at high normalised velocities, indicative of leaking systemic emission at higher normalised velocities. Such a comparison is imperative in a search for outflows, since the broad emission could be interpreted as outflowing signal in star-forming samples.

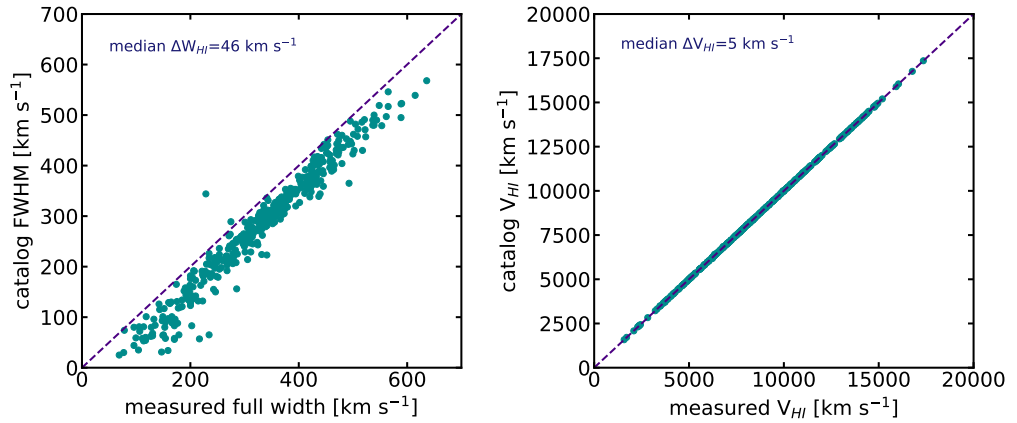


Figure 5.4. A comparison of the catalogued H I FWHMs (W50) versus our measured full linewidths (left) and the same for H I velocities (right). Our linewidths are systematically larger than the catalogued values, with a median difference of $\sim 46 \text{ km s}^{-1}$. The difference between H I velocities is much smaller, with a median difference of only $\sim 5 \text{ km s}^{-1}$. In both plots, the dashed purple line denotes a 1:1 relation. The difference in H I linewidths is crucial in our search for broad emission outflows, since an underestimation of the linewidth can result in leaked systemic emission which can mimic the signature of outflows.

5.5 Results

5.5.1 Neutral and Ionised Outflows

In Figure 5.5 we present the results of our stacking approach of NaD, H α + [N II], CO(1-0) and H I 21cm gas tracers for our MaNGA, xCOLD GASS and xGASS+ALFALFA galaxies. We begin by examining the results seen in the NaD profile, which displays significant blueshifted absorption and redshifted emission characteristic of a P-Cygni profile, which is an unambiguous signature of outflows. A three component fit to the line (following the method outlined in Section 2.2.2) reveals a blueshifted outflow component with velocity $|v_{\text{out}}|=131 \text{ km s}^{-1}$ (160 km s^{-1} after correction for a mean inclination of $i \sim 35^\circ$) and hydrogen column density of $N(H)=10^{21.33} \text{ cm}^{-2}$ (using the same assumptions made in Section 3.4.6), corresponding to a (inclination-corrected) neutral mass outflow rate of $7.55 M_\odot \text{ yr}^{-1}$, consistent with other neutral gas outflow rates derived in Chapter 3 of this Thesis. The redshifted emission is much less stark than the blueshifted absorption, although is a clear indication of resonant re-emission coming from the backside of the galaxy disk (i.e., a receding outflow) and provides compelling evidence for the presence of outflows in our selected galaxies.

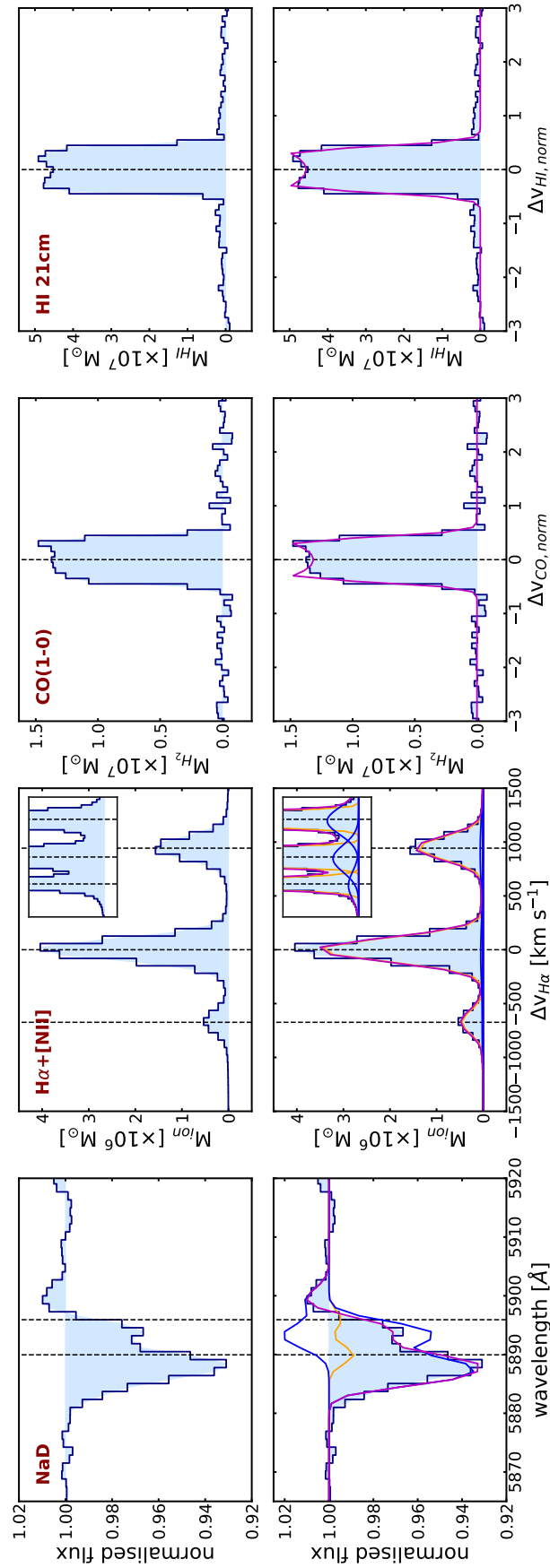


Figure 5.5. The final stacked spectra of our NaD (left column), H α + [NII] (middle left column), CO(1-0) (middle right column) and HI 21cm (right column) tracers from the MaNGA DR15, xCOLD GASS and xGASS+ALFAFA α .100 surveys. The top row shows the stacked spectra only, whilst the bottom row shows the stacked spectra with their best fit models. Stacked flux is outfined by the navy line and light blue fill, whilst orange lines mark fits of a systemic component, blue lines mark outflowing components, and purple mark the total fit.

We next inspect the profiles of the $\text{H}\alpha + [\text{N II}]$ and $[\text{S II}]$ emission. The first three emission lines are close enough to each other ($< 1000 \text{ km s}^{-1}$) to cause some blending of the profiles, however it is still possible to derive accurate fits of the lines due to the high S/N of the spectra and by fitting all five of the aforementioned lines simultaneously. Therefore, to determine whether outflowing gas is seen in ionised gas tracers, we fit the the combined $\text{H}\alpha + [\text{N II}] + [\text{S II}]$ emission with both a single Gaussian fit for each line and a double-Gaussian fit consisting of a narrow and a broad Gaussian profile for each line. For the systemic fits, we allow the amplitude of each line to vary but fix the amplitudes of the $[\text{N II}]$ lines to their intrinsic ratio of $[\text{N II}]\lambda 6548 / [\text{N II}]\lambda 6583 = 0.326$ (Morton 1991), and assume the same width for all lines which is allowed to vary from $0 \leq \text{FWHM} \leq 800 \text{ km s}^{-1}$. For the broad components, we make the same assumptions as the narrow components, but allow the amplitudes to reach no higher than the systemic counterpart and require the width to be larger than the narrow components. Additionally, we also allow a velocity offset of the broad components (the same for each component) of $\Delta v \pm 500 \text{ km s}^{-1}$. A comparison of the two fits (single versus double component) with a BIC reveals that the extra four free parameters in the double component fit are justified, and as such an ionised outflow is detected. We measure an outflow velocity ($v_{\text{out}} = \text{FWHM}/2 + |\Delta v|$) of 439 km s^{-1} (534 km s^{-1} after inclination correction), more than a factor of three larger than the velocity found by the blueshifted absorption in NaD. For an estimation of the electron density within the outflow, we look at the outflowing components of the $[\text{S II}]$ doublet, whose ratio correlates strongly with the observed electron density (Osterbrock 1989). However, we find the flux of the outflowing $[\text{S II}]\lambda 6730$ line is insufficiently bright to infer robust values. As such, we adopt a low value of 50 cm^{-3} (Newman et al. 2012). We subsequently derive a mass outflow rate from the emission lines as follows:

$$\dot{M}_{\text{out}} = \frac{v_{\text{out}} M_{\text{out}}}{R_{\text{out}}}, \quad (5.2)$$

where v_{out} is the *inclination-corrected* outflow velocity, M_{out} the instantaneous gas mass of the outflow, and R_{out} is the assumed radius of the outflow (5 kpc). Thus, integrating over the broad component of $\text{H}\alpha$ and using Equation 5.2, we infer a mass outflow rate of $0.10 M_{\odot} \text{ yr}^{-1}$.

5.5.2 Molecular and Atomic Outflows

Finally, we turn our attention to the stacked CO(1-0) and HI 21cm emission, which serve as tracers of fuel for SF. At first glance, we observe no significant evidence for broad wings either side of the double horned (DH) profiles. To confirm this, we fit both the CO and HI profiles with a single DH profile, composed of a parabolic function accompanied by two equidistant (and identical but mirrored) half-Gaussians used to describe the low- and high-velocity edges of the DH (the ‘‘Gaussian Double Peak’’ function, described in detail in [Tiley et al. 2016](#)), and a two-component profile consisting of a DH profile and broad Gaussian. The number of free parameters for these fits are 4 and 7, respectively. For the DH profile, we allow the height of the parabola and peak of the two Gaussians to reach the maximum observed flux (within errors), whilst restrict the half width of the parabola to $0 \leq \Delta v_{\text{norm}} \leq 1.5$ and the width of the Gaussians to $0 \leq \sigma_{\text{norm}} \leq 2$. For the broad Gaussian, we allow the amplitude to reach no higher than the central parabola of the DH component, whilst restricting the width to greater than that of the DH profile and less than $\sigma_{\text{norm}} \leq 5.0$ and don’t allow for a velocity offset.

Our fits to the CO(1-0) emission and a comparison of the BIC values determine that a two-component fit is unjustified, suggesting that no outflow is present (or seen), despite our stack reaching a (RMS) depth of $\log M_{H_2} \sim 5.7 M_{\odot}$. The HI emission, on the other hand, displays tentative broad emission on either side of the profile, with a measured RMS of $\log M_{\text{HI}} \sim 5.9 M_{\odot}$. A two-component fit to the profile quantitatively confirms the broad emission via a BIC ratio, however the amplitude of the broad Gaussian is detected to $< 2\sigma$ when compared to the noise of the spectrum. If the stacking process is repeated over our 220 pristine galaxies, where the width and velocity of the line are better constrained, we reach a sensitivity of $\log M_{\text{HI}} \sim 6.0 M_{\odot}$ but find the tentative broad emission disappears. Whilst we have performed extensive tests to significantly limit the potential contribution of confusion, leaked systemic emission, or spectral artefacts, we cannot completely rule out some contamination in our main stack and the emission is sufficiently faint that we cannot make robust claims as to its source. Additional, dedicated observations would be required to confirm such emission as outflowing gas. Finally, in Figure 5.1 we note that the mean stellar mass of the combined HI sample is somewhat lower than the MaNGA sample, where we observe outflows. Since this has been shown by several studies to be a considerable factor in optical outflow detections ([Chen et al. 2010](#); [Roberts-Borsani &](#)

Saintonge 2019), as an additional test we perform the same stack over high mass ($\log M_* \geq 10 M_\odot$) galaxies only. 263 galaxies result from this cut, and the absolute differences in the mean properties of the MaNGA and high mass H I sample are far better matched, with differences of $\Delta \log M_* = 0.027 M_\odot$, $\Delta \log \text{SFR} = 0.159 M_\odot \text{yr}^{-1}$ and $\Delta z = 0.006$. In the resulting stack we find very tentative wings of H I emission, which could be suggestive of outflowing gas and a comparison of BIC values from a single DH fit or DH+Gaussian fit reveals the latter is preferred and a supposed detection is found. However, such “wings” are extremely faint and in subtracting the single DH fit from the spectrum and comparing the residual wings to the noise in the spectrum, we find they are only detected to 1.4σ . As such we cannot make robust claims as to an H I outflow detection.

As such, a certain degree of inference is necessary to place upper limits on the mass outflow rate of molecular and atomic gas with our high S/N spectra. To do this, we run simulations of the completeness and reliability for our code to pick up faint outflow signatures of an assumed velocity in our stacked spectra. To do this, we construct synthetic spectra containing both a DH profile and a broad Gaussian, combined with a level of Gaussian noise matching that measured in the stacked CO and H I spectra. Our procedure is as follows: first, in order to derive an independent measurement of systemic emission where we are confident outflow signal is absent, we fit our passive galaxy stack from Section 5.4 with a single DH profile as described above and use this as our profile for systemic emission. Next, we construct a broad Gaussian component by assuming an outflow velocity of 200 km s^{-1} (the choice is based on the low outflow velocities derived in Chapter 3, as well as the median value of 250 km s^{-1} from the Fluetsch et al. (2018) sample of H II starburst galaxies) which we compare to the median FW of the spectra going into the CO and H I stacks ($\text{FW} \approx 284 \text{ km s}^{-1}$ and $\text{FW} \approx 275 \text{ km s}^{-1}$ for CO and H I, respectively) in order to determine the corresponding normalised outflow velocity. The normalised FWHM of the Gaussian is given by $\text{FWHM}_{\text{broad, norm}} = v_{\text{out, norm}} \times 2$ and we determine the normalised outflow velocity from $v_{\text{out, norm}} = v_{\text{out}} / \text{HW}_{\text{median, CO/HI}}$, where $\text{HW}_{\text{median, CO/HI}}$ is the median half-width going into the stacks. The broad Gaussian is then constructed assuming a variety of amplitude ratios ($A_{\text{broad}} / \text{DH}_{\text{sys, peak}}$) and added to the systemic DH profile to create the total spectrum. Random Gaussian noise is then added to the spectrum to match the measured value of the CO and H I spectra and the final profile is subsequently fit with a single DH profile and combined DH+Gaussian profile, as described above but allowing full range to the width of the fit Gaussian profile. The process of Gaussian

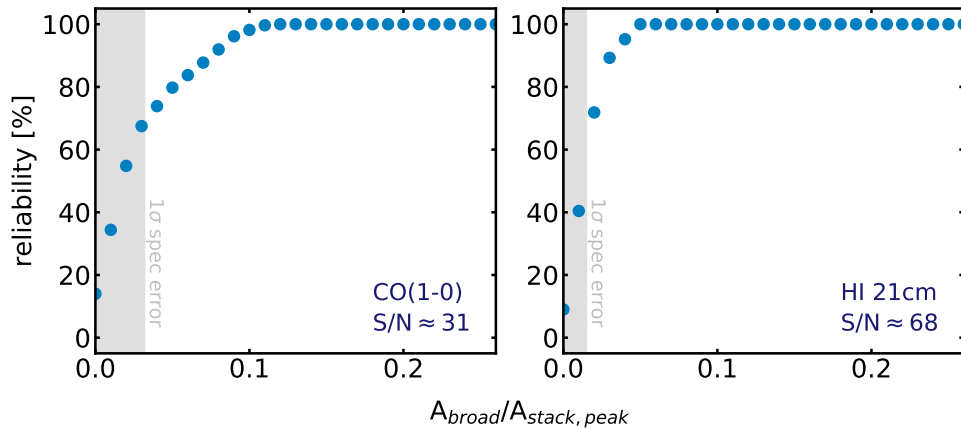


Figure 5.6. The reliability of our code’s outflow detections at various amplitude ratios for simulated spectra of the same S/N of our stacked CO (left) and HI (right) spectra, given an assumed outflow velocity of 200 km s^{-1} . The lowest outflow amplitude ratio (compared to the peak flux of the total spectrum) we can measure whilst maintaining 90% reliability is $A_{\text{broad}}/A_{\text{stack,peak}}=0.075$ (CO) and $A_{\text{broad}}/A_{\text{stack,peak}}=0.031$ (HI).

noise addition and subsequent fitting is repeated $N=100$ times. We subsequently assess the completeness and reliability of our fits, to determine the minimum amplitude of the outflow component that our code can reliably measure, with which to subsequently derive our upper limits. We find in all cases the DH+Gaussian profile is preferred, suggesting 100% completeness, however many of these (particularly at low Gaussian amplitudes) have measured Gaussian FWHM smaller than the DH profile FWHM (i.e., the Gaussian is fitting noise in the centre of the spectrum, not outflow signal). We consider fits with $\text{FWHM}_{\text{broad}}/\text{FWHM}_{\text{DH}} < 1$ as false-positive detections and the completeness is therefore defined as the fraction of fits without false-positives. A plot of reliability for both the simulated CO and HI spectra is shown in Figure 5.6.

We find the minimum outflow amplitude (compared to the peak flux of the stacked spectrum) we can measure with $>90\%$ reliability is $A_{\text{broad}}/A_{\text{stack,peak}}=0.075$ for CO and $A_{\text{broad}}/A_{\text{stack,peak}}=0.031$ for HI, corresponding to outflow gas masses of $\log M_{\text{gas}}/M_{\odot} \sim 8.68$ (9.20) for CO (HI). Using Equation 5.2, we derive upper limits on the mass outflow rate of molecular and atomic gas of $\dot{M}_{\text{CO}} < 19.43 M_{\odot} \text{ yr}^{-1}$ and $\dot{M}_{\text{HI}} < 64.48 M_{\odot} \text{ yr}^{-1}$, respectively. We summarise the parameters of the above findings in Table 5.1.

Table 5.1. The mean properties and parameters of our stacked spectra used to derive multiphase mass outflow rates in this work.

Quantity	CO(1-0)	H I 21cm	NaD	H α
log SFR [$M_{\odot} \text{ yr}^{-1}$]	0.57 ± 0.35	0.39 ± 0.46	0.57 ± 0.38^a	0.57 ± 0.38^a
v_{out} [km s^{-1}]	–	–	131 ± 8	439 ± 11
$v_{\text{out}}/\cos(i)$ [km s^{-1}]	200^b	200^b	160 ± 10	534 ± 14
\dot{M}_{gas}	<19.43	<64.48	7.55 ± 7.20	0.10 ± 0.02
η [M/SFR]	<5.27	<26.20	2.04 ± 2.65	0.03 ± 0.03

^aMean integrated values calculated from an H α luminosity and assuming a Chabrier IMF.

^bAssumed outflow velocities.

5.6 Discussion

5.6.1 Towards a Total, Multiphase Mass Outflow Rate

Although we can derive only upper limits on the mass outflow rate for outflows in *normal* galaxies in the local Universe, such constraints are extremely valuable. As such, in Figure 5.7 we plot our derived rates as a function of the mean SFR and compare these to other results in the literature. Whilst the list of studies we compare to is not a complete one, we are able to provide useful comparisons to a variety of galaxy types in the local Universe.

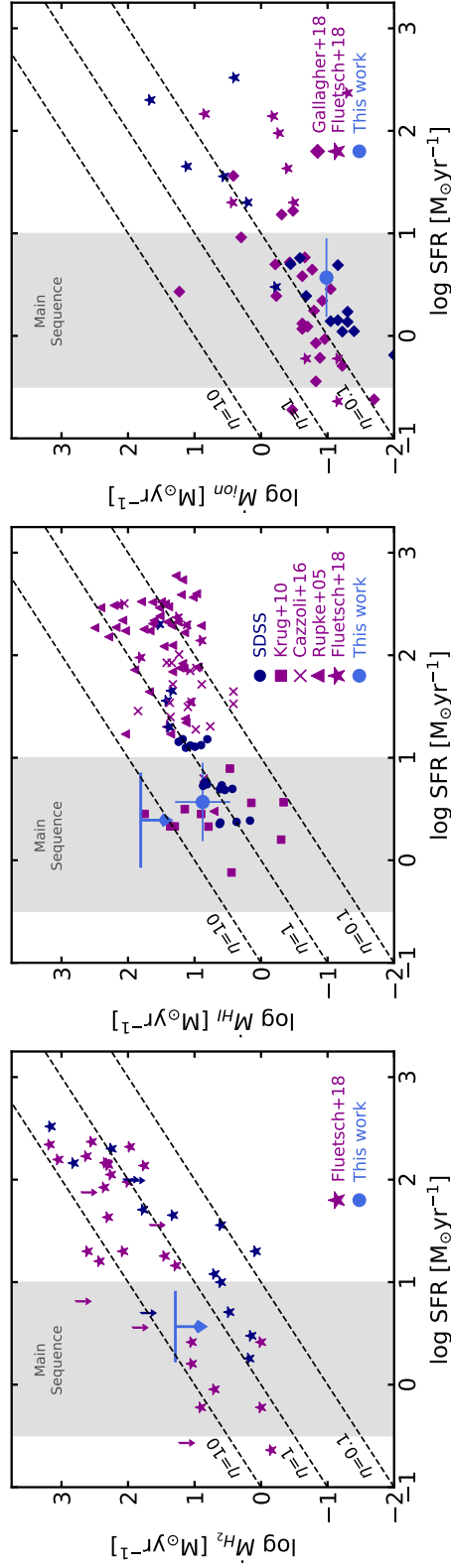


Figure 5.7. The mean H_2 (left), H I (middle) and ionised (right) mass outflow rates compared to the mean SFRs of normal galaxies at $z \sim 0$, as traced by $\text{CO}(1-0)$, $\text{H I } 21\text{cm}$ and Nad , and $\text{H}\alpha$, respectively. Upper limits of the H_2 and $\text{H I } 21\text{cm}$ mass outflow rates are marked by blue arrow upper limits, whilst the rates derived with Nad and $\text{H}\alpha$ are marked by blue circles with errors. The errors quoted here included the 1σ errors from our fitted parameters, whilst the error associated with the mean SFR is simply the standard deviation over all the galaxies in the stack (and galaxy spaxels, in the case of MaNGA data). The results from this study (light blue points and arrows) are compared to the mass outflow rates derived for H II (navy points) and (U)LIRG/AGN (purple points) galaxies from the literature, using multi-transition CO for molecular gas, Nad or C^+ for neutral gas, and $\text{H}\alpha$ or $\text{H}\beta$ for ionised gas. The classification of galaxy type is taken from each relevant study. We further mark the region of SFRs that roughly probe the lower and upper limits of the high mass ($M_* \geq 10^{10} \text{ M}_{\odot}$) galaxy MS (gray shaded region) and draw dashed lines to represent constant mass loading factors of $\eta=0.1, 1, \text{ and } 10$.

In comparing outflow rates of molecular gas, we find our upper limit of $\dot{M}_{\text{CO}} < 19.43 \text{ M}_{\odot} \text{ yr}^{-1}$ consistent with the H II and AGN galaxies from the compilation by [Fluetsch et al. \(2018\)](#) within the marked MS region, although ~ 1 -2 dex lower than the maximum rates found over their full sample. This is perhaps unsurprising given the nature of the galaxies and SFRs probed: most of the [Fluetsch et al. \(2018\)](#) sample reside above the galaxy MS with $\text{SFR} > 10 \text{ M}_{\odot} \text{ yr}^{-1}$ whilst our mean SFR is less than $5 \text{ M}_{\odot} \text{ yr}^{-1}$. However, for the more normal H II galaxies on the MS, their maximum and median mass outflow rate is $4 \text{ M}_{\odot} \text{ yr}^{-1}$ and $2.25 \text{ M}_{\odot} \text{ yr}^{-1}$, respectively, consistent with our upper limit which is a factor of ~ 5 and ~ 8.5 larger, respectively. This consistency also extends to the AGN detections on the MS, which show maximum and median mass outflow rates of $11 \text{ M}_{\odot} \text{ yr}^{-1}$ and $6.5 \text{ M}_{\odot} \text{ yr}^{-1}$, respectively, not too dissimilar to our upper limit and suggestive of limited additional contribution from normal AGN to molecular outflows. As such, our upper limit seems most consistent with AGN detections and would require lowering by a factor of ~ 8 in order to probe H II-driven outflows.

The comparison of an atomic mass outflow rate, traced by H I 21cm emission, is much more challenging due to the large upper limit of $\dot{M}_{\text{HI}} < 64.48 \text{ M}_{\odot} \text{ yr}^{-1}$ set by this work, which is consistent only with the maximum NaD-derived values of (U)LIRG/Seyfert objects from [Krug et al. \(2010\)](#) over the MS, which we re-derive using Equation 3.4 and their relevant parameters in their Table 2. However, a comparison of the H I outflow rate derived with NaD provides a more stringent comparison: we find in general our derived value of $7.55 \text{ M}_{\odot} \text{ yr}^{-1}$ is consistent with other NaD outflow rates across the literature and our SDSS-derived points from Chapter 3, as well as the relation and evolution with SFR observed in Section 3.4.6 and presented in Equation 3.5. Again, for normal galaxies across the MS, we find little difference between galaxies likely to host an AGN (i.e. the results of [Krug et al. 2010](#)) and those without (our SDSS points), reinforcing the notion that *normal* AGN feedback is unlikely to be more significant. Our derived \dot{M}_{NaD} of $7.55 \text{ M}_{\odot} \text{ yr}^{-1}$ is consistent with previously derived values throughout this Thesis but a factor of ~ 8.5 smaller than our 21cm upper limit. We find that the NaD outflow rate is much more comparable to the upper limit of CO, but a factor of ~ 2.6 smaller. This ratio is similar to the results of [Fluetsch et al. \(2018\)](#) for starburst galaxies, using NaD and C^+ as neutral gas tracers.

Finally, a comparison of the ionised gas outflow rate further illustrates the similarity (or consistency) between our derived values and those in the studies we compare to (for both AGN and H II galaxies). The values in the MS region are again consistent with an

evolution described by Equation 3.5 (albeit an order of magnitude lower) and the median mass outflow rate of all H II (AGN) galaxies from the studies of [Fluetsch et al. \(2018\)](#) and [Gallagher et al. \(2018\)](#) in the MS region is $0.07 M_{\odot} \text{yr}^{-1}$ ($0.2 M_{\odot} \text{yr}^{-1}$), virtually identical to our measured value of $0.10 M_{\odot} \text{yr}^{-1}$. In both this work and the study of [Fluetsch et al. \(2018\)](#), the ionised outflow rate is by far the lowest of the three gas phases and essentially insignificant compared to the molecular and neutral gas phases.

Through our stacked points and upper limits, we have added constraints on mass outflow rates of different gas phases, and compared these to other results found for local galaxies, where general agreement and consistency is found. Using NaD as the tracer of neutral gas and summing the outflow rates over all the different gas phases, we find a total mass outflow rate of $\dot{M}_{\text{tot}} \approx 27 M_{\odot} \text{yr}^{-1}$ (or $\dot{M}_{\text{tot}} < 34 M_{\odot} \text{yr}^{-1}$, assuming the upper limit of our derived values in each gas phase), significantly higher than what is typically probed by tracers of a single gas phase. In comparing the different gas phases (CO, NaD, H α) to each other, we find the molecular and neutral gas phases have the potential to be by far the dominant outflowing phases, with $\sim 99\%$ of the total mass outflow rate coming from the two gas phases ($\sim 72\%$ from the molecular gas and $\sim 28\%$ from the neutral gas) and less than 1% coming from the ionised gas. Between the molecular and neutral gas phases, the molecular gas has the potential to be by far the dominant gas phase. Such a picture is even more evident when comparing the data points in Figure 5.7 at $\text{SFR} \gtrsim 10 M_{\odot} \text{yr}^{-1}$, where we see a significant decrease in outflow rates from the molecular to the ionised gas phase.

As such, the emerging picture from our comparisons here are that galaxies of the local Universe display a large range of mass outflow rates, with the highest rates appearing in galaxies with higher SFRs. Galaxies residing on the MS display far reduced rates compared to their starburst counterparts and this applies across all phases. No significant difference is found between the outflow rates of H II galaxies and AGN, suggesting limited enhancement from AGN feedback. The molecular gas phase - the most important for SF - likely contributes the majority of the total outflow rate, with the neutral gas phase contributing virtually equal or slightly less amounts, and the ionised gas contributing negligible amounts. Specifically, using NaD as the tracer of neutral gas, we find relative fractions of $\dot{M}_{H_2}/\dot{M}_{\text{HI}} \lesssim 2.6$ ($\dot{M}_{H_2}/\dot{M}_{\text{HI}} \lesssim 5.0$ assuming upper limits and including errors) and $\dot{M}_{H_2}/\dot{M}_{\text{ion}} \lesssim 187$ ($\dot{M}_{H_2}/\dot{M}_{\text{ion}} \lesssim 228$ assuming upper limits and including errors).

5.6.2 Why Don't We See Atomic or Molecular Outflows?

In Section 5.5 we have seen that clear detections of neutral and ionised outflows - as traced by NaD blueshifted absorption and broad H α emission - are seen in normal galaxies, but similar detections of molecular and atomic gas outflows, as traced by CO(1-0) and H I 21cm emission, appear scarce. Several reasons exist to explain this. The first is that despite the high S/N of our stacked spectra, the mean spectra do not probe a low enough RMS necessary to observe outflowing emission in normal, star-forming galaxies. If we compare the depth of our CO and H I spectra to the spectrum of the ionised gas, where broad emission is seen, we find the optical spectra a factor of ~ 1.7 more sensitive than what our molecular and atomic gas stacks probe. In comparing to the data points of [Fluetsch et al. \(2018\)](#), we find both our CO and their upper limits all lie close to the $\eta \sim 10$ line, whilst virtually all of the detections lie below. Furthermore, for galaxies with $\text{SFR} \leq 10 \text{ M}_{\odot} \text{ yr}^{-1}$ (i.e., on the MS), all of the detections lie below a mass outflow rate threshold of $\sim 10 \text{ M}_{\odot} \text{ yr}^{-1}$ and non-detections above. Furthermore, for H II objects on the MS, we find a median upper limit (combining both our data set and the upper limit of [Fluetsch et al. 2018](#)) of $\lesssim 42 \text{ M}_{\odot} \text{ yr}^{-1}$, whilst the median outflow rate of H II galaxy detections is $2.25 \text{ M}_{\odot} \text{ yr}^{-1}$, more than a factor of ~ 18 lower. As such, it is quite likely that our stack simply does not probe the depth necessary to detect the smaller outflow rates of normal star-forming galaxies.

A second consideration is whether CO molecules and H I atoms survive the turbulent and harsh environments of the outflow: shock fronts and UV radiation in strong outflows can accelerate and heat outflowing gas to high velocities and temperatures, leading to the photodissociation and ionisation of the gas. If this is the case, molecular and atomic gas that isn't properly shielded (either from self-shielding or from dust) could evaporate in the outflow. However, the contribution from shocks is thought to be relatively minor ([Cicone et al. 2012](#); [Zubovas & King 2014](#)) and, given the detection of CO outflows in starburst and AGN galaxies from a variety of sources in the literature, we deem this scenario unlikely.

Finally, a last consideration is that galaxy-wide outflows don't entrain atomic or molecular gas. Whilst this is clearly not the case for more extreme or exotic objects, the outflows observed in normal galaxies are found to be far less extreme, with much smaller velocities and outflow rates. As such, whether the low energetics of the outflow are able to disrupt the gravitationally-bound molecular gas in giant molecular clouds is subject to debate.

5.6.3 Can Outflows Quench Normal Galaxies?

The crucial questions we aim to address in this study are: what are the relative fractions of outflowing gas from different gas phases and can outflows from normal galaxies quench their hosts? In Section 5.6.1 we addressed the former. To constrain the latter, we look to the mass loading factor of our different gas phases. By dividing the mass outflow rates by the associated (total) SFR, we find mass loading factors of $\eta \sim 5.27$, $\eta \sim 2.04$ and $\eta \sim 0.03$ for molecular (CO), neutral (NaD) and ionised ($H\alpha$) gas, respectively. However, considering only one gas phase can severely underestimate the total mass loading factor due to reduced mass outflow rates, as seen in Section 5.6.1. As such, we determine the total, multiphase mass loading factor ($\eta_{\text{tot}} = \eta_{\text{CO}} + \eta_{\text{NaD}} + \eta_{H\alpha}$) and find a value of $\eta_{\text{tot}} \sim 7.34$ (or upper limit $\eta_{\text{tot}} < 12.33$ assuming upper limits and including errors). At face value, this would suggest that outflows are able to expel enough gas to eventually deplete the gas reservoirs of their host galaxies, however this is largely reliant on the true value of molecular gas outflow rate lying close to our upper limit. If we compare our robust outflow rates for neutral and ionised gas only, we find a mass loading factor of $\eta_{\text{NaD}+H\alpha} \sim 2$ (upper limit of $\eta < 4.7$), significantly lower than our derived upper limit of the total mass loading factor and suggestive of the molecular gas playing a crucial role. As such, given the importance of the gas phase and the likely large contribution to the total mass outflow rate, in Figure 5.8 we look at the outflow depletion time of molecular gas, $\tau_{\text{depl}} = M_{\text{gal}}(H_2) / \dot{M}_{\text{out}}(H_2)$, which is the time required to completely remove all the molecular gas from the host assuming no additional gas is transferred to the galaxy.

Using a mean galaxy molecular gas mass of $\log M_{H_2} \sim 9.46$ as probed by our stack, we derive a lower limit depletion time of ~ 150 Myr (or $10^{8.17}$ years), suggestive of a potentially rapid quenching process. This is consistent and similar to the depletion times found by [Fluetsch et al. \(2018\)](#) for H II and AGN galaxies on the MS, but significantly higher than values found for strong starbursts and AGN which, whilst rarer, are able to remove significantly larger amounts of gas on shorter timescales.

However, such a comparison is only valid to first order, and the question of whether outflows can quench their host galaxies or not via ejective feedback is significantly more complex: important to consider are also the outflow velocities relative to the circular velocity of the galaxy, whether the host galaxy has its gas reservoir replenished at any point, and whether the fate of an outflow lies in clearing out into the CGM or falling back

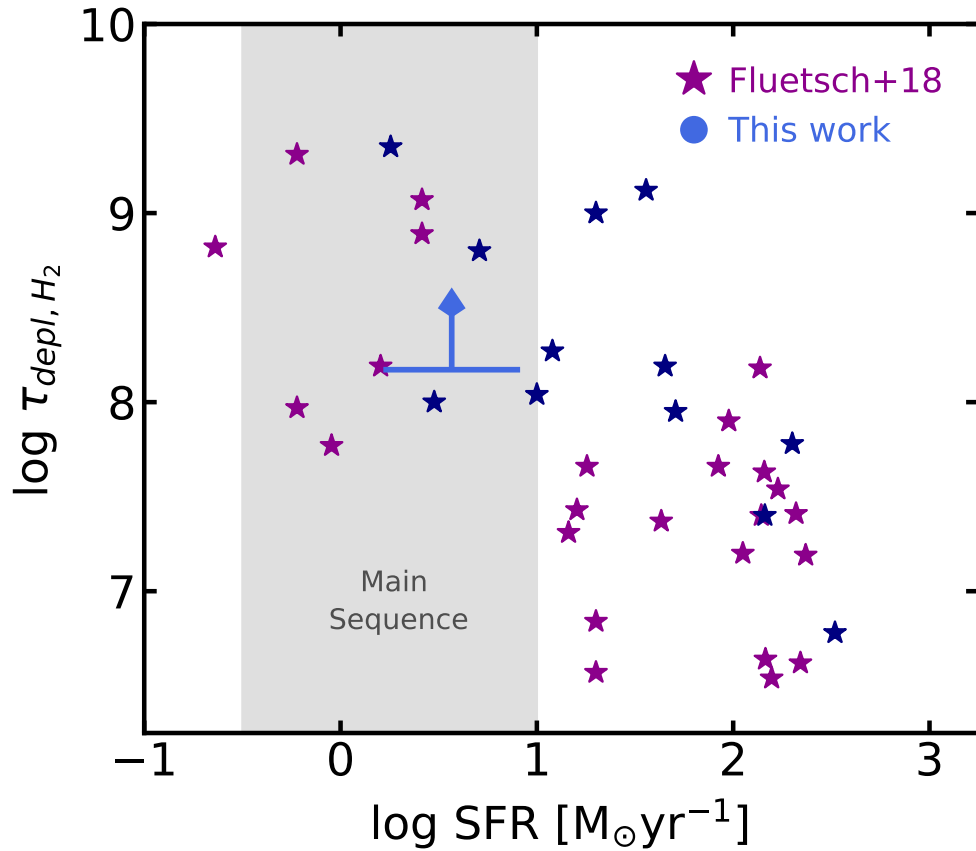


Figure 5.8. The outflow depletion time of molecular gas, defined as $\tau_{\text{depl}} = M_{\text{gal}}(\text{H}_2) / \dot{M}_{\text{out}}(\text{H}_2)$, as a function of host SFR. The colour scheme is the same as in Figure 5.7 and we additionally plot the values found for starburst and AGN galaxies in [Fluetsch et al. \(2018\)](#).

to the galaxy disk in the shape of a galactic fountain. Although our data set does not allow us to directly confirm such a scenario, our derived outflow velocities and mass loss rates suggest that strong ejective feedback in normal star-forming galaxies is absent and the relatively weak outflows seen here are unlikely to eject enough gas out of the galaxy disk to quench the host, thereby moving it from the MS to the red-sequence population.

5.7 Conclusions

We have used observations of CO(1-0), HI 21cm, NaD, and H α from the xCOLD GASS, xGASS, ALFALFA α .100 and MaNGA DR15 surveys to constrain the prevalence and relative fractions of molecular, neutral and ionised outflows in normal galaxies in the local Universe. Using stacking techniques to create high S/N composite spectra, we have

performed extensive tests to ensure broad emission from outflows is unlikely to be caused by confusion, artefacts or RFI effects and stack 65 CO(1-0), 1,077 HI and 78 optical spectra. Our findings based on these stacked spectra are the following:

- Outflowing gas is observed in both NaD and H α tracers through significant blueshifted absorption and broad emission, respectively. From these tracers we infer inclination-corrected outflow velocities of $|v_{\text{out}}|=160 \text{ km s}^{-1}$ and $|v_{\text{out}}|=534 \text{ km s}^{-1}$ and mass outflow rates of $\dot{M}_{\text{NaD}}=7.55 \text{ M}_{\odot} \text{ yr}^{-1}$ and $\dot{M}_{\text{H}\alpha}=0.10 \text{ M}_{\odot} \text{ yr}^{-1}$, respectively.
- In contrast to the optical tracers, we observe no significant broad emission on either side of the CO(1-0) or HI 21cm emission - although do observe tentative broad emission in the HI stacks - despite the high sensitivity of our stacks. As such, we place robust upper limits on the molecular and atomic mass outflow rates of $\dot{M}_{\text{CO}} < 19.43 \text{ M}_{\odot} \text{ yr}^{-1}$ and $\dot{M}_{\text{HI}} < 64.48 \text{ M}_{\odot} \text{ yr}^{-1}$, based on model completeness and reliability at the S/N of our stacks and assuming an outflow velocity of 200 km s^{-1} .
- Combining the upper limits on the molecular (CO(1-0)) outflow rate with our detections of outflowing neutral (NaD) and ionised (H α) gas, we derive a total mass outflow rate of $\dot{M}_{\text{tot}} \approx 27 \text{ M}_{\odot} \text{ yr}^{-1}$, with gas phase ratios of $\dot{M}_{\text{CO}}/\dot{M}_{\text{NaD}} \approx 2.6$ and $\dot{M}_{\text{CO}}/\dot{M}_{\text{H}\alpha} \approx 187$. Dividing each mass outflow rate by the associated SFR and summing the ratios, we find a total, multiphase mass loading factor of $\eta \approx 7.34$ ($\eta < 12.33$), suggesting that estimates of single gas-phase outflow rates are likely to miss significant amounts of outflowing gas. The derived upper limit on the total mass loading factor suggests, to first order, outflows from normal outflows could cause a degree of quenching in the host galaxies. However, accurate determination of the degree of quenching requires careful consideration of the low outflow velocities and fate of the gas, hydrodynamical deceleration by surrounding gas and disk gravity, and knowledge of gas inflow rates used to replenish the cold gas reservoirs.

The multiphase nature of outflows is a crucial constraint towards our understanding of how outflows impact their host galaxies, as it allows us to estimate the total gas mass being ejected out of the galaxy, as well as the relative importance of the different gas phases. Tracers of the molecular gas phase are by far the most valuable, since molecular gas directly

impacts the SF in the disk. However, such constraints are hard to come by and have for the most part only been placed on extreme starbursts or AGN. Here we have progressed on this deficiency by placing important constraints on the multiphase nature of outflows over normal galaxy populations at $z \sim 0$ with stacking methods of large samples of galaxies. However, despite the high S/N of our stacks, molecular and atomic (H I) gas outflows remain undetected. As such, to gain a better understanding of the prevalence of molecular and atomic gas outflows - as well as their quenching potential - a dedicated observational program over a representative sample of galaxies with e.g., ALMA is necessary to reach the required depths in a search for molecular and atomic outflow signatures in normal galaxies. Furthermore, interferometric and IFU observations (with e.g., ALMA/NOEMA and MaNGA) of large samples of normal galaxies would allow us to link the presence of outflowing gas to the presence (or lack of) SF and/or molecular gas over kpc-scales, thereby adding important spatial constraints to the link between outflow activity and the abundance of gas. Finally, with a view to gaining a complete understanding of the outflows' impact on the galaxy system, still required is a thorough understanding of the fate of the expelled gas, and whether the impact of outflows on galaxies is exclusive to ejective feedback or whether preventive feedback can play an important role in halting accretion to the host galaxy. Such dedicated observations, in combination with accurate simulations of outflows and the CGM, would greatly contribute to our understand of outflows and ultimately their potential for converting star-forming galaxies on the MS to passive, “red and dead” galaxies where SF has been extinguished.

Multiwavelength Characterisation of an ACT-Selected, Lensed Dusty Star-forming Galaxy at $z = 2.64$

The work described throughout this Chapter is part of [Roberts-Borsani et al. \(2017\)](#) “Multiwavelength Characterization of an ACT-selected, Lensed Dusty Star-forming Galaxy at $z=2.64$ ”.

6.1 Introduction

A longstanding problem in galaxy evolution is tracking the build-up of stellar mass over cosmic time ([Madau & Dickinson 2014](#), and references therein). Gaining a complete census of the star formation history of the universe relies on a large suite of complementary observations, which can probe different regimes in star formation, including both unobscured (traced by ultraviolet light and nebular narrow emission lines, such as $H\alpha$) and obscured (traced by dust continuum emission) star formation. The discovery and follow-up of 850 μm -bright submillimeter galaxies (SMGs; [Smail et al. 1997](#); [Barger et al. 1998](#); [Hughes et al. 1998](#)) with flux densities from a few to ~ 10 mJy by the Submillimetre Common User Bolometric Array (SCUBA) opened a new window in mapping the buildup of stellar mass in the universe. The past decade has seen significant progress in deep, blank-field

surveys at millimeter and submillimeter wavelengths over small patches of the sky. While rare, SMGs account for a non-negligible fraction of the cosmic SFR at $z > 1$ (Blain et al. 2002; Magnelli et al. 2011; Murphy et al. 2011; Casey et al. 2012a,b; Magnelli et al. 2013; Casey et al. 2014).

Until recently, the properties of SMGs were difficult to constrain, due to the lack of ultraviolet or optical counterparts with which their redshifts could be measured. These starbursting galaxies are hypothesized to be the high-redshift progenitors of massive elliptical galaxies, but display little to no emission at shorter wavelengths. Early work aiming to localize SMGs using radio counterparts (Chapman et al. 2005) had limited success, for a possibly biased sample. More recently, the onset of high sensitivity, large bandwidth millimeter and submillimeter receivers has revolutionized the field of detecting and studying a variety of dusty star-forming galaxy (DSFG) populations (Casey et al. 2014, and references therein), allowing for the determination of the redshifts for a substantial number of objects using bright molecular and atomic fine structure lines (e.g., Weiß et al. 2009; Vieira et al. 2013; Weiß et al. 2013; Strandet et al. 2016). Despite this new discovery space opening for the study of SMGs, many questions remain about the state of their large reservoirs of molecular gas, including the characterisation of their kinematics (Hodge et al. 2012), excitations (Walter et al. 2011), and star formation efficiencies.

In this paper, we present new observations of a lensed DSFG detected by the Atacama Cosmology Telescope (ACT; Swetz et al. 2011), ACT J2029+0120 (hereafter ACT J2029), using the IRAM 30 m telescope, and make the case for possible observations of a molecular outflow. We use these new data to establish the galaxy's redshift, characterize the excitation conditions and other properties of its molecular gas, and confirm its status as a lensed system. In Section 6.2 we describe our earlier observations of the source, which were insufficient to determine its redshift, and the new observations taken at the IRAM 30 m. In Section 6.3 we present the parameters derived from these new observations, and in Section 6.4 we discuss the implications of our observations for ACT J2029's intrinsic properties. Finally, in Section 6.5 we provide a short summary and conclusions of our findings. All magnitudes are in the AB system (Oke & Gunn 1983)

6.2 Observations

ACT J2029 was initially detected as a point source in ACT three-band observations of an equatorial field overlapping the Stripe 82 region of deep SDSS coverage (Gralla et al., in prep). Without deboosting corrections, its measured flux densities at 148, 218, and 277 GHz were measured to be 9.0 ± 2.0 mJy, 22.0 ± 3.0 mJy, and 52.8 ± 6.1 mJy, respectively, with a nominal 218 GHz position of $\alpha=20:29:55.7$ $\delta=+01:20:54.5$ (J2000; $\pm 6''$ positional uncertainty).

6.2.1 Initial Spectroscopy

The source was subsequently further observed for 27,000 s with the Redshift Search Receiver (RSR; Erickson et al. 2007) on the Large Millimeter Telescope (LMT) and a single emission line was detected at a frequency of 95.0031 ± 0.0015 GHz, with an apparent flux of 6.05 ± 0.28 Jy km s⁻¹ and a velocity FWHM (corrected for instrumental resolution) of 236.6 ± 9.1 km s⁻¹. The absence of any other lines in the RSR’s 73–111 GHz bandwidth ruled out the CO(5–4) transition as the detected emission line, or any higher- J transition. However, CO(4–3) at $z = 3.85$, CO(3–2) at $z = 2.64$, CO(2–1) at $z = 1.43$, and CO(1–0) at $z = 0.21$ remained as possible identifications.

The source was then further observed with the Combined Array for Research in Millimeter-wave Astronomy (CARMA) in its compact D configuration at 95 GHz (proposal c1204; PI Baker), with a total of 4.8 hrs on source. Following calibrations of the observations for a synthesized beam of $5.6'' \times 4.4''$, an integrated line spectrum was derived by taking the integrated intensity (moment0) map and summing over all pixels known to contain flux, as described in Section 3 of Alatalo et al. (2013). Integrating over all channels with line emission (spanning 400 km s⁻¹ in velocity), a spatially unresolved detection of line emission was obtained at an RA and DEC of $\alpha=20:29:55.495$ $\delta=+01:20:58.944$ (J2000), which we show in Figure 6.3.

The CARMA position of ACT J2029 revealed an apparent optical counterpart for the DSFG at $\alpha=20:29:55.479$ $\delta=+01:20:58.610$, 2MASX J20295548+0120580 (hereafter 2MASX J20295548), for which optical spectroscopy at the Southern African Large Telescope (SALT; Buckley et al. 2006) was obtained. Longslit observations of the source were carried out using the Robert Stobie Spectrograph (RSS, Burgh et al. 2003; Kobulnicky et al. 2003) for a total exposure time of 1200 s and the data were reduced using the SALT

science pipeline (Crawford et al. 2010). A redshift was verified by visual inspection of the spectra using absorption features from Ca II H and K, the G-band, and Mg I $\lambda 5172.7$ (no emission lines were found), yielding a spectroscopic redshift of $z = 0.3242 \pm 0.0002$ for 2MASX J20295548.

6.2.2 Imaging

In order to perform SED-fitting of ACT J2029, we search for photometric observations of the source. We find the source was observed as part of the 2MASS (Skrutskie et al. 2006) and *WISE* (Wright et al. 2010) All-Sky Data Releases, as well as the Panoramic Survey Telescope and Rapid Response System (Pan-STARRS) Data Release 1 (DR1; Chambers et al. 2016), which became public on 2016 December 19. Thus, optical and NIR photometry is available for the source, with *grizy* photometry reaching 5σ depths of 23.3, 23.2, 23.1, 22.3, 21.3 mag, respectively.

Both ACT J2029 and 2MASX J20295548 were also observed with the Near-Infrared Camera/FabryPérot Spectrometer (NICFPS) instrument on the ARC 3.5 m telescope at the Apache Point Observatory (Vincent et al. 2003) with a *Ks*-band ($\lambda \sim 2.1 \mu\text{m}$) 5σ detection limit of $m = 21.35$ mag. The data were reduced as described in Section 2.3 of Menanteau et al. (2013) and we use this photometry in our SED-fitting of the system, presented in Section 6.4.2.

6.2.3 IRAM 30m

The IRAM 30m observations of ACT J2029 were carried out as part of the 2015 IRAM Summer School, over the nights of 2015 September 13 and 15 using the Eight MIXer Receiver (EMIR, Carter et al. 2012) mounted on the telescope. EMIR has four different bands, E090, E150, E230, and E330, spanning the 3, 2, 1, and 0.9 mm windows respectively. Each band provides ~ 8 GHz of instantaneous, dual-polarization bandwidth.

The data were recorded using the Wideband Line Multiple Autocorrelator (WILMA), which provides a spectral resolution of 2 MHz, corresponding to velocity resolutions of ~ 6 , 3, and 2 km s^{-1} for the E090, E150, and E230 bands, respectively. Dual-frequency EMIR setups were used throughout the observations. We employed E090/E150 (3/2 mm) and E090/E230 (3/1 mm) configurations to search for CO transitions. In these configurations, each receiver has a bandwidth of 4 GHz. The 3 mm receiver was used as a reference and tuned to the previously detected 95 GHz CO transition, while the 2 mm

receiver was tuned to 142.5 GHz and 158 GHz, and the 1 mm receiver to 221 GHz and 253 GHz. Additional lines of high-density gas tracers CS(7–6), HCN(4–3), and HCO⁺(4–3) were targeted with the Fast Fourier Transform Spectrometer (FTS). The FTS backend has a spectral resolution of 195 kHz, corresponding to $\sim 0.5 \text{ km s}^{-1}$ for the E090 band. E090/E230 (3/1 mm) EMIR configurations were repeated with a slightly shifted 3 mm tuning at 97 GHz to better center on the dense gas tracers, and 1 mm frequency tunings at 97 GHz and 221/253 GHz, respectively.

The observations were carried out in wobbler switching mode, with a switching frequency of 1.5 Hz. Pointing was checked frequently and was found to be stable within 3". The calibration was done every 12 minutes using standard hot/cold-load absorber measurements. The data reduction was performed using the GILDAS software's CLASS package. Scans with distorted baselines were excluded from the dataset ($\sim 22\%$), while scans showing platforming (i.e., steep baseline jumps arising in the backend electronics) were corrected for this effect and included. Linear baselines were subtracted from the individual spectra, except for the C I /CO(7–6) spectrum, for which we fit a first, third and fourth order polynomial (see Section 6.3.2 for reasons).

6.3 Results

6.3.1 The Redshift of ACT J2029

For our IRAM 30m observations we adopted an observing strategy similar to that developed by Weiß et al. (2009) to determine the redshift of the object. The 3/2 mm setup was tuned to 95/142 GHz to confirm and improve the line shape of the 95 GHz feature and to test for redshifts $z = 1.43$ and $z = 3.85$, resulting in a non-detection at ~ 142 GHz. Subsequently, the 2 mm band was tuned to 158 GHz, where a second line was detected at 158.3 GHz. This uniquely identifies the 95.0 and 158.3 GHz line features as CO(3–2) and CO(5–4) at a redshift $z = 2.64$. CO(7–6) and CO(8–7) lines at 221.6 and 253.2 GHz were also detected using the 3/1 mm (95/221 GHz) and 3/1 mm (95/253 GHz) setups, respectively. A redshift of $z = 2.64002 \pm 0.00006$ was derived by combining the centroids of all the CO lines using a variance-weighted average. All four CO line profiles are very similar and well described by single Gaussian components, as shown in Figure 6.1. Their line parameters are presented in Table 6.1. The uncertainties associated with the integrated intensities are derived from the uncertainties in the free parameters of the Gaussian fits.

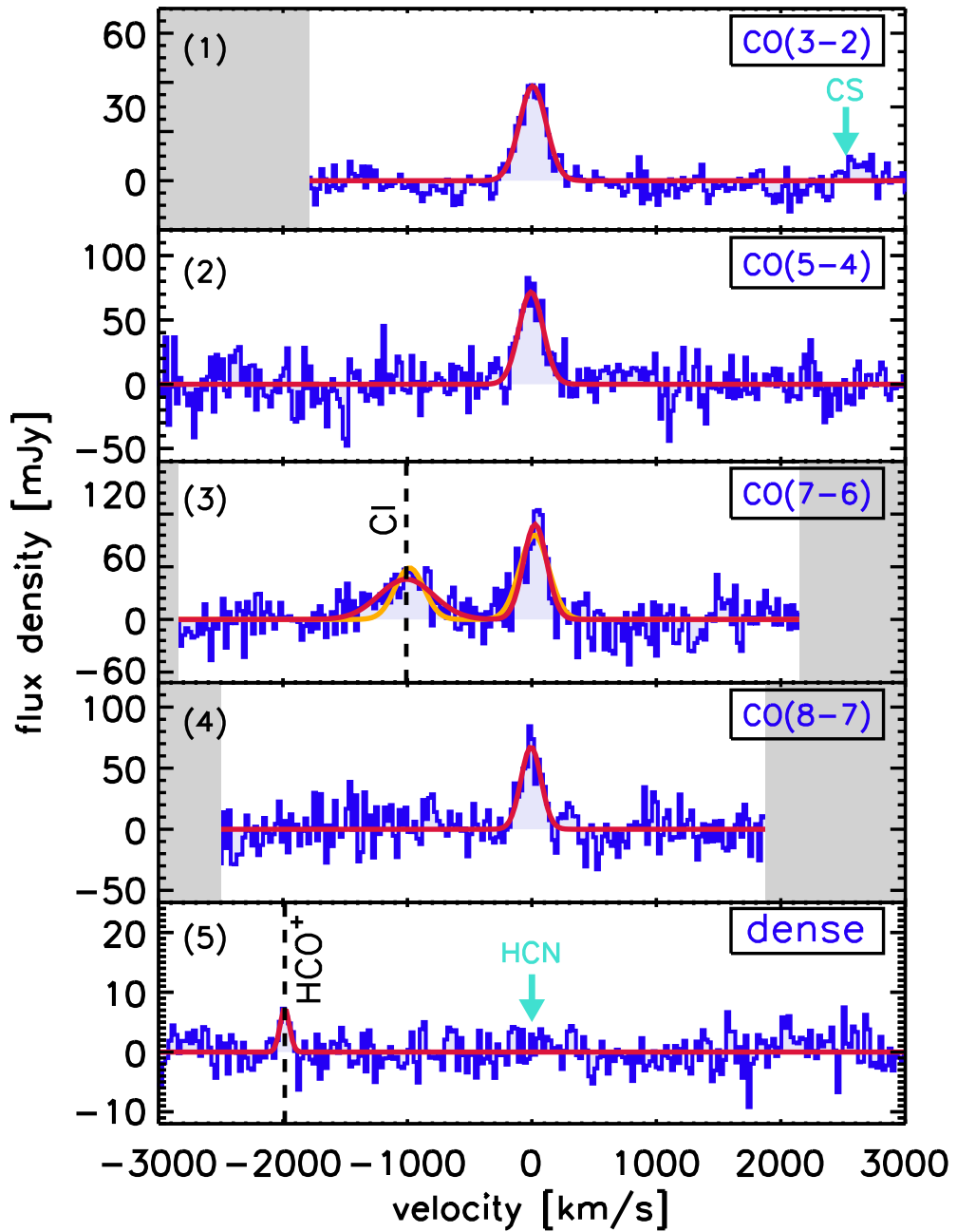


Figure 6.1. Observed ^{12}CO and CI transitions for ACT J2029, taken with the IRAM 30m. The 4 CO transitions observed with WILMA are $J = 3-2$ (panel 1), $5-4$ (panel 2), $7-6$ (panel 3), and $8-7$ (panel 4). Panels 1 and 5 display the upper limits on the other dense gas tracers and the tentative $\text{HCO}^+(4-3)$ detection (taken with the FTS). Panel 3 also shows the CI detection, with a linear baseline fit. The red line indicates the best fit Gaussian function from CLASS and the gray shaded regions mark the limits of our data. The orange line in panel 3 represents a Gaussian fit to the CI line fixed to width of $\text{CO}(7-6)$.

6.3.2 Line Properties

C I($^3\text{P}_2-^3\text{P}_1$) was detected in conjunction with CO(7-6) at 222 GHz using the EMIR 3/1 mm (95/221 GHz) setup with the WILMA backend and applying a linear baseline correction. Like the CO line profiles, the C I line profile is well described by a single Gaussian component, but with a FWHM that is more than double the CO line widths.

In an attempt to constrain the robustness of the potentially larger FWHM, we employed a Monte Carlo approach to randomly select only 50% and 75% of the scans, subtract the baseline with a first order polynomial, and fit single Gaussians to the C I and CO(7-6) lines. This process was repeated five times for each percentile. In all cases, the line width of the C I profile remained extended relative to the CO(7-6). Additionally, we re-fit the profiles from the full data set using velocity bins ranging from 3 to 55 km s⁻¹. We find that the maximum variation from the determined C I line width across all velocity bins is 67.4 km s⁻¹ ($\sim 5\%$), and from the measured peak flux density is 0.3 mJy ($<1\%$). Finally, we tested subtraction of third and fourth order polynomial baselines before fitting a single Gaussian component to the C I profile. This was repeated for four random sets of 75% of the data, as well as for the full data set; all ten fits returned a C I width larger than that of the CO lines. Therefore, the line width and flux determinations appear robust, suggesting real broadening of the C I line compared to the CO lines. Nevertheless, the larger C I FWHM may be due to baseline effects and we caution that independent confirmation of the broadening is required for absolute certainty. The implications of a wider line profile of C I with respect to CO is discussed in Section 6.4.3. The profile of the C I line is also very well fit by several two-component Gaussian fits, with a blueshifted component offset by $\sim 100\text{-}400$ km s⁻¹ from a systemic component. The reduced χ^2 of every two-component fit varies by less than $\Delta\chi^2 \sim 0.01$ relative to other two-component fits, and is always $\Delta\chi^2 \sim 0.001$ lower compared to the single-Gaussian fit. Therefore, we argue a two-component Gaussian fit is not sufficiently justified to replace a single Gaussian fit.

We also report a tentative detection of the HCO⁺(4-3) line at 98 GHz in the 3 mm band using the FTS backend, with an integrated S/N ratio of 3.46. The line is well described by a single Gaussian profile, whose parameters are presented in Table 6.1. The line appears to be blueshifted with respect to the systemic (CO) redshift by more than 100 km s⁻¹, and also has a much narrower width than any of the CO transitions. Using Monte Carlo simulations that account for the peak flux of the HCO⁺ line and the noise

in our spectra, we find that in 10,000 random samples the probabilities of obtaining such a velocity offset and smaller line width with respect to our CO observations are less than 0.1% and 0.01%, respectively. Due to the low S/N ratio, however, it is difficult to draw robust conclusions, so we do not include this line in our analysis. From our observations, we also place strong upper limits on the emission of the HCN(4–3) and CS(7–6) lines, by requiring that line widths be similar to that of the CO emission lines and calculating 3σ integrated intensities. Limits on fluxes and luminosities are provided in Table 6.1.

Table 6.1. All IRAM 30m line detections.

Line	ν_{obs} [GHz]	FWHM [km/s]*	S_ν [mJy]*	I [Jy km/s]*	L' [$\times 10^{10}$ K km s $^{-1}$ pc 2]*	Integration time [s]	EMIR Setup
CO(3-2)	94.997(2)	270.1 \pm 14.8	39.7 \pm 2.8	11.3 \pm 0.5	41.8 \pm 1.9	9900	E090
CO(5-4)	158.321(5)	229.3 \pm 25.2	71.7 \pm 10.2	17.4 \pm 1.5	23.1 \pm 2.1	2820	E150
CO(7-6)	221.59(2)	231.3 \pm 27.7	87.5 \pm 13.1	21.4 \pm 1.9	14.5 \pm 1.3	7620	E230
CO(8-7)	253.25(9)	190.9 \pm 22.7	72.8 \pm 11.6	14.7 \pm 1.5	7.6 \pm 0.8	7140	E230
C1(2-1)	222.4(7)	590.5 \pm 98.8	37.6 \pm 7.9 ^b	23.5 \pm 3.0	15.8 \pm 2.0	7620	E230
CS(7-6)	94.198 ^a	–	< 12.1	< 1.0	< 3.7	24600	E090
HCN(4-3)	97.392 ^a	–	< 8.9	< 0.7	< 2.5	24600	E090
HCO ⁺ (4-3)	98.004 ^a	94.2 \pm 25.6	7.6 \pm 2.8	0.7 \pm 0.2	2.6 \pm 0.7	24600	E090

*All uncertainties are quoted at the 1σ level and all values are uncorrected for lensing. Upper limits are robust to 3σ .

^aExpected redshifted frequency of the line, assuming $z=2.64002 \pm 0.00006$.

^bThe peak flux density derived with the line width fixed to that of the CO(7-6) line is $S_\nu=51.5 \pm 5.77$ mJy.

As shown by [Solomon et al. \(1992\)](#), line luminosity can be expressed in terms of total line flux as:

$$L'_{\text{line}} = 3.25 \times 10^7 S_{\text{line}} \Delta v \nu_{\text{obs}}^{-2} D_L^2 (1+z)^{-3} [\text{K km s}^{-1} \text{ pc}^2], \quad (6.1)$$

where $S_{\text{line}} \Delta v$ is the velocity integrated flux in Jy km s^{-1} , D_L is the luminosity distance in Mpc, and ν_{obs} is the observed central frequency of the line in GHz. The luminosities of all detected lines are derived using Equation 6.1 and are listed in Table 6.1, along with all other line properties.

6.4 Discussion

The observations described above make it possible to characterize the molecular gas in ACT J2029 in an unusual level of detail - a useful opportunity given continuing uncertainties in exactly how DSFGs contribute to the cosmic histories of SF and black hole accretion. We therefore proceed below to use the new data to assess the origin of ACT J2029's molecular excitation, determine whether it is a strongly lensed system, and interpret the anomalous ratios of its CO and C I line widths and fluxes in light of our conclusions on those two points.

6.4.1 CO SLED Indicative of an AGN

Figure 6.2 shows the ^{12}CO spectral line energy distribution (SLED) constructed with our observations, which peaks at the $J=7-6$ transition. In the same plot, we compare our detections to the starbursts, ULIRGs, and AGN hosts that were observed as part of the *Herschel* Comprehensive ULIRG Emission Survey (HerCULES; PI: van der Werf) by [Rosenberg et al. \(2015\)](#), normalized to the CO(5-4) line. It becomes immediately clear that ACT J2029 is most consistent with the Class III objects from [Rosenberg et al. \(2015\)](#), which are mainly AGN hosts, although the observed CO transitions alone cannot definitively rule out a match to the Class II objects. The CO consistency with the Class II and Class III objects suggests that the dense molecular gas in this source is exposed to the harsh radiation field of a central AGN ([van der Werf et al. 2010](#); [Rosenberg et al. 2015](#); [Israel et al. 2015](#)).

In order to better characterize ACT J2029, we used the non-local thermal equilibrium

code RADEX (van der Tak et al. 2007) to model the emitted CO intensities. A large parameter grid, $T_{\text{kin}} = 20 - 200$ K, $n_{\text{H}_2} = 10^2 - 10^7$ cm $^{-3}$, and $N_{\text{CO}}/\Delta v = 10^{17.9} - 10^{19.4}$ cm $^{-2}$ (km s $^{-1}$) $^{-1}$ (assuming $\Delta v=10$ kms $^{-1}$), was sampled, where T_{kin} is the kinetic temperature, $N_{\text{CO}}/\Delta v$ the column density per unit velocity gradient of CO, and n_{H_2} the molecular gas number density. The best reproduction of the observed CO intensities is given by the parameters $T_{\text{kin}} = 117$ K, $n_{\text{H}_2} = 2 \times 10^5$ cm $^{-3}$, and $N_{\text{CO}}/\Delta v = 3 \times 10^{18}$ cm $^{-2}$ (km s $^{-1}$) $^{-1}$. This result is also consistent up to $J=8-7$ with the Class II and Class III objects from the Rosenberg et al. (2015) sample, but is inconsistent with the Class I objects: the fit agrees well with our data up to the $J=8-7$ transition, however it drops rapidly at higher- J . This is likely due to the use of single-component gas fits in our RADEX models, which are sufficient to trace the lower- J transitions but insufficient to accurately trace the higher- J transitions. More sophisticated modelling of the higher- J transitions would likely require multiple-component gas fits and additional data. The best-fit model is highlighted as a dashed red line in Figure 6.2. It is important to note, however, that other similar fitting models exist due to degeneracies between T_{kin} and n_{H_2} . A probability density plot of the sampled models is shown as an inset plot in Figure 6.2.

Several CO SLEDs with similar shapes have also been observed in shocked systems such as the central nuclear region of Centaurus A (Israel et al. 2014) and the shocked AGN-driven molecular outflow in NGC 1266 (Alatalo et al. 2011; Pellegrini et al. 2013; Glenn et al. 2015). In both cases, the CO SLED rises and peaks around CO(7-6), then decreases at higher- J . Such a pattern is also seen in both AGN hosts and shock hosts, however the transitions we have detected in ACT J2029 do not allow us to differentiate between these possibilities. In each of the first two shock-dominated sources noted above, an AGN is also present, mechanically or radiatively driving an outflow, which in turn produces the shocked line ratios in the CO SLED.

Bothwell et al. (2013a) and Spilker et al. (2014) derive average DSFG CO SLEDs that look broadly similar to the SLED for ACT J2029; however, they have slightly shallower slopes (below their peak J) and less pronounced “knees”. In contrast, the CO SLED of Cloverleaf (Bothwell et al. 2013c), a well-known AGN host, has a slope and knee that are in much better agreement with those of ACT J2029. The review by Casey et al. (2014) on high- z DSFGs characterizes the prevalence of AGN hosts among SMGs as high, but not universal, with 1/3 of sources showing signs solely of prolific SF, and 2/3 requiring AGN. Therefore, an additional possibility exists to explain the shape of ACT J2029’s CO

SLED and, although no radio or X-ray detections of ACT J2029 exist, the CO SLED is suggestive of the source hosting an AGN. However, a definitive confirmation of the presence of an AGN will require higher resolution, deeper observations to characterize delensed morphology, or detections of X-rays or radio (jet/lobe) emission.

To assess whether ACT J2029 resembles the high- z Main Sequence of star-forming galaxies, we compare its CO SLED to those of other star-forming objects in the literature. Using CO SLEDs from 4 BzK galaxies to obtain an average CO SLED from CO(1–0), CO(2–1), CO(3–2) and CO(5–4) transitions, [Daddi et al. \(2015\)](#) compare a BzK CO SLED to average CO SLEDs for local (U)LIRGs, SMGs and the inner disk of the Milky Way. Their results suggest ACT J2029 has a CO SLED very similar in shape to those of BzKs and SMGs up to the CO(5–4) transition. However, such a comparison extends only to CO(5–4) whereas the knee of our data occurs at CO(7–6), making it difficult to compare high- J transitions where the nature of the excitation is likely to be determined.

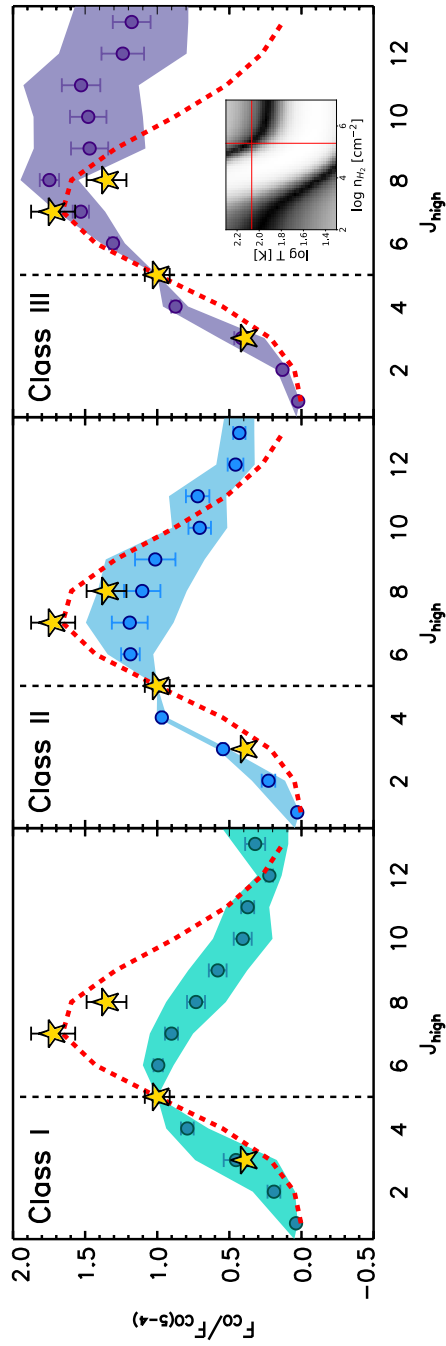


Figure 6.2. The distribution of ^{12}CO line fluxes, normalized to that of the $^{12}\text{CO}(5-4)$ line, for the HerCULES sample of Class I (star-forming objects, left panel), Class II (starbursts and Seyferts, middle panel), and Class III (ULIRGs and QSOs, right panel) objects (Rosenberg et al. 2015). The filled circles represent the mean CO SLED, the colored shaded regions show their $\pm 1\sigma$ deviations off the mean, and the error bars represent the uncertainty of the mean. The ACT J2029 fluxes are represented by the (yellow) stars. The dashed red line in each panel represents the best RADEX fit to the observed CO fluxes, which corresponds to $T_{\text{kin}} = 117$ K, $n_{\text{H}} = 2 \times 10^5 \text{ cm}^{-3}$ and $N_{\text{CO}}/\Delta v = 10^{16} \text{ cm}^{-2}(\text{km s}^{-1})^{-1}$. A T vs. n_{H_2} probability plot is shown as an inset to the right panel, highlighting a range of other possible fits allowed by temperature-density degeneracies. The best RADEX fit is represented by the red crosshairs.

6.4.2 Lensing Status and SED Fitting

As seen in Section 6.2, discrepant CO and optical redshifts are highly suggestive of gravitational lensing. A Pan-STARRS *i*-band image of the system is shown in Figure 6.3, with our CARMA data overlaid, and a *riz* color image is presented in the upper right inset of the plot. A Sérsic profile fit to the image reveals slight excess emission to the northeast and southwest of the elliptical galaxy (see Appendix D), suggestive of a background lensed galaxy. Upon closer inspection of the color inset image, multiple sources appear present and thus the image appears to support this suggestion.

With a secure DSFG redshift in hand, we are now in a position to estimate the lensing magnification quantitatively. Although no lens model is available for our source, [Harris et al. \(2012\)](#) showed for a sample of star-forming galaxies that estimation of the lens magnification is possible using the line width and luminosity of the CO(1–0) transition (see also [Bothwell et al. 2013c](#), [Goto & Toft 2015](#); cf. [Aravena et al. 2016](#), [Sharon et al. 2016](#)). Assuming a CO(3–2)/CO(1–0) luminosity ratio of 0.9 ± 0.4 ([Sharon et al. 2016](#)) and a CO(1–0)/CO(3–2) line width ratio of 1.15 ± 0.06 ([Ivison et al. 2011](#)) for ACT J2029, we estimate a lens magnification $\mu = 25 \pm 11$ using Equation 1 of [Harris et al. \(2012\)](#). Although a lens model is clearly needed to fully confirm any magnification and there is substantial uncertainty in our derived value, it becomes immediately clear that ACT J2029 is likely lensed.¹

To further illustrate and characterise the lensing nature of the DSFG, we make use of the Pan-STARRS *grizy* filters, 2MASS J- and H-band, NICFPS Ks-band, all *WISE* bands, and our ACT photometry to fit an SED to ACT J2029, using the HYPERZ code developed by [Bolzonella et al. \(2000\)](#). The optical photometry was obtained by using the SExtractor ([Bertin & Arnouts 1996](#)) software in dual-image mode on each of the Pan-STARRS images, whilst the NIR photometry was taken from the 2MASS and *WISE* All-Sky Data Releases, respectively. We run HYPERZ with the standard library templates, which include nebular emission lines ([Coleman et al. 1980](#); [Kinney et al. 1996](#); [Fioc & Rocca-Volmerange 1997](#); [Silva et al. 1998](#); [Chary & Elbaz 2001](#); [Bruzual & Charlot 2003](#); [Polletta et al. 2007](#); [Michałowski et al. 2010](#)), a fixed photometric redshift of $z = 2.64$ to match our derived spectroscopic redshift, and a dust column with $A_V \in [0.0-3.0]$ mag following either a [Calzetti et al. \(2000\)](#) starburst or a [Prevot et al. \(1984\)](#) Small Magellanic

¹ We note that a CO(1–0) line width larger than that of CO(3–2) (e.g., as seen by [Ivison et al. 2011](#) for a small SMG sample) would lead to a lower magnification estimate.

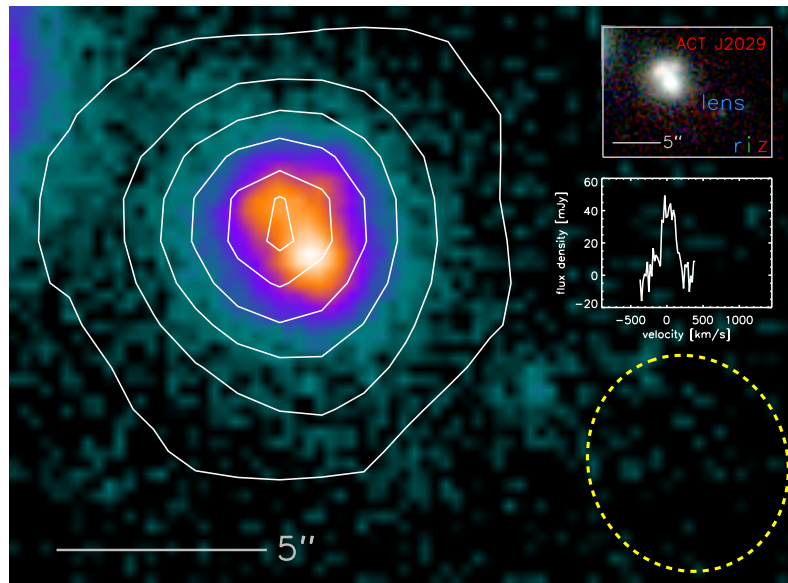


Figure 6.3. A Pan-STARRS *i*-band image of ACT J2029 and 2MASX J20295548 with the CARMA contours overplotted (white). The ellipse at lower right represents the CARMA beamsize. An *riz* color image and the positions of ACT J2029 and 2MASX J20295548 is shown at upper right. The CARMA integrated emission line is shown in the middle right. The two sources in the *i*-band image have positions less than $0.5''$ apart and are spatially blended. However, what appears to be a lensed arc is clearly visible in the *riz* image.

Cloud extinction law. Each template has been fit (by itself) to our data twice, once with the Calzetti et al. (2000) law and once with the Prevot et al. (1984) law. We first use all of our SED constraints and conclude that none of the templates we used can correctly reproduce the photometry of ACT J2029. However, as discussed in the previous section, the most likely hypothesis for our object is that it is lensed by a foreground galaxy at $z=0.3242$, and therefore the photometry at shorter wavelengths, namely shortward of the *WISE* W3 band, is contaminated by the foreground galaxy. If we use only *WISE* W3, W4 and ACT photometric constraints while setting upper limits to all photometry blueward of $\approx 1\mu\text{m}$, we find a better fit with reduced $\chi^2 \sim 1.63$. We also fit a low-redshift SED using only upper limits on all photometry blueward of $\approx 1\mu\text{m}$ and a fixed redshift of $z=0.32$. The derived SEDs are presented in Figure 6.4. It becomes obvious that the optical data are well fit by the low-redshift object, while the *WISE* W3 and W4 bands are elevated and likely contaminated by both objects. We conclude that the elevated *WISE* points suggest that the NIR fluxes are indeed contaminated by the foreground source, 2MASX J20295548, making it impossible to derive a robust SED fit from which one can estimate global properties for ACT J2029. Accurate modeling of the contaminating fluxes

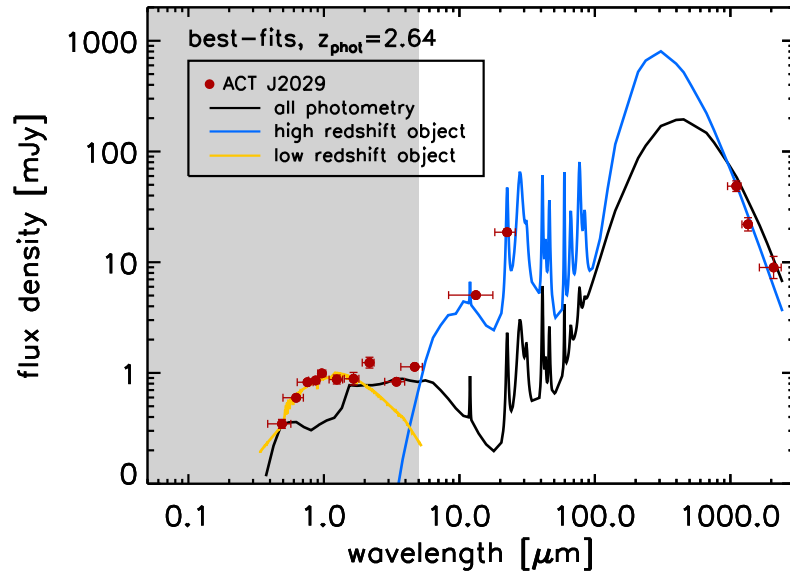


Figure 6.4. The best-fit SEDs for ACT J2029 (black and blue) and 2MASX J20295548 (yellow), fixed to redshifts of $z = 2.64$ and $z = 0.32$, respectively. The gray shaded region represents wavelengths where the photometry is likely contaminated by both the high- z object and the foreground object. The black line illustrates the best fit ACT J2029 SED making use of all available photometry, while the blue line uses the same data but with upper limits to all photometry blueward of the *WISE* W3 band (ie., the shaded region). The yellow line shows the best-fit SED to 2MASX J20295548, applying upper limits to all the photometry in the shaded region. A Calzetti et al. (2000) extinction law was preferred for all fits.

would likely require higher-resolution photometry to fully characterize the low-redshift foreground galaxy.

6.4.3 The Enhanced C I Flux and Velocity

The mean value of the C I(2–1)/CO(3–2) luminosity ratios in Walter et al. (2011) shows that in most SMGs the C I(2–1) line has a luminosity $(0.17 \pm 0.06)L'_{\text{CO}(3-2)}$, consistent for both galaxies that host quasars and those that do not. ACT J2029 shows an excess of C I(2–1) emission compared to CO(3–2), with $L'_{\text{CI}(2-1)}/L'_{\text{CO}(3-2)} = 0.378 \pm 0.051$, twice the mean value for other high-redshift sources. This excess is significant at greater than a 2σ level and is shown in Figure 6.5, which we compare to the lensed and unlensed objects presented in Walter et al. (2011).

Most local and high- z sources do not show substantial C I flux enhancements (Walter et al. 2011; Alaghband-Zadeh et al. 2013; Israel et al. 2015), but there are some marked exceptions. Pellegrini et al. (2013) show that the local AGN-driven molecular outflow host

NGC 1266 displays enhanced C I emission compared to ^{12}CO , as does the nuclear region of Centaurus A (Israel et al. 2014). In both cases, it is argued that the enhanced C I emission is due to the shocked gas chemistry in the nuclear regions where the line emission originates (in both cases, this scenario is supported by the CO SLED). ACT J2029 could be a similar Class III object hosting an AGN in its center, with shocked dense gas contributing to an enhanced C I/CO line ratio.

The difference in the C I and CO linewidths of ACT J2029 is also unusual. In all objects where resolved velocity information is available for both C I and CO, the linewidths of the two lines are consistent (Walter et al. 2011, and references therein). In Section 6.3.2, we showed that the C I(2–1) line is more than twice as wide as the CO lines, suggesting that the source of the C I and CO emission cannot be identical.

If we combine the large linewidth difference with the enhanced C I, an intriguing possibility suggests itself, namely, that we are observing differential lensing of a compact nuclear region of this source, which hosts an AGN-driven molecular outflow. Lensing preferentially enhances compact regions (Hezaveh et al. 2012), so it is possible that the foreground lens (2MASX J20295548) has magnified the nuclear region of ACT J2029, including outflowing gas traced by C I and CO. Rawle et al. (2014) used the Submillimeter Array and the Karl G. Jansky Very Large Array to map the molecular lines of HLS0918, a lensed submillimeter galaxy at $z = 5.2430$. In this case, they were able to spatially differentiate multiple velocity components in the molecular gas, including a very broad (VB) component consistent with an outflowing region. Rawle et al. (2014) show that the ratio of C I(2–1)/CO(7–6) in the VB component is larger than those seen in all other regions, suggestive of enhanced C I (although the velocity structures in HLS0918 are complex, such that degeneracies arise when fitting the components in the blended C I and CO(7–6) lines). It is possible that ACT J2029 exhibits a similar CI-enhanced outflow region, while lacking the complex velocity structures that are observed in the Rawle et al. (2014) source.

6.5 Conclusions

This work presents multi-transition ^{12}CO and C I(2–1) measurements of ACT J2029, a lensed sub-millimeter galaxy found by the ACT survey. Following up on earlier line detections by the LMT and CARMA, we confirm a source redshift of $z = 2.640$. To summarize our work:

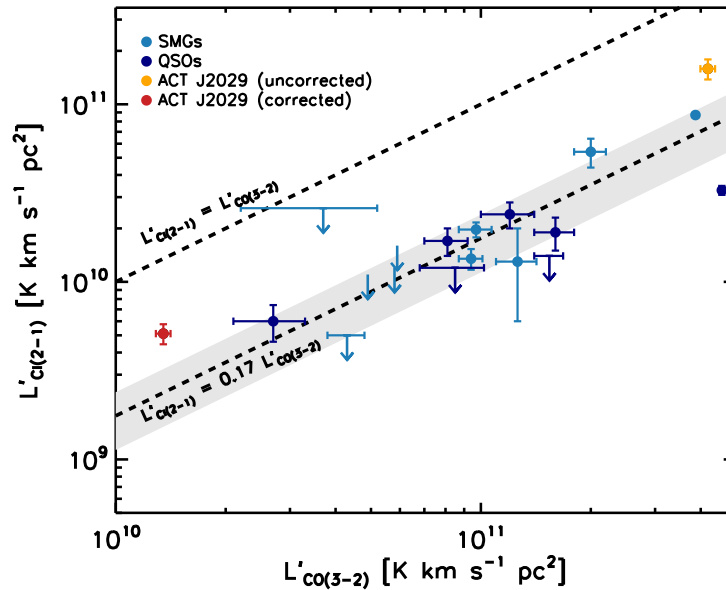


Figure 6.5. The $L'_{\text{CI}(2-1)}/L'_{\text{CO}(3-2)}$ ratio of ACT J2029 (yellow and red, uncorrected and corrected for lensing, respectively) is overplotted with other lensed and unlensed high-redshift QSOs (navy blue) and SMGs (teal) from [Walter et al. \(2011\)](#). All [Walter et al. \(2011\)](#) L' values are uncorrected for lensing. The average $L'_{\text{CI}(2-1)}/L'_{\text{CO}(3-2)}$ line is overplotted, with the 1σ standard deviation limits shaded in gray. Even taking magnification into account, ACT J2029 has a $L'_{\text{CI}(2-1)}/L'_{\text{CO}(3-2)}$ ratio substantially higher than other high-redshift galaxies. Classifications of SMGs and QSOs were taken from the DIGAME catalogs (<http://www.digame-db.online>).

- The CO(3–2), CO(5–4), CO(7–6), CO(8–7), and CI(2–1) transitions are detected at high significance, but only upper limits on the emission of the high-density gas tracers CS(7–6) and HCN(4–3) are obtained. Additionally, we also report a tentative detection of the HCO⁺(4–3) line.
- We confirm a redshift of $z = 2.64$ for ACT J2029, based on IRAM 30m observations of multiple CO lines.
- We construct a CO SLED starting from the four detected CO transitions. Based on a comparison with the star-forming, star-bursting, and AGN-hosts from the HERCULES survey, the CO SLED of ACT J2029 is consistent with a Class II or Class III object, i.e., with a starburst, ULIRG, or powerful AGN host.
- Non-LTE modeling suggests that ACT J2029 is more consistent with a Class III AGN host object, characterized by a $T_{\text{kin}} = 117$ K, $n_{\text{H}_2} = 2 \times 10^5$ cm⁻³, and $N_{\text{CO}}/\Delta v = 3 \times 10^{18}$ cm⁻² (km s⁻¹)⁻¹ modulo non-trivial parameter degeneracies.

-
- We provide convincing evidence to support the lensing status of ACT J2029 by (i) spectroscopically confirming the redshift of a foreground source inconsistent with that of ACT J2029, and whose position lies less than $0.5''$ away, and (ii) estimating a magnification factor of $\mu \approx 25$ for ACT J2029 via the fiducial relation of [Harris et al. \(2012\)](#).
 - The velocity width of the C I line appears to be substantially larger than what is seen in all CO transitions, and the $L'_{\text{CI}(2-1)}/L'_{\text{CO}(3-2)}$ ratio appears to be larger than what is typically seen in lensed and un-lensed SMGs and QSO hosts. The latter discrepancy would be in agreement with what has been observed in shocked systems, such as Centaurus A and NGC 1266. If confirmed, the large C I width and enhanced C I emission could be explained by differential lensing, in which a shocked, centrally concentrated outflow (traced by the enhanced C I) has been preferentially magnified compared to the larger scale molecular gas (traced by CO).

Conclusions and Future Work

Galactic-scale outflows play a crucial role in regulating the gas contents of galaxies in current galaxy evolution models. However, thus far observations have been largely limited to more extreme and exotic objects instead of normal Main Sequence galaxies that produce the vast majority of star formation in the Universe. One of the primary reasons for this is the comparative ease of detecting outflows in extreme objects compared to normal galaxies, due to the intrinsic faintness of outflows and their apparent correlation with increased star formation activity. However, the arrival of large spectroscopic data sets over a wide range of wavelengths has allowed outflow studies to extend out towards higher redshifts and down to normal galaxies. The largest such data sets are focused on observations of the local Universe ($z < 1$) and have provided the basis for this Thesis.

Using data sets from the SDSS, MaNGA, xCOLD GASS and ALFALFA surveys, we have investigated the primary driving mechanisms of outflows in the local Universe, tested their significance as mechanisms for galaxy quenching and their role in regulating the cycling of gas in and out of galaxies, compared their kiloparsec and integrated properties, and added constraints to their multiphase nature. We provided evidence to suggest that, despite being common among star-forming systems, outflows in high mass, normal galaxies do not appear to be an important quenching mechanism through ejective feedback, with or without the presence of a normal AGN.

7.1 Summary

7.1.1 The Prevalence and Properties of Outflows in Normal Galaxies at $z \sim 0$

In order to determine whether outflows are common among the normal star-forming populations of galaxies at low redshifts, and whether they are powerful enough to quench their host galaxies, we used the full SDSS DR7 data set to look at their prevalence and properties among normal inactive and AGN galaxies and constrained the nuclear mass loading factor from mass outflow rates of neutral gas.

Using a stacking methodology combined with Bayesian inference methods to fit the cold NaD ISM absorption doublet, we searched for outflows over parameter space of global galaxy properties including inclination, Σ_{SFR} , SFR and M_* . We began by testing fiducial limits over the i - Σ_{SFR} plane suggested for driving outflows and found outflows in regions of high Σ_{SFR} and low inclinations ($i < 50^\circ$). Our results extended the Σ_{SFR} limit down by an order of magnitude, from $0.1 \text{ M}_\odot \text{ yr}^{-1} \text{ kpc}^{-2}$ to $0.01 \text{ M}_\odot \text{ yr}^{-1} \text{ kpc}^{-2}$, and the limit of inclination from $i < 60^\circ$ to $i < 50^\circ$. Using the latter limit, we next determined the prevalence of outflows over the SFR- M_* plane, separating galaxies by inclination and morphology: we found that outflows are prevalent among the high-mass ($M_* > 10^{10} \text{ M}_\odot$) populations along and above the galaxy Main Sequence, with characteristic outflow velocities of ~ 100 - 300 km s^{-1} and mass outflow rates of $\lesssim 10 \text{ M}_\odot \text{ yr}^{-1}$. For the latter quantity, we found a strong correlation with SFR, where more mass is expelled at high SFRs, and provided a prescription for simulations.

A comparison between galaxies with and without an AGN showed virtually no enhancement in either outflow prevalence or properties, suggesting normal AGN don't play a more important role in driving optically-selected outflows. We analysed whether such outflows could quench their hosts by deriving a mass loading factor and compared their velocities to the circular velocities of the hosts. We found that such outflows showed values of $\eta < 1$ and the vast majority to have $v_{\text{out}} < v_{\text{circ}}$, consistent with them being weak and unlikely to quench the star formation in their hosts. Again, virtually no difference was found between the inactive and AGN galaxies.

In addition to the outflows, we also found clear detections of redshifted absorption - characteristic of inflowing gas - in virtually identical regions of parameter space as the outflows, but only visible at high inclinations ($i > 60^\circ$) and with mass inflow rates $\lesssim 4$

$M_{\odot}\text{yr}^{-1}$. The interplay between the inflows and weak outflows is likely to give rise to a galactic fountain scenario, where gas gets expelled perpendicularly from the galaxy, before slowing down and raining back down onto the galaxy system, possibly delivering additional gas to sustain star formation.

7.1.2 Spatially Resolved Outflow Properties in Star-forming Galaxies

Once the prevalence of normal NaD -outflows over the SFR- M_{*} had been established, we were able to construct a sample of MaNGA DR15 IFU galaxies likely to host an outflow with which to characterise the kpc-scale properties of outflows and the hosts. We first identified galaxies with and without outflows through a stacking of spaxels within $0.25 R_e$ of the centre and subsequently tested the radial extent of their outflows. We found outflow detections extended out to $\sim 1 R_e$, with a rapidly decreasing power (as traced by derived mass outflow rates and loading factors) and local quenching potential, for which we provide prescriptions for simulations. This analysis also revealed that both the mass outflow rates and the mass loading factor show virtually identical trends, that only the central regions could be powerful enough to potential induce some ejective quenching of the local star formation, and that important fractions of outflowing gas can be missed by $3''$ fibers. Because the relation between SF and stellar mass is also found on kpc-scales, we investigated the prevalence of outflows across the local $\Sigma_{\text{SFR}}\text{-}\Sigma_{*}$ plane and found them to be prevalent along and above the local Main Sequence, similar to what was previously found in our SDSS analysis. By looking at the outflow properties we found that an outflow's power increases as a function along the local Main Sequence, with larger outflow EWs, mass outflow rates and mass loading factors observed high up the local Main Sequence. Additionally, we observed a similar NaD EW trend to that found with SDSS, where stacks higher up the Main Sequence display NaD in absorption, whilst stacks lower down transit into emission.

Thanks to the power of IFU spectra, we were able to separate out and stack individual spaxels of a given galaxy property, thereby removing much of the spatial correlations with outflow radius. We investigated correlations with Σ_{SFR} , sSFR, Σ_{*} , $D(4000)$ and A_V and found that the strongest correlations of outflow properties (i.e., $N(\text{HI})$, \dot{M}_{out} , η and EW) occurred with quantities relating to SF (Σ_{SFR} , sSFR, Σ_{*}) and with Σ_{SFR} proving to be the most significant regulator, most likely due to it being the most direct tracer of SF and cold gas.

To understand whether the presence of NaD -outflows has any impact on the cold HI gas fractions of their hosts, we took advantage of follow up GBT observations of 17 outflow galaxies with matched control samples of non-detection galaxies to derive average “gas fraction spectra” via a Monte Carlo approach, and found that the HI gas reservoirs of outflow galaxies appeared lower than their non-detection counterparts. Finally, we also investigated whether the star formation histories of the host galaxies have any effect in separating outflow galaxies from the non-detection galaxies, but find that the timing since the most recent burst of SFR does not appear to be an important regulator for the presence of NaD outflows.

7.1.3 The Multiphase Nature of Outflows

Because each of these analysis had made use of a derived mass loading factor to determine the quenching potential of outflows, we attempted to provide crucial constraints on the average prevalence and outflow rates of multiphase outflows in galaxies using stacking techniques of data from the xCOLD GASS, xGASS, ALFALFA and MaNGA surveys. Using secure results from our SDSS analysis, we again constructed samples of high mass, low inclination galaxies, where outflows are likely to be present. Prior to any analysis, we performed extensive reliability tests and the careful removal of confused galaxies to ensure potential broad emission would not be due to neighbouring sources, artefacts or RFI. With a final sample of unconfused galaxies and reliable measurements of their heliocentric velocities and linewidths, we constructed gas mass stacks of CO(1-0), HI 21cm, NaD, and H α . Detections of blueshifted absorption and broad emission were found in NaD and H α , signalling the presence of outflows in our selected galaxies and allowing us to determine average mass outflow rates of neutral and ionised gas ($\dot{M}_{\text{NaD}}=7.55 \text{ M}_{\odot} \text{ yr}^{-1}$ and $\dot{M}_{\text{H}\alpha}=0.10 \text{ M}_{\odot} \text{ yr}^{-1}$, respectively). The stacked CO(1-0) and HI emission, however, did not reveal any broad component, likely due to the limiting depth probed. As such, valuable upper limits were placed by determining the smallest outflow signal our codes could detect with >90% reliability and estimating mass outflow rates of $\dot{M}_{\text{CO}} < 19.43 \text{ M}_{\odot} \text{ yr}^{-1}$ and $\dot{M}_{\text{HI}} < 64.48 \text{ M}_{\odot} \text{ yr}^{-1}$.

The derived mass outflow rates were compared to recent results in the literature and found to be consistent with those reported for relatively normal galaxies on the MS. Furthermore, by summing the relative contributions, we derived upper limits on a total mass outflow rate and mass loading factor of $\dot{M}_{\text{tot}} < 34 \text{ M}_{\odot} \text{ yr}^{-1}$ and $\eta < 12.33$, respectively.

At face value, this suggests outflows may have the potential to cause a degree of quenching in their host galaxies, however we argued this is largely dependent on the molecular gas upper limit and, when considering the low outflow velocities, the escape velocity of the host galaxies, and the likely interaction with the CGM, the quenching of normal galaxies via ejective feedback is an unlikely scenario.

7.1.4 A Possible Molecular Outflow in a High- z Galaxy

Because outflows often occur in extreme systems at the peak epoch of star formation, we obtained C I and multitransitional CO observations of a dusty, star forming galaxy, ACT J2029 with the IRAM 30m telescope in order to secure the redshift of the source, investigate its multiwavelength nature, and search for the presence of an outflow. We presented detections of CO(3-2), CO(5-4), CO(7-6), CO(8-7), and C I(2-1) at high significance, a tentative detection of HCO⁺(4-3), and placed strong upper limits on the integrated strength of dense gas tracers (HCN(4-3) and CS(7-6)). Using the unique data set, we determined the redshift of the source and used the high S/N CO detections to construct a CO SLED and determine the likely ULIRG/QSO nature of the source. A morphological and photometric modelling from a suite of publicly available photometry of the source determined its lensed nature. We determined that the velocity width of the C I line is potentially larger than seen in all CO transitions for this object, and that the $L'_{\text{C I}(2-1)}/L'_{\text{CO}(3-2)}$ ratio is also larger than seen in other lensed and unlensed submillimeter galaxies and QSO hosts; if confirmed, this anomaly could be an effect of differential lensing of a shocked molecular outflow.

7.2 Future work

The prevalence and first order integrated properties of galactic-scale outflows have now been generally established. However, there are a number of remaining deficiencies in our knowledge of outflows, and it is crucial that these get addressed for the normal star-forming populations at every epoch, over statistically meaningful samples.

The first steps in further understanding the role of outflows in normal galaxy evolution are to add stronger constraints on the multiphase contributions of outflowing gas with deeper data from state-of-the-art facilities and surveys (e.g., ALMA and JWST) and eventually compare these to the multiphase nature on spatially-resolved scales with inter-

ferometric and IFU data sets (e.g., PHANGS, MaNGA and SAMI). This would provide a good indication of the survivability of various gas phases in the outflow and valuable estimates of total mass outflow rates. Additionally, spatially linking outflow presence and kinematics to the presence of SF and gas in the galaxy disk would prove very valuable. Initial attempts at this should be possible with the arrival of large, resolved data sets of molecular gas and optical tracers such as e.g., PHANGS and MaNGA/SAMI).

Secondly, to ensure determinations of outflow rates are robust, urgently needed are further and strong constraints on outflow chemistries and geometries to avoid the use of largely unconstrained assumptions. Examples of these include knowledge of the ionisation fraction, dust depletion, metallicities and radii of the outflows themselves. Again, such an analysis would ideally be conducted over large, representative samples of galaxies where general conclusions can be made for the dominant galaxy types at each epoch.

Thirdly, the degree of influence of outflows on the the CGM - which can be probed via absorption line studies - must be further established. Whilst the presence of metal-enriched gas in galaxy disks, outflows and the CGM has clearly been verified, further work is required to connect the contents and dynamics of the three components: as an example, accurately determining the relative abundances of metals and multiphase gas contents and comparing these with those observed in the CGM for large samples of galaxies would greatly aid in understanding how much gas is able to transfer from the galaxy disk to the CGM or IGM.

Whilst our knowledge of outflows has rapidly progressed in recent years, our knowledge of them is far from complete. However, with the advent of large integrated and interferometric/IFU surveys (e.g., MaNGA, SAMI, PHANGS), as well as current and next generation telescopes (e.g., ALMA, MUSE, JWST, Keck), these are particularly exciting times to study outflows and their role in galaxy evolution across cosmic time.

Appendix A

Appendix A

A.1 SDSS NaD Fitting Properties

Table A.1: The properties of the flow parameters measured over the DISK, HIGH- i , LOW- i , BULGE, i -logSFR and i -logM $_*$ samples for inactive galaxies. For profiles with blueshifted absorption and redshifted emission, b superscript indicates the blueshifted component, whilst the r superscript refers to the redshifted component of the profile.

Sample	SFR	log M $_*/M_\odot$	EW	Δv	$\Delta v/\cos(i)$	b_D	C_f	N(Na I)	N(H)	Profile	Type
DISK	0.13	10.59	0.07	147 \pm 49	521	118 \pm 43	0.75 \pm 0.26	11.94	19.61	Absorption	Inflow
.....	0.18	10.09	0.06	133 \pm 20	484	136 \pm 19	0.84 \pm 0.26	11.86	19.54	Absorption	Inflow
.....	0.21	9.63	0.06	69 \pm 132	535	97 \pm 104	0.71 \pm 0.28	11.90	19.58	Absorption	Inflow
.....	0.36	9.89	0.07	67 \pm 19	503	111 \pm 20	0.87 \pm 0.25	11.88	19.56	Absorption	Inflow
.....	1.08	9.94	0.01 ^b	-260 \pm 87 ^b	-271 ^b	61 \pm 42 ^b	0.26 \pm 0.27 ^b	11.58 ^b	19.25 ^b	Absorption	Outflow
.....	-0.24 ^r	21 \pm 5 ^r	22 ^r	199 \pm 10 ^r	-0.06 \pm 0.01 ^r	13.84 ^r	21.52 ^r	Emission	Outflow
.....	0.67	10.06	0.05	77 \pm 7	284	117 \pm 8	0.83 \pm 0.22	11.79	19.47	Absorption	Inflow
.....	0.70	10.18	0.04	173 \pm 15	1226	71 \pm 13	0.50 \pm 0.25	11.82	19.50	Absorption	Inflow
.....	1.48	10.04	0.02 ^b	-260 \pm 64 ^b	-271 ^b	56 \pm 35 ^b	0.48 \pm 0.26 ^b	11.36 ^b	19.04 ^b	Absorption	Outflow
.....	-0.20 ^r	25 \pm 10 ^r	26 ^r	200 \pm 10 ^r	-0.04 \pm 0.00 ^r	13.98 ^r	21.66 ^r	Emission	Outflow
.....	1.50	10.00	0.01 ^b	-235 \pm 25 ^b	-262 ^b	70 \pm 15 ^b	0.90 \pm 0.23 ^b	11.04 ^b	18.72 ^b	Absorption	Outflow
.....	-0.22 ^r	22 \pm 7 ^r	25 ^r	200 \pm 3 ^r	-0.05 \pm 0.00 ^r	13.86 ^r	21.54 ^r	Emission	Outflow
.....	1.43	10.02	0.01 ^b	-210 \pm 20 ^b	-256 ^b	77 \pm 11 ^b	0.49 \pm 0.23 ^b	11.30 ^b	18.97 ^b	Absorption	Outflow
.....	-0.22 ^r	21 \pm 3 ^r	26 ^r	198 \pm 1 ^r	-0.05 \pm 0.00 ^r	13.91 ^r	21.59 ^r	Emission	Outflow
.....	1.39	10.04	0.01 ^b	-282 \pm 13 ^b	-401 ^b	51 \pm 6 ^b	0.40 \pm 0.24 ^b	11.27 ^b	18.95 ^b	Absorption	Outflow
.....	-0.12 ^r	21 \pm 2 ^r	29 ^r	200 \pm 1 ^r	-0.02 \pm 0.00 ^r	14.45 ^r	22.13 ^r	Emission	Outflow
.....	1.14	10.12	0.04	82 \pm 7	193	104 \pm 7	0.89 \pm 0.21	11.61	19.29	Absorption	Inflow

.....	1.10	10.24	0.04	180±7	631	50±5	0.46±0.23	11.76	19.43	Absorption	Inflow
.....	1.09	10.27	0.04	170±125	1128	80±75	0.84±0.26	11.61	19.28	Absorption	Inflow
.....	1.79	10.08	-0.05	245±45	256	175±33	-0.63±0.25	11.90	19.57	Emission	Outflow
.....	1.95	10.11	-0.06	267±30	297	178±29	-0.94±0.24	11.76	19.44	Emission	Outflow
.....	1.84	10.10	-0.04	286±19	351	170±17	-0.84±0.24	11.67	19.35	Emission	Outflow
.....	1.76	10.17	0.01	195±7	341	50±3	0.32±0.25	11.62	19.30	Absorption	Inflow
.....	1.69	10.25	0.03	184±6	428	50±4	0.88±0.25	11.45	19.13	Absorption	Inflow
.....	1.73	10.37	0.05	186±11	631	66±13	0.22±0.25	12.32	20.00	Absorption	Inflow
.....	2.60	10.17	0.11	-184±56 ^b	-193 ^b	-	-	-	-	P-Cygni	Outflow
.....			-0.06	184±73 ^r	192 ^r	-	-	-	-	P-Cygni	Outflow
.....	2.71	10.22	0.18	-35±28 ^b	-39 ^b	-	-	-	-	P-Cygni	Outflow
.....			-0.13	158±15 ^r	175 ^r	-	-	-	-	P-Cygni	Outflow
.....	2.81	10.22	0.00 ^b	-91±60 ^b	-112 ^b	163±34 ^b	0.43±0.17 ^b	10.18 ^b	17.86 ^b	Absorption	Outflow
.....			-0.09 ^r	180±6 ^r	220 ^r	197±2 ^r	-0.02±0.00 ^r	13.83 ^r	21.51 ^r	Emission	Outflow
.....	2.79	10.39	0.05	187±7	429	64±9	0.95±0.23	11.67	19.35	Absorption	Inflow
.....	2.76	10.48	0.08	185±64	607	77±44	0.74±0.23	11.98	19.66	Absorption	Inflow
.....	4.13	10.28	0.13	-191±40	-199	187±25	0.15±0.23	12.96	20.64	Absorption	Outflow
.....	4.50	10.32	0.03 ^b	-189±21 ^b	-210 ^b	56±48 ^b	0.56±0.24 ^b	11.94 ^b	19.62 ^b	Absorption	Outflow
.....			-0.11 ^r	191±9 ^r	212 ^r	198±6 ^r	-0.14±0.25 ^r	12.89 ^r	20.56 ^r	Emission	Outflow
.....	5.04	10.37	0.07 ^b	-185±4 ^b	-227 ^b	50±6 ^b	0.61±0.22 ^b	12.30 ^b	19.98 ^b	Absorption	Outflow
.....			-0.03 ^r	196±43 ^r	241 ^r	197±34 ^r	-0.32±0.26 ^r	12.00 ^r	19.68 ^r	Emission	Outflow

.....	5.32	10.46	0.04	204±14	355	57±19	0.32±0.26	12.13	19.80	Absorption	Inflow
.....	5.37	10.53	0.08	196±13	444	69±19	0.75±0.24	11.99	19.67	Absorption	Inflow
.....	5.23	10.61	0.11	174±57	581	116±28	0.68±0.24	12.21	19.89	Absorption	Inflow
.....	4.81	10.14	0.18	-237±72	-247	299±35	0.54±0.24	12.51	20.19	Absorption	Outflow
.....	8.18	10.41	0.19	-209±64	-232	244±18	0.28±0.22	12.82	20.50	Absorption	Outflow
HIGH-<i>i</i>	2.68	10.41	0.02	189±5	375	50±2	0.94±0.25	11.34	19.01	Absorption	Inflow
.....	7.42	10.49	0.02	196±25	368	51±27	0.32±0.27	11.88	19.56	Absorption	Inflow
.....	1.69	10.71	0.04	187±7	495	70±10	0.87±0.23	11.66	19.34	Absorption	Inflow
.....	4.16	10.73	0.03	199±6	424	56±7	0.14±0.24	12.44	20.12	Absorption	Inflow
.....	11.02	10.79	0.05	210±31	395	91±34	0.40±0.26	12.06	19.74	Absorption	Inflow
.....	2.99	11.11	0.08	180±19	443	81±24	0.82±0.25	11.96	19.63	Absorption	Inflow
.....	8.55	11.07	0.03	189±31	389	54±33	0.73±0.27	11.48	19.16	Absorption	Inflow
LOW-<i>i</i>	1.18	9.99	0.02 ^b	-234±11 ^b	-293 ^b	53±6 ^b	0.93±0.24 ^b	11.13 ^b	18.81 ^b	Emission	Outflow
.....			-0.22 ^r	20±1 ^r	25 ^r	200±0 ^r	-0.04±0.00 ^r	14.34 ^r	22.02 ^r	Emission	Outflow
.....	2.32	10.06	0.01 ^b	-266±16 ^b	-328 ^b	59±9 ^b	0.53±0.16 ^b	11.22 ^b	18.90 ^b	Absorption	Outflow
.....			-0.12 ^r	20±2 ^r	25 ^r	199±1 ^r	-0.02±0.00 ^r	14.59 ^r	22.27 ^r	Emission	Outflow
.....	1.52	10.33	0.01 ^b	-201±7 ^b	-254 ^b	78±10 ^b	0.33±0.24 ^b	11.65 ^b	19.33 ^b	Absorption	Outflow
.....			-0.27 ^r	20±1 ^r	26 ^r	200±1 ^r	-0.07±0.01 ^r	13.76 ^r	21.43 ^r	Emission	Outflow
.....	3.29	10.39	0.04	-193±8 ^b	-241 ^b	-	-	-	-	P-Cygni	Outflow
.....			-0.03	231±13 ^r	288 ^r	-	-	-	-	P-Cygni	Outflow
.....	8.67	10.48	0.06 ^b	-188±45 ^b	-237 ^b	53±28 ^b	0.71±0.23 ^b	12.14 ^b	19.82 ^b	Absorption	Outflow

.....	-0.04 ^r	195±54 ^r	246 ^r	196±44 ^r	-0.33±0.27 ^r	12.04 ^r	19.72 ^r	Emission	Outflow
.....	0.00 ^b	-226±117 ^b	-284 ^b	57±42 ^b	0.61±0.28 ^b	10.39 ^b	18.07 ^b	Absorption	Outflow
.....	-0.06 ^r	195±5 ^r	245 ^r	200±3 ^r	-0.68±0.23 ^r	11.93 ^r	19.61 ^r	Emission	Outflow
.....	0.04 ^b	-189±2 ^b	-239 ^b	51±5 ^b	0.93±0.22 ^b	11.86 ^b	19.54 ^b	Absorption	Outflow
.....	-0.07 ^r	189±9 ^r	239 ^r	196±5 ^r	-0.02±0.29 ^r	13.58 ^r	21.25 ^r	Emission	Outflow
.....	0.34	-157±99	-200	188±55	0.08±0.28	13.95	21.63	Absorption	Outflow
.....	0.20	-84±103	-111	243±43	0.77±0.26	12.41	20.08	Absorption	Outflow
BULGE	-0.04	303±26	393	84±41	-0.53±0.26	11.92	19.60	Emission	Outflow
.....	0.10	-401±88	-544	340±58	0.25±0.27	12.62	20.30	Absorption	Outflow
.....	0.11	-163±16	-219	196±24	0.64±0.24	12.25	19.93	Absorption	Outflow
.....	0.25	-180±32	-236	164±24	0.10±0.24	13.62	21.30	Absorption	Outflow
.....	0.03	-177±67	-248	75±65	0.38±0.27	11.99	19.66	Absorption	Outflow
.....	0.29	-111±23	-149	200±17	0.17±0.25	13.33	21.01	Absorption	Outflow
.....	0.67	-145±37	-202	266±26	0.37±0.22	13.36	21.04	Absorption	Outflow
.....	0.47	-113±117	-162	282±61	0.14±0.25	13.72	21.40	Absorption	Outflow
<i>i</i> -log SFR	0.15	-162±19	-169	143±30	0.71±0.24	12.35	20.02	Absorption	Outflow
.....	0.41	-158±37	-164	214±26	0.15±0.24	13.63	21.30	Absorption	Outflow
.....	0.06 ^b	-153±6 ^b	-170 ^b	116±13 ^b	0.48±0.22 ^b	12.17 ^b	19.84 ^b	Absorption	Outflow
.....	-0.05 ^r	195±8 ^r	216 ^r	191±5 ^r	-0.60±0.24 ^r	11.92 ^r	19.60 ^r	Emission	Outflow
.....	0.10 ^b	-192±16 ^b	-213 ^b	149±13 ^b	0.90±0.21 ^b	12.06 ^b	19.73 ^b	Absorption	Outflow
.....	-0.15 ^r	55±23 ^r	61 ^r	117±18 ^r	-0.62±0.20 ^r	12.41 ^r	20.09 ^r	Emission	Outflow

.....	12.80	10.70	0.36	-144±35	-161	206±19	0.16±0.24	13.48	21.16	Absorption	Outflow
.....	2.37	10.19	0.05	-157±20	-194	55±26	0.15±0.26	12.86	20.54	Absorption	Outflow
.....	4.94	10.46	0.12	-149±9	-183	82±17	0.06±0.15	13.53	21.20	Absorption	Outflow
.....	13.27	10.69	0.46	-69±8	-84	152±11	0.15±0.02	13.74	21.42	Absorption	Outflow
.....	13.15	10.77	0.23	-76±16	-107	114±16	0.05±0.01	14.31	21.99	Absorption	Outflow
.....	2.30	10.27	0.02	162±28	283	50±19	0.36±0.26	12.21	19.88	Absorption	Inflow
.....	2.19	10.30	0.06	150±54	345	60±37	0.23±0.23	12.74	20.42	Absorption	Inflow
.....	4.74	10.59	0.08	148±4	338	53±11	0.88±0.24	12.36	20.04	Absorption	Inflow
.....	12.42	10.82	0.10	145±76	331	65±47	0.26±0.23	12.83	20.51	Absorption	Inflow
.....	2.11	10.39	0.03	184±59	606	57±37	0.62±0.25	11.70	19.38	Absorption	Inflow
.....	4.52	10.68	0.10	146±51	487	57±31	0.36±0.23	12.79	20.47	Absorption	Inflow
<i>i</i> -log M _*	3.62	10.30	0.15	-152±26	-159	160±35	0.58±0.25	12.46	20.14	Absorption	Outflow
.....	4.50	10.50	0.16	-146±19	-152	173±26	0.91±0.24	12.27	19.94	Absorption	Outflow
.....	6.42	10.69	0.24	-143±24	-149	216±38	0.60±0.25	12.64	20.32	Absorption	Outflow
.....	8.99	10.89	0.20	-178±83	-184	250±57	0.67±0.26	12.50	20.18	Absorption	Outflow
.....	2.52	10.11	0.01 ^b	-206±85 ^b	-228 ^b	65±42 ^b	0.74±0.28 ^b	10.94 ^b	18.61 ^b	Absorption	Outflow
.....			-0.09 ^r	198±8 ^r	219 ^r	199±7 ^r	-0.73±0.26 ^r	12.12 ^r	19.80 ^r	Emission	Outflow
.....	3.71	10.30	0.02 ^b	-173±69 ^b	-192 ^b	71±43 ^b	0.59±0.25 ^b	11.75 ^b	19.43 ^b	Absorption	Outflow
.....			-0.09 ^r	199±11 ^r	222 ^r	199±5 ^r	-0.20±0.26 ^r	12.70 ^r	20.37 ^r	Emission	Outflow
.....	4.95	10.49	0.13	-166±12	-184	54±36	0.10±0.27	13.65	21.33	Absorption	Outflow
.....	6.61	10.69	0.18	-146±21	-162	187±19	0.90±0.24	12.34	20.02	Absorption	Outflow

.....	8.09	10.88	0.17	-147±23	-163	143±28	0.42±0.26	12.64	20.32	Absorption	Outflow
.....	3.63	10.30	0.00 ^b	-234±81 ^b	-287 ^b	86±39 ^b	0.67±0.26 ^b	10.80 ^b	18.48 ^b	Absorption	Outflow
.....			-0.08 ^r	194±32 ^r	238 ^r	195±5 ^r	-0.02±0.26 ^r	13.96 ^r	21.64 ^r	Emission	Outflow
.....	4.89	10.50	0.03 ^b	-172±62 ^b	-211 ^b	88±35 ^b	0.34±0.21 ^b	11.96 ^b	19.64 ^b	Absorption	Outflow
.....			-0.08 ^r	150±21 ^r	184 ^r	192±11 ^r	-0.02±0.02 ^r	14.47 ^r	22.15 ^r	Emission	Outflow
.....	6.88	10.68	0.18	-130±30	-159	117±28	0.07±0.29	13.63	21.31	Absorption	Outflow
.....	8.03	10.88	0.06	-171±42	-209	92±26	0.73±0.25	11.98	19.66	Absorption	Outflow
.....	9.25	11.08	0.19	-108±53	-132	182±42	0.13±0.27	13.28	20.96	Absorption	Outflow
.....	8.03	10.88	0.04	-179±106	-253	95±65	0.33±0.26	12.09	19.76	Absorption	Outflow
.....	3.16	10.31	0.02	166±20	288	50±14	0.96±0.27	11.60	19.27	Absorption	Inflow
.....	7.46	10.88	0.04	148±23	260	56±34	0.64±0.24	12.14	19.82	Absorption	Inflow
.....	2.64	10.30	0.04	153±33	346	51±29	0.81±0.25	12.17	19.84	Absorption	Inflow
.....	3.66	10.50	0.04	162±14	371	50±8	0.84±0.25	12.03	19.71	Absorption	Inflow
.....	4.71	10.69	0.08	148±20	342	50±21	0.97±0.24	12.43	20.11	Absorption	Inflow
.....	6.17	10.87	0.09	148±8	347	51±22	0.49±0.25	12.77	20.44	Absorption	Inflow
.....	8.84	11.04	0.07	156±113	365	73±69	0.46±0.26	12.34	20.01	Absorption	Inflow
.....	3.15	10.51	0.05	160±81	523	72±52	0.56±0.25	12.12	19.80	Absorption	Inflow
.....	3.92	10.69	0.06	162±28	543	60±33	0.72±0.24	12.16	19.84	Absorption	Inflow
.....	5.33	10.86	0.11	153±60	523	67±40	0.95±0.23	12.26	19.94	Absorption	Inflow

Table A.2: The same as Table A.1 but for AGN.

Sample	SFR	$\log M_*/M_\odot$	EW	Δv	$\Delta v/\cos(i)$	b_D	C_f	N(Na I)	N(H)	Profile	Type
DISK	0.34	10.81	-0.16	116±87	120	185±55	-0.82±0.27	12.26	19.94	Emission	Outflow
.....	0.26	10.87	0.02	174±88	403	84±67	0.68±0.27	11.47	19.14	Absorption	Inflow
.....	0.25	10.89	0.13	98±25	356	181±21	0.54±0.24	12.37	20.05	Absorption	Inflow
.....	0.25	10.94	0.22	132±29	819	181±28	0.52±0.24	12.61	20.29	Absorption	Inflow
.....	0.27	10.77	-0.03	180±101	188	178±59	-0.49±0.26	11.79	19.47	Emission	Outflow
.....	0.27	10.76	-0.02	191±116	234	69±71	-0.23±0.26	11.86	19.54	Emission	Outflow
.....	0.20	10.75	0.07	158±22	376	165±13	0.21±0.26	12.52	20.20	Absorption	Inflow
.....	0.23	10.79	0.11	165±31	600	144±15	0.94±0.25	12.03	19.71	Absorption	Inflow
.....	0.39	10.85	0.13	191±31	1342	121±22	0.67±0.26	12.28	19.95	Absorption	Inflow
.....	0.36	10.55	0.04	174±30	415	96±17	0.59±0.25	11.82	19.49	Absorption	Inflow
.....	0.39	10.61	0.08	169±31	630	95±24	0.63±0.23	12.09	19.77	Absorption	Inflow
.....	0.55	10.63	0.12	158±30	1186	144±21	0.62±0.26	12.26	19.94	Absorption	Inflow
.....	0.94	10.40	-0.04	250±104	261	181±50	-0.56±0.26	11.87	19.55	Emission	Outflow
.....	0.90	10.39	-0.05	158±84	175	195±38	-0.86±0.25	11.72	19.40	Emission	Outflow
.....	0.88	10.42	-0.03	296±121	363	177±62	-0.24±0.25	12.10	19.78	Emission	Outflow
.....	0.79	10.42	-0.02	290±95	411	153±65	-0.92±0.25	11.37	19.05	Emission	Outflow
.....	0.63	10.50	0.05	174±43	413	96±26	0.73±0.24	11.77	19.45	Absorption	Inflow
.....	0.71	10.59	0.07	179±39	661	85±27	0.69±0.24	11.97	19.65	Absorption	Inflow

.....	0.96	10.70	0.12	174±24	1220	116±16	0.34±0.24	12.55	20.23	Absorption	Inflow
.....	1.39	10.45	-0.06	185±65	193	198±40	-0.86±0.26	11.85	19.53	Emission	Outflow
.....	1.53	10.47	-0.06	170±52	189	177±36	-0.29±0.24	12.30	19.98	Emission	Outflow
.....	1.43	10.45	-0.06	210±48	257	185±29	-0.37±0.26	12.19	19.87	Emission	Outflow
.....	1.21	10.50	0.01	175±144	306	66±106	0.48±0.28	11.27	18.94	Absorption	Inflow
.....	1.10	10.55	0.05	186±15	441	86±18	0.20±0.25	12.37	20.04	Absorption	Inflow
.....	1.22	10.63	0.10	163±15	599	112±19	0.55±0.19	12.23	19.90	Absorption	Inflow
.....	1.44	10.72	0.12	177±42	1255	95±28	0.92±0.26	12.09	19.76	Absorption	Inflow
.....	2.14	10.40	-0.10	194±25	216	207±24	-0.35±0.25	12.44	20.12	Emission	Outflow
.....	2.11	10.50	0.01 ^b	-194±108 ^b	-275 ^b	52±43 ^b	0.67±0.26 ^b	11.45 ^b	19.13 ^b	Absorption	Outflow
.....	-0.05 ^r	193±31 ^r	273 ^r	193±26 ^r	-0.88±0.23 ^r	11.70 ^r	19.38 ^r	Emission	Outflow
.....	1.85	10.57	0.05	194±47	462	63±35	0.63±0.25	11.84	19.52	Absorption	Inflow
.....	1.90	10.60	0.08	179±19	651	96±21	0.31±0.25	12.39	20.06	Absorption	Inflow
.....	2.36	10.70	0.08	132±94	875	111±52	0.47±0.25	12.22	19.90	Absorption	Inflow
.....	4.23	10.45	0.16	-389±67	-392	290±80	0.88±0.28	12.23	19.91	Absorption	Outflow
.....	2.85	10.50	0.13	-238±44	-249	248±30	0.74±0.27	12.22	19.89	Absorption	Outflow
.....	3.12	10.43	0.07 ^b	-232±26 ^b	-258 ^b	140±19 ^b	0.43±0.25 ^b	12.18 ^b	19.86 ^b	Absorption	Outflow
.....	-0.07 ^r	190±43 ^r	211 ^r	194±36 ^r	-0.57±0.27 ^r	12.06 ^r	19.74 ^r	Emission	Outflow
.....	3.53	10.52	0.08 ^b	-209±35 ^b	-257 ^b	156±19 ^b	0.64±0.24 ^b	12.08 ^b	19.75 ^b	Absorption	Outflow
.....	-0.07 ^r	197±48 ^r	243 ^r	197±39 ^r	-0.23±0.28 ^r	12.45 ^r	20.13 ^r	Emission	Outflow
.....	3.41	10.53	0.08	-198±39	-282	248±12	0.72±0.27	12.04	19.72	Absorption	Outflow

.....	3.39	10.55	0.03	145±85	256	126±60	0.62±0.25	11.73	19.41	Absorption	Inflow
.....	3.14	10.57	0.07	151±22	352	132±20	0.79±0.23	11.92	19.60	Absorption	Inflow
.....	3.08	10.64	0.10	183±17	642	86±22	0.37±0.23	12.44	20.12	Absorption	Inflow
.....	4.80	10.44	0.37	-201±30	-210	261±33	0.64±0.25	12.76	20.44	Absorption	Outflow
.....	5.86	10.63	0.27	-242±72	-271	300±36	0.70±0.26	12.58	20.26	Absorption	Outflow
.....	6.15	10.59	0.27	-172±76	-212	269±37	0.18±0.24	13.21	20.89	Absorption	Outflow
.....	6.66	10.62	0.14	-406±66	-582	442±46	0.77±0.27	12.23	19.91	Absorption	Outflow
.....	6.35	10.66	0.08	197±25	458	73±26	0.75±0.25	12.00	19.67	Absorption	Inflow
.....	6.59	10.71	0.09	199±23	712	71±26	0.75±0.25	12.08	19.75	Absorption	Inflow
.....	11.69	10.57	0.53	-256±96	-268	263±55	0.21±0.25	13.48	21.16	Absorption	Outflow
.....	12.74	10.72	0.60	-258±75	-286	304±41	0.27±0.25	13.42	21.09	Absorption	Outflow
.....	13.38	10.67	0.35	-276±88	-339	322±57	0.22±0.27	13.22	20.89	Absorption	Outflow
.....	13.61	10.76	0.15	128±62	289	146±33	0.60±0.22	12.38	20.06	Absorption	Inflow
.....	11.43	10.69	0.11	142±142	510	136±96	0.95±0.27	12.06	19.74	Absorption	Inflow
HIGH-<i>i</i>	2.82	10.47	0.03	199±20	406	56±21	0.52±0.26	11.78	19.46	Absorption	Inflow
.....	1.72	10.77	0.05	185±9	449	90±11	0.28±0.24	12.28	19.95	Absorption	Inflow
.....	4.64	10.78	0.04	188±21	404	104±21	0.94±0.25	11.61	19.29	Absorption	Inflow
.....	13.61	10.83	0.05	180±116	368	112±72	0.52±0.26	11.94	19.62	Absorption	Inflow
.....	2.61	11.10	0.09	145±27	354	165±20	0.80±0.20	12.05	19.73	Absorption	Inflow
.....	7.13	11.13	0.10	113±59	249	161±32	0.43±0.23	12.36	20.04	Absorption	Inflow
.....	23.11	11.11	0.13	159±132	315	170±82	0.83±0.26	12.17	19.85	Absorption	Inflow

LOW- <i>i</i>	1.31	10.11	-0.05	308±69	376	196±49	-0.46±0.26	12.03	19.71	Emission	Outflow
.....	3.40	10.15	0.13	-355±109	-442	383±68	0.78±0.25	12.22	19.89	Absorption	Outflow
.....	0.53	10.39	-0.01	364±127	462	55±99	-0.71±0.27	11.35	19.03	Emission	Outflow
.....	1.53	10.41	0.03 ^b	-194±80 ^b	-242 ^b	87±39 ^b	0.55±0.27 ^b	11.77 ^b	19.45 ^b	Absorption	Outflow
.....			-0.19 ^r	21±20 ^r	27 ^r	199±5 ^r	-0.04±0.00 ^r	13.98 ^r	21.66 ^r	Emission	Outflow
.....	3.63	10.46	0.05 ^b	-222±31 ^b	-279 ^b	184±30 ^b	0.90±0.25 ^b	11.69 ^b	19.37 ^b	Absorption	Outflow
.....			-0.08 ^r	198±9 ^r	249 ^r	199±6 ^r	-0.16±0.25 ^r	12.68 ^r	20.35 ^r	Emission	Outflow
.....	10.11	10.52	0.20	-246±70	-319	299±30	0.93±0.26	12.31	19.98	Absorption	Outflow
.....	0.58	10.76	-0.02	173±125	217	157±76	-0.74±0.27	11.29	18.97	Emission	Outflow
.....	1.74	10.76	0.00 ^b	-250±106 ^b	-313 ^b	66±32 ^b	0.46±0.16 ^b	10.75 ^b	18.43 ^b	Absorption	Outflow
.....			-0.12 ^r	77±8 ^r	97 ^r	200±5 ^r	-0.03±0.01 ^r	13.87 ^r	21.55 ^r	Emission	Outflow
.....	4.60	10.77	0.05 ^b	-229±29 ^b	-287 ^b	157±18 ^b	0.46±0.24 ^b	12.04 ^b	19.72 ^b	Absorption	Outflow
.....			-0.08 ^r	199±38 ^r	249 ^r	198±33 ^r	-0.08±0.27 ^r	13.02 ^r	20.70 ^r	Emission	Outflow
.....	13.74	10.81	0.23	-336±68	-438	348±48	0.58±0.27	12.58	20.26	Absorption	Outflow
.....	42.22	10.81	0.66	-258±63	-351	323±47	0.42±0.24	13.22	20.90	Absorption	Outflow
.....	6.16	11.12	0.07	-426±136	-550	443±66	0.59±0.26	12.04	19.72	Absorption	Outflow
.....	18.91	11.12	0.44	-212±111	-267	278±52	0.09±0.26	13.92	21.60	Absorption	Outflow
BULGE	0.83	10.07	-0.03	312±73	395	142±62	-0.86±0.27	11.58	19.26	Emission	Outflow
.....	2.27	10.07	0.15	-349±81	-428	164±86	0.03±0.32	14.61	22.29	Absorption	Outflow
.....	2.18	10.44	0.10	-195±22	-253	228±38	0.86±0.25	12.08	19.76	Absorption	Outflow
.....	6.01	10.49	0.27	-255±24	-322	267±27	0.71±0.26	12.61	20.29	Absorption	Outflow

.....	2.44	10.78	0.03	-488±44	-700	449±13	0.35±0.25	11.89	19.57	Absorption	Outflow
.....	6.76	10.80	0.19	-196±42	-258	276±24	0.86±0.24	12.38	20.06	Absorption	Outflow
.....	22.61	10.83	0.61	-227±44	-300	233±32	0.15±0.25	13.91	21.58	Absorption	Outflow
.....	12.44	11.08	0.21	-180±107	-264	237±55	0.05±0.26	13.95	21.62	Absorption	Outflow
<i>i</i> -log SFR	5.78	10.65	0.24	-197±35	-206	228±40	0.68±0.26	12.57	20.25	Absorption	Outflow
.....	2.26	10.37	0.17	-160±34	-178	208±42	0.35±0.26	12.74	20.42	Absorption	Outflow
.....	5.32	10.63	0.26	-195±25	-218	259±25	0.92±0.24	12.48	20.16	Absorption	Outflow
.....	14.30	10.87	0.44	-235±77	-262	305±44	0.28±0.26	13.28	20.96	Absorption	Outflow
.....	2.33	10.32	0.21	-124±28	-155	205±24	0.27±0.25	12.95	20.63	Absorption	Outflow
.....	5.52	10.63	0.25	-133±22	-163	210±15	0.11±0.24	13.50	21.18	Absorption	Outflow
.....	15.17	10.90	0.32	-238±82	-293	245±45	0.11±0.27	13.61	21.29	Absorption	Outflow
.....	5.38	10.63	0.07	-370±90	-529	387±53	0.44±0.27	12.24	19.92	Absorption	Outflow
.....	15.16	10.83	0.12	-362±95	-517	373±71	0.89±0.28	12.17	19.84	Absorption	Outflow
.....	2.21	10.41	0.08	142±34	250	69±25	0.66±0.22	12.27	19.95	Absorption	Inflow
.....	2.08	10.45	0.11	139±26	326	66±16	0.33±0.22	12.74	20.42	Absorption	Inflow
.....	5.08	10.67	0.08	147±10	343	50±31	0.22±0.26	13.09	20.77	Absorption	Inflow
.....	2.13	10.48	0.05	193±59	683	61±33	0.31±0.24	12.18	19.86	Absorption	Inflow
.....	5.00	10.71	0.11	146±56	509	53±40	0.31±0.24	13.01	20.69	Absorption	Inflow
.....	12.34	10.95	0.12	183±46	651	105±28	0.45±0.23	12.48	20.16	Absorption	Inflow
<i>i</i> -log M _*	1.58	10.12	0.08	-288±117	-300	211±96	0.53±0.29	12.21	19.89	Absorption	Outflow
.....	3.47	10.49	0.31	-193±50	-200	256±60	0.51±0.28	12.83	20.51	Absorption	Outflow

.....	7.76	10.67	0.42	-254±36	-263	214±38	0.12±0.27	13.78	21.46	Absorption	Outflow
.....	1.99	10.14	0.17	-149±76	-165	190±64	0.65±0.27	12.44	20.12	Absorption	Outflow
.....	2.92	10.36	0.15	-159±26	-178	112±35	0.67±0.27	12.38	20.06	Absorption	Outflow
.....	3.97	10.49	0.22	-281±63	-311	309±41	0.56±0.27	12.63	20.31	Absorption	Outflow
.....	5.80	10.70	0.29	-185±32	-206	263±36	0.97±0.25	12.51	20.19	Absorption	Outflow
.....	7.18	10.86	0.28	-165±56	-183	238±53	0.08±0.27	13.79	21.47	Absorption	Outflow
.....	10.45	11.05	0.37	-235±51	-263	243±58	0.30±0.27	13.18	20.86	Absorption	Outflow
.....	2.26	10.14	0.11	-159±32	-197	118±34	0.40±0.27	12.48	20.15	Absorption	Outflow
.....	2.97	10.32	0.17	-141±39	-172	182±34	0.81±0.25	12.35	20.02	Absorption	Outflow
.....	4.30	10.50	0.18	-133±49	-164	186±30	0.10±0.25	13.38	21.06	Absorption	Outflow
.....	6.14	10.70	0.38	-113±28	-138	200±20	0.15±0.25	13.59	21.27	Absorption	Outflow
.....	7.24	10.90	0.26	-167±44	-207	186±26	0.08±0.25	13.73	21.41	Absorption	Outflow
.....	11.41	11.06	0.30	-160±68	-198	220±39	0.11±0.26	13.61	21.29	Absorption	Outflow
.....	4.01	10.50	0.14	-153±81	-217	187±54	0.04±0.28	13.92	21.60	Absorption	Outflow
.....	5.92	10.70	0.07	-221±140	-318	186±94	0.86±0.27	11.95	19.63	Absorption	Outflow
.....	8.74	10.87	0.23	-124±118	-179	198±68	0.05±0.27	14.00	21.68	Absorption	Outflow
.....	2.54	10.32	0.03	163±117	288	52±93	0.94±0.28	11.84	19.51	Absorption	Inflow
.....	8.06	11.09	0.06	146±136	257	53±90	0.55±0.27	12.48	20.15	Absorption	Inflow
.....	2.04	10.33	0.03	178±108	422	61±80	0.32±0.26	12.06	19.74	Absorption	Inflow
.....	3.51	10.51	0.03	174±72	407	56±39	0.48±0.24	11.97	19.65	Absorption	Inflow
.....	4.48	10.69	0.12	148±37	343	51±33	0.83±0.23	12.65	20.33	Absorption	Inflow

.....	6.44	10.89	0.07	146±19	337	56±31	0.62±0.26	12.44	20.12	Absorption	Inflow
.....	2.94	10.51	0.04	176±74	645	100±45	0.59±0.24	11.89	19.56	Absorption	Inflow
.....	4.33	10.69	0.06	167±43	584	58±34	0.81±0.26	12.05	19.73	Absorption	Inflow
.....	5.58	10.89	0.15	147±61	501	58±42	0.57±0.23	12.76	20.44	Absorption	Inflow
.....	6.98	11.09	0.18	146±40	522	129±24	0.62±0.22	12.49	20.17	Absorption	Inflow

A.2 SDSS NaD Profiles

In this section we present examples of our NaD fits as described in Section 2.2.2 for the main sample of both inactive galaxies and the AGN sample used throughout the study.

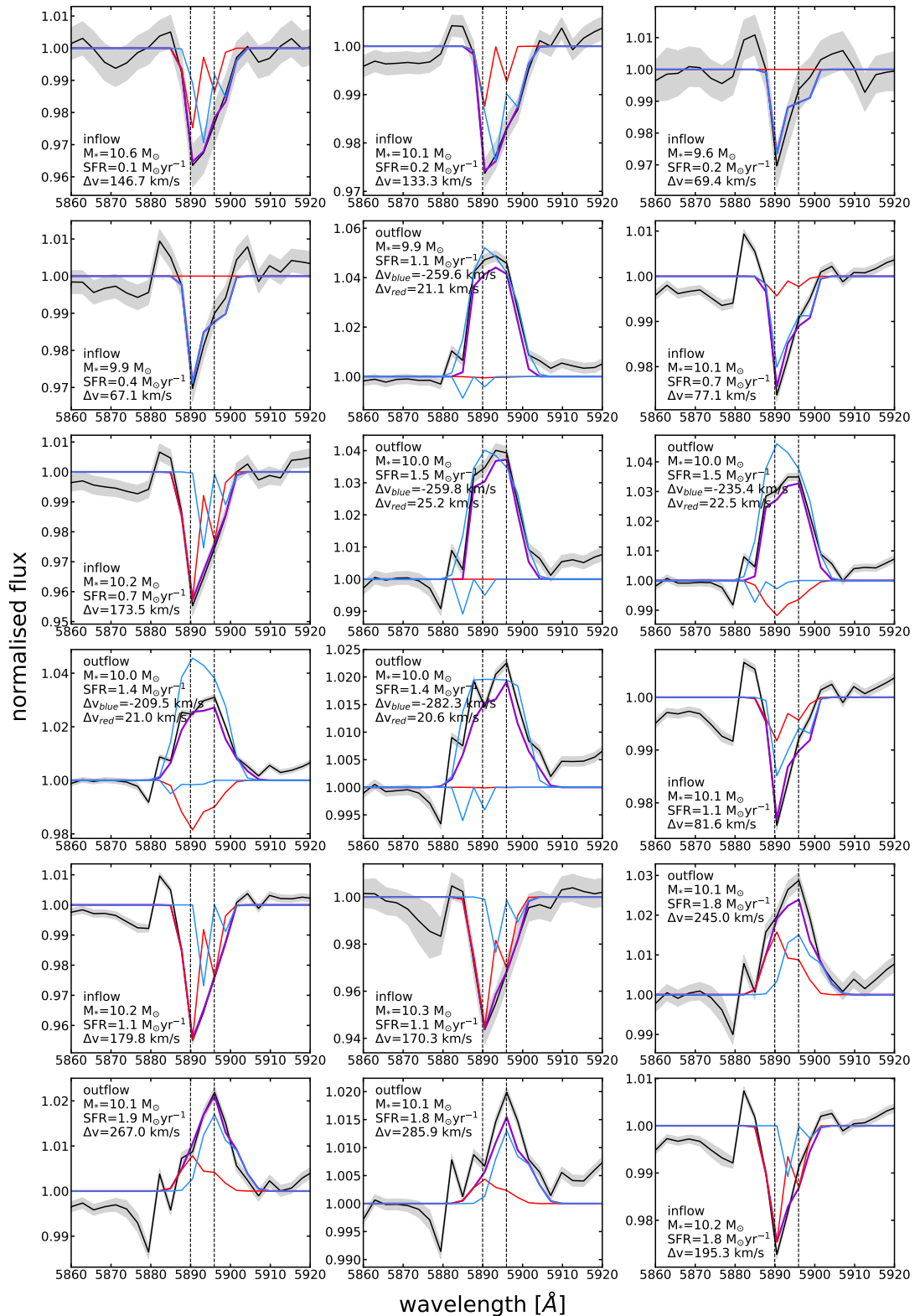


Figure A.1. The normalised NaD ISM profiles from inflow and outflow detections in the DISK, LOW-*i*, HIGH-*i* and BULGE samples for inactive galaxies. The black line is the NaD profile and the gray shade is the flux error. The best-fit two-component models are overplotted: purple denotes the total fit, red is the systemic component, and blue represents the blueshifted or redshifted flow component.

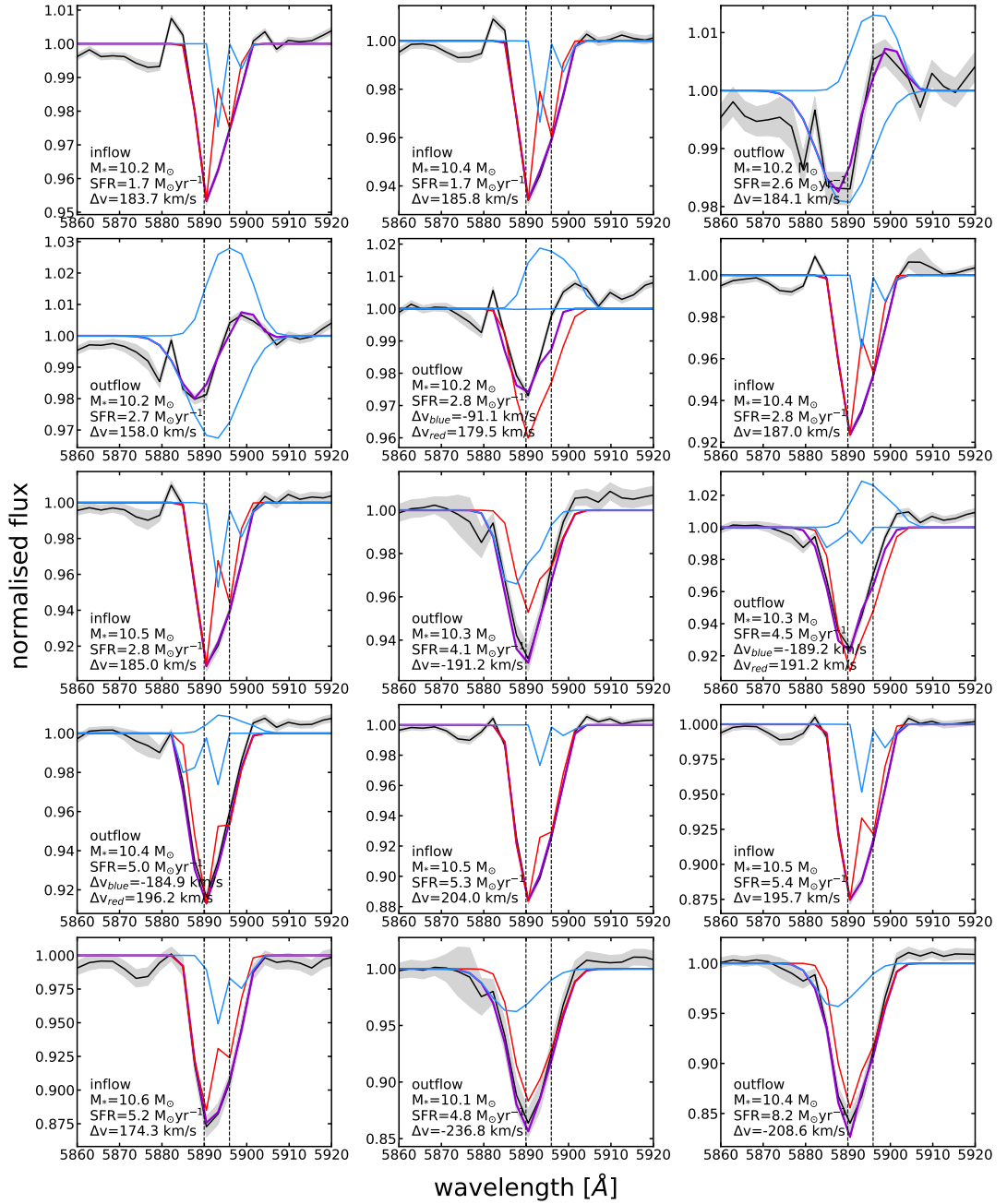


Figure A.1. – continued.

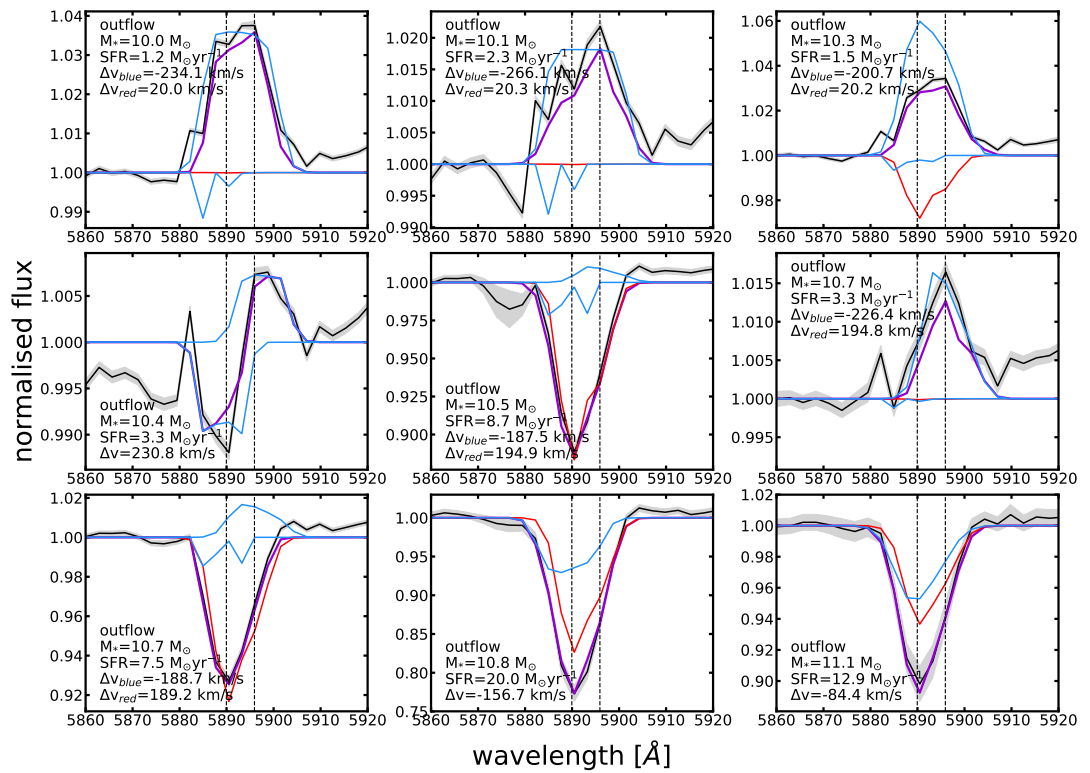


Figure A.1. – continued.

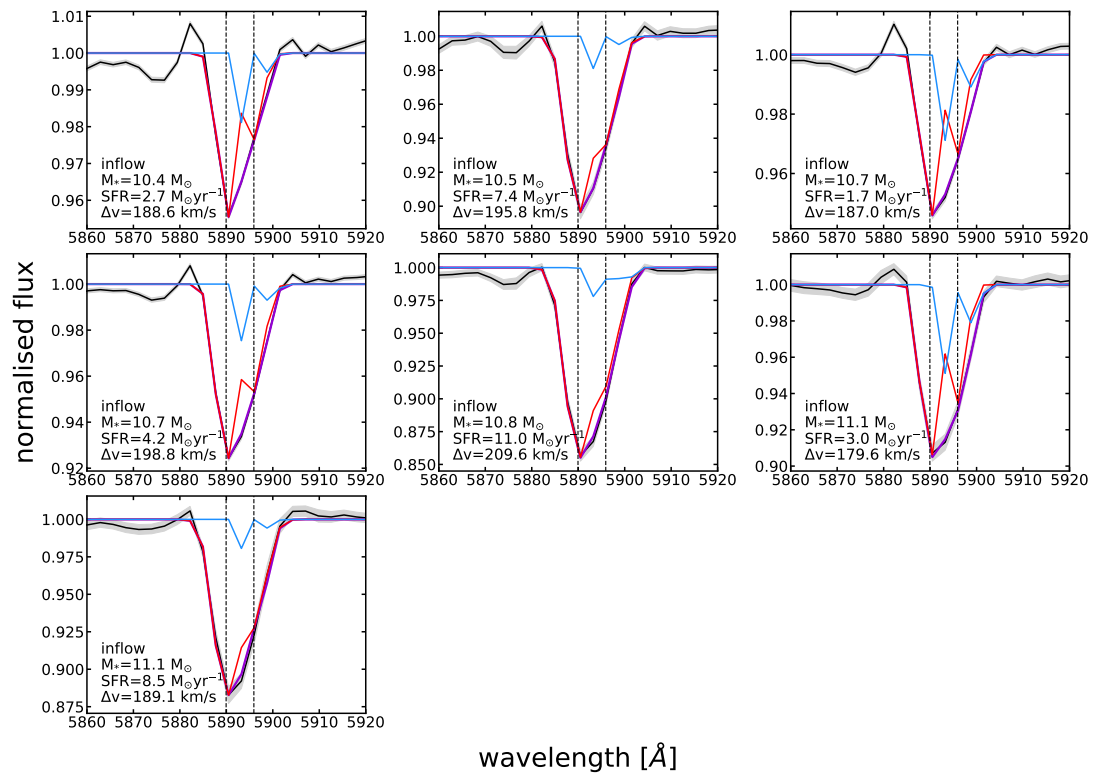


Figure A.1. – continued.

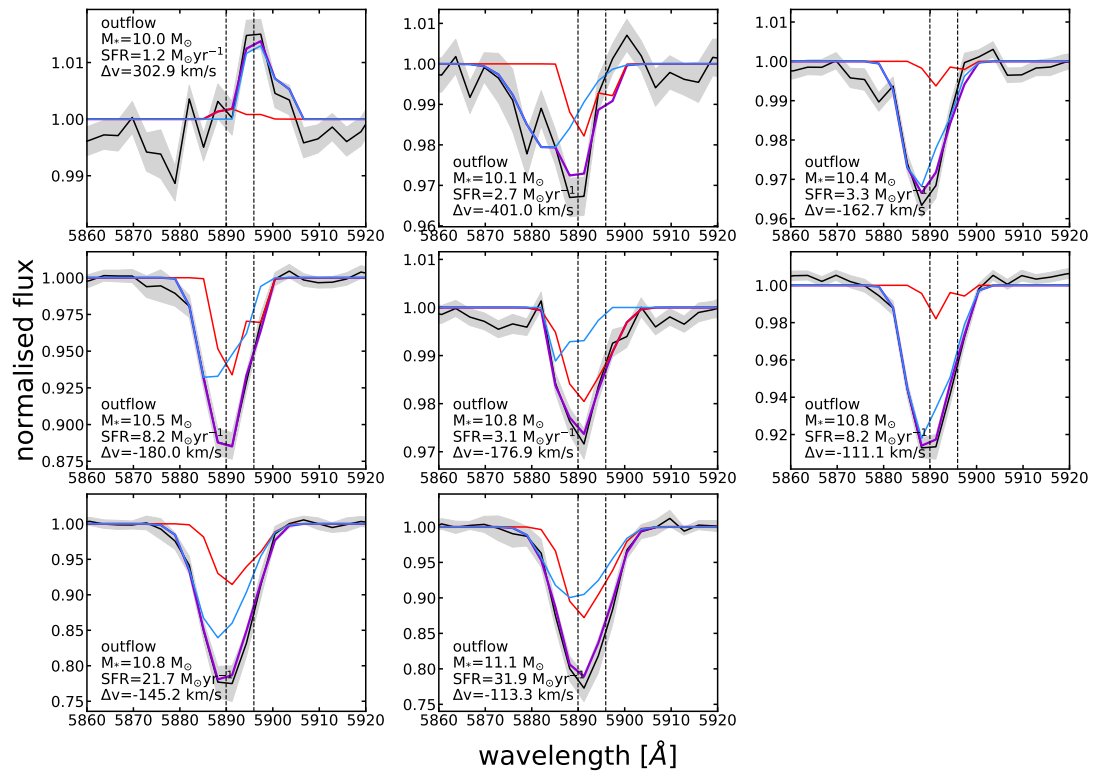


Figure A.1. – continued.

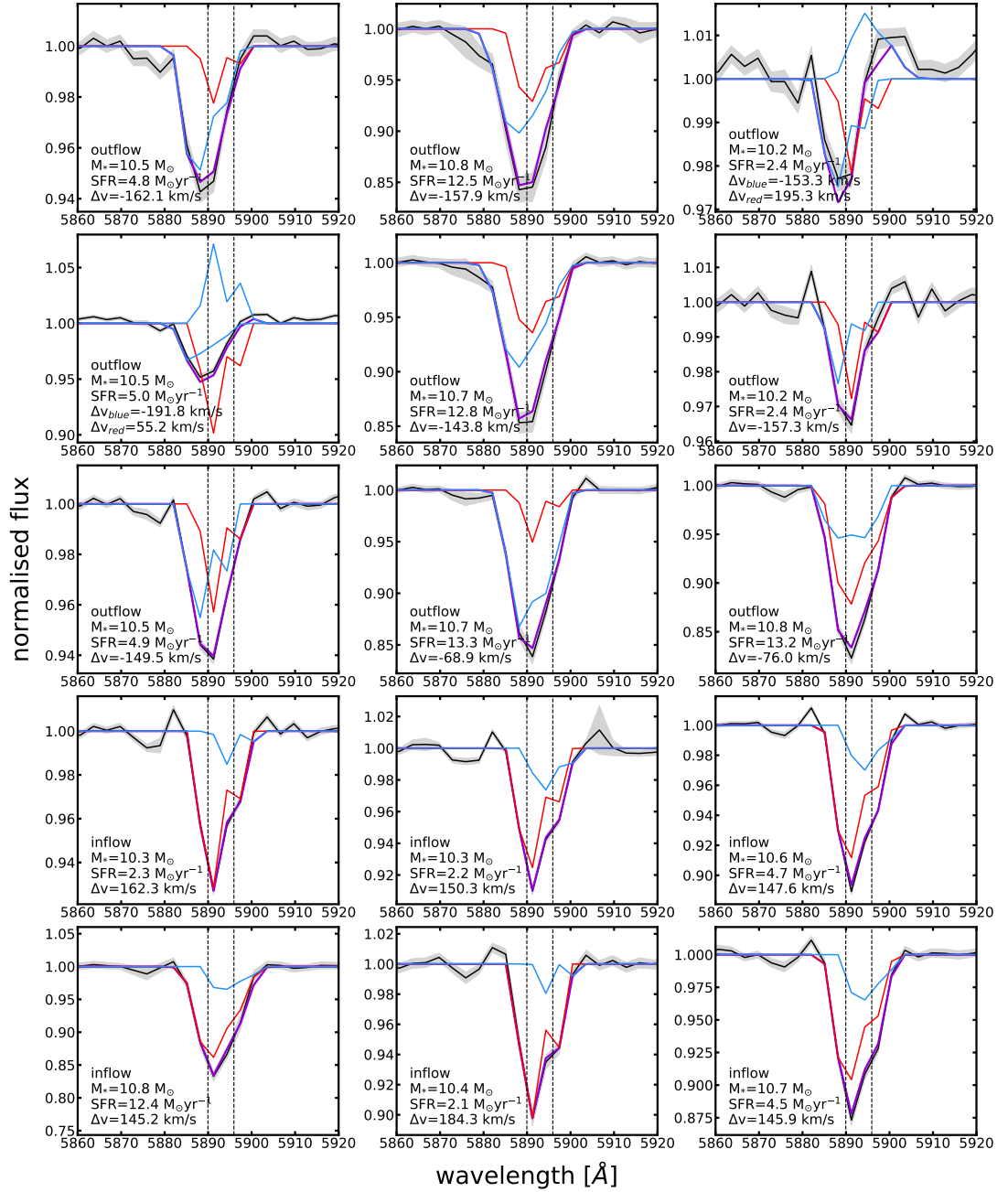


Figure A.1. – continued.

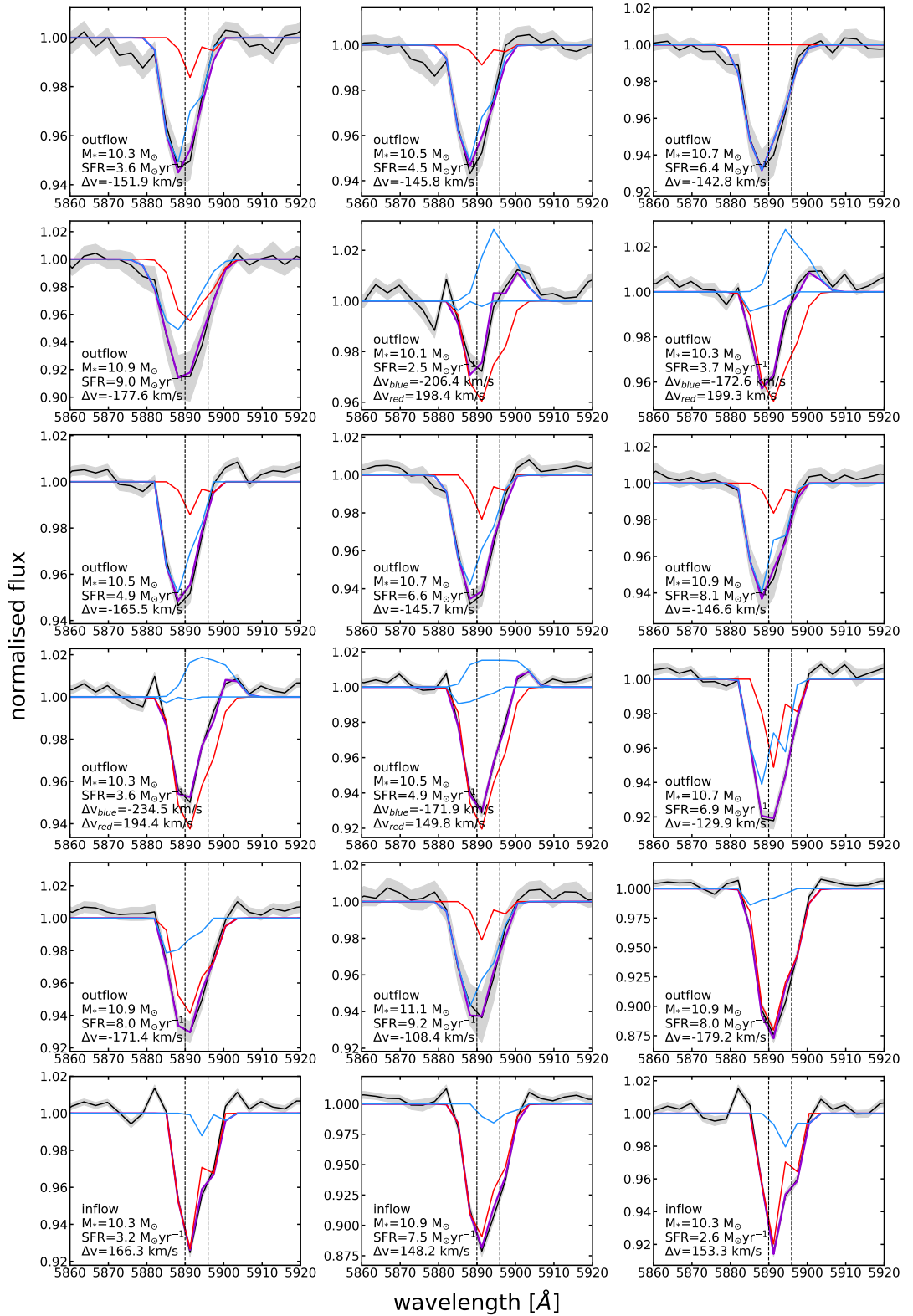


Figure A.1. – continued.

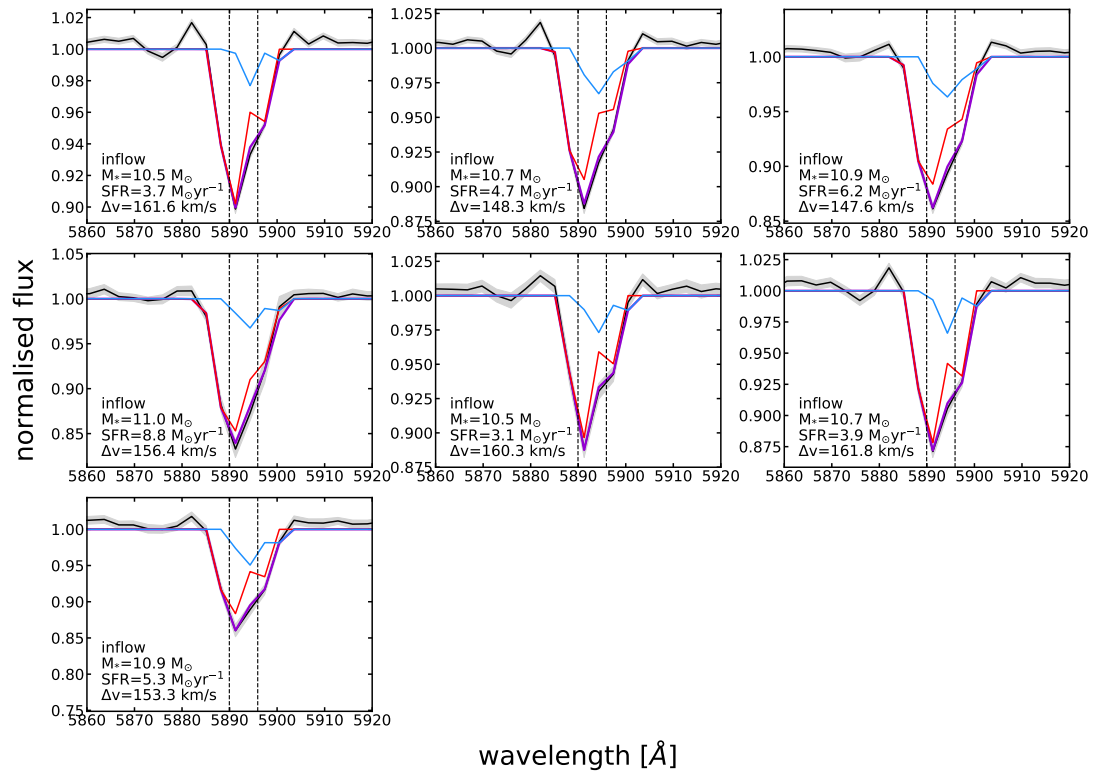


Figure A.1. – continued.

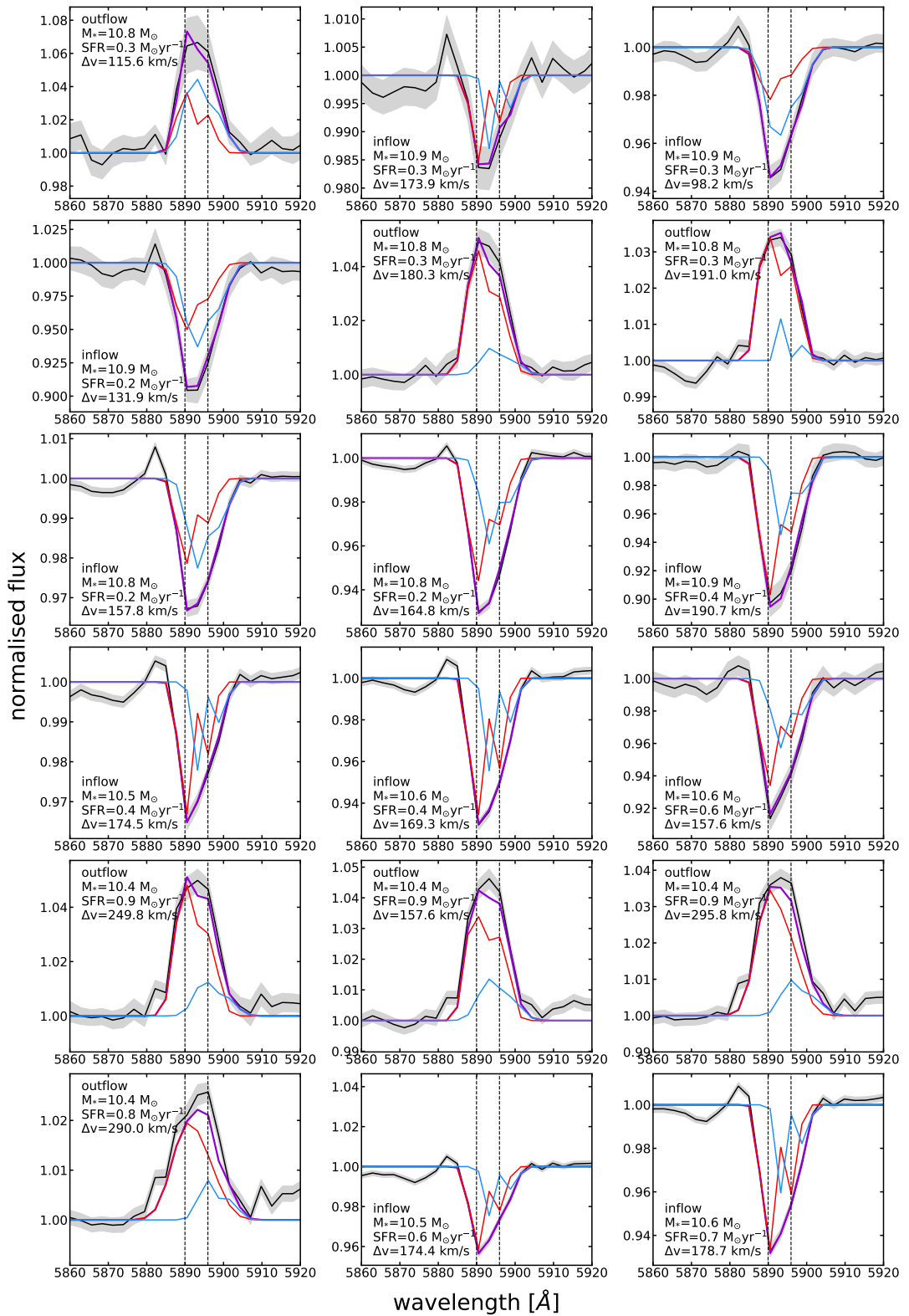


Figure A.2. The same as Figure A.1 but for the AGN sample.

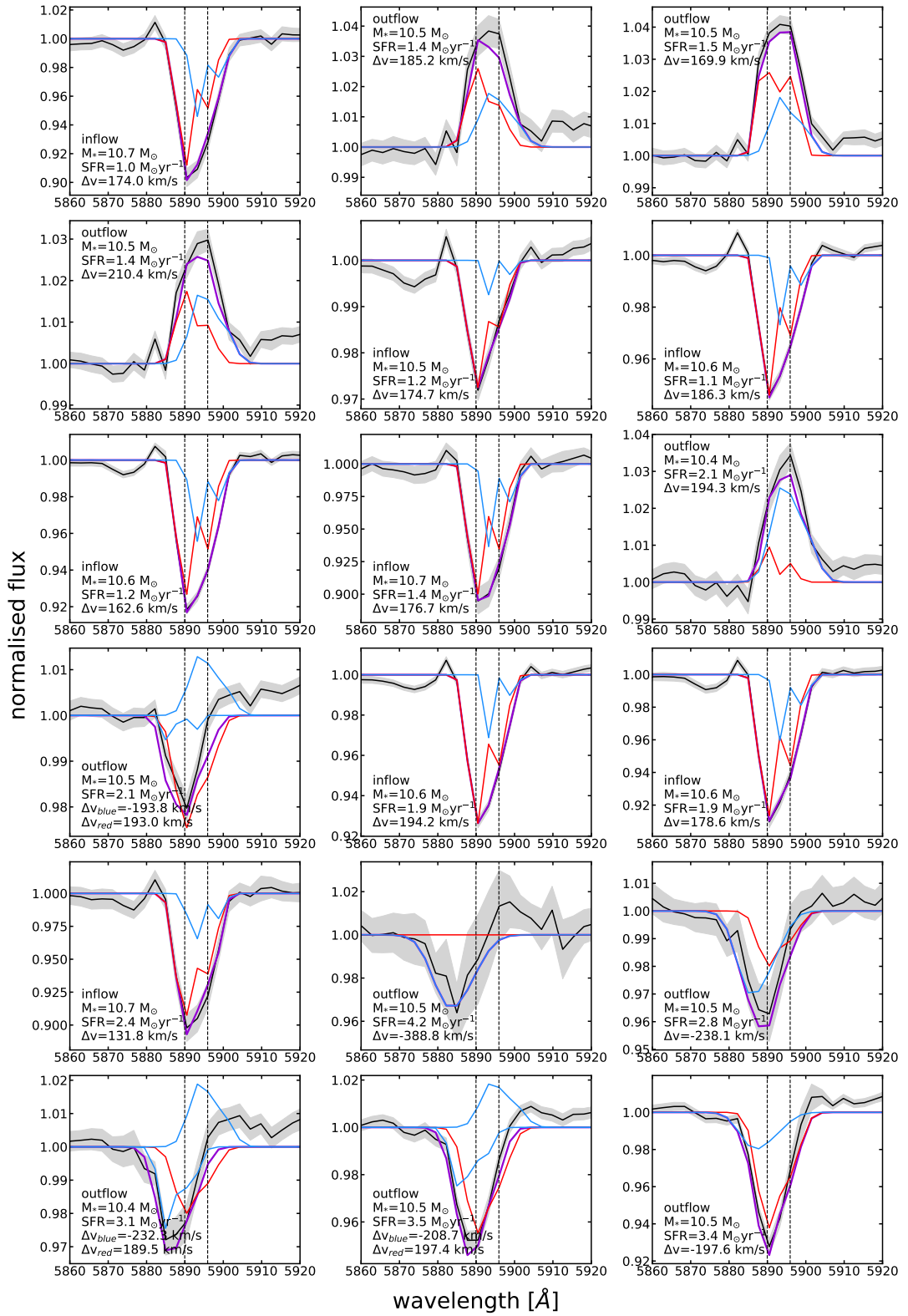


Figure A.2. – continued.

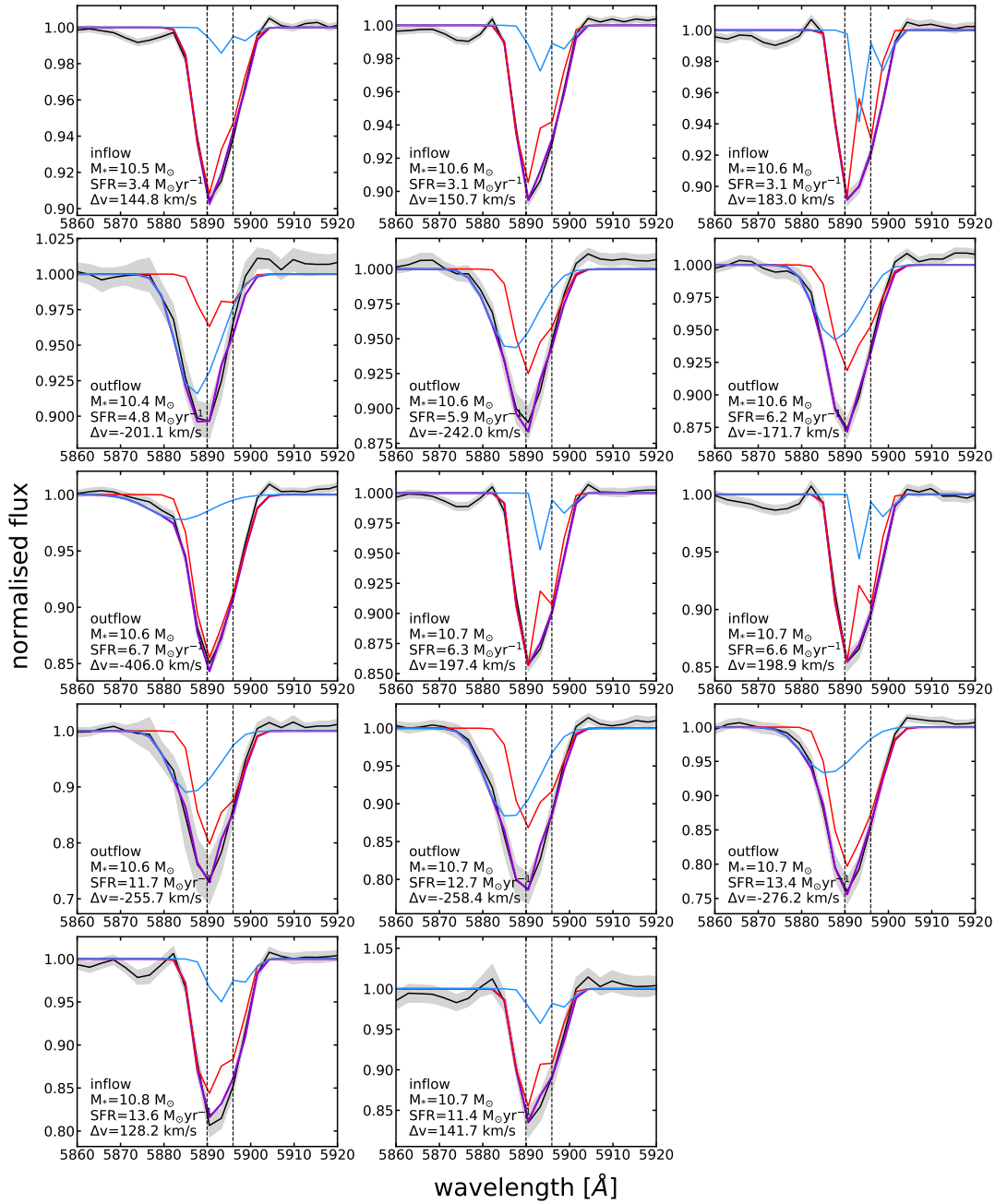


Figure A.2. – continued.

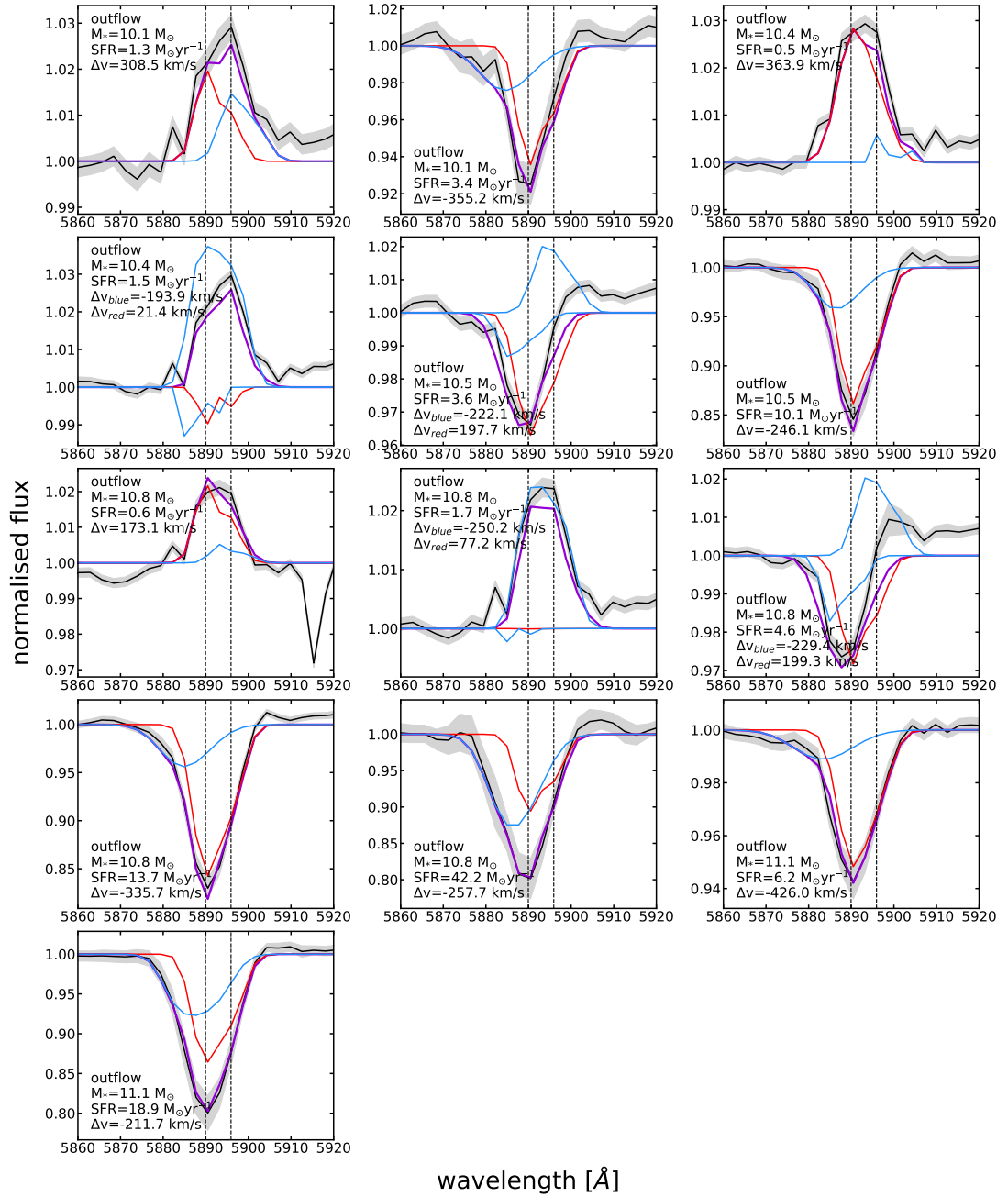


Figure A.2. – continued.

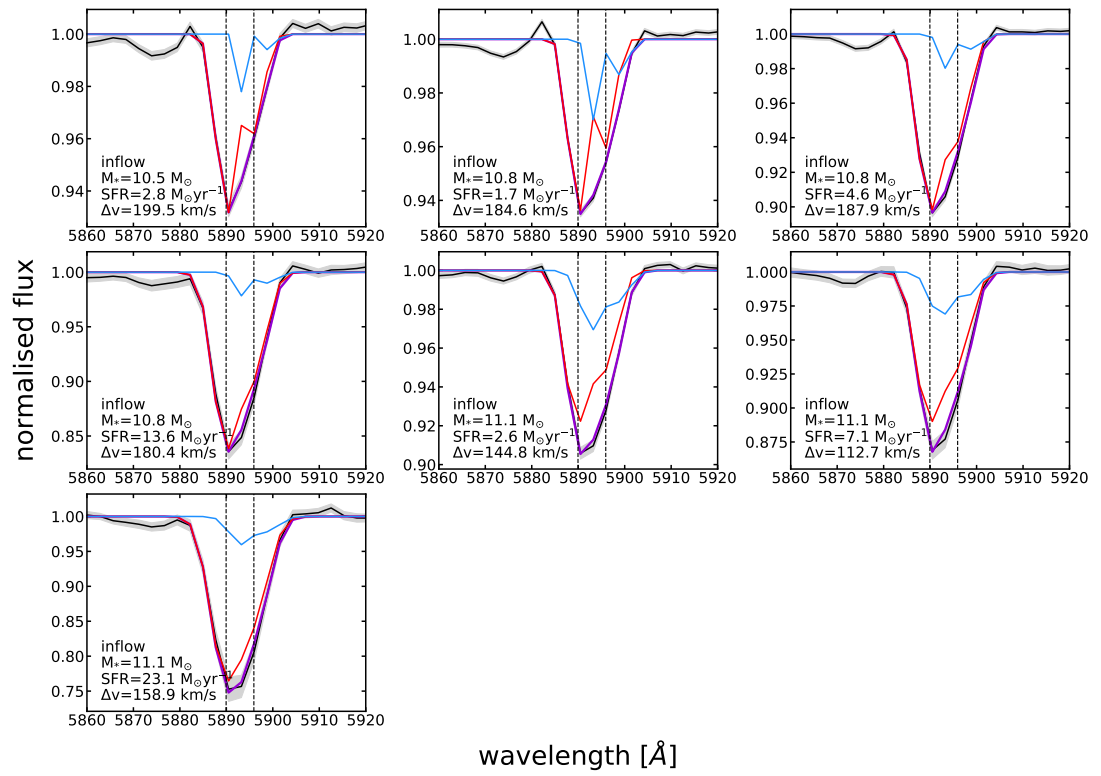


Figure A.2. – continued.

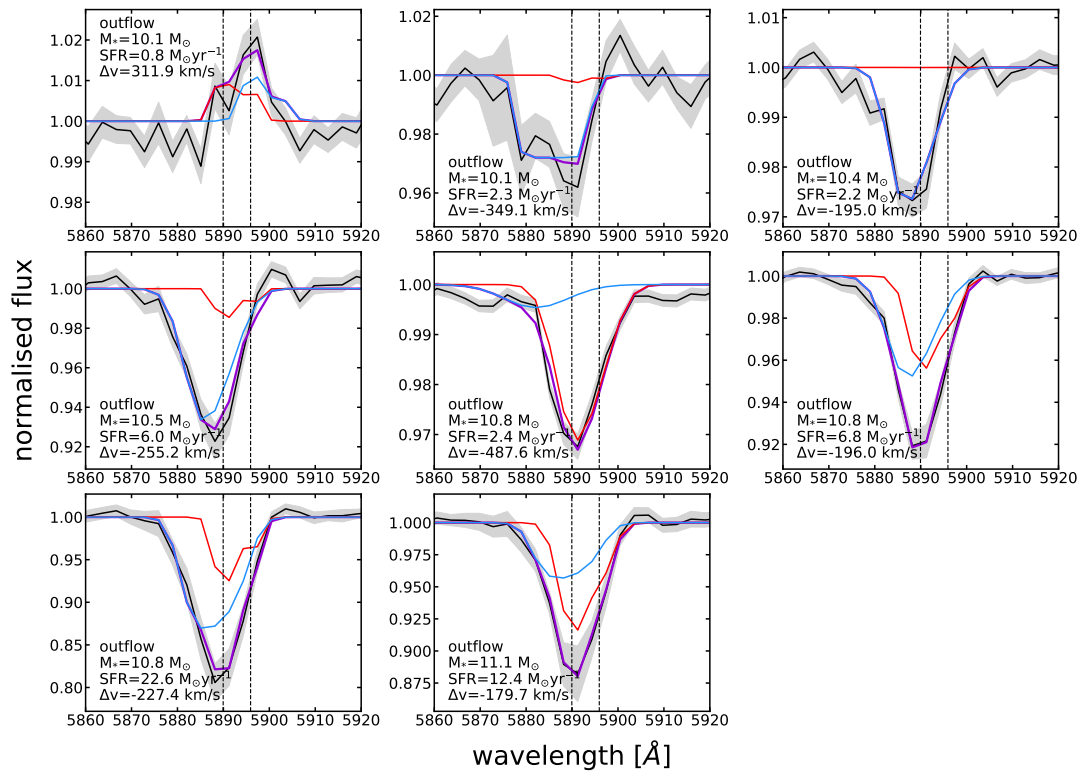


Figure A.2. – continued.

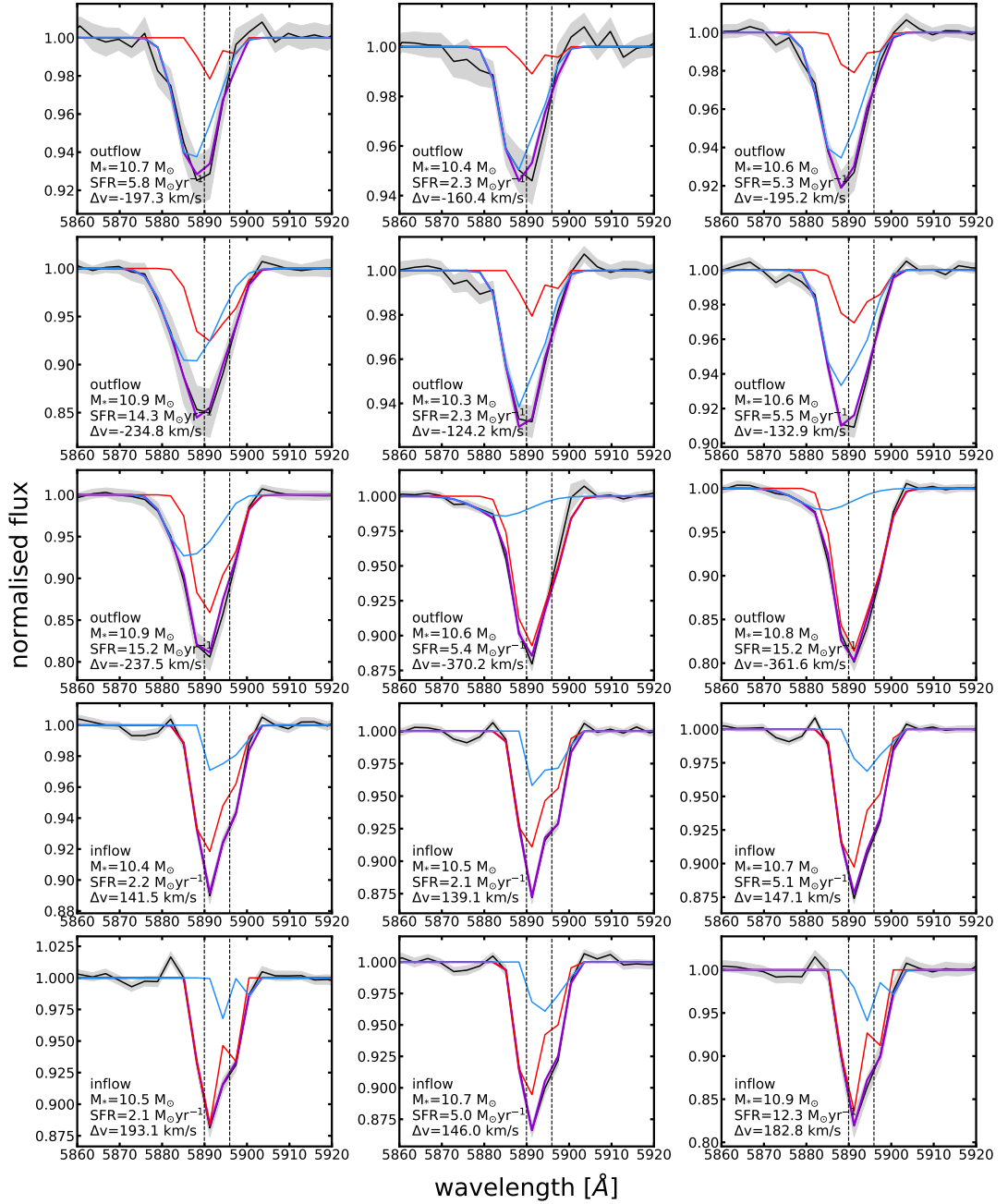


Figure A.2. – continued.

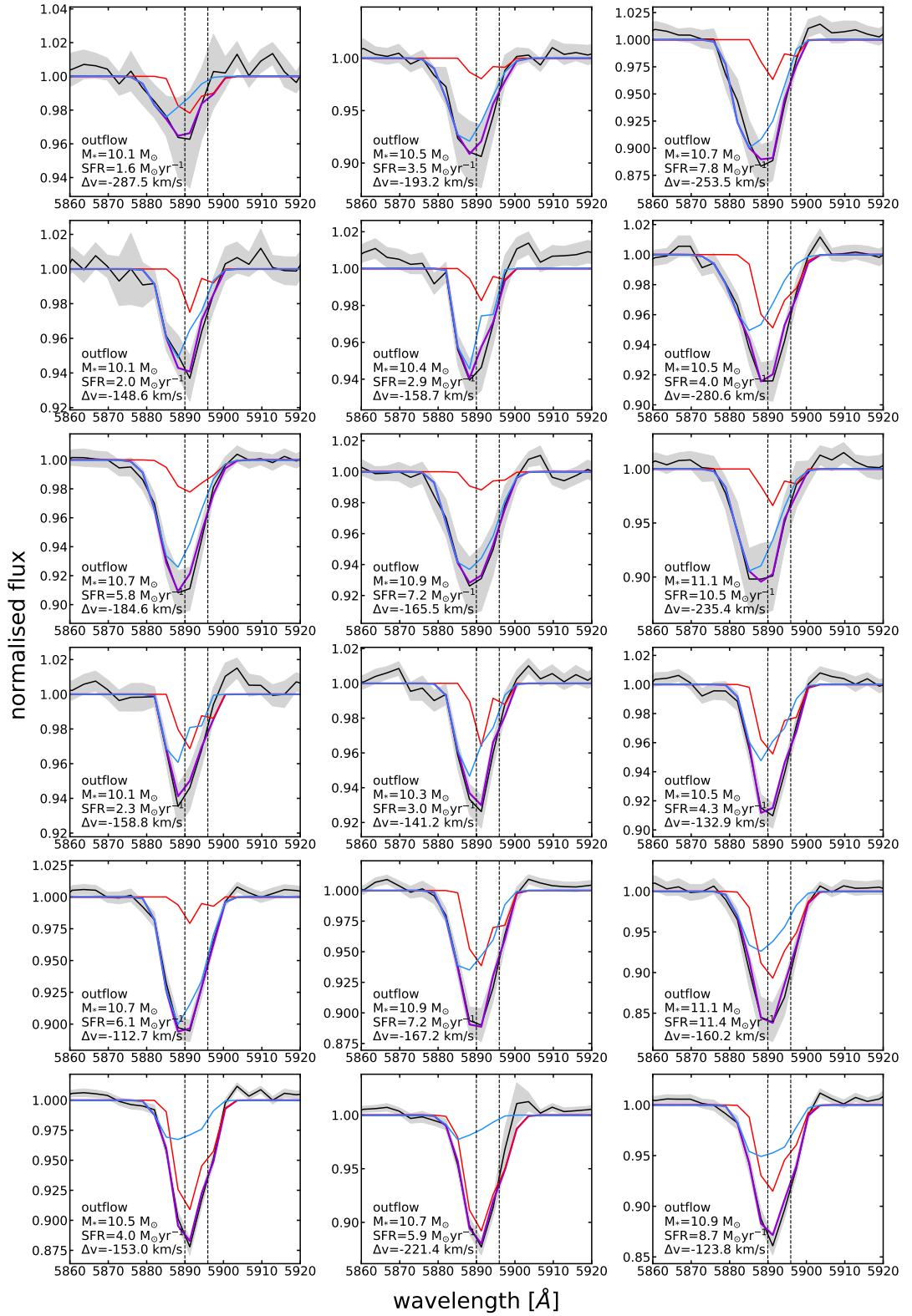


Figure A.2. – continued.

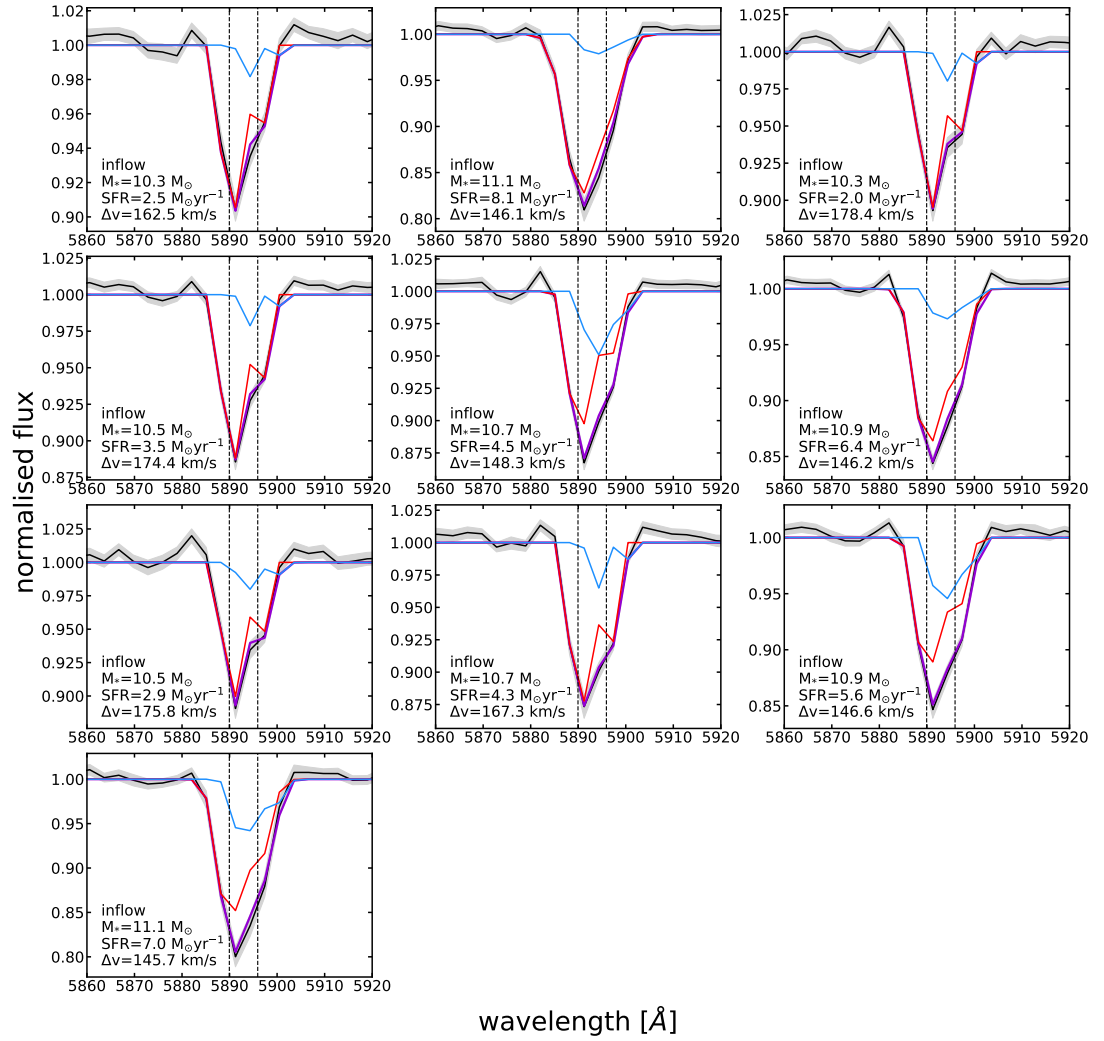


Figure A.2. – continued.

Appendix B

Appendix B

B.1 MaNGA Galaxy Properties

We present here the main global properties of MaNGA DR15 galaxies identified to host either an outflow or inflow in the central regions of the galaxy, whose properties were used in the sample selection. Quantities with superscript *a* mark quantities derived from the NSA catalog, whilst quantities with superscript *b* are derived from the Pipe3D catalog. SFRs and stellar masses are integrated quantities, whilst the line ratios refer to measurements in the central 2.5'' of the galaxy.

Table B.1: The global properties of galaxies identified to host outflows in their central regions.

Plate ID	IFU	RA ^a [deg]	DEC ^a [deg]	z^a	$\log M_*^b$ [M_\odot]	$\log \text{SFR}^b$ [$M_\odot \text{ yr}^{-1}$]	$\log [\text{O III}]/\text{H}\alpha^b$	$\log [\text{N II}]/\text{H}\beta^b$	i^a [deg]	Type
7815	3702	317.90320	11.49694	0.02938	10.47	0.43	-0.73	-0.36	27.49	outflow
8077	3702	41.84637	0.05876	0.02478	10.12	-0.10	-0.59	-0.37	23.92	outflow
8085	3704	51.15552	-0.44402	0.03684	10.72	0.66	-0.74	-0.44	44.23	outflow
8134	1901	113.40018	45.94338	0.07665	10.98	1.29	-0.63	-0.49	27.01	outflow
8146	1901	117.05387	28.22509	0.02706	10.38	0.42	-0.69	-0.43	22.85	outflow
8147	6103	119.03950	26.87578	0.06161	11.06	1.00	-0.72	-0.48	36.35	outflow
8149	3704	120.20722	27.50036	0.01734	10.30	0.62	-0.55	-0.43	32.84	outflow
8155	3703	54.09596	-0.88266	0.02358	10.18	0.27	-0.11	-0.52	25.01	outflow
8253	3703	157.34358	43.17059	0.02726	10.32	0.39	-0.72	-0.47	45.99	outflow
8254	1902	163.21911	43.42840	0.02424	10.09	0.02	-0.81	-0.37	27.02	outflow
8262	9102	184.55357	44.17324	0.02453	10.66	0.72	-0.80	-0.34	39.23	outflow
8309	6104	211.78062	52.96374	0.04333	10.21	0.33	-0.50	-0.53	38.35	outflow
8311	3703	205.01217	23.14297	0.03168	10.84	0.60	-0.40	-0.34	34.63	outflow
8312	12702	245.27087	39.91739	0.03203	10.70	0.52	-0.51	-0.30	43.71	outflow
8312	12703	247.20906	39.83509	0.03585	10.83	0.73	-0.46	-0.36	16.04	outflow
8313	12701	239.49180	41.79259	0.03547	10.78	0.72	-0.52	-0.45	47.27	outflow
8313	12702	240.67742	41.19726	0.03334	10.73	1.06	-0.69	-0.49	48.87	outflow

8317	6102	194.92503	43.75318	0.05781	11.13	1.16	-0.36	-0.39	35.55	outflow
8329	6104	213.11048	45.69041	0.02700	10.54	0.73	-0.43	-0.32	31.33	outflow
8332	3702	207.87281	43.80643	0.03331	10.56	0.67	-0.28	-0.39	39.89	outflow
8333	3701	214.34452	42.28797	0.06861	10.84	0.72	-0.40	-0.34	27.82	outflow
8446	6104	206.54141	36.50439	0.05524	10.54	0.84	-0.52	-0.46	37.46	outflow
8454	12702	153.04902	45.14216	0.07643	11.13	1.40	-0.33	-0.36	44.77	outflow
8454	6104	154.82544	45.81359	0.06348	11.07	1.12	-0.47	-0.33	34.15	outflow
8455	3701	157.17946	39.83888	0.02929	10.34	0.60	-0.58	-0.38	41.65	outflow
8465	12705	198.23632	47.45663	0.02814	10.81	0.11	-0.44	-0.34	47.01	outflow
8465	9102	198.18916	46.93499	0.02768	10.40	0.12	-0.83	-0.47	33.48	outflow
8486	6101	238.03955	46.31979	0.05887	10.88	0.60	-0.44	-0.33	43.53	outflow
8550	12703	247.67443	40.52939	0.02981	10.49	0.05	-0.65	-0.33	31.70	outflow
8550	9102	247.20906	39.83509	0.03585	10.81	0.73	-0.46	-0.35	16.04	outflow
8551	12705	233.94092	44.83480	0.02964	10.59	0.79	-0.56	-0.40	26.90	outflow
8554	3704	184.62322	35.62226	0.03490	10.44	0.35	-0.60	-0.45	29.22	outflow
8588	6101	248.45676	39.26321	0.03176	10.88	0.67	-0.41	-0.34	16.10	outflow
8600	1901	242.58522	43.00964	0.02521	10.19	0.48	-0.16	-0.58	46.99	outflow
8611	3702	261.46394	60.19412	0.02905	10.51	0.13	-0.53	-0.35	41.79	outflow
8616	3703	322.51023	0.46420	0.13506	11.15	1.21	-0.56	-0.38	28.05	outflow
8618	3704	318.86229	9.75782	0.07023	10.94	0.82	-0.59	-0.41	10.25	outflow
8624	9102	263.89258	59.88992	0.02836	10.55	0.27	-0.54	-0.36	48.19	outflow

8626	12703	265.10878	56.70125	0.06928	10.92	0.66	-0.34	-0.33	41.12	outflow
8626	3703	264.66254	56.82424	0.02942	10.33	0.51	-0.45	-0.44	38.56	outflow
8715	9101	119.91012	51.79236	0.05338	10.72	0.63	-0.63	-0.35	48.18	outflow
8725	3703	125.82096	45.89686	0.05373	10.64	0.59	-0.59	-0.34	44.09	outflow
8725	6102	125.45904	45.51964	0.05417	10.66	0.87	-0.66	-0.33	22.84	outflow
8940	1902	120.98713	25.48072	0.07278	11.10	1.29	-0.60	-0.38	29.88	outflow
8945	3702	173.36190	47.28673	0.04555	10.05	0.65	0.07	-0.67	29.13	outflow
8977	9102	119.20025	33.25448	0.06756	10.86	1.16	-0.47	-0.46	35.26	outflow
8992	12704	172.63126	51.45594	0.02559	10.55	0.48	-0.77	-0.52	40.50	outflow
9026	3703	249.34435	44.34712	0.03069	10.48	0.66	-0.87	-0.51	19.68	outflow
9028	9101	243.02559	28.49887	0.05318	10.83	0.84	-0.84	-0.45	27.34	outflow
9029	12702	247.25172	41.28426	0.03189	10.80	0.57	-0.66	-0.49	33.56	outflow
9029	1902	246.48724	41.52207	0.04272	10.03	0.01	-0.74	-0.32	22.29	outflow
9033	1902	223.21854	45.23480	0.13265	11.16	1.27	-0.55	-0.41	37.88	outflow
9033	3703	222.93490	47.86576	0.04988	10.56	0.53	-0.45	-0.35	27.50	outflow
9035	6102	236.65444	43.68365	0.10117	11.03	1.18	-0.55	-0.40	47.29	outflow
9041	9102	235.94192	28.41521	0.03275	10.66	0.67	-0.55	-0.46	33.55	outflow
9042	12703	235.15268	28.51244	0.03275	10.71	0.23	-0.62	-0.37	46.84	outflow
9044	6101	230.68698	29.76960	0.02292	10.24	0.39	-0.78	-0.47	33.96	outflow
9049	9102	248.38654	25.96446	0.04532	10.33	0.35	-0.79	-0.40	18.95	outflow
9088	12704	242.74641	26.34917	0.06459	10.95	0.59	-0.53	-0.39	33.25	outflow

9095	1901	242.81005	24.22502	0.03253	10.62	0.76	-0.72	-0.32	40.78	outflow
9182	1902	120.64756	38.74119	0.11639	11.13	1.21	-0.86	-0.38	33.58	outflow
9195	1902	28.60509	12.66317	0.04466	10.31	0.59	-0.51	-0.40	22.21	outflow
9195	6104	28.96659	14.94028	0.04382	11.00	1.12	-0.59	-0.48	44.11	outflow
9485	1901	120.77803	37.02356	0.07122	10.96	1.40	-0.62	-0.41	16.15	outflow
9487	12703	125.08855	45.53436	0.05413	10.68	0.79	-0.59	-0.41	45.79	outflow
9490	3704	122.51965	19.74559	0.04485	10.32	0.34	-0.27	-0.46	33.68	outflow
9491	12704	119.53574	19.55015	0.06159	10.81	0.88	-0.82	-0.50	41.37	outflow
9491	6101	119.17438	17.99117	0.04124	10.90	1.30	-0.28	-0.34	46.30	outflow
9493	9102	130.93325	22.96240	0.06155	10.82	0.81	-0.60	-0.40	32.95	outflow
9494	3704	128.01990	21.62863	0.05376	10.75	0.95	-0.53	-0.31	44.86	outflow
9506	3701	133.56990	27.26653	0.06378	11.06	1.40	-0.70	-0.46	24.30	outflow
9508	6101	127.13102	26.34868	0.05303	10.59	1.30	-0.39	-0.37	30.04	outflow
9509	1901	122.38423	26.28342	0.02542	10.14	0.26	-0.54	-0.43	37.66	outflow
9869	9102	247.25661	40.53487	0.02785	10.51	0.04	-0.52	-0.31	49.73	outflow
9871	12705	228.37217	42.33025	0.02795	10.63	0.37	-0.68	-0.51	38.57	outflow
9881	3702	203.81165	25.04475	0.02609	10.40	0.31	-0.70	-0.40	31.59	outflow
9883	9102	256.64139	33.69298	0.03015	10.45	0.48	-0.60	-0.33	46.58	outflow
9888	12705	236.90138	26.06377	0.03158	10.94	1.00	-0.55	-0.38	43.63	outflow
7977	9102	332.83066	12.18472	0.06309	10.93	0.83	-0.42	-0.35	49.52	inflow
8081	9101	47.77218	-0.54654	0.02820	10.60	0.32	-0.32	-0.36	49.93	inflow

8084	3702	50.63664	-0.00121	0.02174	10.23	0.43	-0.14	-0.39	41.58	inflow
8322	1901	198.78425	30.40377	0.02315	10.38	0.51	-0.58	-0.33	34.58	inflow
8602	3701	247.36154	38.41940	0.03053	10.18	-0.11	-0.59	-0.38	44.22	inflow
8717	3704	117.51833	34.47932	0.02901	10.60	1.03	-0.68	-0.41	39.23	inflow
8726	3703	116.92145	22.78161	0.02789	10.49	0.55	-0.69	-0.41	28.92	inflow
8952	12705	206.03612	26.34891	0.06507	10.86	0.74	-0.55	-0.40	48.67	inflow
9095	9102	243.08489	23.00202	0.03226	10.65	0.49	-0.55	-0.40	43.45	inflow
9491	1902	120.04224	19.23433	0.07821	11.08	0.85	-0.53	-0.39	39.52	inflow
9497	3703	117.99588	21.70878	0.04990	10.54	0.71	-0.34	-0.34	48.30	inflow
9500	12702	132.59833	25.95408	0.02765	10.64	0.27	-0.53	-0.32	49.67	inflow
9508	6103	127.34368	26.65689	0.05661	10.90	0.54	-0.44	-0.42	46.05	inflow
9868	12705	218.87457	46.20239	0.07314	10.96	1.00	-0.22	-0.40	49.46	inflow

Appendix C

Appendix C

C.1 Spectra from xCOLD GASS, xGASS and ALFALFA

In this Appendix we present plots of the SDSS images, xCOLD GASS CO(1-0) spectra and xGASS/ALFALFA HI spectra of a random selection of 10 galaxies from the sample described in Section 5.2.

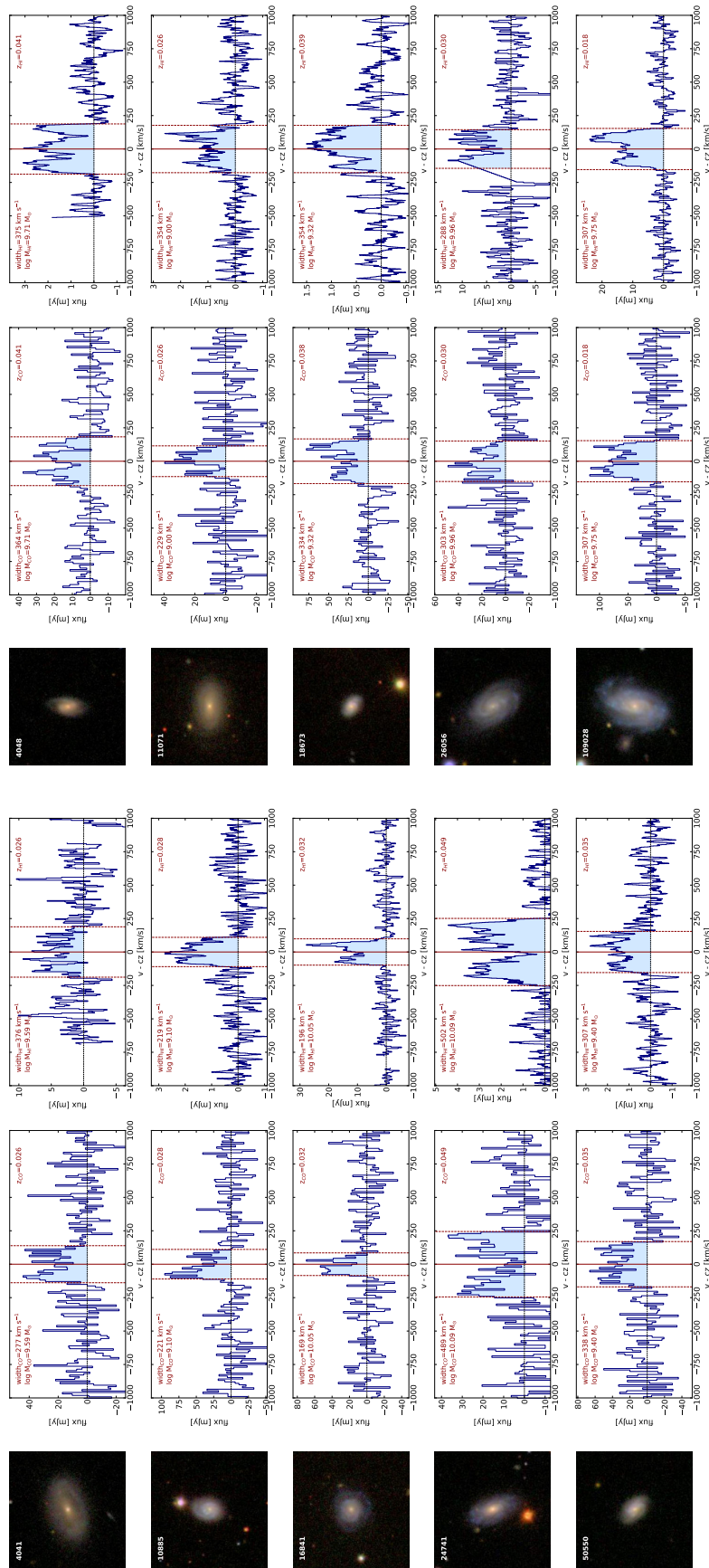


Figure C.1. The 1.25'x1.25' SDSS image (left), IRAM 30m CO(1-0) spectrum (middle) and Arecibo HI 21 cm spectra for 10 random galaxies from the selected sample defined in Section 5.2. Each spectrum has been checked for confusion (within a normalised velocity of ± 5) and baseline issues and the quoted widths and velocities are those measured in the study.

Appendix D

Appendix D

D.1 NIR Sérsic Fit and Potential Lens Morphology

Here we present the morphological analysis of ACT J2029 using the Pan-STARRS data presented in Section 6.2.2. We used the two-dimensional profile fitting tool GALFIT (Peng et al. 2002, 2010a) to study the morphology of the lensing galaxy in the Pan-STARRS *i*-band image. A single component, elliptical Sérsic profile provided a reasonable fit to the morphology resulting in an effective radius of $1.54'' \pm 0.01''$, a Sérsic index of 0.59 ± 0.01 , and an axial ratio of 0.75 ± 0.01 at a position angle of $29^\circ \pm 1^\circ$. The small value of the Sérsic index indicates a fairly compact galaxy. The interesting feature of the fit is the pattern of residuals that appear in the difference image (data minus model) shown in Figure D.1. There is an arc-like excess toward the north/northeast about $1.5''$ from the fitted center of the galaxy and another, more compact, excess $\sim 0.4''$ southwest of the center. We estimate the summed intensity of these features to be at least one magnitude fainter than the lensing galaxy. These results are suggestive (but not definitive) of NIR emission from the background lensed galaxy. Higher resolution imaging will be needed to confirm this.

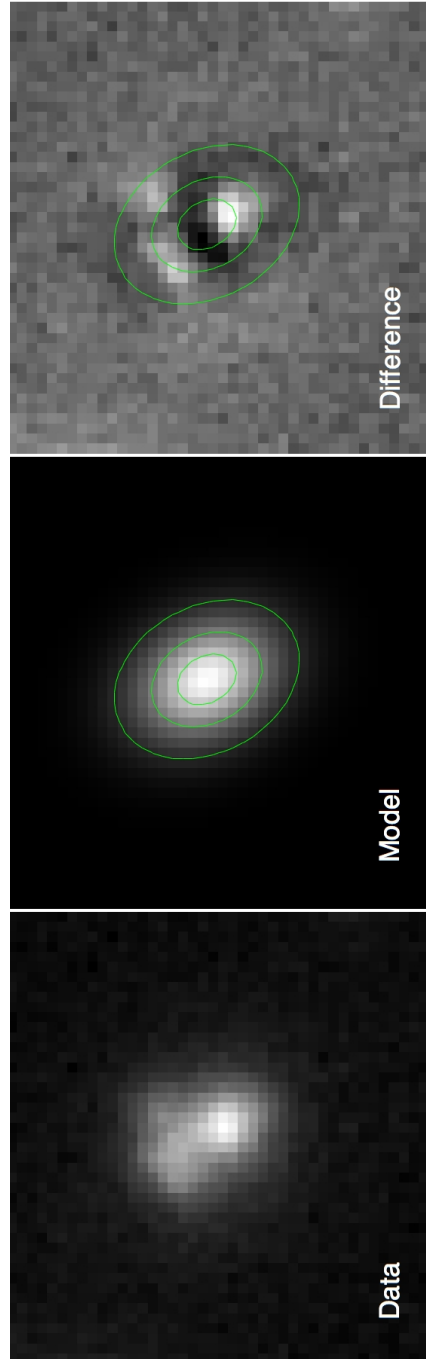


Figure D.1. The GALFIT analysis of the foreground galaxy in the Pan-STARRS i -band image. The left panel shows the i -band image, centered on ACT J2029, the middle panel shows the GALFIT Sérsic profile fit of the foreground galaxy, and the right panel shows the difference between the left and middle panels (ie., the data minus the model). NIR excess can be seen towards the northeast and southwest of the center.

Bibliography

Abazajian K. N., et al., 2009, [The Astrophysical Journal Supplement Series](#), 182, 543

Abdurro'uf Akiyama M., 2017, [MNRAS](#), 469, 2806

Alagband-Zadeh S., et al., 2013, [MNRAS](#), 435, 1493

Alatalo K., et al., 2011, [ApJ](#), 735, 88

Alatalo K., et al., 2013, [MNRAS](#), 432, 1796

Aller L. H., Goldberg L., 1971, Atoms, stars, and nebulae

Anglés-Alcázar D., et al., 2017, [MNRAS](#), 470, 4698

Aravena M., et al., 2016, [MNRAS](#), 457, 4406

Baldry I. K., et al., 2004, [ApJ](#), 600, 681

Baldry I. K., et al., 2006, [MNRAS](#), 373, 469

Baldwin J. A., et al., 1981, [PASP](#), 93, 5

Ball N. M., et al., 2008, [MNRAS](#), 383, 907

Balogh M. L., et al., 2004, [ApJ](#), 615, L101

Barger A. J., et al., 1998, [Nature](#), 394, 248

Battisti A. J., et al., 2016, [ApJ](#), 818, 13

Behroozi P. S., et al., 2013, [ApJ](#), 770, 57

Bell E. F., et al., 2003, [The Astrophysical Journal Supplement Series](#), 149, 289

Bell E. F., et al., 2004, [ApJ](#), 608, 752

- Bertin E., Arnouts S., 1996, *Astronomy and Astrophysics Supplement Series*, 117, 393
- Bigiel F., Blitz L., 2012, *ApJ*, 756, 183
- Bigiel F., et al., 2008, *AJ*, 136, 2846
- Bigiel F., et al., 2016, *ApJ*, 822, L26
- Blain A. W., et al., 2002, *Physics Reports*, 369, 111
- Blanton M. R., et al., 2003, *ApJ*, 594, 186
- Blumenthal G. R., et al., 1984, *Nature*, 311, 517
- Bolzonella M., et al., 2000, *A&A*, 363, 476
- Boomsma R., et al., 2008, *A&A*, 490, 555
- Bothwell M. S., et al., 2013a, *MNRAS*, 429, 3047
- Bothwell M. S., et al., 2013b, *MNRAS*, 433, 1425
- Bothwell M. S., et al., 2013c, *ApJ*, 779, 67
- Bouché N., et al., 2010, *ApJ*, 718, 1001
- Brinchmann J., et al., 2004, *MNRAS*, 351, 1151
- Bruzual G., Charlot S., 2003, *MNRAS*, 344, 1000
- Buchner J., et al., 2014, *A&A*, 564, A125
- Buckley D. A. H., et al., 2006, in *Society of Photo-Optical Instrumentation Engineers (SPIE) Conference Series*. p. 62670Z, doi:10.1117/12.673750
- Bundy K., et al., 2015, *ApJ*, 798, 7
- Burgh E. B., et al., 2003, in Iye M., Moorwood A. F. M., eds, *Society of Photo-Optical Instrumentation Engineers (SPIE) Conference Series Vol. 4841, Instrument Design and Performance for Optical/Infrared Ground-based Telescopes*. pp 1463–1471, doi:10.1117/12.460312
- Calzetti D., et al., 2000, *ApJ*, 533, 682

- Cannon J. M., et al., 2005, *ApJ*, 618, 247
- Cano-Díaz M., et al., 2012, *A&A*, 537, L8
- Cano-Díaz M., et al., 2016, *ApJ*, 821, L26
- Cappellari M., 2017, *MNRAS*, 466, 798
- Cappellari M., Emsellem E., 2004, *PASP*, 116, 138
- Carniani S., et al., 2015, *A&A*, 580, A102
- Carniani S., et al., 2016, *A&A*, 591, A28
- Carniani S., et al., 2017, *A&A*, 605, A105
- Carter M., et al., 2012, *A&A*, 538, A89
- Casey C. M., et al., 2012a, *ApJ*, 761, 139
- Casey C. M., et al., 2012b, *ApJ*, 761, 140
- Casey C. M., et al., 2014, *Physics Reports*, 541, 45
- Catinella B., et al., 2018, *MNRAS*, 476, 875
- Cazzoli S., et al., 2016, *A&A*, 590, A125
- Chambers K. C., et al., 2016, arXiv e-prints, p. [arXiv:1612.05560](https://arxiv.org/abs/1612.05560)
- Chapman S. C., et al., 2005, *ApJ*, 622, 772
- Chary R., Elbaz D., 2001, *ApJ*, 556, 562
- Chen Y.-M., et al., 2010, *AJ*, 140, 445
- Chevalier R. A., Clegg A. W., 1985, *Nature*, 317, 44
- Chisholm J., et al., 2016, *MNRAS*, 457, 3133
- Chisholm J., et al., 2017, *MNRAS*, 469, 4831
- Chung A., et al., 2011, *ApJ*, 732, L15
- Cicone C., et al., 2012, *A&A*, 543, A99

-
- Cicone C., et al., 2014, *A&A*, 562, A21
- Cicone C., et al., 2016, *A&A*, 588, A41
- Coil A. L., et al., 2011, *ApJ*, 743, 46
- Coleman G. D., et al., 1980, *The Astrophysical Journal Supplement Series*, 43, 393
- Colless M., et al., 2001, *MNRAS*, 328, 1039
- Combes F., et al., 2013, *A&A*, 558, A124
- Concas A., et al., 2017, arXiv e-prints, p. [arXiv:1710.08423](https://arxiv.org/abs/1710.08423)
- Crawford S. M., et al., 2010, in *Observatory Operations: Strategies, Processes, and Systems III*. p. 773725, [doi:10.1117/12.857000](https://doi.org/10.1117/12.857000)
- Cresci G., et al., 2015, *ApJ*, 799, 82
- Croom S. M., et al., 2012, *MNRAS*, 421, 872
- Daddi E., et al., 2007, *ApJ*, 670, 156
- Daddi E., et al., 2015, *A&A*, 577, A46
- Davé R., et al., 2012, *MNRAS*, 421, 98
- Davies R. L., et al., 2019a, *ApJ*, 873, 122
- Davies R. L., et al., 2019b, *ApJ*, 873, 122
- Dekel A., et al., 2009, *Nature*, 457, 451
- Dekel A., et al., 2013, *MNRAS*, 435, 999
- Elbaz D., et al., 2007, *A&A*, 468, 33
- Ellison S. L., et al., 2018, *MNRAS*, 474, 2039
- Erickson N., et al., 2007, in Baker A. J., et al., eds, *Astronomical Society of the Pacific Conference Series Vol. 375, From Z-Machines to ALMA: (Sub)Millimeter Spectroscopy of Galaxies*. p. 71
- Faber S. M., et al., 2007, *ApJ*, 665, 265

-
- Feroz F., et al., 2009, [MNRAS](#), 398, 1601
- Feruglio C., et al., 2010, [A&A](#), 518, L155
- Fioc M., Rocca-Volmerange B., 1997, [A&A](#), 500, 507
- Fiore F., et al., 2017, [A&A](#), 601, A143
- Fluetsch A., et al., 2018, arXiv e-prints, p. [arXiv:1805.05352](#)
- Förster Schreiber N. M., et al., 2018, arXiv e-prints, p. [arXiv:1807.04738](#)
- Fraternali F., Binney J. J., 2006, [MNRAS](#), 366, 449
- Fraternali F., Binney J. J., 2008, [MNRAS](#), 386, 935
- Fraternali F., et al., 2002, [AJ](#), 123, 3124
- Gallagher R., et al., 2018, arXiv e-prints, p. [arXiv:1806.03311](#)
- García-Burillo S., et al., 2014, [A&A](#), 567, A125
- García-Burillo S., et al., 2015, [A&A](#), 580, A35
- Genzel R., et al., 2014, [ApJ](#), 796, 7
- Giocoli C., et al., 2010, [MNRAS](#), 404, 502
- Giovanelli R., et al., 1994, [AJ](#), 107, 2036
- Glenn J., et al., 2015, [ApJ](#), 800, 105
- Gonçalves T. S., et al., 2012, [ApJ](#), 759, 67
- González Delgado R. M., et al., 2016, [A&A](#), 590, A44
- Goto T., Toft S., 2015, [A&A](#), 579, A17
- Guo H., et al., 2016, [MNRAS](#), 459, 3040
- Harris A. I., et al., 2012, [ApJ](#), 752, 152
- Haynes M. P., et al., 2011, [AJ](#), 142, 170
- Haynes M. P., et al., 2018, [ApJ](#), 861, 49

- Heald G. H., et al., 2007, *ApJ*, 663, 933
- Heckman T. M., 2002, in Mulchaey J. S., Stocke J. T., eds, *Astronomical Society of the Pacific Conference Series Vol. 254, Extragalactic Gas at Low Redshift*. p. 292 ([arXiv:astro-ph/0107438](https://arxiv.org/abs/astro-ph/0107438))
- Heckman T. M., et al., 2000, *The Astrophysical Journal Supplement Series*, 129, 493
- Heckman T. M., et al., 2015, *ApJ*, 809, 147
- Hezaveh Y. D., et al., 2012, *ApJ*, 761, 20
- Ho I. T., et al., 2014, *MNRAS*, 444, 3894
- Ho I. T., et al., 2016, *MNRAS*, 457, 1257
- Ho S. H., et al., 2017, *ApJ*, 835, 267
- Hodge J. A., et al., 2012, *ApJ*, 760, 11
- Hsieh B. C., et al., 2017, *ApJ*, 851, L24
- Hughes D. H., et al., 1998, *Nature*, 394, 241
- Ilbert O., et al., 2010, *ApJ*, 709, 644
- Ilbert O., et al., 2013, *A&A*, 556, A55
- Israel F. P., et al., 2014, *A&A*, 562, A96
- Israel F. P., et al., 2015, *A&A*, 578, A95
- Ivison R. J., et al., 2011, *MNRAS*, 412, 1913
- Jacoby G. H., et al., 1984, *The Astrophysical Journal Supplement Series*, 56, 257
- Jones M. G., et al., 2015, *MNRAS*, 449, 1856
- Kamphuis P., 2008, PhD thesis, University of Groningen
- Karim A., et al., 2011, *ApJ*, 730, 61
- Kassin S. A., et al., 2007, *ApJ*, 660, L35
- Kauffmann G., et al., 2003a, *MNRAS*, 341, 33

- Kauffmann G., et al., 2003b, [MNRAS](#), 346, 1055
- Kaviraj S., et al., 2013, [MNRAS](#), 429, L40
- Kennicutt Robert C. J., 1998, [ApJ](#), 498, 541
- Kereš D., et al., 2005, [MNRAS](#), 363, 2
- Kewley L. J., et al., 2006, [MNRAS](#), 372, 961
- Kinney A. L., et al., 1996, [ApJ](#), 467, 38
- Kobulnicky H. A., et al., 2003, in Iye M., Moorwood A. F. M., eds, Society of Photo-Optical Instrumentation Engineers (SPIE) Conference Series Vol. 4841, Instrument Design and Performance for Optical/Infrared Ground-based Telescopes. pp 1634–1644, [doi:10.1117/12.460315](#)
- Kornei K. A., et al., 2012, [ApJ](#), 758, 135
- Kroupa P., 2001, [MNRAS](#), 322, 231
- Krug H. B., et al., 2010, [ApJ](#), 708, 1145
- Le Borgne J.-F., et al., 2003, [A&A](#), 402, 433
- Leroy A. K., et al., 2008, [AJ](#), 136, 2782
- Li C., White S. D. M., 2009, [MNRAS](#), 398, 2177
- Lilly S. J., et al., 2013, [ApJ](#), 772, 119
- Liu G., et al., 2015, [The Astrophysical Journal Supplement Series](#), 221, 9
- López-Cobá C., et al., 2019, [MNRAS](#), 482, 4032
- Madau P., Dickinson M., 2014, [Annual Review of Astronomy and Astrophysics](#), 52, 415
- Magdis G. E., et al., 2010, [ApJ](#), 714, 1740
- Magdis G. E., et al., 2012, [ApJ](#), 760, 6
- Magnelli B., et al., 2011, [A&A](#), 528, A35
- Magnelli B., et al., 2013, [A&A](#), 553, A132

-
- Maiolino R., et al., 2012, [MNRAS](#), 425, L66
- Maiolino R., et al., 2017, [Nature](#), 544, 202
- Maragkoudakis A., et al., 2017, [MNRAS](#), 466, 1192
- Marasco A., Fraternali F., 2011, [A&A](#), 525, A134
- Marasco A., et al., 2012, [MNRAS](#), 419, 1107
- Maraston C., Strömbäck G., 2011, [MNRAS](#), 418, 2785
- Marinacci F., et al., 2010, [MNRAS](#), 404, 1464
- Martin C. L., 2005, [ApJ](#), 621, 227
- Martin D. C., et al., 2007, [The Astrophysical Journal Supplement Series](#), 173, 342
- Martin C. L., et al., 2012, [ApJ](#), 760, 127
- Masters K. L., et al., 2010, [MNRAS](#), 404, 792
- Masters K. L., et al., 2019, arXiv e-prints, p. [arXiv:1901.05579](#)
- Matthews L. D., Wood K., 2003, [ApJ](#), 593, 721
- Menanteau F., et al., 2013, [ApJ](#), 765, 67
- Michałowski M., et al., 2010, [A&A](#), 514, A67
- Mo H. J., White S. D. M., 2002, [MNRAS](#), 336, 112
- Morton D. C., 1991, [The Astrophysical Journal Supplement Series](#), 77, 119
- Muratov A. L., et al., 2015, [MNRAS](#), 454, 2691
- Murphy E. J., et al., 2011, [ApJ](#), 732, 126
- Muzzin A., et al., 2013, [ApJ](#), 777, 18
- Nedelchev B., et al., 2017, arXiv e-prints, p. [arXiv:1705.07994](#)
- Netzer H., 2009, [MNRAS](#), 399, 1907
- Newman S. F., et al., 2012, [ApJ](#), 761, 43

-
- Noeske K. G., et al., 2007, *ApJ*, 660, L43
- O'Donnell J. E., 1994, *ApJ*, 422, 158
- Oke J. B., Gunn J. E., 1983, *ApJ*, 266, 713
- Olsen K. P., et al., 2015, *ApJ*, 814, 76
- Oosterloo T., et al., 2007, *AJ*, 134, 1019
- Oppenheimer B. D., Davé R., 2008, *MNRAS*, 387, 577
- Oppenheimer B. D., et al., 2010, *MNRAS*, 406, 2325
- Osterbrock D. E., 1989, *Astrophysics of gaseous nebulae and active galactic nuclei*
- Ostriker E. C., Shetty R., 2011, *ApJ*, 731, 41
- Pellegrini E. W., et al., 2013, *ApJ*, 779, L19
- Peng C. Y., et al., 2002, *AJ*, 124, 266
- Peng C. Y., et al., 2010a, *AJ*, 139, 2097
- Peng Y.-j., et al., 2010b, *ApJ*, 721, 193
- Phillips A. C., 1993, *AJ*, 105, 486
- Planck Collaboration et al., 2016, *A&A*, 594, A13
- Polletta M., et al., 2007, *ApJ*, 663, 81
- Pozzetti L., et al., 2007, *A&A*, 474, 443
- Prevot M. L., et al., 1984, *A&A*, 132, 389
- Prochaska J. X., et al., 2011, *ApJ*, 734, 24
- Rawle T. D., et al., 2014, *ApJ*, 783, 59
- Rich J. A., et al., 2011, *ApJ*, 734, 87
- Rich J. A., et al., 2015, *ApJSS*, 221, 28
- Roberts-Borsani G. W., Saintonge A., 2019, *MNRAS*, 482, 4111

- Roberts-Borsani G. W., et al., 2017, *ApJ*, 844, 110
- Rodighiero G., et al., 2010, *A&A*, 518, L25
- Rodighiero G., et al., 2011, *ApJ*, 739, L40
- Rodighiero G., et al., 2014, *MNRAS*, 443, 19
- Rodríguez del Pino B., et al., 2019, *MNRAS*, 486, 344
- Rosenberg M. J. F., et al., 2015, *ApJ*, 801, 72
- Rossa J., Dettmar R. J., 2003a, *A&A*, 406, 493
- Rossa J., Dettmar R. J., 2003b, *A&A*, 406, 505
- Rubin K. H. R., et al., 2012, *ApJ*, 747, L26
- Rubin K. H. R., et al., 2014, *ApJ*, 794, 156
- Rupke D. S. N., Veilleux S., 2015, *ApJ*, 801, 126
- Rupke D. S., et al., 2005a, *The Astrophysical Journal Supplement Series*, 160, 87
- Rupke D. S., et al., 2005b, *The Astrophysical Journal Supplement Series*, 160, 115
- Rupke D. S. N., et al., 2017, *ApJ*, 850, 40
- Saintonge A., et al., 2012, *ApJ*, 758, 73
- Saintonge A., et al., 2013, *ApJ*, 778, 2
- Saintonge A., et al., 2016, *MNRAS*, 462, 1749
- Saintonge A., et al., 2017, *The Astrophysical Journal Supplement Series*, 233, 22
- Salim S., et al., 2007, *The Astrophysical Journal Supplement Series*, 173, 267
- Sánchez-Blázquez P., et al., 2006, *MNRAS*, 371, 703
- Sánchez S. F., et al., 2012, *A&A*, 538, A8
- Sánchez S. F., et al., 2013, *A&A*, 554, A58
- Sánchez S. F., et al., 2016a, *Rev. Mex. Astron. Astrofis.*, 52, 21

-
- Sánchez S. F., et al., 2016b, *Rev. Mex. Astron. Astrofis.*, **52**, 171
- Sargent M. T., et al., 2012, *ApJ*, **747**, L31
- Sarzi M., et al., 2016, *MNRAS*, **456**, L25
- Savage B. D., Sembach K. R., 1996, *Annual Review of Astronomy and Astrophysics*, **34**, 279
- Schawinski K., et al., 2014, *MNRAS*, **440**, 889
- Schaye J., et al., 2015, *MNRAS*, **446**, 521
- Schlegel D. J., et al., 1998, *ApJ*, **500**, 525
- Schmidt M., 1959, *ApJ*, **129**, 243
- Schreiber C., et al., 2015, *A&A*, **575**, A74
- Schruba A., et al., 2011, *AJ*, **142**, 37
- Shapiro P. R., Field G. B., 1976, *ApJ*, **205**, 762
- Sharon C. E., et al., 2016, *ApJ*, **827**, 18
- Shen S., et al., 2003, *MNRAS*, **343**, 978
- Silk J., Mamon G. A., 2012, *Research in Astronomy and Astrophysics*, **12**, 917
- Silva L., et al., 1998, *ApJ*, **509**, 103
- Simons R. C., et al., 2015, *MNRAS*, **452**, 986
- Skrutskie M. F., et al., 2006, *AJ*, **131**, 1163
- Smail I., et al., 1997, *ApJ*, **490**, L5
- Solomon P. M., et al., 1992, *ApJ*, **398**, L29
- Solomon P. M., et al., 1997, *ApJ*, **478**, 144
- Somerville R. S., et al., 2008, *MNRAS*, **391**, 481
- Spilker J. S., et al., 2014, *ApJ*, **785**, 149
- Springob C. M., et al., 2005, *ApJSS*, **160**, 149

-
- Strandet M. L., et al., 2016, [ApJ](#), 822, 80
- Strateva I., et al., 2001, [AJ](#), 122, 1861
- Sturm E., et al., 2011, [ApJ](#), 733, L16
- Sugahara Y., et al., 2017, [ApJ](#), 850, 51
- Swetz D. S., et al., 2011, [The Astrophysical Journal Supplement Series](#), 194, 41
- Tacconi L. J., et al., 2013, [ApJ](#), 768, 74
- Talbot M. S., et al., 2018, [MNRAS](#), 477, 195
- Tiley A. L., et al., 2016, [MNRAS](#), 461, 3494
- Tomczak A. R., et al., 2016, [ApJ](#), 817, 118
- Tremonti C. A., et al., 2004, [ApJ](#), 613, 898
- Tremonti C. A., et al., 2007, [ApJ](#), 663, L77
- Usero A., et al., 2015, [AJ](#), 150, 115
- Vazdekis A., et al., 2010, [MNRAS](#), 404, 1639
- Veilleux S., et al., 2005, [Annual Review of Astronomy and Astrophysics](#), 43, 769
- Veilleux S., et al., 2013, [ApJ](#), 776, 27
- Vieira J. D., et al., 2013, [Nature](#), 495, 344
- Vincent M. B., et al., 2003, in Iye M., Moorwood A. F. M., eds, Society of Photo-Optical Instrumentation Engineers (SPIE) Conference Series Vol. 4841, Instrument Design and Performance for Optical/Infrared Ground-based Telescopes. pp 367–375, [doi:10.1117/12.459488](https://doi.org/10.1117/12.459488)
- Vogelsberger M., et al., 2013, [MNRAS](#), 436, 3031
- Vogelsberger M., et al., 2014, [MNRAS](#), 444, 1518
- Walter F., et al., 2002, [ApJ](#), 580, L21
- Walter F., et al., 2011, [ApJ](#), 730, 18

-
- Weiner B. J., et al., 2006, [ApJ](#), 653, 1027
- Weiner B. J., et al., 2009, [ApJ](#), 692, 187
- Weiß A., et al., 2009, [ApJ](#), 705, L45
- Weiß A., et al., 2013, [ApJ](#), 767, 88
- Westfall K. B., et al., 2019, arXiv e-prints, p. [arXiv:1901.00856](#)
- Whitaker K. E., et al., 2014, [ApJ](#), 795, 104
- Whitaker K. E., et al., 2015, [ApJ](#), 811, L12
- White S. D. M., Rees M. J., 1978, [MNRAS](#), 183, 341
- Wise M. W., Silva D. R., 1996, [ApJ](#), 461, 155
- Wright E. L., et al., 2010, [AJ](#), 140, 1868
- York D. G., et al., 2000, [AJ](#), 120, 1579
- Zschaechner L. K., et al., 2015, [ApJ](#), 799, 61
- Zubovas K., King A. R., 2014, [MNRAS](#), 439, 400
- van de Voort F., et al., 2011, [MNRAS](#), 415, 2782
- van der Tak F. F. S., et al., 2007, [A&A](#), 468, 627
- van der Werf P. P., et al., 2010, [A&A](#), 518, L42